HAL
open science

Numerical Methods and Analysis for Degenerate Parabolic Equations and Reaction-Diffusion Systems

Ricardo Ruiz Baier

To cite this version:

Ricardo Ruiz Baier. Numerical Methods and Analysis for Degenerate Parabolic Equations and Reaction-Diffusion Systems. Modeling and Simulation. Universidad de Concepcion, 2008. English. NNT : . tel-00326395

HAL Id: tel-00326395

https://theses.hal.science/tel-00326395v1

Submitted on 2 Oct 2008

HAL is a multi-disciplinary open access archive for the deposit and dissemination of scientific research documents, whether they are published or not. The documents may come from teaching and research institutions in France or abroad, or from public or private research centers.

L'archive ouverte pluridisciplinaire **HAL**, est destinée au dépôt et à la diffusion de documents scientifiques de niveau recherche, publiés ou non, émanant des établissements d'enseignement et de recherche français ou étrangers, des laboratoires publics ou privés.

Numerical Methods and Analysis for Degenerate Parabolic Equations and Reaction-Diffusion Systems

Ricardo Ruiz Baier

DRAFT October 2, 2008

Tesis para optar al grado de Doctor en Ciencias Aplicadas con Mención en Ingeniería Matemática

Departamento de Ingeniería Matemática
Universidad de Concepción
2008

Universidad de Concepción
Departamento de Ingeniería Matemática
Casilla 160-C, Concepción, Chile
Phone +45 45253351, Fax +45 45882673
rruiz@ing-mat.udec.cl
www.ing-mat.udec.cl

Copyright © 2008 by Ricardo Ruiz Baier
ISSN 0909-3192
All rights reserved

Abstract

This dissertation deals with different aspects of numerical and mathematical analysis of systems of possibly degenerate partial differential equations. Under particular conditions, solutions to these equations in the considered applications exhibit steep gradients, and in the degenerate case, sharp fronts and discontinuities. This calls for a concentration of computational effort in zones of strong variation. To achieve this goal we introduce suitable finite volume methods and fully adaptive multiresolution schemes for spatially one, two and three-dimensional, possibly degenerate reaction-diffusion systems, focusing on sedimentation processes in the mineral industry and traffic flow problems, two and three-dimensional reaction-diffusion systems modelling population dynamics, combustion processes, cardiac propagation and models of pattern formation and chemotaxis in mathematical biology. We are also interested in the study of convergence of the finite volume approximations, and the wellposedness and regularity analysis of weak solutions.

Resumen

Esta tesis trata diferentes aspectos en el análisis numérico y matemático de sistemas de ecuaciones diferenciales parciales parabólicas degeneradas. Los enfoques principales corresponden a extensiones de métodos de multiresolución para resolver numéricamente ecuaciones diferenciales parciales parabólicas en una dimensión espacial, que aparecen naturalmente en el modelamiento de procesos de sedimentación de partículas en la industria minera y en problemas de tráfico vehicular; sistemas de reacción-difusión en dos y tres dimensiones espaciales, que modelan dinámicas de poblaciones, procesos de combustión, propagación de actividad eléctrica en problemas cardiacos, biología celular; convergencia de las soluciones aproximadas obtenidas mediante métodos de volúmenes finitos; y análisis de existencia, unicidad y regularidad de soluciones débiles de los problemas anteriormente mencionados.

Preface

This dissertation was prepared and it is submitted in partial fulfillment of the requirements for acquiring the degree of *Doctor en Ciencias Aplicadas con mención en Ingeniería Matemática*, at the Universidad de Concepción, Chile. Although this thesis has been written as a monograph, it is based on a collection of eight research papers written during the period 2006–2008, and elsewhere submitted for publication. Therefore there might be minor differences in notation between Sections. These papers are listed below:

[7] M. Bendahmane, R. Bürger and R. Ruiz, *A multiresolution space-time adaptive scheme for the bidomain model in electrocardiology*. Math. Biosc., submitted.

[8] M. Bendahmane, R. Bürger and R. Ruiz, *Convergence of a finite volume scheme for cardiac propagation*. Numer. Meth. for PDEs., submitted.

[9] M. Bendahmane, R. Bürger, R. Ruiz and Kai Schneider, *Adaptive multiresolution schemes with local time stepping for two dimensional degenerate reaction-diffusion systems*. Appl. Num. Math., submitted.

[10] M. Bendahmane, R. Bürger, R. Ruiz and K. Schneider, *Adaptive multiresolution schemes for reaction–diffusion systems*, submitted.

[11] M. Bendahmane, R. Bürger, R. Ruiz and J.M. Urbano, *On a doubly nonlinear diffusion model of chemotaxis with prevention of overcrowding*. Math. Methods Appl. Sci., submitted.

[40] R. Bürger, R. Ruiz, K. Schneider and M. Sepúlveda, *Fully adaptive multiresolution schemes for strongly degenerate parabolic equations in one space dimension*. Math. Model. Numer. Anal., 42 (2008), pp. 535–563.

[41] R. Bürger, R. Ruiz, K. Schneider and M. Sepúlveda, *Fully adaptive multiresolution schemes for strongly degenerate parabolic equations with discontinuous flux*. J. Engrg. Math., 60 (2008), pp. 365–385.

[42] R. Bürger, R. Ruiz, K. Schneider, and M. Sepúlveda, *Fully adaptive multiresolution schemes for an extended clarifier–thickener model*, Proc. Appl. Math. Mech., to appear.

Furthermore, the thesis also contains unpublished material. The work presented in this thesis is, to the best of my knowledge and belief, original except as acknowledged in the text. I hereby declare that I have not submitted this material, either in full or in part, for a degree at this or any other institution.

Concepción, December 2008

Ricardo Ruiz Baier

Acknowledgements

Firstly, I would wish to express my gratitude to God Almighty for his everlasting grace and loving forgiveness. *"I still love you Lord, in the same old fashioned way"*. Secondly I thank my family and close friends for their constant support and faith in my scientific career.

I am greatly indebted to my thesis advisors Prof. Raimund Bürger, Prof. Mostafa Bendahmane and to my former advisor Prof. Mauricio Sepúlveda for their helpful suggestions and fruitful discussions. In addition, I wish to thank the valuable advices and encouraging comments (going beyond mathematics most of the time) received from Prof. Gabriel Gatica and Prof. Freddy Paiva. I am also extremely grateful to the rest of the PhD fellows at the *Cabina 6* for their friendship, kindness and for creating a comfortable atmosphere of hard work and collaboration.

I also gratefully acknowledge the invitation and kind hospitality of Prof. José Miguel Urbano from the Center for Mathematics at the University of Coimbra, Portugal and Prof. Kai Schneider from the Laboratoire de Modélisation et Simulation Numerique en Mécanique du CNRS and Centre de Mathématiques et d' Informatique at the Université de Provence, Marseille, France. I truly enjoyed the months spent at these centers.

Next, thanks are also due to the different sources of financial support: Mecesup projects UCO0406 and UCO9907, Dirección de Postgrado de la Universidad de Concepción, CMUC/FCT, Agence Nationale de la Recherche project M2TFP and Conicyt Fellowship.

Last but not least, I would like to express my upmost gratitude to my loving wife Verónica, for her unconditional love. This work is dedicated to her.

Contents

Abstract **i**

Resumen ***(in spanish)*** **iii**

Preface **v**

Acknowledgements **vii**

Introduction **xi**

1 Relevant models and analysis **1**

1.1 Strongly degenerate parabolic equations 1

1.2 Degenerate parabolic equations with discontinuous flux 4

1.3 A class of reaction-diffusion systems 8

1.4 The macroscopic bidomain and monodomain models 11

1.5 Doubly nonlinear chemotaxis model 16

2 Reference finite volume methods **41**

2.1 A FVM for degenerate parabolic equations 41

2.2 A FVM for reaction-diffusion systems 45

2.3 A FVM for the bidomain equations . . . 46

2.4 A FVM for a doubly nonlinear chemotaxis model . . . 63

3 Multiresolution and wavelets **65**

3.1 Wavelet basis and detail coefficients . . . 65

3.2 Graded tree data structure . . . 72

3.3 Choice of the threshold parameter . . . 75

4 Time-step accelerating methods and algorithms **79**

4.1 Local time stepping . . . 79

4.2 A Runge-Kutta-Fehlberg method . . . 82

4.3 A general multiresolution algorithm . . . 84

5 Numerical simulations **87**

5.1 Strongly degenerate parabolic equations . . . 87

5.2 Degenerate parabolic equations with discontinuous flux . . . 102

5.3 A class of reaction-diffusion systems . . . 117

5.4 The monodomain and bidomain models . . . 128

5.5 A doubly nonlinear diffusion model of chemotaxis . . . 142

6 Summary and concluding remarks **153**

Introduction

Mathematical background and motivation

Degenerate parabolic equations arise in the mathematical description of a wide variety of phenomena, not only in the natural sciences but also in engineering and economics. To mention a few examples, consider problems arising in different contexts: gas dynamics, melting processes, certain biological models, the pricing of assets in economics, composite media. Usually the interfaces corresponding to degeneracies in the constitutive function separate different media in the physical problem. The importance of these equations from the applications' viewpoint is equally interesting from that of analysis, since it requires the design of novel techniques to attack the always valid questions of existence, uniqueness and regularity of solutions. This subject is therefore of substantial and growing interest in science and engineering.

In general, even though the nature and origin of the degeneracies may be different, their very presence would imply a weakening the structure and for instance, that the well known regularizing properties of parabolic equations may be lost [150]. Therefore, is of interest to understand the extent to which this weakening of the structure, in the equation at zones where the degeneracies arise, compromises the features of parabolic problems, not only in the analysis, but also in the construction, implementation and validation of numerical methods.

Let us start by devoting particular attention to several kind of applications all having the common ingredient of being modeled by degenerate nonlinear parabolic systems. As we will see throughout this thesis, our study will be highly motivated by these applications, for which we provide a systematic exposition of the main ideas.

Sedimentation processes and traffic flow problems.- Sedimentation processes are of critical importance, especially in the field of solid-liquid separations in the chemical, mining, pulp and paper, wastewater, food, pharmaceutical, ceramic and other industries. Mathematical models for these processes are of obvious theoretical and practical importance. One of the most important breakthroughs in the modelling of mineral processing was Kynch's kinematic sedimentation theory published in 1952. Mathematically, this theory gives rise to a nonlinear first-order scalar conservation law for the local solids concentration. Extensions of this theory include continuous sedimentation, flocculent and polydisperse suspensions, vessels with varying cross-section, centrifuges, several space dimensions [31]. Here we are specifically interested in a theory of sedimentation-consolidation processes of flocculated suspensions outlined in [18]. In these models, the behavior of the local solids concentration is governed by a strongly degenerate parabolic equation. On the

other hand, the well-known Lighthill-Whitham-Richards (LWR) kinematic traffic flow model [110, 130] for unidirectional flow on a single-lane highway is based on the principle of conservation of cars, governed by a one-dimensional conservation law. Over the years, numerous extensions and improvements of the LWR model have been proposed, including the diffusively corrected kinematic wave model (DCKWM) [123] which extends the LWR model by introducing a strongly degenerating diffusion term. From the model viewpoint, this extension accounts for the drivers' delay in their response to events, and an anticipating distance, which means that drivers adjust their velocity to the density seen the mentioned distance ahead. This model can be further extended to include abruptly changing road surface conditions [32]. The result is a strongly degenerate convection-diffusion equation, where the diffusion term, accounting for the drivers' behavior, is effective only where the local car density exceeds a critical value, and the convective flux function depends discontinuously on the location. In [32] the authors introduce an appropriate entropy solution concept defining generalized solutions, uniqueness of these solutions, and existence for a particular subcase (namely, the case where the diffusion does not involve a discontinuous parameter) by a convergence proof for a simple upwind difference scheme. We mention the relevant work of Carrillo [43] that permit applying Kružkov's "doubling of the variables" technique to strongly degenerate parabolic equations. Solutions of strongly degenerate parabolic equations, which include scalar conservation laws as a special case, are in general discontinuous, and need to be defined as weak solutions along with an entropy condition to select the physically relevant weak solution. This property excludes the application of standard numerical schemes for uniformly parabolic equations having smooth solutions; rather, appropriate schemes are based on finite volume schemes for hyperbolic conservation laws. In addition, the local nature of the processes involved calls for numerical methods considering both space and time adaptivity.

A degenerate reaction-diffusion system and some applications.- Reaction-diffusion systems are mathematical models that describe how the concentration of one or more substances distributed in space changes under the influence of two processes: local chemical reactions in which the substances are converted into each other, and diffusion which causes the substances to spread out in space. As this description implies, reaction-diffusion systems are naturally applied in chemistry. However, the equations can also describe dynamical processes of non-chemical nature. Examples are found in biology, geology, finance and physics. Mathematically, reaction-diffusion systems take the form of semi-linear parabolic partial differential equations [155]. First consider an initial-boundary value problem for a scalar reaction-diffusion equation with zero-flux boundary conditions, which may serve as a scalar prototype degenerate reaction-diffusion model. For the non-degenerate case, in a biological setting, this system corresponds to the population dynamics of the spruce band-worm [121], and models the growth of the population by a logistic expression and the rate of mortality due to predation by other species. Most standard spatial models of population dynamics simply assume constant diffusion, where the diffusion coefficient measures the dispersal efficiency of the species. Motivated by Witelski [154], who advanced degenerate diffusion in the context of population dynamics, we utilize herein a strongly degenerate diffusion coefficient. The introduction of strongly degenerate diffusion gives rise to difficulties in the wellposedness analysis, specifically in the correct formulation of the zero flux boundary conditions. For the case of non-homogeneous Dirichlet boundary conditions, however, Mascia, Porretta, and Terracina [112] demonstrated existence and uniqueness of L^∞ entropy solutions. As an extension of the applications of a simple thermo-diffusive model describing a combustion process, as those considered e.g. in [132, 133], we are interested in the simulation of the interaction between *flame balls*. A flame ball denotes a slowly propagating spherical flame structure in a premixed gaseous mixture, and the phenomenon is modeled by a reaction-diffusion system characterized by single-step Arrhenius kinetics and radiative heat losses. In this kind of settings, only diffusion, radiation, and chemical reaction interact. Because buoyant convection can destroy such structures, usually these processes are experimentally studied in weak gravity fields. On the other hand, similar governing equations also arises in mathematical biology as a well-known reaction-diffusion system modelling the interaction between two chemical species. Under certain conditions, it produces stationary solutions with Turing-type spatial patterns [121, 147] and a standard proof of existence and uniqueness can be found for instance in [25]. As in the previous case, here we introduce strongly degenerate diffusion coefficients and it turns out that, even if the stability analysis does *not* apply to the degenerate case, we numerically

observe the phenomenon of pattern formation. Again the problem from the wellposedness viewpoint in the degenerate case, is the presence of zero-flux boundary conditions. A successful technique for proving uniqueness of (entropy weak) solutions to degenerate parabolic equations with Dirichlet boundary condition is based on Kružkov's method [105].

These equations produce solutions that vary smoothly wherever the solution causes the PDE to be parabolic, but produce sharp fronts, or even discontinuities, close to solution values at which the equation degenerates, so suitable methods coming from the community of hyperbolic equations are a proper device to efficiently capture these fronts. In these cases an adaptive strategy is extremely useful, especially when the front is well localized in space, since fine grids are only needed in small subregions of the computational domain, e.g. in the region of the thin flame front. On the other hand, chemical reactions are known to involve a large range of temporal scales, especially in long-time evolutions. Then an adaptive time stepping strategy would be also recommendable.

The macroscopic bidomain model.- The obvious difficulty of performing direct measurements in electrocardiology has motivated wide interest in the numerical simulation of cardiac models. In 1952, Hodgkin and Huxley [91] introduced the first mathematical model of wave propagation in squid nerve, which was modified later on to describe several phenomena in biology. This led to the first physiological model of cardiac tissue [124] and many others. Among these models, the *bidomain model*, firstly introduced by Tung [146], is one of the most accurate and complete models for the theoretical and numerical study of the electric activity in cardiac tissue. The bidomain equations result from the principle of conservation of current between the intra- and extracellular domains, followed by a homogenization process (see e.g. [12, 54, 102]) derived from a scaled version of a cellular model on a periodic structure of cardiac tissue. Mathematically, the bidomain model is a coupled system consisting of a scalar, possibly degenerate parabolic PDE coupled with a scalar elliptic PDE for the transmembrane potential and the extracellular potential, respectively. These equations are supplemented by a time-dependent ODE for the so-called gating variable, which is defined at every point of the spatial computational domain. Here, the term "bidomain" reflects that in general, the intra- and extracellular tissues have different longitudinal and transversal (with respect to the fiber) conductivities; if these are equal, then the model is termed *monodomain model*, and the elliptic PDE reduces to an algebraic equation. The degenerate structure of the mathematical formulation of the bidomain model is essentially due to the differences between the intra- and extracellular anisotropy of the cardiac tissue [12, 57]. We also stress that standard theory for coupled parabolic–elliptic systems (see e.g. [47]) does not apply naturally for the analysis of the bidomain equations, since the anisotropies of the intra and extracellular media differ and the resulting system is of degenerate parabolic type. Colli Franzone and Savaré [57] present a weak formulation for the bidomain model and show that it has a structure suitable to apply the theory of evolution variational inequalities in Hilbert spaces. Bendahmane and Karlsen [12] prove existence and uniqueness for the bidomain equations using, for the existence part, the Faedo-Galerkin method and compactness theory, and Bourgault, Coudière, and Pierre [23] prove existence and uniqueness for the bidomain equations, first reformulating the problem into a single parabolic PDE and then applying a semigroup approach.

From a computational viewpoint, the bidomain model represents a challenge since the width of an excitation front is roughly two orders of magnitude smaller than the long axis of a human-size right ventricle. This local feature, along with strongly varying time scales in the reaction terms, produces solutions with sharp propagating wave fronts in the potential field, which almost precludes simulations with uniform grids. Clearly, cardiac simulations should be based on space- (and also time-) adaptive methods. Substantial contributions have been made in space adaptivity for cardiac models, including adaptive mesh refinement (AMR) (e.g., [48, 144]), adaptive finite element methods using a posteriori error techniques (see, e.g., [54]) or multigrid methods applied to finite elements. Also in [129] a domain-decomposition method using an alternating direction implicit (ADI) method is presented. With respect to time adaptivity, Skouibine, Trayanova, and Moore [140] present a predictor-corrector time stepping strategy to accelerate a given finite differences scheme for the bidomain equations using active membrane kinetics (Luo Rudy phase II). Cherry, Greenside, and

Henriquez [48] use local time stepping, similar to the method introduced in the germinal work of Berger and Oliger [16], to accelerate a reference scheme. We mention that there are also parallelized versions of part of the methods mentioned above (see e.g. [55, 136]).

A generalized chemotaxis model.- We will focus on another degenerate parabolic system given by a generalization of the well known Keller-Segel equations. This model describes the aggregation of slime molds caused by their chemotactical features. Migration of cells plays an important role in a wide variety of biological phenomena. Several organisms as bacteria, protozoa and more complex organisms move, as in the case of chemotaxis, in response and toward to a chemical gradient, in order to find mates, food, etc. And, it is often noticed that the organisms tend to aggregate. Our generalization basically consists in considering a double nonlinearity and two-point degeneracy in the diffusive term. From the viewpoint of the model, this generalization accounts for including the possibility of the process to be held in a non-Newtonian medium and it also accounts for considering a switch to repulsion at high densities, known as volume-filling effect, prevention of overcrowding or density control.

We mention that the Keller-Segel equations is a widely studied model, see e.g. Murray [121] for a general background and Horstmann [93] for a fairly complete survey on the Keller-Segel model and the variants that have been proposed. Nonlinear diffusion equations for biological populations that degenerate at least in one side were proposed in the 1970s by Gurney and Nisbet [84] and Gurtin and McCamy [85]; more recent works include those by Witelski [154], Dkhil [64], Burger et al. [26] and Bendahmane et al. [14]. Furthermore, well-posedness results for these kinds of models include, for example, the existence of radial solutions exhibiting chemotactic collapse [90], the local-in-time existence, uniqueness and positivity of classical solutions, and results on their blow-up behavior [156], and existence and uniqueness using the abstract theory developed in [1], see [109]. Burger et al. [26] prove the global existence and uniqueness of the Cauchy problem in $\mathbb{R}^N$ for linear and nonlinear diffusion with prevention of overcrowding. The model proposed herein exhibits an even higher degree of nonlinearity, and offers further possibilities to describe chemotactic movement; for example, one could imagine that the cells or bacteria are actually placed in a medium with a non-Newtonian rheology. In fact, the evolution p-Laplacian equation $u_t = \operatorname{div}(|\nabla u|^{p-2}\nabla u)$, $p > 1$, is also called non-Newtonian filtration equation, see [71] and [155, Chapter 2] for surveys. Coming back to the Keller-Segel model, we conclude the discussion of models by mentioning that another effort to endow this model with a more general diffusion mechanism had been made recently by Biler and Wu [21], who consider fractional diffusion. Various results on the Hölder regularity of weak solutions to quasilinear parabolic systems are based on the work by DiBenedetto [65]; In this thesis we also contribute to this direction. Specifically for a chemotaxis model, Bendahmane, Karlsen, and Urbano [14] proved the existence and Hölder regularity of weak solutions for a version of (1.45) for $p = 2$. For a detailed description of the intrinsic scaling method and some applications we refer to the books [65, 150].

Numerical methods: Finite volumes and multiresolution

Finite volume methods are discretization methods well suited for the numerical study of several types of partial differential equations [76]. These techniques lead in general to robust numerical schemes. Being based on an integral formulation, they are somehow closer to the physical setting than the partial differential equation itself. In recent years enormous progress has been made in the design of high-resolution finite volume schemes for the approximation of discontinuous solutions to conservation laws. High resolution schemes are of at least second-order accuracy in regions where the solution is smooth, and on the other hand resolve discontinuities sharply and without spurious oscillations. However, the main advantage of resolution is achieved by these methods at the price of increased computational cost, specially when we consider systems, multidimensional problems and long term physical models. Here is where the multiresolution

approach enters into the scene. Adaptive multiresolution schemes were introduced in the 1990s for hyperbolic conservation laws with the aim to accelerate discretization schemes while controlling the error [87]. This approach has been exploited in different directions. Fully adaptive multiresolution schemes for hyperbolic equations are developed in [53]. In addition to CPU time reduction thanks to the reduced number of costly flux evaluations, these schemes also allow a significant reduction of memory requirements by using dynamic data structures. An overview on multiresolution techniques for conservation laws is given by Müller [118], see also Chiavassa et al. [51]. Fully adaptive multiresolution schemes for parabolic equations are presented in [134]. Some approaches to define adaptive space discretizations emerge from ad hoc criteria, while others are based on a posteriori error estimators using control strategies by solving computationally expensive adjoint problems [2, 142]. Adaptive mesh refinement methods introduced by Berger et al. [16] are now widely used for many applications using structured or unstructured grids, see e.g. [3, 15]. First applications of multiresolution schemes to scalar degenerate parabolic equations were presented in [38, 135]. In [38], the multiresolution method combines the switch between central interpolation or exact computation of numerical flux with a thresholded wavelet transform applied to cell averages of the solution to control the switch. The multiresolution method used in [38] closely follows the work of Harten [87]. Within that version, the differential operator is always evaluated on the finest grid, but computational effort is saved by replacing, wherever the solution is sufficiently smooth, exact flux evaluations by approximate flux values that have been obtained more cheaply by interpolation from coarser grids. Though the version of the multiresolution method of [38] is effective for our first kind of problems, it does not provide memory savings. In contrast to [38], the method presented in [135] and herein does provide significant memory savings, since the multiresolution representation of the solution is stored in a graded tree [53, 118, 134], whose leaves are the finite volumes for which the numerical divergence is computed. This means that the numerical flux is actually evaluated on the borders of these finite volumes. Since the flux is computed only at these positions, but not on all positions of the fine grid (as in [38]), we refer to our method as *fully* adaptive. On the other hand, the properties of the underlying discretization allow to derive an optimal choice of the threshold parameter for the adaptive multiresolution computations, as suggested in [53]. This choice guarantees that the perturbation error of the adaptive multiresolution scheme is of the same order than the discretization error of the finite volume scheme. We also extend the adaptive multiresolution scheme for parabolic PDEs [134] and strongly degenerate parabolic PDEs in one space dimension [40, 41] to the case of two-dimensional systems of degenerate parabolic PDEs. In each time step, the solution is encoded with respect to a multiresolution basis corresponding to a hierarchy of nested grids. The size of the details determines the level of refinement needed to obtain an accurate local representation of the solution. Therefore, an adaptive mesh is evolved in time by refining and coarsening in a suitable way. The multiresolution approach is applied to an explicit finite volume method in each time step. Since the computational effort required for integrating a system of equations for one time step is usually substantially higher for an implicit scheme when compared to explicit schemes, implicit schemes may be less efficient that explicit ones, especially when the overall number of time steps is large [48].

Another purpose is to provide time adaptivity to the introduced schemes. Earlier efforts in this direction, which include [40, 52, 69, 77] and the references therein, were based on using the same time step to advance the solution on all parts of the computational domain, and controlling the time step through an embedded pair of Runge-Kutta schemes (known as Runge-Kutta-Fehlberg schemes). In these procedures, one compares the numerical solution after each time step with an (approximate) reference solution, and adjusts the time step if the discrepancy is unacceptable. We here also adapt the locally varying time stepping strategy recently introduced for multiresolution schemes for conservation laws and multidimensional systems in [108, 119]. This strategy is not precisely (time-)adaptive for scalar equations, since the time step for each level remains the same for all times. However, in the case of nonlinear systems, coupling of components entering the CFL condition makes it necessary to compute the time step after each iteration, according the evolving CFL condition, and therefore we have a scheme adaptive in time. Our results in terms of CPU time savings are encouraging and the strategy is consistent with a CFL condition, in contrast to the approach based one the Runge-Kutta-Fehlberg device. We mention that in [119] the authors also combine local time stepping and

multiresolution for implicit schemes, and that more details are also given in the germinal papers of Berger and Oliger [16], Osher and Sanders [125] and the references therein. We point out that these strategies are of different nature, but do not exclude each other, i.e., it is possible to combine them to obtain a potentially more powerful method (as is discussed e.g. in [70]).

Outline of the thesis

Chapter 1 contains a description of the main mathematical models studied in this thesis. We mention some of the difficulties from the mathematical viewpoint, and we discuss some recent approaches to tackle these difficulties. Specifically, Section 1.1 provides some preliminaries in the study of scalar strongly degenerate parabolic equations arising in models of sedimentation processes and traffic flow problems. Then, in Section 1.2 we present a variant of the previous Section in the case of discontinuous flux function, and in Section 1.3 a class of degenerate reaction-diffusion systems modelling several phenomena is examined. Next, in Section 1.4, the bidomain and monodomain models of cardiac tissue are outlined. The general bidomain model can be expressed as a coupled system of a parabolic PDE and an elliptic PDE plus an ODE for the evolution of the local gating variable, while the monodomain model, which arises as a particular sub-case of the bidomain model, is defined by a reaction-diffusion equation, which is again supplemented with an ODE for the gating variable. Finalizing Chapter 1, Section 1.5 addresses the existence and regularity of weak solutions for a fully parabolic model of chemotaxis, with prevention of overcrowding, that degenerates in a two-sided fashion, including an extra nonlinearity represented by a p-Laplacian diffusion term. To prove the existence of weak solutions, a Schauder fixed-point argument is applied to a regularized problem and the compactness method is used to pass to the limit. The local Hölder regularity of weak solutions is established using the method of intrinsic scaling. The results are a contribution to showing, qualitatively, to what extent the properties of the classical Keller-Segel chemotaxis models are preserved in a more general setting. More concisely, Section 1.5.1 deals with the general proof of the first main result (existence of weak solutions). We give the detailed proof of existence of solutions to a non-degenerate problem, then we state and prove a fixed-point-type lemma, and therefore we get to the conclusion of the proof of Theorem 1.6. In Section 1.5.2 we use the method of intrinsic scaling to prove Theorem 1.7, establishing the Hölder continuity of weak solutions to the problem. Chapter 2 is devoted to the construction of the finite volume schemes used to solve the problems presented in Chapter 1. Specifically, in Section 2.1 a numerical scheme is developed to solve a class of scalar strongly degenerate parabolic equations. This scheme is based on a finite volume discretization using the approximation of Engquist-Osher [73] for the flux and explicit time stepping. The first-order version of this scheme is a monotone upwind scheme and we also utilize a spatially second-order MUSCL-type discretization. In Section 2.2 we present several finite volume schemes for two-dimensional reaction-diffusion systems. The applications include phenomena in population dynamics, combustion models, Turing instabilities and chemotaxis-growth systems. All basic schemes presented are first order in space and time, and the discretization is carried out in Cartesian meshes. Section 2.3 deals with the construction of an appropriate finite volume method for the solution of both the parabolic-elliptic system and the reaction-diffusion equation arising from the bidomain and monodomain equations modeling the electrical activity of the myocardial tissue. First we introduce an explicit finite volume method in Cartesian meshes, for which we provide a stability condition, and then we develop an implicit formulation for arbitrary meshes in the special case of axial symmetry. For the latter we establish existence and uniqueness of solutions to the finite volume scheme, and show that it converges to a weak solution of the bidomain model. The convergence proof is based on deriving series of a priori estimates and using a general L^p compactness criterion. Next, in Chapter 3, we develop the multiresolution analysis used to endow the reference finite volume schemes with space adaptivity. More precisely, we present the main ingredients of the multiresolution framework in one-space dimension and we extend the description to the two-dimensional case. In Section 3.1, we introduce the wavelet basis underlying the multiresolution representation with the pertinent projection operator, the

prediction operator and the detail coefficients. Small detail coefficients on fine levels of resolution may be discarded (this operation is called thresholding), which allows for substantial data compression. In Section 3.2, we recall the graded tree data structure used for storage of the numerical solution, and which is introduced for ease of navigation. In Section 3.3 we first recall the results of the rigorous error analyses of Cohen et al. [53] and Roussel et al. [134] referring to conservation laws and strictly parabolic equations, respectively, and then show how this analysis motivates the choice of a reference tolerance ε_{R} for degenerate reaction-diffusion systems, in a fashion similar to the treatment of scalar degenerate parabolic equations [40, 41]. The quantity ε_{R} determines the comparison values ε_l used for the thresholding operation at each level l of resolution. Overall, the basic goal is to choose the threshold values in such a way that the resulting multiresolution scheme has the same order of accuracy as the usual finite volume scheme. Chapter 4 is concerned with the detailed description of two strategies for the adaptive evolution in time of the space-adaptive multiresolution scheme, namely the locally varying time stepping (LTS, Section 4.1) and a variant of the well-known Runge-Kutta-Fehlberg (RKF, Section 4.2) method, which allows to adaptively control the time step. Here we also present in Section 4.3 a general algorithm to accurately describe the multiresolution procedures. In Chapter 5 we provide numerical examples putting into evidence the efficiency of the underlying methods, namely in Sections 5.1 and 5.2 we deal with strongly degenerate parabolic equations in one space dimension including batch sedimentation processes, models for clarifier-thickener units and traffic flow problems. Then in Section 5.3 we show a wide variety of examples in two space dimensions describing population dynamics, interaction between flame balls, Turing instabilities and chemotaxis-growth models. Results for the monodomain and bidomain models in electrocardiology are shown in Section 5.4, and in Section 5.5 we present further examples showing, qualitatively, to what extent the properties of the classical Keller-Segel chemotaxis models are preserved in a more general setting, namely by introducing a p-Laplacian term in the species diffusion. Finally some conclusions that can be drawn from this thesis about the relevance of our results, effectiveness of our methods, and statement of current and possible further extensions to our research are given in Chapter 6. To facilitate access to the reader, this Thesis will be rendered as self-contained as possible.

Chapter 1

Relevant models and analysis

This Chapter provides a description of the mathematical models driven by the applications studied in this thesis, and is intended to motivate our research not only toward the analysis but also to the construction of appropriate numerical methods. Even when it is not our purpose to develop in detail the deduction of the governing equations, we briefly comment their mathematical background and current challenges. By the end of this Chapter, we propose a new model for chemotactical movement which consists in a degenerate parabolic system with a doubly nonlinear diffusion term, and we prove existence and Hölder continuity of weak solutions.

1.1 Strongly degenerate parabolic equations

Consider degenerate parabolic PDEs of the type

$$u_t + b(u)_x = A(u)_{xx}, \quad (x,t) \in Q_T := I \times \mathcal{T}, \quad I \subset \mathbb{R}, \quad \mathcal{T} := (0,T), \tag{1.1}$$

where the function $b(u)$ is assumed to be Lipschitz continuous and piecewise smooth with $b(u) > 0$ for $u \in (0, u_{\max})$ and $b(u) = 0$ otherwise, where $u_{\max}$ is a given maximum solution value, and $A(u) = \int_0^u a(s)\,ds$, where $a(u)$ is a bounded, non negative integrable function. (In the sequel, whenever we refer to (1.1), it is understood that $b(u)$ and $A(u)$ satisfy these assumptions.) Wherever $a(u)$ vanishes, (1.1) degenerates into a first-order hyperbolic conservation law. Since degeneracy is allowed to occur not only at isolated solution values, but on u-intervals of positive length, (1.1) is called *strongly* degenerate parabolic.

For the interval $I := (x_a, x_b)$, the zero-flux initial-boundary value problem, Problem A, is defined by (1.1) and the initial and boundary conditions

$$u(x,0) = u_0(x), \quad x \in I, \tag{1.2}$$

$$\big(b(u) - A(u)_x\big)(x_\ell, t) = 0, \quad t \in \mathcal{T},\, x_\ell \in \{x_a, x_b\}. \tag{1.3}$$

Problem B arises from replacing the zero-flux boundary condition (1.3) by the periodicity condition

$$u(x_a, t) = u(x_b, t), \quad t \in \mathcal{T}.$$

Problems A and B admit an existence and uniqueness analysis if the functions $b(u)$ and $A(u)$ satisfy the assumptions stated above. In addition, we assume that the initial function u_0 satisfies a regularity condition [27], which we here state in terms of a spatial discretization that will also be used for the corresponding finite volume approximation.

For the purpose of illustration, we recall here the definition of an entropy solution of Problem A [27, 29].

Definition 1.1 A function $u \in L^\infty(Q_T) \cap BV(Q_T)$ is an *entropy solution* of the initial-boundary value problem (1.1), (1.2), (1.3) (Problem A) if the following conditions are satisfied:

1. The integrated diffusion coefficient has the regularity $A(u)_x \in L^2(Q_T)$.
2. The boundary condition (1.3) holds in the following sense:

$$\gamma(x_\ell, t)\big(b(u) - A(u)_x\big) = 0, \quad t \in \mathcal{T},\ x_\ell \in \{x_a, x_b\},$$

   where γ is the trace operator.
3. The initial condition (1.2) holds in the following sense:

$$\lim_{t \downarrow 0} u(x,t) = u_0(x) \quad \textit{for almost all } x \in I.$$

4. The following entropy inequality holds for all test functions $\varphi \in C_0^\infty(Q_T)$, $\varphi \geq 0$, and all $k \in \mathbb{R}$:

$$\iint_{Q_T} \Big\{ |u-k|\varphi_t + \operatorname{sgn}(u-k)\big[b(u) - b(k) - A(u)_x\big]\varphi_x \Big\}\, dt\, dx \geq 0.$$

The proof of existence of an entropy solution by the method of vanishing viscosity is outlined in [29]. That paper also presents a sketch of the uniqueness proof, which relies on results by Carrillo [43] that permit applying Kružkov's "doubling of the variables" technique to strongly degenerate parabolic equations. These results allow us to state the following theorem; a similar analysis can be conducted for Problem B.

Theorem 1.2 *The initial-boundary value problem* (1.1), (1.2), (1.3) *(Problem A) has a unique entropy solution.*

Sedimentation-consolidation processes.- The analysis of strongly degenerate parabolic equations has in part been motivated by a theory of sedimentation-consolidation processes of flocculated suspensions outlined in [18]. Roughly speaking, sedimentation is a process in which particles or aggregates are separated from a liquid only under the force of gravity. This is probably the most important industrial large-scale method used in chemistry and mineral processing [127]. In solutions relatively diluted, particles do not behave discretely but they tend to aggregate each other during the sedimentation process.

We here limit ourselves here to one-dimensional batch settling of a suspension of initial concentration $u_0 = u_0(x)$ in a column of depth H, where $u_0(x) \in [0, u_{\max}]$ and $u_{\max}$ is a maximum solids volume fraction. The relevant initial-boundary value problem is Problem A, (1.1)–(1.3), with $x_a = 0$ and $x_b = H$. The unknown is the solid concentration u as a function of time t and depth x. The suspension is characterized by the hindered settling function $b(u)$ and the integrated diffusion coefficient $A(u)$, which models the sediment

compressibility. The function $b(u)$ is assumed to be continuous and piecewise smooth with $b(u) > 0$ for $u \in (0, u_{\max})$ and $b(u) = 0$ for $u \le 0$ and $u \ge u_{\max}$. A typical example is

$$b(u) = \begin{cases} v_\infty u(u_{\max} - u)^K & \text{for } u \in (0, u_{\max}), \\ 0 & \text{otherwise}, \end{cases} \qquad v_\infty > 0, \quad K > 0, \tag{1.4}$$

where $v_\infty > 0$ is the settling velocity of a single particle in unbounded fluid. Moreover, in the framework of the sedimentation-consolidation model we have that $a(u) := b(u)\sigma_{\mathrm{e}}'(u)/(\Delta_\varrho g u)$, where $\Delta_\varrho > 0$ is the solid-fluid density difference, g is the acceleration of gravity, and $\sigma_{\mathrm{e}}'(u)$ is the derivative of the material specific effective solid stress function $\sigma_{\mathrm{e}}(u)$. We assume that the solid particles touch each other at a critical concentration value (or gel point) $0 \le u_{\mathrm{c}} \le u_{\max}$, and that $\sigma_{\mathrm{e}}(u), \sigma_{\mathrm{e}}'(u) = 0$ for $u \le u_{\mathrm{c}}$ and $\sigma_{\mathrm{e}}(u), \sigma_{\mathrm{e}}'(u) > 0$ for $u > u_{\mathrm{c}}$. This implies that $a(u) = 0$ for $u \le u_{\mathrm{c}}$, such that this application motivates an equation of type (1.1) that is indeed strongly degenerate parabolic. A typical function is

$$\sigma_{\mathrm{e}}(u) = \begin{cases} 0 & \text{for } u \le u_{\mathrm{c}}, \\ \sigma_0[(u/u_{\mathrm{c}})^\beta - 1] & \text{for } u > u_{\mathrm{c}}, \end{cases} \qquad \sigma_0 > 0, \quad \beta > 1. \tag{1.5}$$

Traffic flow with driver reaction.- The classical Lighthill-Whitham-Richards (LWR) kinematic wave model [110, 130] for unidirectional traffic flow on a single-lane highway starts from the principle of "conservation of cars" $u_t + (uv)_x = 0$ for $x \in \mathbb{R}$ and $t > 0$, where u is the density of cars as a function of distance x and time t and $v = v(x,t)$ is the velocity of the car located at position x at time t. The basic assumption of the LWR model is that v is a function of u only, $v = v(u)$, i.e, each driver instantaneously adjusts his velocity to the local car density. A common choice is $v(u) = v_{\max} V(u)$, where $v_{\max}$ is a maximum velocity a driver assumes on a free highway, and $V(u)$ is a hindrance function taking into account the presence of other cars that urges each driver to adjust his speed. Thus, the flux is

$$b(u) := uv(u) = v_{\max} u V(u) \text{ for } 0 \le u \le u_{\max}, \quad b(u) = 0 \text{ otherwise},$$

where $u_{\max}$ is the maximum "bumper-to-bumper" car density. The simplest choice is the linear interpolation $V(u) = V_1(u) := 1 - u/u_{\max}$; but we may also consider the alternative Dick-Greenberg model [68, 81]

$$V(u) = V_2(u) := \min\{1, \Theta \ln(u_{\max}/u)\}, \quad \Theta > 0. \tag{1.6}$$

The diffusively corrected kinematic wave model (DCKWM) [32, 123] extends the LWR model by a strongly degenerating diffusion term. This model incorporates a reaction time τ, representing drivers' delay in their response to events, and an anticipating distance $L_{\tilde{a}}$, which means that drivers adjust their velocity to the density seen the distance $L_{\tilde{a}}$ ahead. We use the equation [123] $L_{\tilde{a}} = \max\{(v(u))^2/(2\tilde{a}), L_{\min}\}$, where $(v(u))^2/(2\tilde{a})$ is the distance required to decelerate to full stop from speed $v(u)$ at deceleration $\tilde{a}$, and $L_{\min}$ is a minimal anticipation distance, regardless of how small the velocity is. If one assumes that reaction time and anticipation distance are only effective when the local car density exceeds a critical value u_{c}, then the governing equation (replacing $u_t + b(u)_x = 0$) of the DCKWM is the strongly degenerate parabolic equation

$$u_t + b(u)_x = A(u)_{xx}, \quad x \in \mathbb{R},\ t > 0, \tag{1.7}$$

where for simplicity we suppress dependence on the parameters τ and $L_{\tilde{a}}$, and

$$A(u) := \int_0^u a(s)\, ds, \quad a(u) := \begin{cases} 0 & \text{if } u \le u_{\mathrm{c}}, \\ -uv_{\max} V'(u)\big(L_{\tilde{a}}(u) + \tau v_{\max} u V'(u)\big) & \text{if } u > u_{\mathrm{c}}. \end{cases} \tag{1.8}$$

There are at least two motivations for a critical density u_{c}. One of them is based on the Dick-Greenberg model (1.6); obviously, $V_2'(u) = 0$ for $u \le u_{\mathrm{c}} := u_{\max} \exp(-1/\Theta)$, so that (1.8) is satisfied for $V(u) = V_2(u)$.

A more general viewpoint is that u_c is a threshold value in the sense that the drivers' reaction can be considered instantaneous in relatively free traffic flow, i.e. when $u \leq u_c$, and otherwise is modeled by the diffusion term. Both motivations give rise to the same behavior of the diffusion coefficient. Moreover, we assume that $V(u)$ is chosen such that $a(u) > 0$ for $u_c < u < u_{\max}$. Consequently, the right-hand side of (1.7) vanishes on the interval $[0, u_c]$, and possibly at the maximum density $u_{\max}$. Thus, the governing equation of the DCKWM model (1.7) is strongly degenerate parabolic.

1.2 Degenerate parabolic equations with discontinuous flux

In this Section, we specifically consider equations of the type

$$u_t + f\big(\boldsymbol{\gamma}(x), u\big)_x = \big(\gamma_1(x) A(u)_x\big)_x \quad \text{for } x \in \Pi_T := \mathbb{R} \times (0, T], \tag{1.9}$$

where we assume that for each x, the function $f(\boldsymbol{\gamma}(x), \cdot) : \mathbb{R} \to \mathbb{R}$ is piecewise smooth and Lipschitz continuous, and that $\boldsymbol{\gamma}(x)$ is a vector of scalar parameters that are discontinuous at most at a finite number of points. On the other hand, we assume that the integrated diffusion function $A(\cdot)$ is Lipschitz continuous and piecewise smooth with $A(v) \geqslant A(u)$ for $v > u$. We admit intervals $[\alpha, \beta]$ with $A(u) = \text{const.}$ for all $u \in [\alpha, \beta]$, such that (1.9) degenerates into the first-order equation

$$u_t + f\big(\boldsymbol{\gamma}(x), u\big)_x = 0 \tag{1.10}$$

wherever $u \in [\alpha, \beta]$.

Equation (1.9) combines two independent non-standard ingredients of conservation laws: the strongly degenerate diffusion term $A(u)_{xx}$, and the flux $f(\boldsymbol{\gamma}(x), u)$ that depends discontinuously on the spatial position x.

As already mentioned above, the basic difficulty associated with degenerate parabolic equations like (1.9), which is clearly related to (1.1), is that their solutions need to be defined as weak, in general discontinuous solutions along with an entropy condition to select the physically relevant weak solution. Moreover, if degeneracy occurs on u-intervals of positive length (and not only at isolated points), (1.9) is called *strongly degenerate*. Clearly, solutions of (1.9) are in general discontinuous, and need to be characterized as weak solutions along with an entropy condition.

We briefly review some recent results for equations that include either ingredient. In [29] the existence of BV entropy weak solutions to an initial-boundary value problem for (1.1) in the sense of Kružkov [105] and Vol'pert and Hudjaev [152, 153] is shown via the vanishing viscosity method, while their uniqueness is shown by a technique due to Carrillo [43]. The well-posedness of multi-dimensional Dirichlet initial-boundary value problems for strongly degenerate parabolic equations is shown in [112]. Further recent contributions to the analysis of strongly degenerate parabolic equations include [45, 46, 98, 113].

In the context of the clarifier-thickener model, the analysis of (1.9) for the case $A \equiv 0$, that is, of the first-order conservation law with discontinuous flux (1.10), has been topic of a recent series of papers including [35, 33, 34], in which a rigorous mathematical (existence and uniqueness) and numerical analysis is provided. The main ingredient in these clarifier-thickener models is equation (1.10), where the (with respect to u, nonconvex) flux f and the discontinuous vector-valued coefficient $\boldsymbol{\gamma} = (\gamma_1, \gamma_2)$ are given functions. When $\boldsymbol{\gamma}$ is smooth, Kružkov's theory [105] ensures the existence of a unique and stable entropy weak solution to (1.10). Kružkov's theory does not apply when $\boldsymbol{\gamma}$ is discontinuous. In [35], a variant of Kružkov's notion of entropy weak solution for (1.10) that accounts for the discontinuities in $\boldsymbol{\gamma}$ is introduced and existence and uniqueness (stability) of such entropy solutions in a certain functional class are proved. The existence of such

solutions follows from the convergence of various numerical schemes such as front tracking [33], a relaxation scheme [34, 96], and upwind difference schemes [35].

Strongly degenerate parabolic equations with discontinuous fluxes are also studied in [101, 99, 100]. In [101] equations like (1.9) are studied with a concave convective flux $u \mapsto f(\boldsymbol{\gamma}(x), u)$ and with $(\gamma_1(x)A(u)_x)_x$ replaced by $A(u)_{xx}$. Existence of an entropy weak solution is established by proving convergence of a difference scheme of the type discussed in this Section. Uniqueness and stability issues for entropy weak solutions are studied in [99] for a particular class of equations. These analyses are extended to the traffic and clarifier-thickener models studied herein in [32] and [36], respectively.

Traffic flow with driver reaction and discontinuous road surface conditions.- Following Mochon [117], Bürger and Karlsen [32] extend the DCKWM traffic model to variable road surface conditions by replacing the coefficient $v_{\max}$ in the flux term $v_{\max}uV(u)$ by a discontinuously varying function $v_{\max} = v_{\max}(x)$. However, the degenerate diffusion term models driver psychology and should therefore not depend on road surface conditions. Consequently, the new model equation for the traffic model is

$$u_t + f\big(\gamma(x), u\big)_x = A(u)_{xx}, \quad f\big(\gamma(x), u\big) := \gamma(x)uV(u), \quad \gamma(x) := v_{\max}(x). \tag{1.11}$$

For simplicity, we assume that on the major part of the highway, the maximum velocity assumes a constant value $v^0_{\max}$, which is also used as the value of $v_{\max}$ entering the definition of $A(u)$ in (1.8), and that there is an interval $[a, b]$ on which the maximum velocity assumes an exceptional value $v^*_{\max} \neq v^0_{\max}$:

$$v_{\max}(x) = \gamma(x) = \begin{cases} v^*_{\max} & \text{for } x \in [a, b], \\ v^0_{\max} & \text{otherwise.} \end{cases} \tag{1.12}$$

The initial-value problem for equation (1.11) with Cauchy data $u(x, 0) = u_0(x)$ for $x \in \mathbb{R}$ is well posed [32], but we here insist on using a finite domain that can completely be represented by our data structure. Therefore we consider a circular road of length L, the initial condition

$$u(x, 0) = u_0(x), \quad x \in [0, L], \tag{1.13}$$

and the periodic boundary condition

$$u(0, t) = u(L, t), \quad t \in (0, T]. \tag{1.14}$$

Consequently, the "traffic model" is defined by the periodic initial-boundary value problem (1.11), (1.13), (1.14) under the assumptions (1.8) and (1.12), where we assume $0 < a < b < L$.

A clarifier-thickener model.- As stated in the previous subsection, the analysis of (1.1) has in part been motivated by a theory of sedimentation-consolidation processes of flocculated suspensions [18, 36], in which the unknown is the solids concentration u as a function of time t and depth x. The particular suspension is characterized by the hindered settling function $b(u)$ and the integrated diffusion coefficient $A(u)$, which models the sediment compressibility. The function $b(u)$ is assumed to be continuous and piecewise smooth with $b(u) > 0$ for $u \in (0, u_{\max})$ and $b(u) = 0$ for $u \leqslant 0$ and $u \geqslant u_{\max}$. A typical example is (1.4) where $v_\infty > 0$ is the settling velocity of a single particle in unbounded fluid. Moreover, we have that

$$A(u) := \int_0^u a(s)\, ds, \quad a(u) := \frac{f(u)\sigma_{\mathrm{e}}'(u)}{\Delta_\varrho g u}. \tag{1.15}$$

Here, $\Delta_\varrho > 0$ is the solid-fluid density difference, g is the acceleration of gravity, and $\sigma_{\mathrm{e}}'(u)$ is the derivative of the material specific effective solid stress function $\sigma_{\mathrm{e}}(u)$. We assume that the solid particles touch each other at a critical concentration value (or gel point) $0 \leqslant u_{\mathrm{c}} \leqslant u_{\max}$, and that

$$\sigma_{\mathrm{e}}(u), \sigma_{\mathrm{e}}'(u) \begin{cases} = 0 & \text{for } u \leqslant u_{\mathrm{c}}, \\ > 0 & \text{for } u > u_{\mathrm{c}}. \end{cases}$$

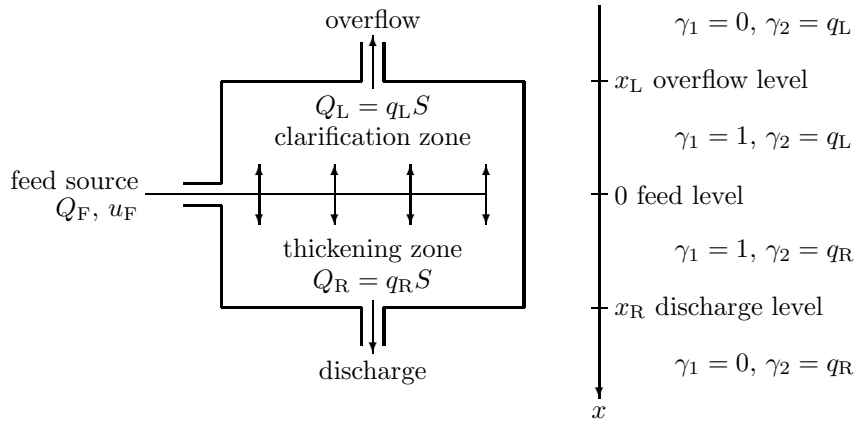

Figure 1.1: *A clarifier-thickener model.*

This implies that $a(u) = 0$ for $u \leqslant u_c$, such that also this application motivates a strongly degenerate parabolic equation (1.10). A typical function is

$$\sigma_e(u) = \begin{cases} 0 & \text{for } u \leqslant u_c, \\ \sigma_0[(u/u_c)^\beta - 1] & \text{for } u > u_c, \end{cases} \quad \sigma_0 > 0,\ \beta > 1.$$

The extension of the one-dimensional sedimentation-consolidation equation (1.1) (if $b(u)$ and $A(u)$ have the interpretation given herein) to continuous sedimentation processes leads to the so-called *clarifier-thickener model* [36], see Figure 1.1. We consider a cylindrical vessel of constant cross-sectional area S, which occupies the depth interval $[x_L, x_R]$ with $x_L < 0$ and $x_R > 0$. At depth $x = 0$, fresh suspension of a given feed concentration $u_F \in [0, u_{max}]$ is pumped into the unit at a volume rate $Q_F > 0$. Within the unit, the feed flow is divided into an upwards directed and a downwards-directed bulk flow with the signed volume rates $Q_L \leqslant 0$ and $Q_R \geqslant 0$, where conservation of suspension implies $Q_F = Q_R - Q_L$. Furthermore, we assume that the feed suspension is loaded with solids at the given feed concentration u_F. Finally, at $x = x_L$ and $x = x_R$, overflow and underflow pipes are provided through which the material leaves the clarifier-thickener unit. We assume that the solid and the fluid phases move at the same velocity through these pipes, so that the solid-fluid relative velocity is zero for $x < x_L$ and $x > x_R$, which means that the term $b(u) - A(u)_x$ is "switched off" outside $[x_L, x_R]$. See [36] for details.

We only consider vessels with a constant interior cross-sectional area S and define the velocities $q_L := Q_L/S$ and $q_R := Q_R/S$. Then the final clarifier-thickener model is given by (1.9) with

$$f\big(\boldsymbol{\gamma}(x), u\big) = \gamma_2(x)(u - u_F) + \gamma_1(x)b(u), \tag{1.16}$$

where we use the discontinuous parameters

$$\gamma_1(x) = \begin{cases} 1 & \text{for } x \in (x_L, x_R), \\ 0 & \text{otherwise}, \end{cases} \qquad \gamma_2(x) = \begin{cases} q_L & \text{for } x \leqslant 0, \\ q_R & \text{for } x > 0. \end{cases} \tag{1.17}$$

We assume the initial concentration distribution

$$u(x, 0) = u_0(x), \quad x \in \mathbb{R}; \quad u_0(x) \in [0, u_{max}]. \tag{1.18}$$

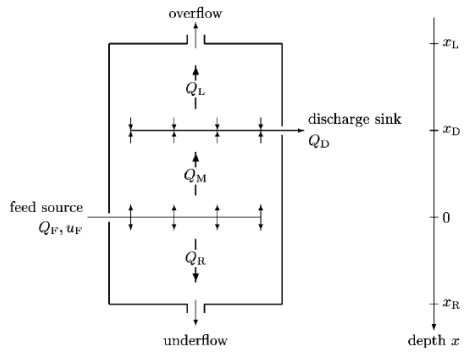

Figure 1.2: *Extended model for the clarifier-thickener model.*

Thus, the clarifier-thickener model is specified by (1.9) with the discontinuous fluxes defined by the continuous functions $u \mapsto b(u), A(u)$ given by (1.4) and (1.15), the discontinuous parameters (1.16), (1.17), and the initial condition (1.18).

An extended clarifier-thickener model.-A further extension to the one-dimensional clarifier-thickener model is considered by introducing a singular discharge sink through which material is extracted from the unit (see [30]). The difficulty of introducing such term is that it cannot be incorporated into the flux function. More precisely, this term is represented by a new non-conservative transport term.

Let us consider the equation

$$u_t + f\big(\boldsymbol{\gamma}(x), u\big)_x = \gamma^3(x) u_x \quad \text{for } x \in \Pi_T := \mathbb{R} \times (0, T], \tag{1.19}$$

where $f : \mathbb{R}^{n+1} \to \mathbb{R}$ is a piecewise smooth and Lipschitz continuous function, and $\boldsymbol{\gamma}(x) := (\gamma^1(x), \gamma^2(x))$ is a vector of scalar parameters, which are discontinuous at most in a finite number of points. The unknown is the solids concentration u as function of time t and depth x. A schematic representation of a clarifier-thickener unit is given in Figure 1.2.

The extended model for the clarifier–thickener is given by (1.19) along with the initial condition (1.18) and f as in (1.16) where the discontinuous parameters are

$$\gamma^1(x) = \begin{cases} 1 & x \in [x_L, x_R], \\ 0 & \text{otherwise}, \end{cases} \quad \gamma^2(x) = \begin{cases} \tilde{q}_R - q_F & x \leqslant 0, \\ \tilde{q}_R & x > 0 \end{cases} \quad \gamma^3(x) = \begin{cases} 0 & x < x_D, \\ -q_D & x > x_D. \end{cases}$$

Function $b(u)$ is defined in (1.4) where $v_\infty > 0$ is the settling velocity of a particle in an unbounded fluid, u_F denotes the feed concentration, $x_L < x_D < 0 < x_R$ are the overflow, sink, and discharge levels respectively, $\tilde{q}_R < 0$ and $q_F > 0$ are given bulk flow velocities describing operating conditions, and q_D is another velocity related to sink control. This model is defined by a conservation law with a flux that is discontinuous at the source and transition points, but not at the singular sink point.

The wellposedness analysis for a reduced model (discarding the discontinuities of the flux) is provided in [30].

1.3 A class of reaction-diffusion systems

A single-species reaction-diffusion model.- Consider the following initial-boundary value problem for a scalar reaction-diffusion equation, where $\mathbf{x} = (x, y)$ and $(x, y, t) \in Q_T := \Omega \times [0, T]$, $\Omega \subset I\!R^2$:

$$u_t = f(u, \mathbf{x}) + \Delta A(u), \tag{1.20a}$$

$$u(\mathbf{x}, 0) = u_0(\mathbf{x}) \quad \text{on } \Omega, \tag{1.20b}$$

$$\nabla A(u) \cdot \mathbf{n} = 0 \quad \text{on } \Sigma_T := \partial\Omega \times [0, T]. \tag{1.20c}$$

This problem may serve as a scalar prototype degenerate reaction-diffusion model. Here, the zero-flux boundary condition (1.20c) implies that the reaction-diffusion domain is isolated from the external environment. For $f(u, \mathbf{x}) = f(u)$, (1.20a) appears in [121] in an ecological setting, where u denotes the population density of a species, and $f(u)$ is its dynamics, where it is assumed that $f(0) = 0$ and $f'(0) \neq 0$. For example, $f(u) = u(1 - u) - u^2/(1 + u^2)$ corresponds to the population dynamics of the spruce band-worm [121], and models the growth of the population by a logistic expression and the rate of mortality due to predation by other animals. We modify this expression by a radial spatial factor, and use

$$\begin{aligned} f(u, \mathbf{x}) &:= 10 \left(\exp(-5r)u(1 - u) + \big(\exp(-5r) - 1\big) \frac{u^2}{1 + u^2} \right), \\ r &:= \sqrt{(x - 0.5)^2 + (y - 0.5)^2}, \end{aligned} \tag{1.21}$$

which means that the birth of individuals is concentrated near the center $(0.5, 0.5)$, and mortality increases with increasing distance from the origin. On the other hand, most standard spatial models of population dynamics simply assume that $A(u) = Du$, where the constant diffusion coefficient $D > 0$ measures the dispersal efficiency of the species under consideration. Motivated by Witelski [154], who advanced degenerate diffusion in the context of population dynamics, we utilize herein the strongly degenerate diffusion coefficient

$$A(u) = \begin{cases} 0 & \text{for } u \leqslant u_{\mathrm{c}}, \\ D(u - u_{\mathrm{c}}) & \text{otherwise}, \end{cases} \tag{1.22}$$

where $u_{\mathrm{c}} > 0$ is an assumed critical (threshold) value of u beyond which diffusion will take place. (1.20) gives rise to a single-species example in Section 5.3.

The difficulty in the wellposedness analysis of the problem (1.20) lies in the boundary condition (1.20c) when A is strongly degenerate. It is quite difficult to give a correct formulation of the zero flux boundary conditions. For the case of non-homogeneous Dirichlet boundary conditions, however, Mascia, Porretta, and Terracina [112] demonstrated existence and uniqueness of L^∞ entropy solutions. In the special case where the function A is strictly increasing, the classical framework of variational solutions of parabolic equations is sufficient to satisfy this wish.

A two-species reaction-diffusion model.- Another model is given by the following initial-boundary value problem for a reaction-diffusion system on Q_T:

$$u_t = \gamma f(u, v) + \Delta A(u) \quad \text{on } Q_T, \tag{1.23a}$$

$$v_t = \gamma g(u, v) + d\Delta B(v) \quad \text{on } Q_T, \tag{1.23b}$$

$$u(\mathbf{x}, 0) = u_0(\mathbf{x}), \quad v(\mathbf{x}, 0) = v_0(\mathbf{x}) \quad \text{for } \mathbf{x} \in \Omega, \tag{1.23c}$$

$$\nabla A(u) \cdot \mathbf{n} = \nabla B(u) \cdot \mathbf{n} = 0 \quad \text{on } \Sigma_T. \tag{1.23d}$$

We study this system in the context of two applications, namely as a model of combustion and as a two-species model of mathematical biology.

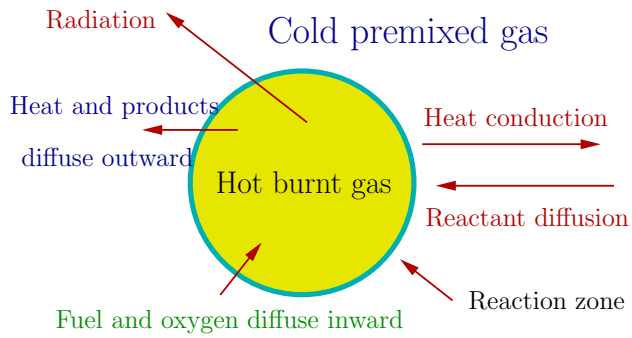

Figure 1.3: *Sketch of the reduced dimensionless thermo-diffusive model.*

For $A(u) = B(u) = u$, $d = 1/\mathrm{Le}$ and $\gamma = 1$, (1.23) represents a reduced dimensionless thermo-diffusive model describing a combustion process, where Le is the Lewis number. We restrict ourselves to a simple chemical reaction with only two reactants and one product, the first reactant and the product being highly diluted in the second reactant; and we neglect gravity (see Figure 1.3).

Since the chemical reaction takes place in a lean premixed gas, we focus on the limiting reactant, and denote by v its normalized partial mass, while u represents normalized temperature. The reaction rates are given by an Arrhenius law:

$$f(u,v) := \frac{\beta^2}{2} v \exp\left(\frac{\beta(1-u)}{\alpha(1-u)-1}\right), \quad g(u,v) := -f(u,v),$$

where α and β are the temperature rate and the dimensionless activation energy, called Zeldovich number, respectively. In Section 5.3.2, this model is employed to simulate the interaction between two flame balls, as an extension of the applications of the same model that were considered in [132, 133]. Here, a *flame ball* denotes a slowly propagating spherical flame structure in a premixed gaseous mixture.

If radiation effects are taken into account, (1.23a) is replaced by

$$u_t = \gamma f(u,v) + S(u) + \Delta A(u) \quad \text{on } Q_T, \tag{1.24}$$

where the dimensionless heat loss due to radiation S follows the Stefan-Boltzmann law

$$S(u) = \rho\big[(u + \alpha^{-1} - 1)^4 - (\alpha^{-1} - 1)^4\big], \tag{1.25}$$

and the dimensionless coefficient ρ controls the radiation level. Conditions (1.23d) imply that the process takes place inside a box with adiabatic walls. See [133] for details and a discussion of the case with one flame ball. The interaction of two flame balls including radiation is also simulated in Section 5.3.2.

On the other hand, (1.23) also arises in mathematical biology as a well-known reaction-diffusion system modelling the interaction between two chemical species with respective concentrations u and v. Under certain conditions, it produces stationary solutions with Turing-type spatial patterns [121, 147]. To simulate the formation of such a pattern, we here select the kinetics between each species due to Schnakenberg [137]:

$$f(u,v) = a - u + u^2 v, \quad g(u,v) = b - u^2 v. \tag{1.26}$$

Alternative choices of f and g that lead to Turing-type patterns are discussed in [120, 121]. For

$$A(u) = B(u) = u, \tag{1.27}$$

this system has a uniform positive steady state (u^0, v^0) given by $u^0 = a+b$ and $v^0 = b/(a+b)^2$, where $b > 0$ and $a+b > 0$, and under certain conditions, (1.23) has a unique solution. See for instance [25] for the proof of existence and uniqueness.

We recall from [121, Sect. 2.3] some results on the conditions under which (1.23) produces a diffusion-driven instability giving rise to Turing-type pattern in the non-degenerate case. A necessary condition is satisfaction of the inequalities $f_u+g_v < 0$, $f_u g_v - f_v g_u > 0$, $df_u+g_v > 0$ and $(df_u+g_v)^2 - 4d(f_u g_v - f_v g_u) > 0$. Evaluating these inequalities for the system (1.23a), (1.23b) and the particular kinetics (1.26) yields the inequalities

$$\begin{aligned} &0 < b-a < (a+b)^3, \quad (a+b)^2 > 0, \\ &d(b-a) > (a+b)^3, \quad \big(d(b-a)-(a+b)^3\big)^2 > 4d(a+b)^4. \end{aligned} \tag{1.28}$$

To characterize the stationary pattern that arises from a choice of (a,b) that satisfies (1.28), we define

$$L^{\pm}(a,b,d) := \frac{d(b-a)-(a+b)^3 \pm \sqrt{[d(b-a)-(a+b)^3]^2 - 4d(a+b)^4}}{2d(a+b)}.$$

The analysis of general rectangular domains [121] implies that in the non degenerate case, the unstable patterned solution of the initial-boundary value problem (1.23) is given by

$$\mathbf{w}(x,y,t) = \sum_{m,n} \mathbf{c}_{nm} \exp\big(\lambda(k^2)t\big) \cos(n\pi x)\cos(m\pi y),$$

where the constants $\mathbf{c}_{nm}$ depend on a Fourier series of the initial conditions for $\mathbf{w}$, and the summation takes place over all numbers n and m that satisfy

$$\gamma L^-(a,b,d) =: k_1^2 < k^2 = \pi^2(n^2+m^2) < k_2^2 := \gamma L^+(a,b,d),$$

and $\lambda(k^2)$ is the positive solution of the following equation, where f_u, f_v, g_u and g_v are evaluated at (u^0, v^0):

$$\lambda^2 + \lambda\big(k^2(1+d) - \gamma(f_u+g_v)\big) + dk^4 - \gamma(df_u+g_v)k^2 + \gamma^2(f_u g_v - f_v g_u) = 0.$$

In Section 5.3.3, we present a numerical solution of (1.23) with the kinetics (1.26) and the diffusion coefficients (1.27), where parameters are chosen according to the preceding discussion such that indeed a Turing-type pattern is produced. On the other hand, also in Section 5.3.3, we present a simulation where (1.27) is replaced by the degenerate diffusion functions

$$A(u) = \begin{cases} 0 & \text{for } u \leqslant u_{\mathrm{c}}, \\ u - u_{\mathrm{c}} & \text{otherwise} \end{cases}, \quad B(u) = \begin{cases} 0 & \text{for } u \leqslant v_{\mathrm{c}}, \\ u - v_{\mathrm{c}} & \text{otherwise}, \end{cases} \quad u_{\mathrm{c}}, v_{\mathrm{c}} \geq 0. \tag{1.29}$$

It turns out that even if the stability analysis does *not* apply to the degenerate case, our numerical experiments lead to the formation of a pattern.

We mention that the mathematical analysis of the system (1.23) is still an open problem because of the presence of the boundary condition (1.23d). A successful technique for proving uniqueness of (entropy weak) solutions to degenerate parabolic equations with Dirichlet boundary condition is based on Kružkov's method [105]. Related to this approach we mention that Holden, Karlsen, and Risebro [92] prove existence and uniqueness of entropy solutions of weakly coupled systems of degenerate parabolic equations in an unbounded domain. Our system is an example of the degenerate reaction-diffusion system analyzed in [92], but is equipped here with the boundary condition (1.23d).

A chemotaxis-growth system.- We assume that $\Omega \subset I\!R^2$ is convex, bounded and open. Now the studied model is the following generalization of the Keller-Segel equations [94, 103] for chemotactical movement:

$$\begin{aligned} u_t &= \nabla \cdot \big(\sigma \nabla u - u \nabla \chi(v)\big) + g(u) \quad \text{on } Q_T, \\ v_t &= h(u,v) + d\Delta v \quad \text{on } Q_T, \\ u(\mathbf{x},0) &= u_0(\mathbf{x}), \quad v(\mathbf{x},0) = v_0(\mathbf{x}) \quad \text{on } \Omega, \\ \nabla u \cdot \mathbf{n} &= \nabla v \cdot \mathbf{n} = 0 \quad \text{on } \Sigma_T. \end{aligned} \tag{1.30}$$

The system (1.30) describes the aggregation of slime molds caused by their chemotactical features. Cell migration appears in numerous biological phenomena. In the case of chemotaxis, cells (or an organism) move in response to a chemical gradient. Specifically, (1.30) corresponds to the model proposed by Mimura and Tsujikawa [114] for the spatio-temporal aggregation patterns shown by the bacteria *Escherichia coli*. This model incorporates four effects: diffusion, chemotaxis, production of chemical substance, and population growth. In the absence of growth, $u = u(\mathbf{x}, t)$ usually represents the density of the cell population of the amoebae *Dictyostelium discoideum*, $v = v(\mathbf{x}, t)$ is the concentration of the chemo-attractant (*cAMP: cyclic Adenosine Monophosphate*), and χ denotes the chemotactical sensitivity function, which may be given by

$$\chi(v) = \nu v, \quad \nu > 0, \tag{1.31}$$

where ν is a chemotactical parameter. The function g takes into account the growth rate of the population, and can be given by

$$g(u) = u^2(1-u). \tag{1.32}$$

Moreover, $\sigma > 0$ and and $d > 0$ are constant diffusion rates for both components. The function h describes the rates of production and degradation of the chemo-attractant; here, we choose

$$h(u,v) = \alpha u - \beta v, \quad \alpha, \beta \geqslant 0. \tag{1.33}$$

For this case it is known that if $0 \leqslant u_0 \in L^2(\Omega)$, $0 \leqslant v_0 \in H^{1+r}(\Omega)$, and $\partial\Omega$ is smooth enough, (1.30) possesses a unique global solution (see, e.g., [20]); and if u_0 and v_0 are radial and $\|u_0\|_{L^1}$ is sufficiently large, then $\|u(t)\|_{L^2}$ blows up in finite time. On the other hand, Efendiev, Kläre, and Lasser [72] analyzed the fractal dimension of the exponential attractor in dependence of ν. Our Examples of Section 5.3.4 are based on examples presented in [72], and presents numerical solutions of (1.30) for various values of ν. We will return to the discussion of chemotaxis models in Section 1.5.

1.4 The macroscopic bidomain and monodomain models

Since direct measurements represent an obvious difficulty in electro-cardiology, there exists a wide interest in the numerical simulations of cardiac models. In the 1950s, Hodgkin and Huxley [91] introduced the first mathematical model of wave propagation in squid nerve, and later on, this model was modified to describe several phenomena in biology, which led to the first physiological model of cardiac tissue [124] and many others. Among these models, the *bidomain model*, firstly introduced by Tung [146], is one of the most accurate and complete models for the theoretical and numerical study of the electric activity in cardiac tissue. The bidomain equations result from the conservation of current between the intra- and extracellular domains, followed by a homogenization process (see e.g. [12, 54, 102]) derived from a scaled version of a cellular model on a periodic structure of cardiac tissue. Mathematically, the bidomain model in its relevant form for our interests, is a scalar, parabolic, possibly degenerate, parabolic PDE for the transmembrane potential, which is coupled with an elliptic PDE for the extracellular potential, and involves a time-dependent ODE for the so-called gating variable, which is defined at any point of the spatial computational domain. Here,

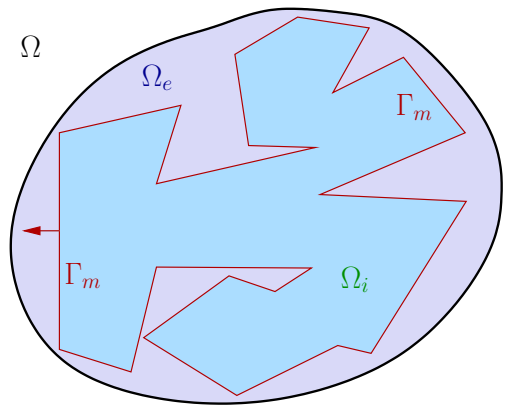

Figure 1.4: *Sketch of the microscopic bidomain model. Ω: Cardiac tissue, Ω_e: extracellular medium, Ω_i: intracellular medium, Γ_m: cell membrane.*

the term "bidomain" reflects that in general, the intra- and extracellular tissues have different longitudinal and transversal (with respect to the fiber) conductivities; if these are equal, then the model reduces to the *monodomain* model, and the elliptic PDE reduces to an algebraic equation. The bidomain model represents a computational challenge since for example, the width of an excitation front is about two orders of magnitude smaller than the long axis of a human-size right ventricle. This local feature, along with strongly varying time scales in the reaction terms, causes solutions to produce sharp propagating wave fronts in the potential field, which makes simulations with uniform grids nearly impossible. Here space (and also time) adaptive methods come to play a very important role in cardiac simulations.

The spatial domain for our models is an bounded open subset $\Omega \subset I\!R^3$ with smooth boundary $\partial\Omega$. This represents a two-dimensional slice of the cardiac muscle regarded as two interpenetrating and superimposed (anisotropic) continuous media: the intracellular (i) and extracellular (e), occupying the same two-dimensional area, and which are separated from each other (and connected at each point) by the cardiac cellular membrane. This model is obtained after an homogenization process, initially considering both media separated as in Figure 1.4.

Here $u_{\mathrm{i}} = u_{\mathrm{i}}(t,x)$ and $u_{\mathrm{e}} = u_{\mathrm{e}}(t,x)$ represent the spatial cellular at $(x,t) \in \Omega_T := \Omega \times (0,T)$ of the *intracellular* and *extracellular* electric potentials, respectively, and the difference between them

$$v = v(t,x) := u_{\mathrm{i}} - u_{\mathrm{e}}$$

is known as the *transmembrane* potential. The conductivity of the tissue is represented by scaled tensors $\mathbf{M}_{\mathrm{i}}(x)$ and $\mathbf{M}_{\mathrm{e}}(x)$ given by

$$\mathbf{M}_j(x) = \sigma_j^{\mathrm{t}}\mathbf{I} + (\sigma_j^l - \sigma_j^{\mathrm{t}})\mathbf{r}a_l(x)\mathbf{r}a_l^{\mathrm{T}}(x),$$

where $\sigma_j^{\mathrm{l}} = \sigma_j^{\mathrm{l}}(x) \in C^1(I\!R^2)$ and $\sigma_j^{\mathrm{t}} = \sigma_j^{\mathrm{t}}(x) \in C^1(I\!R^2)$, $j \in \{\mathrm{e},\mathrm{i}\}$, are the intra- and extracellular conductivity along and transverse respectively to the direction of the fiber (parallel to $\mathbf{r}a_l(x)$, see Figure 1.5).

For fibers aligned with the axis, which will be not necessarily our case, $\mathbf{M}_{\mathrm{i}}(x)$ and $\mathbf{M}_{\mathrm{e}}(x)$ are diagonal matrices:

$$\mathbf{M}_{\mathrm{i}}(x) = \begin{bmatrix} \sigma_{\mathrm{i}}^{\mathrm{l}} & 0 \\ 0 & \sigma_{\mathrm{i}}^{\mathrm{t}} \end{bmatrix}, \qquad \mathbf{M}_{\mathrm{e}}(x) = \begin{bmatrix} \sigma_{\mathrm{e}}^{\mathrm{l}} & 0 \\ 0 & \sigma_{\mathrm{e}}^{\mathrm{t}} \end{bmatrix},$$

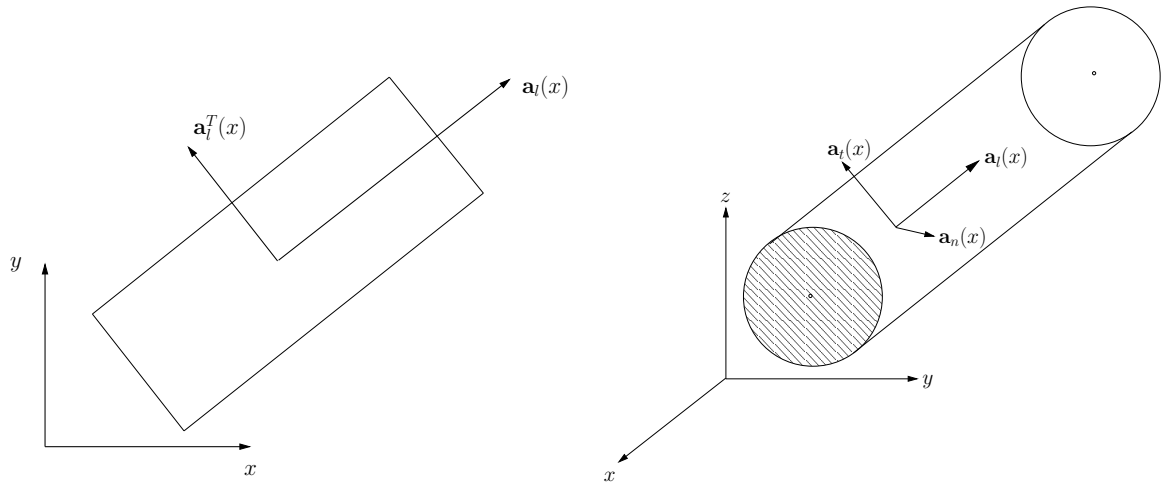

Figure 1.5: *Orientation of the local and global coordinate systems of a single strand of fiber.*

for the two-dimensional case and

$$\mathbf{M}_{\mathrm{i}}(x) = \begin{bmatrix} \sigma_{\mathrm{i}}^l & 0 & 0 \\ 0 & \sigma_{\mathrm{i}}^t & 0 \\ 0 & 0 & \sigma_{\mathrm{i}}^n \end{bmatrix}, \qquad \mathbf{M}_{\mathrm{e}}(x) = \begin{bmatrix} \sigma_{\mathrm{e}}^l & 0 & 0 \\ 0 & \sigma_{\mathrm{e}}^t & 0 \\ 0 & 0 & \sigma_{\mathrm{e}}^n \end{bmatrix}.$$

for the three-dimensional case. When the so-called *anisotropy ratios* $\sigma_{\mathrm{i}}^{\mathrm{l}}/\sigma_{\mathrm{i}}^{\mathrm{t}}$ and $\sigma_{\mathrm{e}}^{\mathrm{l}}/\sigma_{\mathrm{e}}^{\mathrm{t}}$ are equal, we are in the case of *equal anisotropy*, but generally the conductivities in the longitudinal direction l are higher than those across the fiber (direction t); such a case is called *strong anisotropy* of electrical conductivity and since the fibers usually rotate from bottom to top, this type of anisotropy is often refereed as *rotational anisotropy*.

The following coupled reaction-diffusion system forms the (in general, anisotropic) bidomain model [143, 157]:

$$\begin{aligned} \beta c_{\mathrm{m}} \partial_t v - \operatorname{div}\big(\mathbf{M}_{\mathrm{i}}(x)\nabla u_{\mathrm{i}}\big) + \beta I_{\mathrm{ion}}(v,w) &= 0, \\ \beta c_{\mathrm{m}} \partial_t v + \operatorname{div}\big(\mathbf{M}_{\mathrm{e}}(x)\nabla u_{\mathrm{e}}\big) + \beta I_{\mathrm{ion}}(v,w) &= -I_{\mathrm{app}}, \\ \partial_t w - H(v,w) &= 0, \qquad (x,t) \in \Omega_T. \end{aligned} \tag{1.34}$$

Here, $c_{\mathrm{m}} > 0$ is the so-called *surface capacitance* of the membrane, β is the surface-to-volume ratio, and $w(t,x)$ is the so-called *gating variable*, which also takes into account the concentration variables. The stimulation currents applied to the extracellular space are represented by the function $I_{\mathrm{app}} = I_{\mathrm{app}}(t,x)$ satisfying

$$\int_\Omega I_{\mathrm{app}}(t,x)\,dx = 0 \quad \text{for a.e. } t \in (0,T).$$

The functions H and I_{ion} correspond to the Mitchell-Schaeffer membrane model [116] for the membrane and ionic currents, which is the one of the simplest among a wide variety of such models:

$$H(v,w) = \frac{w_\infty(v/v_p) - w}{R_{\mathrm{m}} c_{\mathrm{m}} \eta_\infty(v/v_p)}, \quad I_{\mathrm{ion}}(v,w) = \frac{v_p}{R_{\mathrm{m}}}\left(\frac{v}{v_p\eta_2} - \frac{v^2(1-v/v_p)w}{v_p^2\eta_1}\right), \tag{1.35}$$

where the dimensionless time constant η_∞ and the state variable constant w_∞ are given by

$$\eta_\infty(s) := \begin{cases} \eta_3 & \text{for } s < \eta_5, \\ \eta_4 & \text{otherwise,} \end{cases} \quad w_\infty(s) = \begin{cases} 1 & \text{for } s < \eta_5, \\ 0 & \text{otherwise,} \end{cases}$$

respectively. The quantity R_{m} is the surface resistivity of the membrane, and v_p and $\eta_1, \ldots, \eta_5$ are given parameters. A simpler choice for the membrane kinetics is the widely known FitzHugh-Nagumo model [78, 122], often used by researchers to avoid computational difficulties such as the presence of a large number of coupling variables. This model is specified by

$$H(v,w) = av - bw, \quad I_{\mathrm{ion}}(v,w) = -\lambda\big(w - v(1-v)(v-\theta)\big), \tag{1.36}$$

where a, b, λ and θ are given parameters. The system (1.34) can be written equivalently in terms of v and u_{e} as the following strongly coupled parabolic–elliptic PDE-ODE system (see e.g. [143, 157]):

$$\beta c_{\mathrm{m}}\partial_t v + \operatorname{div}\big(\mathbf{M}_{\mathrm{e}}(x)\nabla u_{\mathrm{e}}\big) + \beta I_{\mathrm{ion}}(v,w) = I_{\mathrm{app}}, \tag{1.37a}$$

$$-\operatorname{div}\big((\mathbf{M}_{\mathrm{i}}(x) + \mathbf{M}_{\mathrm{e}}(x))\nabla u_{\mathrm{e}}\big) = \operatorname{div}\big(\mathbf{M}_{\mathrm{i}}(x)\nabla v\big), \tag{1.37b}$$

$$\partial_t w - H(v,w) = 0, \qquad (x,t) \in \Omega_T. \tag{1.37c}$$

We supplement (1.37) with no-flux boundary conditions, representing an isolated cardiac tissue:

$$\big(\mathbf{M}_j(x)\nabla u_j\big)\cdot\mathbf{n} = 0 \text{ on } \Sigma_T := \partial\Omega \times (0,T), \quad j \in \{\mathrm{e},\mathrm{i}\}, \tag{1.38}$$

and with initial conditions for the transmembrane potential and gating variable:

$$v(0,x) = v_0(x), \quad w(0,x) = w_0(x), \quad x \in \Omega. \tag{1.39}$$

For sake of continuity for the solution v of the bidomain model, we require the initial datum v_0 to be compatible with (1.38). Therefore, if we fix both $u_j(0,x)$, $j \in \{\mathrm{e},\mathrm{i}\}$ as initial data, the problem may become unsolvable, since the time derivative involves only $v = u_{\mathrm{i}} - u_{\mathrm{e}}$. Thus, we impose the compatibility condition

$$\int_\Omega u_{\mathrm{e}}(t,x)\,dx = 0 \text{ for a.e. } t \in (0,T). \tag{1.40}$$

In the case that $\mathbf{M}_{\mathrm{i}} \equiv \lambda\mathbf{M}_{\mathrm{e}}$ for some constant $\lambda \in I\!R$, the system (1.34) is equivalent to a scalar parabolic equation for the transmembrane potential v, coupled to an ODE for the gating variable w. This is known as the *monodomain model*:

$$\begin{aligned} \beta c_{\mathrm{m}}\partial_t v - \operatorname{div}\left(\frac{\mathbf{M}_{\mathrm{i}}}{1+\lambda}\nabla v\right) + \beta I_{\mathrm{ion}}(v,w) &= \frac{\lambda}{1+\lambda} I_{\mathrm{app}}, \\ \partial_t w - H(v,w) &= 0, \qquad (x,t) \in \Omega_T. \end{aligned} \tag{1.41}$$

This model is, of course, much less involved and requires substantially less computational effort than the bidomain model, and even though the assumption of equal anisotropy ratios is very strong and generally unrealistic, the monodomain model is adequate for a qualitative investigation of the repolarization sequences and the patterns of the action potential durations distribution [56].

We will assume that the functions $\mathbf{M}_{\mathrm{j}}$, $\mathrm{j} \in \{\mathrm{e},\mathrm{i}\}$, $I_{\mathrm{app}}, I_{\mathrm{ion}}$ and H are sufficiently smooth so that the following definition of weak solution makes sense. Namely, we assume that $H, I_{\mathrm{app}}, I_{\mathrm{ion}} \in L^2(\Omega_T)$ and

$$\mathbf{M}_{\mathrm{j}} \in L^\infty(\Omega), \quad \mathbf{M}_{\mathrm{j}}\xi\cdot\xi \geqslant C_M|\xi|^2, \tag{1.42}$$

for a.e. $x \in \Omega$, for all $\xi \in I\!R^3$, $\mathrm{j} \in \{\mathrm{e},\mathrm{i}\}$ and constant $C_M > 0$.

We can decompose the ionic current I_{ion} (for both the FitzHugh-Nagumo model) in the form $I_{\mathrm{ion}}(v,w) =: I_{1,\mathrm{ion}}(v) + I_{2,\mathrm{ion}}(w)$. Then, regarding the $v-$component of the ionic current $I_{1,\mathrm{ion}}$, it is straightforwardly seen that there exists a constant $C_I > 0$ such that (see e.g. [57])

$$\frac{I_{1,\mathrm{ion}}(v_1) - I_{1,\mathrm{ion}}(v_2)}{v_1 - v_2} \geq -C_I, \quad \forall v_1 \neq v_2.$$

Additionally, there is a constant $C_I' > 0$ such that

$$0 < \liminf_{|v|\to\infty} \left| \frac{I_{1,\mathrm{ion}}(v)}{v^3} \right| \leq \limsup_{|v|\to\infty} \left| \frac{I_{1,\mathrm{ion}}(v)}{v^3} \right| \leq C_I'. \tag{1.43}$$

These inequalities will be needed in the proof of uniqueness of weak solution and convergence of the numerical scheme, respectively.

For later reference, we now state the definitions of a weak solution for the bidomain and the monodomain model, respectively.

Definition 1.3 A triple $\mathbf{u} = (v, u_\mathrm{e}, w)$ of functions is a *weak solution of the bidomain model* (1.37)–(1.39) if $v, u_\mathrm{e} \in L^2(0,T;H^1(\Omega))$, $w \in C([0,T], L^2(\Omega))$, (1.40) is satisfied and

$$\begin{aligned}
&\beta c_m \int_\Omega v_0(x)\varphi(0,x)\,dx + \beta c_m \iint_{\Omega_T} v\partial_t\varphi\,dx\,dt - \iint_{\Omega_T} \mathbf{M}_\mathrm{e}(x)\nabla u_\mathrm{e}\cdot\nabla\varphi\,dx\,dt \\
&\qquad + \beta \iint_{\Omega_T} I_\mathrm{ion}\varphi\,dx\,dt = \iint_{\Omega_T} I_\mathrm{app}\varphi\,dx\,dt, \\
&\iint_{\Omega_T} (\mathbf{M}_\mathrm{i}(x) + \mathbf{M}_\mathrm{e}(x))\nabla u_\mathrm{e}\cdot\nabla\psi\,dx\,dt = \iint_{\Omega_T} \mathbf{M}_\mathrm{i}(x)\nabla v\cdot\nabla\psi\,dx\,dt, \\
&-\int_\Omega w_0(x)\xi(0,x)\,dx - \iint_{\Omega_T} w\partial_t\xi\,dx\,dt = \iint_{\Omega_T} H\xi\,dx\,dt,
\end{aligned} \tag{1.44}$$

for all test functions $\varphi, \psi, \xi \in \mathcal{D}([0,T)\times\bar{\Omega})$.

Definition 1.4 A pair $\mathbf{u} = (v, w)$ of functions is a *weak solution of the monodomain model* (1.41) if $v \in L^2(0,T;H^1(\Omega))$, $w \in C([0,T], L^2(\Omega))$, and

$$\begin{aligned}
&\beta c_\mathrm{m} \int_\Omega v_0(x)\varphi(0,x)\,dx \\
&+ \iint_{\Omega_T} \left\{ \beta c_\mathrm{m} v\partial_t\varphi + \beta I_\mathrm{ion}\varphi - \frac{1}{1+\lambda}\mathbf{M}_\mathrm{i}\nabla v\cdot\nabla\varphi \right\} dx\,dt = \frac{\lambda}{1+\lambda}\iint_{\Omega_T} I_\mathrm{app}\varphi\,dx\,dt, \\
&-\int_\Omega w_0(x)\xi(0,x)\,dx - \iint_{\Omega_T} w\partial_t\xi\,dx\,dt = \iint_{\Omega_T} H\xi\,dx\,dt,
\end{aligned}$$

for all test functions $\varphi, \xi \in \mathcal{D}([0,T)\times\bar{\Omega})$.

We mention that the wellposedness analysis for the bidomain model has already been studied. See e.g. [57], where C. Franzone and Savaré present a weak formulation for the bidomain model and show that it has a structure suitable to apply the theory of evolution variational inequalities in Hilbert spaces. A different approach is presented in [12], where Bendahmane and Karlsen prove existence and uniqueness for the bidomain equations using for the existence, the Faedo-Galerkin method and compactness theory, Veneroni [151] derives existence, uniqueness and regularity results for a slightly different version of the degenerate bidomain equations, and in [23] Bourgault, Coudière and Pierre prove existence and uniqueness for the bidomain equations, first reformulating the problem into a single parabolic PDE and then applying a semigroup approach.

1.5 A doubly nonlinear diffusion model of chemotaxis

In this section we study the existence and regularity of weak solutions of the following parabolic system, which is a generalization of the well-known Keller-Segel model [93, 103, 121] of chemotaxis:

$$\partial_t u - \operatorname{div}\left(|\nabla A(u)|^{p-2}\nabla A(u)\right) + \operatorname{div}\left(\chi u f(u)\nabla v\right) = 0 \quad \text{in } Q_T := \Omega \times (0,T), \tag{1.45a}$$

$$\partial_t v - d\Delta v = g(u,v) \quad \text{in } Q_T, \tag{1.45b}$$

$$|\nabla A(u)|^{p-2} a(u)\frac{\partial u}{\partial \eta} = 0, \quad \frac{\partial v}{\partial \eta} = 0 \quad \text{on } \Sigma_T := \partial\Omega \times (0,T), \tag{1.45c}$$

$$u(x,0) = u_0(x), \quad v(x,0) = v_0(x) \quad \text{on } \Omega, \tag{1.45d}$$

where $T > 0$ and $\Omega \subset \mathbb{R}^N$ is a bounded domain with sufficiently piecewise smooth boundary $\partial\Omega$ and outer unit normal η. Equation (1.45a) is *doubly nonlinear*, since we apply the p-Laplacian diffusion operator, where we assume $2 \le p < \infty$, to the integrated diffusion function $A(u) := \int_0^u a(s)\,ds$, where $a(u)$ is a non-negative integrable function with support on the interval $[0,1]$.

Migration of cells plays an important role in a wide variety of biological phenomena. Several organisms as bacteria, protozoa and more complex organisms move, as in the case of chemotaxis, in response and toward to a chemical gradient, in order to find mates, food, etc. And, it is often noticed that the organisms tend to aggregate. In the biological phenomenon described by (1.45), the quantity $u = u(x,t)$ is the density of organisms such as bacteria or cells. The conservation PDE (1.45a) incorporates two competing mechanisms, namely the density-dependent diffusive motion of the cells, described by the doubly nonlinear diffusion term, and a motion in response and toward to the gradient ∇v of the concentration $v = v(x,t)$ of a substance called *chemoattractant*. The movement in response to ∇v also involves the density-dependent probability $f(u)$ for a cell located at (x,t) to find space in its neighboring location, and a constant χ describing chemotactic sensitivity. On the other hand, the PDE (1.45b) describes the diffusion of the chemoattractant, where $d > 0$ is a diffusion constant and the function $g(u,v)$ describes the rates of production and degradation of the chemoattractant; a common choice is

$$g(u,v) = \alpha u - \beta v, \quad \alpha, \beta \ge 0.$$

We assume that there exists a maximal population density of cells u_{m} such that $f(u_{\mathrm{m}}) = 0$. This corresponds to a switch to repulsion at high densities, known as volume-filling effect, prevention of overcrowding or density control (see [14]). This means that cells stop to accumulate at a given point of Ω after their density attains a certain threshold value, and the chemotactic cross-diffusion term $\chi u f(u)$ vanishes identically when $u \ge u_{\mathrm{m}}$. We also assume that the diffusion coefficient $a(u)$ takes the form $a(u) = \epsilon u(1 - u_{\mathrm{m}})$, $\epsilon > 0$, so that (1.45a) degenerates for $u = 0$ and $u = u_{\mathrm{m}}$, while $a(u) > 0$ for $0 < u < u_{\mathrm{m}}$. Normalizing variables by $\tilde{u} = u/u_{\mathrm{m}}$, $\tilde{v} = v$, and $\tilde{f}(\tilde{u}) = f(\tilde{u}u_{\mathrm{m}})$ we have $\tilde{u}_{\mathrm{m}} = 1$, so in the sequel we will omit tildes in the notation.

The novelty of the present approach is that we address the question of the regularity of weak solutions. This is delicate analytical issue as the structure of the equation combines a degeneracy of p-Laplacian type with a two-sided point degeneracy in the diffusive term. We prove the local Hölder continuity for the weak solutions of (1.45). Our approach is based on the method of intrinsic scaling (see [65, 150]). The novelty lies in tackling the two types of degeneracy simultaneously and finding the right geometric setting for the concrete structure of the PDE. The resulting analysis combines the technique used by Urbano [149] to study the case of a diffusion coefficient $a(u)$ that decays like a power at both degeneracy points (with $p = 2$) with the technique by Porzio and Vespri [128] to study the p-Laplacian, with $a(u)$ degenerating at only one side. We recover both results as particular cases of the one studied here. To our knowledge, the p-Laplacian is a new ingredient in chemotaxis models, so we also include a few numerical examples that illustrate the

behavior of solutions of (1.45) for $p > 2$, compared with solutions to the standard case $p = 2$, but including nonlinear diffusion.

Concerning uniqueness of solution, the presence of a nonlinear degenerate diffusion term and a nonlinear transport term represents a disadvantage because we cannot naturally prove uniqueness of weak solution. In contrast, in [26] the authors prove uniqueness of solutions for a degenerate parabolic-elliptic system set in an unbounded domain; and they used a method which relies on a continuous dependence estimate from [98] that does not apply to our problem, because it is difficult to bound Δv in $L^\infty(Q_T)$ due to the parabolic nature of the second equation in (1.45).

Before stating our main results, we provide the definition of a weak solution to (1.45), and recall the notion of certain functional spaces. We denote by p' the conjugate exponent of p (we will restrict ourselves to the degenerate case $p \geq 2$): $\frac{1}{p} + \frac{1}{p'} = 1$. Moreover, $C_w(0, T, L^p(\Omega))$ denotes the space of continuous functions with values in (a closed ball of) $L^p(\Omega)$ endowed with the weak topology, and $\langle \cdot, \cdot \rangle$ is the duality pairing between $W^{1,p}(\Omega)$ and its dual $(W^{1,p}(\Omega))'$.

Definition 1.5 A weak solution of (1.45) is a pair (u, v) of functions satisfying the following conditions:

$$
\begin{aligned}
&0 \leq u(x,t) \leq 1 \text{ and } v(x,t) \geq 0 \text{ for a.e. } (x,t) \in Q_T,\\
&u \in C_w\big(0,T,L^2(\Omega)\big), \quad \partial_t u \in L^{p'}\big(0,T;(W^{1,p}(\Omega))'\big), \quad u(0) = u_0,\\
&A(u) = \int_0^u a(s)\,ds \in L^p\big(0,T;W^{1,p}(\Omega)\big),\\
&v \in L^\infty(Q_T) \cap L^r\big(0,T;W^{1,r}(\Omega)\big) \cap C\big(0,T,L^r(\Omega)\big) \quad \text{for all } r > 1,\\
&\partial_t v \in L^2\big(0,T;(H^1(\Omega))'\big), \quad v(0) = v_0,
\end{aligned}
$$

and, for all $\varphi \in L^p(0,T;W^{1,p}(\Omega))$ *and* $\psi \in L^2(0,T;H^1(\Omega))$,

$$
\begin{aligned}
&\int_0^T \langle \partial_t u, \varphi \rangle\, dt + \iint_{Q_T} \Big\{ |\nabla A(u)|^{p-2} \nabla A(u) - \chi u f(u) \nabla v \Big\} \cdot \nabla \varphi \, dx\, dt = 0,\\
&\int_0^T \langle \partial_t v, \psi \rangle\, dt + d \iint_{Q_T} \nabla v \cdot \nabla \psi \, dx\, dt = \iint_{Q_T} g(u,v) \psi \, dx\, dt.
\end{aligned}
$$

To ensure that all terms and coefficients are sufficiently smooth for this definition to make sense, we require that $f \in C^2[0,1]$ and $f(1) = 0$, and assume that the diffusion coefficient $a(\cdot)$ has the following properties: $a \in C^1[0,1]$, $a(0) = a(1) = 0$, and $a(s) > 0$ for $0 < s < 1$. Moreover, we assume that there exist constants $\delta \in (0, 1/2)$ and $\gamma_2 \geq \gamma_1 > 1$ such that

$$
\begin{aligned}
\gamma_1 \phi(s) \leq a(s) \leq \gamma_2 \phi(s) \quad &\text{for } s \in [0, \delta],\\
\gamma_1 \psi(1-s) \leq a(s) \leq \gamma_2 \psi(1-s) \quad &\text{for } s \in [1-\delta, 1],
\end{aligned}
\tag{1.46}
$$

where we define the functions $\phi(s) := s^{\beta_1/(p-1)}$ and $\psi(s) := s^{\beta_2/(p-1)}$ for $\beta_2 > \beta_1 > 0$.

Our first main result is the following existence theorem for weak solutions.

Theorem 1.6 *If* $u_0, v_0 \in L^\infty(\Omega)$ *with* $0 \leq u_0 \leq 1$ *and* $v_0 \geq 0$ *a.e. in* Ω*, then there exists a weak solution to the degenerate system* (1.45) *in the sense of Definition 1.5.*

In Section 1.5.1, we first prove the existence of solutions to a regularized version of (1.45) by applying the Schauder fixed-point theorem. The regularization basically consists in replacing the degenerating diffusion

coefficient $a(u)$ by the regularized, strictly positive diffusion coefficient $a_\varepsilon(u) := a(u) + \varepsilon$, where $\varepsilon > 0$ is the regularization parameter. Once the regularized problem is solved, we send the regularization parameter ε to zero to produce a weak solution of the original system (1.45) as the limit of a sequence of such approximate solutions. Convergence is achieved by means of *a priori* estimates and compactness arguments.

We denote by $\partial_t Q_T$ the parabolic boundary of Q_T, define $\tilde{M} := \|u\|_{\infty,Q_T}$, and recall the definition of the intrinsic parabolic p-distance from a compact set $K \subset Q_T$ to $\partial_t Q_T$ as

$$p\text{-dist}(K; \partial_t Q_T) := \inf_{(x,t)\in K,\ (y,s)\in\partial_t Q_T} \big(|x-y| + \tilde{M}^{(p-2)/p}|t-s|^{1/p}\big).$$

Our second main result is the interior local Hölder regularity of weak solutions.

Theorem 1.7 *Let u be a bounded local weak solution of (1.45) in the sense of Definition 1.5, and $\tilde{M} = \|u\|_{\infty,Q_T}$. Then u is locally Hölder continuous in Q_T, i.e., there exist constants $\gamma > 1$ and $\alpha \in (0,1)$ depending only on the data such that for every compact $K \subset Q_T$, $\forall (x_1,t_1),(x_2,t_2) \in K$:*

$$\big|u(x_1,t_1) - u(x_2,t_2)\big| \le \gamma \tilde{M} \left\{ \frac{|x_1-x_2| + \tilde{M}^{(p-2)/p}|t_2-t_1|^{1/p}}{p\text{-dist}(K;\partial_t Q_T)} \right\}^{\alpha}.$$

In Section 1.5.2, we prove Theorem 1.7 by the technique of intrinsic scaling. This method is based on regarding the underlying PDE in a geometry dictated by its degenerate structure, and this is achieved via an accommodation of the degeneracies by rescaling the standard parabolic cylinders by a factor that depends on the particular form of the degeneracies, and on the oscillation of the solution in these cylinders. This will allow us to obtain homogeneous energy estimates over the rescaled cylinders, in the same fashion that it is done for the heat equation. The decisive part of the proof consists in the proper choice of the intrinsic geometry. In the present case, the intrinsic geometry needs to take into account the p-Laplacian structure of the diffusion term, and that the diffusion coefficient $a(u)$ vanishes at $u = 0$ and $u = 1$. At the core of the proof is the study of two alternative cases of similar nature, following a standard argument [65]. In either case the conclusion is that when going from a rescaled cylinder into a smaller one, the oscillation of the solution decreases in a way that can be quantified.

In the statement of Theorem 1.7 and its proof, we focus on the interior regularity of u; that of v follows from classical theory of parabolic PDEs [107]. Moreover, standard adaptations of the method are sufficient to extend results to the parabolic boundary, see [65, 67].

1.5.1 Existence of solutions

We first prove of the existence of solutions to a non-degenerate, regularized version of problem (1.45) using the Schauder fixed-point theorem, and our treatment closely follows that of [14]. We define the following closed subset of the Banach space $L^p(Q_T)$:

$$\mathcal{K} := \big\{ u \in L^p(Q_T) \ : \ 0 \le u(x,t) \le 1 \text{ for a.e. } (x,t) \in Q_T \big\}.$$

Weak solution to a non-degenerate problem.-We define the new diffusion term $A_\varepsilon(s) := A(s) + \varepsilon s$, $a_\varepsilon(s) = a(s) + \varepsilon$, and consider, for each fixed $\varepsilon > 0$, the non-degenerate problem

$$\partial_t u_\varepsilon - \operatorname{div}\big(|\nabla A_\varepsilon(u_\varepsilon)|^{p-2}\nabla A_\varepsilon(u_\varepsilon)\big) + \operatorname{div}\big(\chi f(u_\varepsilon)\nabla v_\varepsilon\big) = 0 \quad \text{in } Q_T, \tag{1.47a}$$

$$\partial_t v_\varepsilon - d\Delta v_\varepsilon = g(u_\varepsilon, v_\varepsilon) \quad \text{in } Q_T, \tag{1.47b}$$

$$|\nabla A_\varepsilon(u_\varepsilon)|^{p-2}a_\varepsilon(u_\varepsilon)\frac{\partial u_\varepsilon}{\partial \eta} = 0, \quad \frac{\partial v_\varepsilon}{\partial \eta} = 0 \quad \text{on } \Sigma_T, \tag{1.47c}$$

$$u_\varepsilon(x,0) = u_0(x), \quad v_\varepsilon(x,0) = v_0(x) \quad \text{for } x \in \Omega. \tag{1.47d}$$

With $\mathbf{u} \in \mathcal{K}$ fixed, let v be the unique solution of the problem

$$\partial_t v_\varepsilon - d\Delta v_\varepsilon = g(\mathbf{u}, v_\varepsilon) \quad \text{in } Q_T, \tag{1.48a}$$

$$\frac{\partial v_\varepsilon}{\partial \eta} = 0 \quad \text{on } \Sigma_T, \quad v_\varepsilon(x,0) = v_0(x) \quad \text{for } x \in \Omega. \tag{1.48b}$$

Given the function v_ε, let u_ε be the unique solution of the following quasilinear parabolic problem, where v_0 and u_0 are functions satisfying the assumptions of Theorem 1.6:

$$\begin{aligned} &\partial_t u_\varepsilon - \operatorname{div}\left(|\nabla A_\varepsilon(u_\varepsilon)|^{p-2}\nabla A_\varepsilon(u_\varepsilon)\right) + \operatorname{div}\left(\chi u_\varepsilon f(u_\varepsilon)\nabla v_\varepsilon\right) = 0 \quad \text{in } Q_T, \\ &|\nabla A_\varepsilon(u_\varepsilon)|^{p-2}a_\varepsilon(u_\varepsilon)\frac{\partial u_\varepsilon}{\partial \eta} = 0 \quad \text{on } \Sigma_T, \quad u_\varepsilon(x,0) = u_0(x) \quad \text{for } x \in \Omega. \end{aligned} \tag{1.49}$$

Since for any fixed $\mathbf{u} \in \mathcal{K}$, (1.48a) is uniformly parabolic, standard theory for parabolic equations [107] immediately leads to the following lemma.

Lemma 1.8 *If $v_0 \in L^\infty(\Omega)$, then problem (1.48) has a unique weak solution v_ε, with $v_\varepsilon \in L^\infty(Q_T) \cap L^r(0,T;W^{2,r}(\Omega)) \cap C(0,T;L^r(\Omega))$, for all $r > 1$, satisfying in particular*

$$\begin{aligned} \|v_\varepsilon\|_{L^\infty(Q_T)} + \|v_\varepsilon\|_{L^\infty(0,T;L^2(\Omega))} &\le C, \\ \|v_\varepsilon\|_{L^2(0,T;H^1(\Omega))} &\le C, \\ \|\partial_t v_\varepsilon\|_{L^2(Q_T)} &\le C, \end{aligned} \tag{1.50}$$

where $C > 0$ is a constant that depends only on $\|v_0\|_{L^\infty(\Omega)}$, α, β, and $\operatorname{meas}(Q_T)$.

The following lemma (see [107]) holds for the quasilinear problem (1.49).

Lemma 1.9 *If $u_0 \in L^\infty(\Omega)$, then, for any $\varepsilon > 0$, there exists a unique weak solution $u_\varepsilon \in L^\infty(Q_T) \cap L^p(0,T;W^{1,p}(\Omega))$ to problem (1.49).*

The fixed-point method.- We define a map $\Theta : \mathcal{K} \to \mathcal{K}$ such that $\Theta(\mathbf{u}) = u$, where u_ε solves (1.49), i.e., Θ is the solution operator of (1.49) associated with the coefficient $\mathbf{u}$ and the solution v coming from (1.48). By using the Schauder fixed-point theorem, we now prove that Θ has a fixed point. First, we need to show that Θ is continuous. Let $\{\mathbf{u}_n\}_{n\in\mathbb{N}}$ be a sequence in $\mathcal{K}$ and $\mathbf{u} \in \mathcal{K}$ be such that $\mathbf{u}_n \to \mathbf{u}$ in $L^p(Q_T)$ as $n \to \infty$. Define $u_{\varepsilon n} := \Theta(\mathbf{u}_n)$, i.e., $u_{\varepsilon n}$ is the solution of (1.49) associated with $\mathbf{u}_n$ and the solution $v_{\varepsilon n}$ of (1.48). To show that $u_{\varepsilon n} \to \Theta(\mathbf{u})$ in $L^p(Q_T)$, we start with the following lemma.

Lemma 1.10 *The solutions $u_{\varepsilon n}$ to problem (1.49) satisfy*

(i) $0 \le u_{\varepsilon n}(x,t) \le 1$ *for a.e.* $(x,t) \in Q_T$.

(ii) The sequence $\{u_{\varepsilon n}\}_{n\in\mathbb{N}}$ is bounded in $L^p(0,T;W^{1,p}(\Omega)) \cap L^\infty(0,T;L^p(\Omega))$.

(iii) The sequence $\{u_{\varepsilon n}\}_{n\in\mathbb{N}}$ is relatively compact in $L^p(Q_T)$.

Proof. The proof follows from that of Lemma 2.3 in [14] if we take into account that $\{\partial_t u_{\varepsilon n}\}_{n\in\mathbb{N}}$ is uniformly bounded in $L^{p'}(0,T;(W^{1,p}(\Omega))')$.

The following lemma contains a classical result (see [107]).

Lemma 1.11 *There exists a function $v_\varepsilon \in L^2(0,T;H^1(\Omega))$ such that the sequence $\{v_{\varepsilon n}\}_{n\in\mathbb{N}}$ converges strongly to v in $L^2(0,T;H^1(\Omega))$.*

Lemmas 1.9–1.11 imply that there exist $u_\varepsilon \in L^p(0,T;W^{1,p}(\Omega))$ and $v_\varepsilon \in L^2(0,T;H^1(\Omega))$ such that, up to extracting subsequences if necessary, $u_{\varepsilon n} \to u_\varepsilon$ strongly in $L^p(Q_T)$ and $v_{\varepsilon n} \to v_\varepsilon$ strongly in $L^2(0,T;H^1(\Omega))$ as $n \to \infty$, so Θ is indeed continuous on $\mathcal{K}$. Moreover, due to Lemma 1.10, $\Theta(\mathcal{K})$ is bounded in the set

$$\mathcal{W} := \big\{u \in L^p\big(0,T;W^{1,p}(\Omega)\big) \ : \ \partial_t u \in L^{p'}\big(0,T;(W^{1,p}(\Omega))'\big)\big\}.$$

Similarly to the results of [139], it can be shown that $\mathcal{W} \hookrightarrow L^p(Q_T)$ is compact, and thus Θ is compact. Now, by the Schauder fixed point theorem, the operator Θ has a fixed point u_ε such that $\Theta(u_\varepsilon) = u_\varepsilon$. This implies that there exists a solution $(u_\varepsilon, v_\varepsilon)$ of

$$\begin{aligned}
&\forall \varphi, \psi \in L^p(0,T;W^{1,p}(\Omega)) : \\
&\int_0^T \langle \partial_t u_\varepsilon, \varphi\rangle \, dt \\
&\quad + \iint_{Q_T} \Big\{|\nabla A_\varepsilon(u_\varepsilon)|^{p-2}\nabla A_\varepsilon(u_\varepsilon) - \chi u_\varepsilon f(u_\varepsilon)\nabla v_\varepsilon\Big\} \cdot \nabla\varphi \, dx\, dt = 0, \\
&\int_0^T \langle \partial_t v_\varepsilon, \psi\rangle \, dt + d\iint_{Q_T} \nabla v_\varepsilon \cdot \nabla\psi \, dx\, dt = \iint_{Q_T} g(u_\varepsilon, v_\varepsilon)\psi \, dx\, dt.
\end{aligned} \tag{1.51}$$

Existence of weak solutions.- We now pass to the limit $\varepsilon \to 0$ in solutions $(u_\varepsilon, v_\varepsilon)$ to obtain weak solutions of the original system (1.45). From the previous lemmas and considering (1.47b), we obtain the following result.

Lemma 1.12 *For each fixed $\varepsilon > 0$, the weak solution $(u_\varepsilon, v_\varepsilon)$ to (1.47) satisfies the maximum principle*

$$0 \le u_\varepsilon(x,t) \le 1 \quad \text{and} \quad v_\varepsilon(x,t) \ge 0 \quad \text{for a.e. } (x,t) \in Q_T. \tag{1.52}$$

Moreover, the first two estimates of (1.50) in Lemma 1.8 are independent of ε.

Lemma 1.12 implies that there exists a constant $C > 0$, which does not depend on ε, such that

$$\|v_\varepsilon\|_{L^\infty(Q_T)} + \|v_\varepsilon\|_{L^\infty(0,T;L^2(\Omega))} \le C, \quad \|v_\varepsilon\|_{L^2(0,T;H^1(\Omega))} \le C. \tag{1.53}$$

Notice that, from (1.52) and (1.53), the term $g(u_\varepsilon, v_\varepsilon)$ is bounded. Thus, in light of classical results on L^r regularity, there exists another constant $C > 0$ independently of ε such that

$$\|\partial_t v_\varepsilon\|_{L^r(Q_T)} + \|v_\varepsilon\|_{L^r(0,T;W^{1,r}(\Omega))} \le C.$$

Taking $\varphi = A_\varepsilon(u_\varepsilon)$ as a test function in (1.51) yields

$$\int_0^T \langle \partial_t u_\varepsilon, A(u_\varepsilon)\rangle \, dt + \varepsilon \int_0^T \langle \partial_t u_\varepsilon, u_\varepsilon\rangle \, dt + \iint_{Q_T} |\nabla A(u_\varepsilon)|^p \, dx\, dt$$

$$-\iint_{Q_T} \chi f(u_\varepsilon)\nabla v_\varepsilon \cdot \nabla A_\varepsilon(u_\varepsilon)\,dx\,dt = 0;$$

then, using (1.53), the uniform L^∞ bound on u_ε, an application of Young's inequality to the term $\nabla v_\varepsilon \cdot \nabla A_\varepsilon(u_\varepsilon)$, and defining $\mathcal{A}(s) := \int_0^s A(r)\,dr$ we obtain

$$\sup_{0\le t\le T}\int_\Omega \mathbf{A}(u_\varepsilon)(x,t)\,dx + \varepsilon \sup_{0\le t\le T}\int_\Omega \frac{|u_\varepsilon(x,t)|^2}{2}\,dx + \iint_{Q_T} |\nabla A(u_\varepsilon)|^p\,dx\,dt \le C, \tag{1.54}$$

for some constant $C > 0$, independent of ε.

Let $\varphi \in L^p(0,T;W^{1,p}(\Omega))$. Using the weak formulation (1.51), (1.53) and (1.54), we arrive at

$$\begin{aligned}\left|\int_0^T \langle \partial_t u_\varepsilon, \varphi\rangle\,dt\right| &\le \left\||\nabla A_\varepsilon(u_\varepsilon)|^{p-2}\nabla A_\varepsilon(u_\varepsilon)\right\|_{L^p(Q_T)}\|\nabla\varphi\|_{L^p(Q_T)}\\ &\quad + \chi\left\|u_\varepsilon f(u_\varepsilon)\right\|_{L^\infty(Q_T)}\|\nabla v_\varepsilon\|_{L^p(Q_T)}\|\nabla\varphi\|_{L^p(Q_T)}\\ &\le C\|\varphi\|_{L^p(0,T;W^{1,p}(\Omega))},\end{aligned}$$

for some constant $C > 0$ independent of ε. From this we deduce the bound

$$\|\partial_t u_\varepsilon\|_{L^{p'}(0,T;(W^{1,p}(\Omega))')} \le C. \tag{1.55}$$

Therefore, by (1.53)–(1.55) and standard compactness results (see [139]) we can extract subsequences, which we do not relabel, such that, as $\varepsilon \to 0$,

$$\begin{cases} u_\varepsilon \to u \text{ and } A_\varepsilon(u_\varepsilon) \to A(u) \text{ strongly in } L^p(Q_T) \text{ and a.e.,}\\ v_\varepsilon \to v \text{ strongly in } L^2(Q_T),\\ \nabla v_\varepsilon \to \nabla v \text{ weakly in } L^2(Q_T) \text{ and } \nabla A_\varepsilon(u_\varepsilon) \to \nabla A(u) \text{ weakly in } L^p(Q_T),\\ |\nabla A_\varepsilon(u_\varepsilon)|^{p-2}\nabla A_\varepsilon(u_\varepsilon) \to \Gamma_1 \text{ weakly in } L^{p'}(Q_T),\\ v_\varepsilon \to v \text{ weakly in } L^2(0,T;H^1(\Omega)),\\ \partial_t u_\varepsilon \to \partial_t u \text{ weakly in } L^{p'}(0,T;(W^{1,p}(\Omega))') \text{ and}\\ \partial_t v_\varepsilon \to \partial_t v \text{ weakly in } L^2(0,T;(H^1(\Omega))'). \end{cases} \tag{1.56}$$

The following Lemma is known as the Aubin lemma, see e.g. [139].

Lemma 1.13 *Let $X \subset B \subset Y$ be Banach spaces where the first embedding is compact. If the set of functions $\mathcal{F}$ is bounded in $L^\infty(0,T;X)$ and the set $\partial_t\mathcal{F} := \{\partial_t\mathcal{F} \ : \ f \in \mathcal{F}\}$ is bounded in $L^r(0,T;Y)$, $r > 1$; then $\mathcal{F}$ is relatively compact in $C(0,T;B)$.*

From the compact embedding $W^{1,p}(\Omega) \subset L^1(\Omega)$ we have that the embedding $L^\infty(\Omega) \subset (W^{1,p}(\Omega))'$ is also compact, and according to Lemma 1.13 with $X = W^{1,p}(\Omega)$, $B = (W^{1,p}(\Omega))'$ and $\mathcal{F} = \{u_\varepsilon\}_{\varepsilon>0}$, we can also conclude that $\{u_{\varepsilon_n}\}_{n\in\mathbb{N}}$ for any sequence $\varepsilon_n \to 0$ is a Cauchy sequence in $C(0,T;(W^{1,p}(\Omega))')$. We also have the following lemma, se [14] for its proof.

Lemma 1.14 *The functions v_ε converge strongly to v in $L^2(0,T;H^1(\Omega))$ as $\varepsilon \to 0$.*

Next, we identify Γ_1 as $|\nabla A(u)|^{p-2}\nabla A(u)$ when passing to the limit $\varepsilon \to 0$ in (1.51). Due to this particular nonlinearity, we cannot employ the monotonicity argument used in [14]; rather, we will utilize a Minty-type argument [115] and make repeated use of the following "weak chain rule" (see e.g. [22] for a proof).

Lemma 1.15 *Let $b : \mathbb{R} \to \mathbb{R}$ be Lipschitz continuous and nondecreasing. Assume $u \in L^\infty(Q_T)$ such that $\partial_t u \in L^{p'}(0,T;(W^{1,p}(\Omega))')$, $b(u) \in L^p(0,T;W^{1,p}(\Omega))$, $u(x,0) = u_0(x)$ a.e. on Ω, and $u_0 \in L^\infty(\Omega)$. If we define $B(u) = \int_0^u b(\xi)d\xi$, then there holds for all $\phi \in \mathcal{D}([0,T]\times\Omega)$ and for any $s \in (0,T)$*

$$-\int_0^s \langle \partial_t u, b(u)\phi\rangle \, dt = \int_0^s \int_\Omega B(u)\partial_t\phi \, dx\, dt + \int_\Omega B(u_0)\phi(x,0)\, dx - \int_\Omega B(u(x,s))\phi(x,s)\, dx.$$

Lemma 1.16 *There hold $\Gamma_1 = |\nabla A(u)|^{p-2}\nabla A(u)$ and $\nabla A_\varepsilon(u_\varepsilon) \to \nabla A(u)$ strongly in $L^p(Q_T)$.*

Proof. We define $\mathcal{Q}_T := \{(t,s,x) \ : \ (x,s) \in Q_t, \ t \in [0,T]\}$. The first step will be to show that $\forall \sigma \in L^p(0,T;W^{1,p}(\Omega))$:

$$\iiint_{\mathcal{Q}_T} \big(\Gamma_1 - |\nabla A(u)|^{p-2}\nabla A(u)\big)\cdot\big(\nabla A(u) - \nabla\sigma\big)\, dx\, ds\, dt \geq 0. \tag{1.57}$$

For all fixed $\varepsilon > 0$ we have the decomposition

$$\begin{aligned}
&\iiint_{\mathcal{Q}_T} \big(|\nabla A_\varepsilon(u_\varepsilon)|^{p-2}\nabla A_\varepsilon(u_\varepsilon) - |\nabla\sigma|^{p-2}\nabla\sigma\big)\cdot\big(\nabla A(u) - \nabla\sigma\big)\, dx\, ds\, dt \\
&\qquad = I_1 + I_2 + I_3, \\
&I_1 := \iiint_{\mathcal{Q}_T} |\nabla A_\varepsilon(u_\varepsilon)|^{p-2}\nabla A_\varepsilon(u_\varepsilon)\cdot\big(\nabla A(u) - \nabla A_\varepsilon(u_\varepsilon)\big)\, dx\, ds\, dt, \\
&I_2 := \iiint_{\mathcal{Q}_T} \big(|\nabla A_\varepsilon(u_\varepsilon)|^{p-2}\nabla A_\varepsilon(u_\varepsilon) - |\nabla\sigma|^{p-2}\nabla\sigma\big)\cdot\big(\nabla A_\varepsilon(u_\varepsilon) - \nabla\sigma\big)\, dx\, ds\, dt, \\
&I_3 := \iiint_{\mathcal{Q}_T} |\nabla\sigma|^{p-2}\nabla\sigma\cdot\big(\nabla A_\varepsilon(u_\varepsilon) - \nabla A(u)\big)\, dx\, ds\, dt.
\end{aligned}$$

Clearly, $I_2 \geq 0$ and from (1.56) we deduce that $I_3 \to 0$ as $\varepsilon \to 0$. For I_1, if we multiply (1.47a) by $\phi \in L^p(0,T;W^{1,p}(\Omega))$ and integrate over $\mathcal{Q}_T := \{(t,s,x) \ : \ (x,s) \in Q_t, \ t \in [0,T]\}$, we obtain

$$\begin{aligned}
&\int_0^T\int_0^t \langle \partial_t u_\varepsilon, \phi\rangle\, ds\, dt - \iiint_{\mathcal{Q}_T} \chi u_\varepsilon f(u_\varepsilon)\nabla v_\varepsilon\cdot\nabla\phi\, dx\, ds\, dt \\
&\qquad + \iiint_{\mathcal{Q}_T} |\nabla A_\varepsilon(u_\varepsilon)|^{p-2}\nabla A_\varepsilon(u_\varepsilon)\cdot\nabla\phi\, dx\, ds\, dt = 0.
\end{aligned}$$

Now, if we take $\phi = A(u) - A_\varepsilon(u_\varepsilon) \in L^p(0,T;W^{1,p}(\Omega))$ and use Lemma 1.15, we obtain

$$\begin{aligned}
I_1 &= -\int_0^T\int_0^t \langle \partial_t u_\varepsilon, A(u)\rangle\, ds\, dt + \int_0^T\int_0^t \langle \partial_t u_\varepsilon, A_\varepsilon(u_\varepsilon)\rangle\, ds\, dt \\
&\quad + \iiint_{\mathcal{Q}_T} \chi u_\varepsilon f(u_\varepsilon)\nabla v_\varepsilon\cdot\big(\nabla A(u) - \nabla A_\varepsilon(u_\varepsilon)\big)\, dx\, ds\, dt \\
&= -\int_0^T\int_0^t \langle \partial_t u_\varepsilon, A(u)\rangle\, ds\, dt + \iint_{Q_T} \mathbf{A}_\varepsilon(u_\varepsilon)\, dx\, dt - T\int_\Omega \mathbf{A}_\varepsilon(u_0)\, dx \\
&\quad + \iiint_{\mathcal{Q}_T} \chi u_\varepsilon f(u_\varepsilon)\nabla v_\varepsilon\cdot\big(\nabla A(u) - \nabla A_\varepsilon(u_\varepsilon)\big)\, dx\, ds\, dt.
\end{aligned}$$

Therefore, using (1.56) and Lemma 1.14, we conclude that

$$\lim_{\varepsilon\to 0} I_1 = -\int_0^T\int_0^t \langle \partial_t u, A(u)\rangle\, ds\, dt + \int_0^T\int_\Omega \mathbf{A}(u(x,t))\, dx\, dt - T\int_\Omega \mathbf{A}(u_0(x))\, dx,$$

and from Lemma 1.15, this yields $I_1 \to 0$ as $\varepsilon \to 0$. Consequently, we have shown that

$$\iiint_{Q_T} \big(|\nabla A_\varepsilon(u_\varepsilon)|^{p-2}\nabla A_\varepsilon(u_\varepsilon) - |\nabla A(u)|^{p-2}\nabla A(u)\big) \cdot \big(\nabla A(u) - \nabla A_\varepsilon(u_\varepsilon)\big)\, dx\, ds\, dt \le 0,$$

which proves (1.57). Choosing $\sigma = A(u) - \lambda\xi$ with $\lambda \in \mathbb{R}$ and $\xi \in L^p(0,T;W^{1,p}(\Omega))$ and combining the two inequalities arising from $\lambda > 0$ and $\lambda < 0$, we obtain the first assertion of the lemma. The second assertion directly follows from (1.57).

With the above convergences we are now able to pass to the limit $\varepsilon \to 0$, and we can identify the limit (u, v) as a (weak) solution of (1.45). In fact, if $\varphi \in L^p(0,T;W^{1,p}(\Omega))$ is a test function for (1.51), then by (1.56) it is now clear that

$$\int_0^T \langle \partial_t u_\varepsilon, \varphi\rangle\, dt \to \int_0^T \langle \partial_t u, \varphi\rangle\, dt \quad \text{as } \varepsilon \to 0,$$

$$\iint_{Q_T} |\nabla A_\varepsilon(u_\varepsilon)|^{p-2}\nabla A_\varepsilon(u_\varepsilon)\cdot\nabla\varphi\, dx\, dt \to \iint_{Q_T} |\nabla A(u)|^{p-2}\nabla A(u)\cdot\nabla\varphi\, dx\, dt \quad \text{as } \varepsilon \to 0.$$

Since $h(u_\varepsilon) = u_\varepsilon f(u_\varepsilon)$ is bounded in $L^\infty(Q_T)$ and by Lemma 1.14, $v_\varepsilon \to v$ in $L^2(0,T;H^1(\Omega))$, it follows that

$$\iint_{Q_T} \chi u_\varepsilon f(u_\varepsilon)\nabla v_\varepsilon \cdot \nabla\varphi\, dx\, dt \to \iint_{Q_T} \chi u f(u)\nabla v\cdot\nabla\varphi\, dx\, dt \quad \text{as } \varepsilon \to 0.$$

We have thus identified u as the first component of a solution of (1.45). Using a similar argument, we can identify v as the second component of a solution.

1.5.2 Hölder continuity of weak solutions

Preliminaries.- We start by recasting Definition 1.5 in a form that involves the Steklov average defined for a function $w \in L^1(Q_T)$ and $0 < h < T$, by

$$w_h := \begin{cases} \dfrac{1}{h}\displaystyle\int_t^{t+h} w(\cdot,\tau)\, d\tau & \text{if } t \in (0, T-h], \\ 0 & \text{if } t \in (T-h, T]. \end{cases}$$

The proof of the following technical lemma can be obtained using general theory of L^p spaces (see e.g., [65]). This lemma will be used to allow the passage to the limit when using the Steklov average.

Lemma 1.17 *If $w \in L^{q,r}(Q_T)$ then, as $h \to 0$, the Steklov average w_h converges to w in $L^{q,r}(Q_{T-\varepsilon})$, for every $\varepsilon \in (0,T)$. If $w \in C(0,T;L^q(\Omega))$ then, as $h \to 0$, the Steklov average $w_h(\cdot,t)$ converges to $w(\cdot,t)$ in $L^q(\Omega)$, for every $t \in (0, T-\varepsilon)$ and every $\varepsilon \in (0,T)$.*

Definition 1.18 A local weak solution u for (1.45) is a measurable function such that, for every compact $K \subset \Omega$ and for all $0 < t < T-h$, $\forall \varphi \in W_0^{1,p}(K)$:

$$\int_{K\times\{t\}} \Big\{\partial_t(u_h)\varphi + \big(|\nabla A(u)|^{p-2}\nabla A(u)\big)_h \cdot \nabla\varphi - \big(\chi u f(u)\nabla v\big)_h \cdot \nabla\varphi\Big\}\, dx = 0. \tag{1.58}$$

The following technical lemma on the geometric convergence of sequences (see e.g., [66, Lemma 4.2, Ch. I]) will be used later.

Lemma 1.19 *Let $\{X_n\}$ and $\{Z_n\}$, $n \in \mathbb{N}_0$, be sequences of positive real numbers satisfying*

$$X_{n+1} \leq Cb^n\big(X_n^{1+\alpha} + X_n^{\alpha} Z_n^{1+\kappa}\big), \quad Z_{n+1} \leq Cb^n\big(X_n + Z_n^{1+\kappa}\big),$$

where $C > 1$, $b > 1$, $\alpha > 0$ and $\kappa > 0$ are given constants. Then $X_n, Z_n \to 0$ as $n \to \infty$ provided that

$$X_0 + Z_0^{1+\kappa} \leq (2C)^{-(1+\kappa)/\sigma} b^{-(1+\kappa)/\sigma^2}, \quad \text{with } \sigma = \min\{\alpha, \kappa\}.$$

We will need as well, the following embedding theorem (see e.g., [65])

Theorem 1.20 *Let $p > 1$. There exists a constant γ depending only on N and p such that for every $v \in V_0^p(\Omega_T)$,*

$$\|v\|_{p,\Omega_T}^p \leq \gamma ||v| > 0|^{\frac{p}{N+p}} \|v\|_{V^p(\Omega_T)}^p.$$

The rescaled cylinders.- Let $B_\rho(x_0)$ denote the ball of radius ρ centered at x_0. Then, for a point $(x_0, t_0) \in \mathbb{R}^{n+1}$, we denote the cylinder of radius ρ and height τ by

$$(x_0, t_0) + Q(\tau, \rho) := B_\rho(x_0) \times (t_0 - \tau, t_0).$$

Intrinsic scaling is based on measuring the oscillation of a solution in a family of nested and shrinking cylinders whose dimensions are related to the degeneracy of the underlying PDE. To formalize this, we fix $(x_0, t_0) \in Q_T$; after a translation, we may assume that $(x_0, t_0) = (0, 0)$. Then let $\varepsilon > 0$ and let $R > 0$ be small enough so that $Q(R^{p-\varepsilon}, 2R) \subset Q_T$, and define

$$\mu^+ := \operatorname*{ess\,sup}_{Q(R^{p-\varepsilon},2R)} u, \qquad \mu^- := \operatorname*{ess\,inf}_{Q(R^{p-\varepsilon},2R)} u, \qquad \omega := \operatorname*{ess\,osc}_{Q(R^{p-\varepsilon},2R)} u \equiv \mu^+ - \mu^-.$$

Now construct the cylinder $Q(a_0 R^p, R)$, where

$$a_0 = \left(\frac{\omega}{2}\right)^{2-p} \frac{1}{\phi(\omega/2^m)^{p-1}},$$

with m to be chosen later. To ensure that $Q(a_0 R^p, R) \subset Q(R^{p-\varepsilon}, 2R)$, we assume that

$$\frac{1}{a_0} = \left(\frac{\omega}{2}\right)^{p-2} \phi\left(\frac{\omega}{2^m}\right)^{p-1} > R^\varepsilon, \tag{1.59}$$

and therefore the relation

$$\operatorname*{ess\,osc}_{Q(a_0 R^p,R)} u \leq \omega \tag{1.60}$$

holds. Otherwise, the result is trivial as the oscillation is comparable to the radius. We mention that for ω small and for $m > 1$, the cylinder $Q(a_0 R^p, R)$ is long enough in the $t-$direction, so that we can *accommodate* the degeneracies of the problem. Without loss of generality, we will assume $\omega < \delta < 1/2$. We emphasize that we introduced the cylinder $Q(R^{p-\varepsilon}, 2R)$ and assumed (1.59) so that (1.60) is valid for the constructed cylinder $Q(a_0 R^p, R)$.

Consider now, inside $Q(a_0 R^p, R)$, smaller subcylinders of the form

$$Q_R^{t^*} \equiv (0, t^*) + Q(dR^p, R), \qquad d = \left(\frac{\omega}{2}\right)^{2-p} \frac{1}{[\psi(\omega/4)]^{p-1}}, \qquad t^* < 0.$$

These are contained in $Q(a_0R^p, R)$ if $a_0R^p \geq -t^* + dR^p$, which holds whenever $\phi(\omega/2^m) \leq \psi(\omega/4)$ and

$$t^* \in \left(\frac{(\omega/2)^{2-p}R^p}{\psi(\omega/4)^{p-1}} - \frac{(\omega/2)^{p-2}R^p}{\phi(\omega/2^m)^{p-1}}, 0 \right).$$

These particular definitions of a_0 and of d turn out to be the natural extensions to the case $p > 2$ of their counterparts in [149]. Here, the scaling factor $(\omega/2)^{2-p}$ takes into account the structure of the $p-$Laplacian term, and the terms $[\psi(\omega/4)]^{p-1}$, $[\phi(\omega/2^m)]^{p-1}$ will take care of the two-sidedly degeneracy structure of $a(u)$. Notice that for $p = 2$ and $a(u) \equiv 1$, we recover the standard parabolic cylinders.

The structure of the proof will be based on the analysis of the following alternative: either there is a cylinder $Q_R^{t^*}$ where u is essentially away from its infimum, or such a cylinder can not be found and thus u is essentially away from its supremum in all cylinders of that type. Both cases lead us to the conclusion that the essential oscillation of u when going to a smaller cylinder decreases by a factor that can be quantified, and which does *not* depend on ω.

Remark 1.5.1 *(See [128, Remark 4.2]) Let us introduce quantities of the type $B_iR^\theta\omega^{-b_i}$, where B_i and $b_i > 0$ are constants that can be determined a priori from the data, independently of ω and R, and θ depending only on N and p. We assume without loss of generality, that*

$$B_iR^\theta\omega^{-b_i} \leq 1.$$

If this was not be valid, then we would have $\omega \leq CR^\varepsilon$ for the choices $C = \max_i B_i^{1/b}$ and $\varepsilon = \theta/\min_i b_i$, and the result would be trivial.

The first alternative.-

Lemma 1.21 *There exists $\nu_0 \in (0,1)$, independent of ω and R, such that if*

$$\left|\left\{(x,t) \in Q_R^{t^*} \ : \ u(x,t) > 1 - \omega/2\right\}\right| \leq \nu_0 \left|Q_R^{t^*}\right| \tag{1.61}$$

for some cylinder of the type $Q_R^{t^*}$, then $u(x,t) < 1 - \omega/4$ a.e. in $Q_{R/2}^{t^*}$.

Proof. Let $u_\omega := \min\{u, 1 - \omega/4\}$, take the cylinder for which (1.61) holds, define

$$R_n = \frac{R}{2} + \frac{R}{2^{n+1}}, \quad n \in \mathbb{N}_0,$$

and construct the family

$$Q_{R_n}^{t^*} := (0, t^*) + Q(dR_n^p, R_n) = B_{R_n} \times (\tau_n, t^*), \quad \tau_n := t^* - dR_n^p, \quad n \in \mathbb{N}_0;$$

note that $Q_{R_n}^{t^*} \to Q_{R/2}^{t^*}$ as $n \to \infty$. Let $\{\xi_n\}_{n\in\mathbb{N}}$ be a sequence of piecewise smooth cutoff functions satisfying

$$\begin{cases} \xi_n = 1 \text{ in } Q_{R_{n+1}}^{t^*}, \quad \xi_n = 0 \text{ on the parabolic boundary of } Q_{R_n}^{t^*}, \\ |\nabla\xi_n| \leq \dfrac{2^{n+1}}{R}, \quad 0 \leq \partial_t\xi_n \leq \dfrac{2^{p(n+1)}}{dR^p}, \quad |\Delta\xi_n| \leq \dfrac{2^{p(n+1)}}{R^p}, \end{cases} \tag{1.62}$$

and define

$$k_n := 1 - \frac{\omega}{4} - \frac{\omega}{2^{n+2}}, \quad n \in \mathbb{N}_0.$$

Now take $\varphi = [(u_\omega)_h - k_n]^+\xi_n^p$, $K = B_{R_n}$ in (1.58) and integrate in time over (τ_n, t) for $t \in (\tau_n, t^*)$. Applying integration by parts to the first term gives

$$\begin{aligned}
F_1 :=& \int_{\tau_n}^t \int_{B_{R_n}} \partial_s u_h [(u_\omega)_h - k_n]^+ \xi_n^p \, dx \, ds \\
=& \frac{1}{2} \int_{\tau_n}^t \int_{B_{R_n}} \partial_s \Big(\big([(u_\omega)_h - k_n]^+\big)^2 \Big) \xi_n^p \, dx \, ds \\
&+ \Big(1 - \frac{\omega}{4} - k_n\Big) \int_{\tau_n}^t \int_{B_{R_n}} \partial_s \Big(\Big(\Big[u - \Big(1 - \frac{\omega}{4}\Big)\Big]^+ \Big)_h \Big) \xi_n^p \, dx \, ds \\
=& \frac{1}{2} \int_{B_{R_n} \times \{t\}} \big([u_\omega - k_n]_h^+\big)^2 \xi_n^p \, dx \, ds - \frac{1}{2} \int_{B_{R_n} \times \{\tau_n\}} \big([u_\omega - k_n]_h^+\big)^2 \xi_n^p \, dx \, ds \\
&- \frac{p}{2} \int_{\tau_n}^t \int_{B_{R_n}} \big([u_\omega - k_n]_h^+\big)^2 \xi_n^{p-1} \partial_s \xi_n \, dx \, ds \\
&+ \Big(1 - \frac{\omega}{4} - k_n\Big) \int_{\tau_n}^t \int_{B_{R_n}} \partial_s \Big(\Big(\Big[u - \Big(1 - \frac{\omega}{4}\Big)\Big]^+ \Big)_h \Big) \xi_n^p \, dx \, ds.
\end{aligned}$$

In light of standard convergence properties of the Steklov average, we obtain

$$\begin{aligned}
F_1 \to F_1^* :=& \frac{1}{2} \int_{B_{R_n} \times \{t\}} \big([u_\omega - k_n]^+\big)^2 \xi_n^p \, dx \, ds \\
&- \frac{p}{2} \int_{\tau_n}^t \int_{B_{R_n}} \big([u_\omega - k_n]^+\big)^2 \xi_n^{p-1} \partial_s \xi_n \, dx \, ds \\
&+ \Big(1 - \frac{\omega}{4} - k_n\Big) \Big(\int_{B_{R_n} \times \{t\}} \Big[u - \Big(1 - \frac{\omega}{4}\Big)\Big]^+ \xi_n^p \, dx \, ds \\
&- p \int_{B_{R_n} \times \{\tau_n\}} \Big[u - \Big(1 - \frac{\omega}{4}\Big)\Big]^+ \xi_n^{p-1} \partial_s \xi_n \, dx \, ds \Big) \quad \text{as } h \to 0.
\end{aligned}$$

Using (1.62) and the nonnegativity of the third term, we arrive at

$$\begin{aligned}
F_1^* \geq& \frac{1}{2} \int_{B_{R_n} \times \{t\}} \big([u_\omega - k_n]^+\big)^2 \xi_n^p \, dx \\
&- \frac{p}{2d} \Big(\frac{\omega}{4}\Big)^2 \frac{2^{p(n+1)}}{R^p} \int_{\tau_n}^t \int_{B_{R_n}} \chi_{\{u_\omega \geq k_n\}} \, dx \, ds \\
&- \frac{p}{d} \Big(\frac{\omega}{4}\Big)^2 \frac{2^{p(n+1)}}{R^p} \int_{\tau_n}^t \int_{B_{R_n}} \chi_{\{u \geq 1 - \omega/4\}} \, dx \, ds \\
\geq& \frac{1}{2} \int_{B_{R_n} \times \{t\}} \big([u_\omega - k_n]^+\big)^2 \xi_n^p \, dx \\
&- \frac{3}{2} \frac{p}{d} \Big(\frac{\omega}{4}\Big)^2 \frac{2^{p(n+1)}}{R^p} \int_{\tau_n}^t \int_{B_{R_n}} \chi_{\{u_\omega \geq k_n\}} \, dx \, ds,
\end{aligned}$$

the last inequality coming from $u \geq 1 - \omega/4 \Rightarrow u_\omega \geq k_n$. Since $[u_\omega - k_n]^+ \leq \omega/4$, we know that

$$\begin{aligned}
\big([u_\omega - k_n]^+\big)^2 &= \big([u_\omega - k_n]^+\big)^{2-p} \big([u_\omega - k_n]^+\big)^p \\
&\geq \Big(\frac{\omega}{4}\Big)^{2-p} \big([u_\omega - k_n]^+\big)^p \\
&\geq \Big(\frac{\omega}{2}\Big)^{2-p} \big([u_\omega - k_n]^+\big)^p,
\end{aligned}$$

therefore, the definition of d implies that

$$\begin{aligned} F_1^* \geq & \frac{1}{2}\left(\frac{\omega}{2}\right)^{2-p} \int_{B_{R_n}\times\{t\}} \left([u_\omega - k_n]^+\right)^p \xi_n^p \, dx \\ & - \frac{3}{2} p 2^{p-2} \left(\frac{\omega}{4}\right)^p \frac{2^{p(n+1)}}{R^p} \psi(\omega/4)^{p-1} \int_{\tau_n}^t \int_{B_{R_n}} \chi_{\{u_\omega \geq k_n\}} \, dx \, ds. \end{aligned} \tag{1.63}$$

We now deal with the diffusive term. The term

$$F_2 := \int_{\tau_n}^t \int_{B_{R_n}} \left(a(u)^{p-1} |\nabla u|^{p-2} \nabla u\right)_h \cdot \nabla \left\{ [(u_\omega)_h - k_n]^+ \xi_n^p \right\} dx \, ds$$

converges for $h \to 0$ to

$$\begin{aligned} F_2^* := & \int_{\tau_n}^t \int_{B_{R_n}} a(u)^{p-1} |\nabla u|^{p-2} \nabla u \\ & \cdot \nabla \left\{ [u_\omega - k_n]^+ \xi_n^p \right\} dx \, ds \\ = & \int_{\tau_n}^t \int_{B_{R_n}} a(u)^{p-1} |\nabla u|^{p-2} \nabla u \\ & \cdot \left(\nabla (u_\omega - k_n)^+ \xi_n^p + p (u_\omega - k_n)^+ \xi_n^{p-1} \nabla \xi_n \right) dx \, ds \\ = & \int_{\tau_n}^t \int_{B_{R_n}} a(u)^{p-1} |\xi_n \nabla (u_\omega - k_n)^+|^p \, dx \, ds + \tilde{F}_2^*, \end{aligned}$$

where we define

$$\tilde{F}_2^* := p \int_{\tau_n}^t \int_{B_{R_n}} a(u)^{p-1} |\nabla u|^{p-2} \nabla u \cdot \nabla \xi_n (u_\omega - k_n)^+ \xi_n^{p-1} \, dx \, ds.$$

Since $\nabla (u_\omega - k_n)^+$ is nonzero only within the set $\{k_n < u < 1 - \omega/4\}$ and $a(u) \geq \gamma_1 \psi(\omega/4)$ on $\{k_n < u < 1 - \omega/4\}$, we may estimate the first term of F_2^* from below as follows:

$$\begin{aligned} & \int_{\tau_n}^t \int_{B_{R_n}} a(u)^{p-1} \left| \xi_n \nabla (u_\omega - k_n)^+ \right|^p dx \, ds \geq \\ & \qquad [\gamma_1 \psi(\omega/4)]^{p-1} \int_{\tau_n}^t \int_{B_{R_n}} \left| \xi_n \nabla (u_\omega - k_n)^+ \right|^p dx \, ds. \end{aligned} \tag{1.64}$$

Let us now focus on $\tilde{F}_2^*$. Using that $\nabla (u_\omega - k_n)^+$ is nonzero only within the set $\{k_n < u < 1 - \omega/4\}$, integrating by parts, and using (1.46) and (1.62), we obtain

$$\begin{aligned} \left| \tilde{F}_2^* \right| \leq & p \int_{\tau_n}^t \int_{B_{R_n}} |a(u)|^{p-1} |\nabla (u_\omega - k_n)^+|^{p-1} |\nabla \xi_n| (u_\omega - k_n)^+ \xi_n^{p-1} \, dx \, ds \\ & + \left| p \left(1 - \frac{\omega}{4} - k_n\right) \int_{\tau_n}^t \int_{B_{R_n}} \xi_n^{p-1} \nabla \xi_n \right. \\ & \qquad \left. \cdot \nabla \left\{ \frac{1}{p-1} \left(\int_{1-\omega/4}^u a(s) \, ds \right)_+^{p-1} \right\} dx \, ds \right| \\ \leq & p \left[\gamma_2 \psi(\omega/2)\right]^{p-1} \int_{\tau_n}^t \int_{B_{R_n}} |\nabla \xi_n| (u_\omega - k_n)^+ \left| \xi_n \nabla (u_\omega - k_n)^+ \right|^{p-1} dx \, ds \end{aligned}$$

$$+\frac{p\omega}{4}\Bigg|-\int_{\tau_n}^{t}\int_{B_{R_n}}\left(\int_{1-\omega/4}^{u}a(s)\,ds\right)_{+}^{p-1}$$
$$\times\left((p-1)\xi_n^{p-2}|\nabla\xi_n|^2+\xi_n^{p-1}\Delta\xi_n\right)dx\,ds\Bigg|.$$

Next, we consider that

$$\left(\int_{1-\omega/4}^{u}a(s)\,ds\right)^{+}\leq\frac{\omega}{4}\psi\left(\omega/4\right),$$

and apply Young's inequality

$$ab\leq\frac{\epsilon_2^r}{r}a^r+\frac{b^{r'}}{r'\epsilon_2^{r'}}\quad\text{if } a,b\geq 0,\quad \frac{1}{r}+\frac{1}{r'}=1,$$

for the choices

$$r=p,\quad a=|\nabla\xi_n|(u_\omega-k_n)^+,\quad b=\left|\nabla(u_\omega-k_n)^+\right|^{p-1}\quad\text{and}$$
$$\epsilon_1^{-p'}=\frac{p'}{p}\frac{(\gamma_1^{p-1}-1)\psi(\omega/4)^{p-1}}{\gamma_2^{p-1}\psi(\omega/2)^{p-1}}>0.$$

This leads to

$$\begin{aligned}\left|\tilde{F}_2^*\right|\leq&\frac{1}{\epsilon_1^p}\left[\gamma_2\psi\left(\omega/2\right)\right]^{p-1}\left(\frac{\omega}{4}\right)^p\frac{2^{p(n+1)}}{R^p}\int_{\tau_n}^{t}\int_{B_{R_n}}\chi_{\{u_\omega\geq k_n\}}\,dx\,ds\\
&+(p-1)\epsilon_1^{p'}\left[\gamma_2\psi(\omega/2)\right]^{p-1}\int_{\tau_n}^{t}\int_{B_{R_n}}\left|\xi_n\nabla(u_\omega-k_n)^+\right|^p dx\,ds\\
&+p^2\left(\frac{\omega}{4}\right)^p\psi\left(\omega/4\right)^{p-1}\frac{2^{p(n+1)}}{R^p}\int_{\tau_n}^{t}\int_{B_{R_n}}\chi_{\{u_\omega\geq k_n\}}\,dx\,ds\\
\leq&\left\{\frac{(p-1)\gamma_2^{p-1}\psi\left(\omega/2\right)^{p-1}}{(\gamma_1^{p-1}-1)\psi\left(\omega/4\right)^{p-1}}\right\}^{p-1}\left[\gamma_2\psi(\omega/2)\right]^{p-1}\left(\frac{\omega}{4}\right)^p\\
&\qquad\times\frac{2^{p(n+1)}}{R^p}\int_{\tau_n}^{t}\int_{B_{R_n}}\chi_{\{u_\omega\geq k_n\}}\,dx\,ds\\
&+\left(\gamma_1^{p-1}-1\right)\psi\left(\omega/4\right)^{p-1}\int_{\tau_n}^{t}\int_{B_{R_n}}\left|\xi_n\nabla(u_\omega-k_n)^+\right|^p dx\,ds\\
&+p^2\left(\frac{\omega}{4}\right)^p\psi\left(\omega/4\right)^{p-1}\frac{2^{p(n+1)}}{R^p}\int_{\tau_n}^{t}\int_{B_{R_n}}\chi_{\{u_\omega\geq k_n\}}\,dx\,ds,\end{aligned}\tag{1.65}$$

Hence, from (1.64) and (1.65) and taking into account that

$$\left[\frac{\psi\left(\omega/2\right)}{\psi\left(\omega/4\right)}\right]^{p(p-1)}=\left(\frac{4}{2}\right)^{p\beta_2}=2^{p\beta_2},$$

we obtain

$$\begin{aligned}F_2^*\geq&\psi\left(\omega/4\right)^{p-1}\int_{\tau_n}^{t}\int_{B_{R_n}}\left|\xi_n\nabla(u_\omega-k_n)^+\right|^p dx\,ds\\
&-\left\{p^2+2^{p\beta_2}\left[\frac{p'\gamma_2^p}{p(\gamma_1^{p-1}-1)}\right]^{p-1}\right\}\left(\frac{\omega}{4}\right)^p\\
&\qquad\times\frac{2^{p(n+1)}}{R^p}\psi\left(\omega/4\right)^{p-1}\int_{\tau_n}^{t}\int_{B_{R_n}}\chi_{\{u_\omega\geq k_n\}}\,dx\,ds.\end{aligned}\tag{1.66}$$

Finally, for the lower order term

$$F_3 := \int_{\tau_n}^t \int_{B_{R_n}} \big(\chi u f(u) \nabla v\big)_h \cdot \nabla\big\{[(u_\omega)_h - k_n]^+ \xi_n^p\big\}\, dx\, ds$$

we have

$$\begin{aligned} F_3 \to F_3^* := &\int_{\tau_n}^t \int_{B_{R_n}} \chi u f(u) \nabla v \cdot \big(\nabla (u_\omega - k_n)^+ \xi_n^p \\ &\qquad + p(u_\omega - k_n)^+ \xi_n^{p-1} \nabla \xi_n\big)\, dx\, ds \\ = &\int_{\tau_n}^t \int_{B_{R_n}} \chi u f(u) \nabla v \cdot \nabla (u_\omega - k_n)^+ \xi_n^p\, dx\, ds \\ &+ p \int_{\tau_n}^t \int_{B_{R_n}} \chi u f(u) \nabla v \cdot \nabla \xi_n (u_\omega - k_n)^+ \xi_n^{p-1}\, dx\, ds \quad \text{as } h \to 0. \end{aligned}$$

Applying Young's inequality with

$$r = p, \quad a = \nabla (u_\omega - k_n)^+ \xi_n, \quad b = \chi u f(u) \xi_n^{p-1} \nabla v \quad \text{and} \quad \epsilon_2^p = \frac{p}{2} \psi(\omega/4)^{p-1} > 0,$$

using the fact that $(u_\omega - k_n)^+ \le \omega/4$ and defining $M := \|\chi u f(u)\|_{L^\infty(Q_T)}$, we may estimate F_3^* by

$$\begin{aligned} F_3^* \le &\frac{\epsilon_2^p}{p} \int_{\tau_n}^t \int_{B_{R_n}} \big|\nabla (u_\omega - k_n)^+ \xi_n\big|^p\, dx\, ds + \frac{M^{p'}}{p' \epsilon_2^{p'}} \int_{\tau_n}^t \int_{B_{R_n}} |\nabla v|^{p'} \chi_{\{u_\omega \ge k_n\}}\, dx\, ds \\ &+ pM \int_{\tau_n}^t \int_{B_{R_n}} |\nabla v| \left(\frac{\omega}{4}\right) |\nabla \xi_n| \chi_{\{u_\omega \ge k_n\}}\, dx\, ds \\ \le &\frac{1}{2} \psi(\omega/4)^{p-1} \int_{\tau_n}^t \int_{B_{R_n}} \big|\nabla (u_\omega - k_n)^+ \xi_n\big|^p\, dx\, ds \\ &+ \frac{(p/2)^{-p'/p}}{p'} \frac{M^{p'}}{\psi(\omega/4)} \int_{\tau_n}^t \int_{B_{R_n}} |\nabla v|^{p'} \chi_{\{u_\omega \ge k_n\}}\, dx\, ds \\ &+ \epsilon_3^p \left(\frac{\omega}{4}\right)^p \int_{\tau_n}^t \int_{B_{R_n}} |\nabla \xi_n|^p \chi_{\{u_\omega \ge k_n\}}\, dx\, ds \\ &+ \frac{pM^{p'}}{p' \epsilon_3^{p'}} \int_{\tau_n}^t \int_{B_{R_n}} |\nabla v|^{p'} \chi_{\{u_\omega \ge k_n\}}\, dx\, ds. \end{aligned}$$

Applying Young's inequality with

$$a = |\nabla \xi_n| \omega/4, \quad b = M |\nabla v|, \quad \epsilon_3^{p'} = \psi(\omega/4) > 0$$

to the last two terms in the last right-hand side and using (1.62), we obtain

$$\begin{aligned} F_3^* \le F_3^{**} := &\frac{1}{2} \psi(\omega/4)^{p-1} \int_{\tau_n}^t \int_{B_{R_n}} \big|\nabla (u_\omega - k_n)^+ \xi_n\big|^p\, dx\, ds \\ &+ \frac{M^{p'}}{p' \psi(\omega/4)} \left[\left(\frac{p}{2}\right)^{-p'/p} + p\right] \int_{\tau_n}^t \int_{B_{R_n}} |\nabla v|^{p'} \chi_{\{u_\omega \ge k_n\}}\, dx\, ds \\ &+ \left(\frac{\omega}{4}\right)^p \frac{2^{p(n+1)}}{R^p} \psi(\omega/4)^{p-1} \int_{\tau_n}^t \int_{B_{R_n}} \chi_{\{u_\omega \ge k_n\}}\, dx\, ds. \end{aligned}$$

Additionally, using the Hölder inequality, we may write

$$\int_{\tau_n}^{t}\int_{B_{R_n}} |\nabla v|^{p'}\chi_{\{u_\omega\geq k_n\}}\,dx\,ds \leq \|\nabla v\|^{p'}_{L^{p'p}(Q_T)}\left(\int_{\tau_n}^{t}\left|A^+_{k_n,R_n}(\sigma)\right|d\sigma\right)^{1-1/p},$$

where $|A^+_{k_n,R_n}(\sigma)|$ is the N-dimensional measure of the set

$$A^+_{k_n,R_n}(\sigma) := \left\{x\in B_{R_n}\ :\ u(x,\sigma)>k_n\right\}.$$

Thus we obtain

$$\begin{aligned} F_3^{**} \leq{}& \frac{1}{2}\psi(\omega/4)^{p-1}\int_{\tau_n}^{t}\int_{B_{R_n}}\left|\xi_n\nabla(u_\omega-k_n)^+\right|^p dx\,ds \\ &+\left(\frac{\omega}{4}\right)^p\frac{2^{p(n+1)}}{R^p}\psi\left(\omega/4\right)^{p-1}\int_{\tau_n}^{t}\int_{B_{R_n}}\chi_{\{u_\omega\geq k_n\}}\,dx\,ds \\ &+\frac{M^{p'}}{p'\psi\left(\omega/4\right)}\left[\left(\frac{p}{2}\right)^{-p'/p}+p\right]\|\nabla v\|^{p'}_{L^{p'p}(Q_T)}\left(\int_{\tau_n}^{t}\left|A^+_{k_n,R_n}(\sigma)\right|d\sigma\right)^{1-1/p}. \end{aligned} \tag{1.67}$$

Combining the resulting estimates (1.63), (1.66), (1.67) and multiplying by $2(\omega/2)^{p-2}$ yields

$$\begin{aligned} &\operatorname*{ess\,sup}_{\tau_n\leq t\leq t^*}\int_{B_{R_n}\times\{t\}}\left([u_\omega-k_n]^+\right)^p\xi_n^p\,dx\,ds+\frac{2}{d}\int_{\tau_n}^{t^*}\int_{B_{R_n}}\left|\xi_n\nabla(u_\omega-k_n)^+\right|^p dx\,ds \\ &\leq\left\{\frac{3}{2}p2^{p-2}+p^2+2^{p\beta_2}\left[\frac{p'\gamma_2^p}{p(\gamma_1^{p-1}-1)}\right]^{p-1}\right\}\left(\frac{\omega}{4}\right)^p \\ &\quad\times\frac{2^{p(n+1)}}{R^p}\frac{2}{d}\int_{\tau_n}^{t^*}\int_{B_{R_n}}\chi_{\{u_\omega\geq k_n\}}\,dx\,ds \\ &\quad+2\frac{(\omega/2)^{p-2}M^{p'}}{p'\psi\left(\omega/4\right)}\left[\left(\frac{p}{2}\right)^{-p'/p}+p\right]\|\nabla v\|^{p'}_{L^{p'p}(Q_T)}\left(\int_{\tau_n}^{t^*}\left|A^+_{k_n,R_n}(\sigma)\right|d\sigma\right)^{1-1/p}. \end{aligned} \tag{1.68}$$

Next we perform a change in the time variable putting $\bar{t}:=\frac{1}{d}(t-t^*)$, which transforms $Q(dR_n^p,R_n)$ into $Q^{t^*}_{R_n}$. Furthermore, if we define $\bar{u}_\omega(\cdot,\bar{t}):=u_\omega(\cdot,t)$ and $\bar{\xi}_n(\cdot,\bar{t})=\xi_n(\cdot,t)$, then defining for each n,

$$A_n:=\int_{-R_n^p}^{0}\int_{B_{R_n}}\chi_{\{\bar{u}_\omega\geq k_n\}}\,dx\,d\bar{t}=\frac{1}{d}\int_{\tau_n}^{t}\int_{B_{R_n}}\chi_{\{u_\omega\geq k_n\}}\,dx\,ds$$

we may rewrite (1.68) more concisely as

$$\begin{aligned} &\left\|(\bar{u}_\omega-k_n)^+\bar{\xi}_n\right\|^p_{V^p(Q^{t^*}_{R_n})}\leq \\ &\quad 2\left\{\frac{3}{2}p2^{p-2}+p^2+2^{p\beta_2}\left[\frac{p'\gamma_2^p}{p(\gamma_1^{p-1}-1)}\right]^{p-1}\right\}\left(\frac{\omega}{4}\right)^p\frac{2^{p(n+1)}}{R^p}A_n \\ &\quad+2\left[\left(\frac{p}{2}\right)^{-p'/p}+p\right]\frac{M^{p'}}{p'}\left(\frac{\omega}{2}\right)^{(p-2)/p}\psi\left(\omega/4\right)^{1-p-1/p}\|\nabla v\|^{p'}_{L^{p'p}(Q_T)}A_n^{1-1/p}, \end{aligned} \tag{1.69}$$

where $V^p(\Omega_T)=L^\infty(0,T;L^p(\Omega))\cap L^p(0,T;W^{1,p}(\Omega))$ endowed with the norm

$$\|u\|^p_{V^p(\Omega_T)}=\operatorname*{ess\,sup}_{0\leq t\leq T}\|u(\cdot,t)\|^p_{p,\Omega}+\|\nabla u\|^p_{p,\Omega_T}.$$

Next, observe that by application of the embedding theorem 1.20, we get

$$\frac{1}{2^{p(n+1)}}\left(\frac{\omega}{4}\right)^p A_{n+1}=|k_n-k_{n+1}|^pA_{n+1}$$

$$
\begin{aligned}
&\leq \left\|(\bar{u}_\omega - k_n)^+\right\|^p_{p,Q(R^p_{n+1},R_{n+1})} \\
&\leq \left\|(\bar{u}_\omega - k_n)^+\bar{\xi}_n\right\|^p_{p,Q(R^p_n,R_n)} \\
&\leq C\left\|(\bar{u}_\omega - k_n)^+\bar{\xi}_n\right\|^p_{V^p(Q^{t^*}_{R_n})} A_n^{p/(N+p)}.
\end{aligned}
$$

Now, applying (1.69), we get

$$
\begin{aligned}
\frac{1}{2^{p(n+1)}}\left(\frac{\omega}{4}\right)^p A_{n+1} \leq{}& 2C\left\{\frac{3}{2}p2^{p-2} + p^2 + 2^{p\beta_2}\left[\frac{p'\gamma_2^p}{p(\gamma_1^{p-1}-1)}\right]^{p-1}\right\} \\
&\times \left(\frac{\omega}{4}\right)^p \frac{2^{p(n+1)}}{R^p} A_n^{1+p/(N+p)} \\
&+ 2C\left[\left(\frac{p}{2}\right)^{-q/p} + p\right]\frac{M^{p'}}{p'}\left(\frac{\omega}{2}\right)^{(p-2)/p} \\
&\times \psi(\omega/4)^{1-p-1/p}\|\nabla v\|^{p'}_{L^{p'p}(Q_T)} A_n^{1-1/p+p/(N+p)}.
\end{aligned}
\tag{1.70}
$$

Now let us define

$$
X_n := \frac{A_n}{|Q(R^p_n, R_n)|}, \qquad Z_n := \frac{A_n^{1/p}}{|B_{R_n}|}, \quad n \in \mathbb{N}_0.
$$

Dividing (1.70) by $\frac{1}{2^{p(n+1)}}\left(\frac{\omega}{4}\right)^p |Q(R^p_{n+1}, R_{n+1})|$ yields

$$
\begin{aligned}
X_{n+1} \leq{}& 2^{pn}\Bigg(2C\left\{\frac{3}{2}p2^{p-2} + p^2 + 2^{p\beta_2}\left[\frac{p'\gamma_2^p}{p(\gamma_1^{p-1}-1)}\right]^{p-1}\right\} X_n^{1+p/(N+p)} \\
&+ 2^{3-2/p+p}C\left[\left(\frac{p}{2}\right)^{-p'/p} + p\right]\frac{M^{p'}}{p'}\left(\frac{\omega}{2}\right)^{p-2} \\
&\times \psi\left(\omega/4\right)^{1-p-1/p} R^{N\kappa}\|\nabla v\|^q_{L^{p'p}(Q_T)} X_n^{p/(N+p)} Z_n^{p-1}\Bigg) \\
\leq{}& \gamma 2^{pn}\left(X_n^{1+\alpha} + X_n^\alpha Z_n^{1+\kappa}\right), \qquad n \in \mathbb{N}_0,
\end{aligned}
$$

with $\alpha = p/(N+p) > 0$, $\kappa = p-2 > 0$ and

$$
\begin{aligned}
\gamma := 2C\max\Bigg\{&\frac{3}{2}p2^{p-2} + p^2 + 2^{p\beta_2}\left[\frac{p'\gamma_2^p}{p(\gamma_1^{p-1}-1)}\right]^{p-1}, \\
&2^{3-2/p+p}\left[\left(\frac{p}{2}\right)^{-p'/p} + p\right]\frac{M^{p'}}{p'}\left(\frac{\omega}{2}\right)^{p-2}\left[\psi\left(\omega/4\right)\right]^{1-p-1/p} R^{N\kappa}\Bigg\} > 0.
\end{aligned}
$$

(In the choice of κ we need the assumption that p is *strictly* larger than 2.) In the spirit of Remark 1.5.1, let us assume that

$$
\left(\frac{\omega}{2}\right)^{p-2}\left[\psi\left(\omega/4\right)\right]^{1-p-1/p} R^{N\kappa} \leq 1.
$$

Therefore, with this assumption we conclude that γ is independent of ω and R.

Reasoning analogously, we obtain

$$
Z_{n+1} \leq \gamma 2^{pn}\left(X_n + Z_n^{1+\kappa}\right).
$$

Now, let $\sigma = \min\{\alpha, \kappa\}$ and notice that, if we set $\nu_0 := 2\gamma^{-(1+\kappa)/\sigma}(2^p)^{-(1+\kappa)/\sigma^2}$, it follows from (1.61) that

$$
X_0 + Z_0^{1+\kappa} \leq 2\gamma^{-(1+\kappa)/\sigma}(2^p)^{-(1+\kappa)/\sigma^2}.
$$

Then, using Lemma 1.19, we are able to conclude that $X_n, Z_n \to 0$ as $n \to \infty$. Finally, notice that $R_n \to R/2$ and $k_n \to 1-\omega/4$, and this implies that

$$\begin{aligned}\big|\big\{(x,t) \in Q\big((R/2)^p, R/2\big) \ : \ \bar{u}_\omega(x,\bar{t}) \geq 1-\omega/4\big\}\big| \\ = \big|\big\{(x,t) \in Q^{t^*}_{R/2} \ : \ u(x,t) > 1-\omega/4\big\}\big| = 0.\end{aligned}$$

This completes the proof.

Now we show that the conclusion of Lemma 1.21 is valid in a full cylinder of the type $Q(\tau,\rho)$. To this end, we exploit that at the time level $-\hat{t} := t^* - d(R/2)^p$, the function $x \mapsto u(x,t)$ is strictly below $1-\omega/4$ in the ball $B_{R/2}$. We will use this time level as an initial condition to make the conclusion of the lemma hold up to $t=0$, eventually shrinking the ball. This requires the use of logarithmic estimates.

Given constants a, b, c with $0 < c < a$, we define the nonnegative function

$$\begin{aligned}\varrho^{\pm}_{a,b,c}(s) &:= \left(\ln \frac{a}{a+c-(s-b)|_{\pm}}\right)^+ \\ &= \begin{cases} \ln \dfrac{a}{a+c\pm(b-s)} & \text{if } b\pm c \lesseqgtr s \lesseqgtr b \pm (a+c), \\ 0 & \text{if } s \lesseqgtr b \pm c, \end{cases}\end{aligned} \tag{1.71}$$

whose first derivative is given by

$$\big(\varrho^{\pm}_{a,b,c}\big)'(s) = \begin{cases} \dfrac{1}{(b-s)\pm(a+c)} & \text{if } b\pm c \lesseqgtr s \lesseqgtr b\pm(a+c) \\ 0 & \text{if } s \lesseqgtr b \pm c \end{cases} \quad \gtreqless 0,$$

and its second derivative, away from $s = b \pm c$, is

$$\big(\varrho^{\pm}_{a,b,c}\big)'' = \big\{\big(\varrho^{\pm}_{a,b,c}\big)'\big\}^2 \geq 0.$$

Given u bounded in $(x_0,t_0)+Q(\tau,\rho)$ and a number k, define

$$H^{\pm}_{u,k} := \operatorname*{ess\,sup}_{(x_0,t_0)+Q(\tau,\rho)} \big|(u-k)^{\pm}\big|,$$

and the function

$$\Psi^{\pm}\big(H^{\pm}_{u,k}, (u-k)^{\pm}, c\big) := \varrho^{\pm}_{H^{\pm}_{u,k},k,c}(u), \qquad 0 < c < H^{\pm}_{u,k}.$$

Lemma 1.22 *For every number $\nu_1 \in (0,1)$, there exists $s_1 \in \mathbb{N}$, independent of ω and R, such that*

$$\big|\big\{x \in B_{R/4} \ : \ u(x,t) \geq 1-\omega/2^{s_1}\big\}\big| \leq \nu_1 |B_{R/2}| \quad \text{for all } t \in (-\hat{t}, 0).$$

Proof. Let $k = 1-\omega/4$ and

$$c = \omega/2^{2+n}, \tag{1.72}$$

with $n \in \mathbb{N}$ to be chosen. Let $0 < \zeta(x) \leq 1$ be a piecewise smooth cutoff function defined on $B_{R/2}$ such that $\zeta = 1$ in $B_{R/4}$ and $|\nabla\zeta| \leq C/R$. Now consider the weak formulation (1.58) with $\varphi = 2\varrho^+(u_h)(\varrho^+)'(u_h)\zeta^p$ for $K = B_{R/2}$, where ϱ^+ is the function defined in (1.71). After an integration in time over $(-\hat{t}, t)$, with $t \in (-\hat{t}, 0)$, we obtain $G_1 + G_2 - G_3 = 0$, where we define

$$G_1 := 2\int_{-\hat{t}}^{t}\int_{B_{R/2}} \partial_s\{u_h\}\varrho^+(u_h)(\varrho^+)'(u_h)\zeta^p \, dx\, ds,$$

$$G_2 := 2\int_{-\hat{t}}^{t}\int_{B_{R/2}} \big(|\nabla A(u)|^{p-2}a(u)\nabla u\big)_h \cdot \nabla\big\{\varrho^+(u_h)(\varrho^+)'(u_h)\zeta^p\big\}\,dx\,ds,$$
$$G_3 := 2\int_{-\hat{t}}^{t}\int_{B_{R/2}} \big(\chi u f(u)\nabla v\big)_h \cdot \nabla\big\{\varrho^+(u_h)(\varrho^+)'(u_h)\zeta^p\big\}\,dx\,ds.$$

Using the properties of ζ, we arrive at

$$\begin{aligned} G_1 &= \int_{-\hat{t}}^{t}\int_{B_{R/2}} \partial_s\left\{\varrho^+(u_h)\right\}^2\zeta^p\,dx\,ds \\ &= \int_{B_{R/2}\times\{t\}} \left\{\varrho^+(u_h)\right\}^2\zeta^p\,dx - \int_{B_{R/2}\times\{-\hat{t}\}} \left\{\varrho^+(u_h)\right\}^2\zeta^p\,dx. \end{aligned}$$

Due to Lemma 1.21, at time $-\hat{t}$ the function $x \mapsto u(x,t)$ is strictly below $1-\omega/4$ in the ball $B_{R/2}$, and therefore $\varrho^+(u(x,-\hat{t})) = 0$ for $x \in B_{R/2}$. Consequently,

$$\begin{aligned} G_1 &\to \int_{B_{R/2}\times\{t\}} \left\{\varrho^+(u)\right\}^2\zeta^p\,dx - \int_{B_{R/2}\times\{-\hat{t}\}} \left\{\varrho^+(u)\right\}^2\zeta^p\,dx \\ &= \int_{B_{R/2}\times\{t\}} \left\{\varrho^+(u)\right\}^2\zeta^p\,dx \quad \text{as } h\to 0. \end{aligned} \tag{1.73}$$

The definition of $H^{\pm}_{u,k}$ implies that

$$u-k \le H^+_{u,k} = \operatorname*{ess\,sup}_{Q(\hat{t},R/2)}\left|\left(u-1+\frac{\omega}{4}\right)^+\right| \le \frac{\omega}{4}. \tag{1.74}$$

If $H^+_{u,k}=0$, the result is trivial; so we assume $H^+_{u,k}>0$ and (1.72), n will be chosen large enough so that

$$0 < \frac{\omega}{2^{2+n}} < H^+_{u,k}.$$

Therefore, since $H^+_{u,k}+k-u+c>0$, the function $\varrho^+(u)$ is defined in the whole cylinder $Q(\hat{t},R/2)$ by

$$\varrho^{\pm}_{H^+_{u,k},k,c}(u) = \begin{cases} \ln\dfrac{H^+_{u,k}}{H^+_{u,k}+c+k-u} & \text{if } u>k+c, \\ 0 & \text{otherwise.} \end{cases}$$

Relation (1.74) implies that

$$\frac{H^+_{u,k}}{H^+_{u,k}+c+k-u} \le \frac{\frac{\omega}{4}}{2c-\frac{\omega}{4}} = 2^n, \quad \text{and therefore } \varrho^+(u)\le n\ln 2; \tag{1.75}$$

in the nontrivial case $u>k+c$, we also have an estimate for the derivative of the logarithmic function:

$$\left|(\varrho^+)'(u)\right|^{2-p} = \left|\frac{-1}{H^+_{u,k}+c+k-u}\right|^{2-p} \le \left|\frac{1}{c}\right|^{2-p} = \left(\frac{\omega}{2^{2+n}}\right)^{p-2}. \tag{1.76}$$

With these estimates at hand, we have for the diffusive term:

$$\begin{aligned} G_2 \to G_2^* &:= 2\int_{-\hat{t}}^{t}\int_{B_{R/2}} a(u)^{p-1}|\nabla u|^{p-2}\nabla u\cdot\nabla\big\{\varrho^+(u)(\varrho^+)'(u)\zeta^p\big\}\,dx\,ds \\ &= \int_{-\hat{t}}^{t}\int_{B_{R/2}} a(u)^{p-1}|\nabla u|^p\big\{2\big(1+\varrho^+(u)\big)\left[(\varrho^+)'(u)\right]^2\zeta^p\big\}\,dx\,ds + \tilde{G}_2^* \end{aligned}$$

as $h \to 0$, where we define

$$\tilde{G}_2^* := 2p \int_{-\hat{t}}^{t} \int_{B_{R/2}} a(u)^{p-1} |\nabla u|^{p-2} \nabla u \cdot \nabla \zeta \left\{ \varrho^+(u) (\varrho^+)'(u) \zeta^{p-1} \right\} dx\, dt.$$

Applying Young's inequality with the choices

$$r = p,\ a = |\nabla u|^{p-1} \zeta^{p-1} \left|(\varrho^+)'(u)\right|^{2/p'},\ b = \left|(\varrho^+)'(u)\right|^{1-2/p'} |\nabla \zeta| \text{ and } \epsilon_4 = 1,$$

we obtain

$$\begin{aligned}
\left|\tilde{G}_2^*\right| &\le 2p \int_{-\hat{t}}^{t} \int_{B_{R/2}} a(u)^{p-1} |\nabla u|^{p-1} |\nabla \zeta| \varrho^+(u) \left|(\varrho^+)'(u)\right| \zeta^{p-1}\, dx\, ds \\
&= 2p \int_{-\hat{t}}^{t} \int_{B_{R/2}} a(u)^{p-1} \varrho^+(u) |\nabla u|^{p-1} \zeta^{p-1} \\
&\qquad \times \left|(\varrho^+)'(u)\right|^{2/p'} \left|(\varrho^+)'(u)\right|^{1-2/p'} |\nabla \zeta|\, dx\, ds \\
&\le 2\epsilon_4^p \int_{-\hat{t}}^{t} \int_{B_{R/2}} a(u)^{p-1} \varrho^+(u) |\nabla u|^p \left[(\varrho^+)'(u)\right]^2 \zeta^p\, dx\, ds \\
&\quad + \frac{2p}{p' \epsilon_4^q} \int_{-\hat{t}}^{t} \int_{B_{R/2}} a(u)^{p-1} \varrho^+(u) |\nabla \zeta|^p \left|(\varrho^+)'(u)\right|^{2-p}\, dx\, ds \\
&= 2 \int_{-\hat{t}}^{t} \int_{B_{R/2}} a(u)^{p-1} \varrho^+(u) |\nabla u|^p \left[(\varrho^+)'(u)\right]^2 \zeta^p\, dx\, ds \\
&\quad + 2(p-1) \int_{-\hat{t}}^{t} \int_{B_{R/2}} a(u)^{p-1} \varrho^+(u) |\nabla \zeta|^p \left|(\varrho^+)'(u)\right|^{2-p}\, dx\, ds.
\end{aligned}$$

In light of this estimate, we obtain

$$\begin{aligned}
G_2^* &= 2 \int_{-\hat{t}}^{t} \int_{B_{R/2}} a(u)^{p-1} |\nabla u|^p \left[(\varrho^+)'(u)\right]^2 \zeta^p\, dx\, ds \\
&\quad - 2(p-1) \int_{-\hat{t}}^{t} \int_{B_{R/2}} a(u)^{p-1} \varrho^+(u) |\nabla \zeta|^p \left|(\varrho^+)'(u)\right|^{2-p}\, dx\, ds \\
&\ge 2 \left[\gamma_1 \psi(\omega/4)\right]^{p-1} \int_{-\hat{t}}^{t} \int_{B_{R/2}} |\nabla u|^p \left[(\varrho^+)'(u)\right]^2 \zeta^p\, dx\, ds \\
&\quad - 2(p-1) \int_{-\hat{t}}^{t} \int_{B_{R/2}} a(u)^{p-1} \varrho^+(u) |\nabla \zeta|^p \left|(\varrho^+)'(u)\right|^{2-p}\, dx\, ds \\
&\ge 2 \left[\gamma_1 \psi(\omega/4)\right]^{p-1} \int_{-\hat{t}}^{t} \int_{B_{R/2}} |\nabla u|^p \left[(\varrho^+)'(u)\right]^2 \zeta^p\, dx\, ds \\
&\quad - 2(p-1) n \ln 2 \left(\frac{C}{R}\right)^p \left(\frac{\omega}{2^{2+n}}\right)^{p-2} \int_{-\hat{t}}^{t} \int_{B_{R/2}} a(u)^{p-1} \chi_{\{u > 1-\omega/4\}}\, dx\, ds
\end{aligned}$$

and finally,

$$\begin{aligned}
G_2^* &\ge 2 \left[\gamma_1 \psi(\omega/4)\right]^{p-1} \int_{-\hat{t}}^{t} \int_{B_{R/2}} |\nabla u|^p \left[(\varrho^+)'(u)\right]^2 \zeta^p\, dx\, ds \\
&\quad - 2(p-1) n \ln 2 \left(\frac{C}{R}\right)^p \left(\frac{\omega}{2^{2+n}}\right)^{p-2} \hat{t} |B_{R/2}| \left[\gamma_2 \psi(\omega/4)\right]^{p-1},
\end{aligned} \tag{1.77}$$

where we have used the estimates (1.75), (1.76), the properties of ζ, and the fact that

$$\gamma_1\psi(\omega/4) \le a(u) \le \gamma_2\psi(\omega/4) \quad \text{on the set } \{u > 1-\omega/4\}.$$

Moreover, from the definition of $\hat{t}$ and our choice for t^* (recall that $t^* \ge dR^p - a_0R^p$), there holds

$$\hat{t} \le a_0R^p = \left(\frac{\omega}{2}\right)^{2-p} \frac{R^p}{\phi(\omega/2^m)^{p-1}}, \tag{1.78}$$

and taking into account (1.78), we obtain from (1.77) that

$$\begin{aligned} G_2^* \ge{}& 2\left[\gamma_1\psi(\omega/4)\right]^{p-1} \int_{-\hat{t}}^t \int_{B_{R/2}} |\nabla u|^p \left[(\varrho^+)'(u)\right]^2 \zeta^p \, dx\, ds \\ &- 2(p-1)n\ln 2 C^p 2^{(1+n)(2-p)} |B_{R/2}| \left[\gamma_2 \frac{\psi(\omega/4)}{\phi(\omega/2^m)}\right]^{p-1}. \end{aligned} \tag{1.79}$$

On the other hand, for the lower order term, by passing to the limit $h \to 0$ we have

$$\begin{aligned} G_3 \to G_3^* :={}& 2\int_{-\hat{t}}^t \int_{B_{R/2}} \chi u f(u) \nabla v \cdot \nabla u \left\{ \left(1+\varrho^+(u)\right) \left[(\varrho^+)'(u)\right]^2 \zeta^p \right\} dx\, ds \\ &+ 2p \int_{-\hat{t}}^t \int_{B_{R/2}} \chi u f(u) \nabla v \cdot \nabla \zeta \left\{ \varrho^+(u)(\varrho^+)'(u)\zeta^{p-1} \right\} dx\, ds \\ \le{}& 2M \int_{-\hat{t}}^t \int_{B_{R/2}} \left(1+\varrho^+(u)\right) \left[(\varrho^+)'(u)\right]^2 \zeta^p |\nabla u||\nabla v| \, dx\, ds \\ &+ 2pM \int_{-\hat{t}}^t \int_{B_{R/2}} \varrho^+(u) \left|(\varrho^+)'(u)\right|^{1-2/p'} \\ &\quad \times |\nabla v||\nabla\zeta| \left|(\varrho^+)'(u)\right|^{2/p'} \zeta^{p-1} \, dx\, ds. \end{aligned}$$

Applying Young's inequality to the first term of the last right-hand side with

$$r = p, \quad a = |\nabla u|, \quad b = |\nabla v| \quad \text{and} \quad \epsilon = \left(\frac{p\psi(\omega/4)^{p-1}}{M(1+n\ln 2)}\right)^{1/p},$$

and to the second term with

$$r = p, \quad a = \left|(\varrho^+)'(u)\right|^{1-2/p'}, \quad b = |\nabla v| \left|(\varrho^+)'(u)\right|^{2/p'} \zeta^{p-1} \quad \text{and} \quad \epsilon = 1,$$

we obtain

$$\begin{aligned} G_3^* \le{}& 2\psi(\omega/4)^{p-1} \int_{-\hat{t}}^t \int_{B_{R/2}} |\nabla u|^p \left[(\varrho^+)'(u)\right]^2 \zeta^p \, dx\, ds \\ &+ 2M \int_{-\hat{t}}^t \int_{B_{R/2}} \varrho^+(u) |\nabla\zeta| \left[(\varrho^+)'(u)\right]^{2-p} dx\, ds \\ &+ 2M \frac{p-1}{p} \left(\frac{p\psi(\omega/4)^{p-1}}{M(1+n\ln 2)}\right)^{1/(1-p)} \\ &\quad \times \int_{-\hat{t}}^t \int_{B_{R/2}} \left(1+\varrho^+(u)\right) \left[(\varrho^+)'(u)\right]^2 \zeta^p |\nabla v|^{p'} \, dx\, ds \\ &+ 2M(p-1) \int_{-\hat{t}}^t \int_{B_{R/2}} \varrho^+(u) |\nabla\zeta| |\nabla v|^{p'} \left[(\varrho^+)'(u)\right]^2 \zeta^p \, dx\, ds. \end{aligned}$$

Using the estimates (1.75) and (1.76) and the properties of ζ, we then get

$$
\begin{aligned}
G_3^* \le{}& 2\psi(\omega/4)^{p-1}\int_{-\hat t}^{t}\int_{B_{R/2}}|\nabla u|^p\big[(\varrho^+)'(u)\big]^2\zeta^p\,dx\,ds\\
&+2Mn\ln 2\frac{C}{R}\left(\frac{\omega}{2^{2+n}}\right)^{p-2}\hat t|B_{R/2}|\\
&+2M\frac{p-1}{p}\left(\frac{p\psi(\omega/4)^{p-1}}{M(1+n\ln 2)}\right)^{1/(1-p)}(1+n\ln 2)\left(\frac{\omega}{2^{2+n}}\right)^{-2}\\
&\quad\times\int_{-\hat t}^{t}\int_{B_{R/2}}|\nabla v|^{p'}\chi_{\{u>1-\omega/4\}}\,dx\,ds\\
&+2M(p-1)n\ln 2\frac{C}{R}\left(\frac{\omega}{2^{2+n}}\right)^{-2}\int_{-\hat t}^{t}\int_{B_{R/2}}|\nabla v|^{p'}\chi_{\{u>1-\omega/4\}}\,dx\,ds.
\end{aligned}
$$

Then, applying the Hölder inequality and recalling the definition of $\hat t$, we get

$$
\begin{aligned}
G_3^* \le{}& 2\psi(\omega/4)^{p-1}\int_{-\hat t}^{t}\int_{B_{R/2}}|\nabla u|^p\big[(\varrho^+)'(u)\big]^2\zeta^p\,dx\,ds\\
&+2MCn\ln 2\,2^{(1+n)(2-p)}\phi(\omega/2^m)^{1-p}|B_{R/2}|R^{p-1}\\
&+2M(p-1)\left\{\left(\frac{p\psi\,(\omega/4)^{p-1}}{M(1+n\ln 2)}\right)^{1/(1-p)}\frac{1+n\ln 2}{p}+\frac{C}{R}n\ln 2\right\}\left(\frac{\omega}{2^{2+n}}\right)^{-2}\\
&\quad\times\|\nabla v\|^{p'}_{L^{p'p}(Q_T)}\left(a_0R^p|B_{R/2}|\right)^{1-1/p}.
\end{aligned}
$$

In addition, thanks to Remark 1.5.1, we may obtain the estimates

$$
\begin{aligned}
&\left(\frac{\omega}{2^{2+n}}\right)^{-2}\left(\frac{p^{-p'}\psi\,(\omega/4)^{p-1}}{M(1+n\ln 2)}\right)^{1/(1-p)}a_0^{1-1/p}R^{p-1}\le 1,\\
&C\left(\frac{\omega}{2^{2+n}}\right)^{-2}a_0^{1-1/p}R^{p-2}\le 1,\quad \phi\left(\frac{\omega}{2^m}\right)^{1-p}R^{p-1}\le 1,
\end{aligned}
$$

and this finally gives

$$
\begin{aligned}
G_3^* \le{}& 2\psi\,(\omega/4)^{p-1}\int_{-\hat t}^{t}\int_{B_{R/2}}|\nabla u|^p\big[(\varrho^+)'(u)\big]^2\zeta^p\,dx\,ds\\
&+2MCn\ln 2\,2^{(1+n)(2-p)}|B_{R/2}|\\
&\quad+2M(p-1)Cn\ln 2\|\nabla v\|^{p'}_{L^{p'p}(Q_T)}|B_{R/2}|^{1-1/p}.
\end{aligned}
\tag{1.80}
$$

Combining the estimates (1.73), (1.79) and (1.80) yields

$$
\begin{aligned}
&\int_{B_{R/2}\times\{t\}}\big\{\varrho^+(u)\big\}^2\zeta^p\,dx\,ds\\
&\le 2M(p-1)Cn\ln 2\|\nabla v\|^{p'}_{L^{p'p}(Q_T)}|B_{R/2}|^{1-1/p}\\
&\quad+(1-\gamma_1^{p-1})2\left[\psi\,(\omega/4)\right]^{p-1}\int_{-\hat t}^{t}\int_{B_{R/2}}|\nabla u|^p\big[(\varrho^+)'(u)\big]^2\zeta^p\,dx\,ds\\
&\quad+2n\ln 2\,2^{(1+n)(2-p)}|B_{R/2}|\left\{MC+(p-1)C^p\gamma_2^{p-1}\left[\frac{\psi\,(\omega/4)}{\phi\,(\omega/2^m)}\right]^{p-1}\right\},
\end{aligned}
$$

and since $\gamma_1 > 1$ and $n > 0$, this implies

$$\begin{aligned}
&\sup_{-\hat{t}\le t\le 0}\int_{B_{R/2}\times\{t\}}\left\{\varrho^+(u)\right\}^2\zeta^p\,dx\\
&\le 2M(p-1)Cn\ln 2\|\nabla v\|^{p'}_{L^{p'p}(Q_T)}|B_{R/2}|^{1-\frac{1}{p}}\\
&\quad+2n\ln 2\,2^{2-p}|B_{R/2}|\left\{MC+(p-1)C^p\gamma_2^{p-1}\left[\frac{\psi\left(\omega/4\right)}{\phi\left(\omega/2^m\right)}\right]^{p-1}\right\}.
\end{aligned}\tag{1.81}$$

Since the integrand in the left-hand side of (1.81) is nonnegative, the integral can be estimated from below by integrating over the smaller set $S=\{x\in B_{R/2}\ :\ u(x,t)\ge 1-\omega/2^{2+n}\}\subset B_{R/2}$. Thus, noticing that

$$\zeta=1\quad\text{and}\quad\left\{\varrho^+(u)\right\}^2\ge\left(\ln(2^{n-1})\right)^2=(n-1)^2(\ln 2)^2\quad\text{on } S,$$

we obtain that (1.81) reads

$$\begin{aligned}
&\left|\left\{x\in B_{R/2}\ :\ u(x,t)\ge 1-\omega/2^{2+n}\right\}\right|\\
&\quad\le\frac{2Cn|B_{R/4}|}{(n-1)^2\ln 2}\left\{2^{2-p}\left[MC+(p-1)C^p\gamma_2^{p-1}\left[\frac{\psi\left(\omega/4\right)}{\phi\left(\omega/2^m\right)}\right]^{p-1}\right]\right.\\
&\qquad\left.+M(p-1)\|\nabla v\|^{p'}_{L^{p'p}(Q_T)}\right\}
\end{aligned}$$

for all $t\in(-\hat{t},0)$. To prove the lemma we just need to choose s_1 depending on ν_1 such that $s_1=2+n$ with

$$\begin{aligned}
n>1+\frac{2C}{\nu_1\ln 2}&\left\{2^{2-p}\left[MC+(p-1)C^p\gamma_2^{p-1}\left[\frac{\psi\left(\omega/4\right)}{\phi\left(\omega/2^m\right)}\right]^{p-1}\right]\right.\\
&\left.+M(p-1)\|\nabla v\|^{p'}_{L^{p'p}(Q_T)}\right\},
\end{aligned}$$

since if $n\ge 1+2/\alpha$ then $n/(n-1)^2\le\alpha$, $\alpha>0$. Furthermore, s_1 is independent of ω because

$$\left[\frac{\psi\left(\omega/4\right)}{\phi\left(\omega/2^m\right)}\right]^{p-1}=\left[\frac{(\omega/4)^{\beta_2/(p-1)}}{(\omega/2^m)^{\beta_1/(p-1)}}\right]^{(p-1)}=\omega^{\beta_2-\beta_1}2^{m\beta_1-2\beta_2}\le 2^{m\beta_1-2\beta_2}.$$

The last inequality holds since $\beta_2>\beta_1$. Now, the first alternative is established by the following proposition.

Proposition 1.23 *The numbers $\nu_1\in(0,1)$ and $s_1\gg 1$ can be chosen a priori independent of ω, R such that if (1.61) holds, then*

$$u(x,t)<\mu^+-\frac{\omega}{2^{s_1+1}}\quad\text{a.e. in } Q(\hat{t},R/8).$$

We omit the proof of Proposition 1.23 because it is based on the argument of [65, Lemma 3.3] and [149], using for the extension the same technique applied in the proof of Lemma 1.21.

Corollary 1.24 *There exist numbers $\nu_0,\sigma_0\in(0,1)$ independent of ω and R such that if (1.61) holds, then*

$$\operatorname*{ess\,osc}_{Q(\hat{t},R/8)} u\le\sigma_0\omega.$$

Proof. In light of Proposition 1.23, we know that there exists a number s_1 such that

$$\operatorname*{ess\,sup}_{Q(\hat{t},R/8)} u \leq \mu^+ - \frac{\omega}{2^{s_1+1}},$$

and this yields

$$\operatorname*{ess\,osc}_{Q(\hat{t},R/8)} u = \operatorname*{ess\,sup}_{Q(\hat{t},R/8)} u - \operatorname*{ess\,inf}_{Q(\hat{t},R/8)} u = \mu^+ - \frac{1}{2^{s_1+1}} - \mu^- \leq \left(1 - \frac{1}{2^{s_1+1}}\right)\omega.$$

In this way, choosing $\sigma_0 = 1 - 1/2^{s_1+1}$, which is independent of ω, we may complete the proof.

The second alternative.- Let us suppose now that (1.61) does not hold. Then the complementary case is valid and for every cylinder $Q_R^{t^*}$ we have

$$\left|\left\{(x,t) \in Q_R^{t^*} \ : \ u(x,t) < \omega/2\right\}\right| \leq (1-\nu_0)\left|Q_R^{t^*}\right|. \tag{1.82}$$

Following an analogous analysis to the performed in the case in which the solution is near its degeneracy at one, a similar conclusion is obtained for the second alternative. Specifically, we first use logarithmic estimates to extend the result to a full cylinder and then we conclude that the solution is essentially away from 0 in a cylinder $Q(\tau,\rho)$. In this way we prove the following corollary.

Corollary 1.25 *Let $\tilde{t}$ denote the second-alternative-counterpart of $\hat{t}$. Then there exists $\sigma_1 \in (0,1)$, depending only on the data, such that*

$$\operatorname*{ess\,osc}_{Q(\tilde{t},R/8)} u \leq \sigma_1 \omega.$$

Since (1.61) or (1.82) must be valid, the conclusion of Corollary 1.24 or 1.25 must hold. Thus, choosing $\sigma = \max\{\sigma_0, \sigma_1\}$ and $t^\diamond = \min\{\hat{t}, \tilde{t}\}$, we have proved the following proposition.

Proposition 1.26 *There exists a constant $\sigma \in (0,1)$, depending only on the data, such that*

$$\operatorname*{ess\,osc}_{Q(t^\diamond,R/8)} u \leq \sigma\omega.$$

To finalize the proof (see, e.g., [65], [150], or the proof of [67, Th. 2]), let us define a sequence of nested cylinders Q_n, such that the essential oscillation of the solution u in these cylinders tends to zero as $n \to \infty$, i.e., define the sequence ω_n converging to zero such that

$$\operatorname*{ess\,osc}_{Q_n} u \leq \omega_n.$$

We argue that this fact implies the local Hölder continuity of u in Q_T. Indeed, it is possible to determine a priori, in terms of the data only, $\gamma > 1$ and $\alpha \in (0,1)$ such that for all the cylinders $Q(a_0\rho^p, \rho)$ with $0 < \rho \leq R$, it holds

$$\operatorname*{ess\,osc}_{Q(a_0\rho^p,\rho)} u \leq \gamma \left(\frac{\rho}{R}\right)^\alpha. \tag{1.83}$$

Let $\widetilde{M} = \|u\|_{\infty,Q_T}$. Fix $(x_i,t_i) \in K$, $i = 1,2$ such that $t_2 > t_1$ and construct the cylinder $(x_2,t_2) + Q(\widetilde{M}^{2-p}R^p, R)$. This cylinder is contained in Q_T if we choose

$$R \leq \inf_{x\in K,\ y\in\partial_t Q_T} |x-y| \quad \text{ and } \widetilde{M}^{\frac{p-2}{p}} R \leq \inf_{t\in K} t^{\frac{1}{p}};$$

therefore, in particular, we may take $2R = p - \mathsf{dist}(K; \partial_t Q_T)$. To prove Hölder continuity in time, firstly assume that $t_2 - t_1 < \widetilde{M}^{2-p} R^p$. Then, there exists $\rho \in (0, R)$ such that $t_2 - t_1 = \widetilde{M}^{2-p} \rho^p$, i.e,

$$\rho = \widetilde{M}^{\frac{p-2}{p}} |t_2 - t_1|^{\frac{1}{p}}.$$

Inequality (1.83) applied in the cylinder $(x_2, t_2) + Q(a_0 \rho^p, \rho)$ implies

$$|u(x_2, t_2) - u(x_1, t_1)| \leq \gamma \widetilde{M} \left\{ \frac{\widetilde{M}^{\frac{p-2}{p}} |t_2 - t_1|^{\frac{1}{p}}}{p - \mathsf{dist}(K; \partial_t Q_T)} \right\}^{\alpha},$$

and alternatively, if $t_2 - t_1 \geq \widetilde{M}^{2-p} R^p$ then we have

$$|u(x_2, t_2) - u(x_1, t_1)| \leq 4 \widetilde{M} \left\{ \frac{\widetilde{M}^{\frac{p-2}{p}} |t_2 - t_1|^{\frac{1}{p}}}{p - \mathsf{dist}(K; \partial_t Q_T)} \right\}.$$

The Hölder continuity in space is proved in a similar fashion. Putting all previous results together, we finally end up with the proof of the local Hölder continuity of u in Q_T.

Chapter 2

Reference finite volume methods

It is the purpose of this Chapter to discuss in detail the construction of numerical methods for solving the problems presented in Chapter 1. Specifically we will construct appropriate finite volume methods, motivated by their most appealing feature which is that the resulting solution satisfies the conservation of quantities such as mass, momentum, energy, and species. This approach can itself lead to valuable insight into the phenomena and also into the mathematical structure of the problem. Furthermore, because the flux entering a given volume is identical to that leaving the adjacent volume, these methods are naturally conservative. It is well known that this feature implies that finite volume methods automatically satisfy, for instance, jump conditions and hence give physically correct weak solutions even when computing discontinuous solutions, such as those arising in strongly degenerate parabolic equations.

2.1 A class of strongly degenerate parabolic equations

Let $J \in \mathbb{N}$ denote the number of space steps, $\Delta x := (x_b - x_a)/J$, $x_{j+1/2} := x_a + (j+1/2)\Delta x$ for $j = 0, \ldots, J-1$, $I_j := [x_{j-1/2}, x_{j+1/2})$ and

$$u_j^0 := \frac{1}{\Delta x} \int_{I_j} u_0(x)\, dx, \quad j = 0, \ldots, J. \tag{2.1}$$

For Problem A, we assume that $u_0 \in BV(I)$, $0 \le u_0(x) \le u_{\max}$ for all $x \in \bar{I}$, and that there exists a constant $M > 0$ such that

$$\sum_{m=1}^{J-1} \left| A\big(u_{m+1}^0\big) - 2A\big(u_m^0\big) + A\big(u_{m-1}^0\big) \right| \le M\Delta x \quad \text{uniformly in } \Delta x; \tag{2.2}$$

note that this requests, in particular, that M be independent of J. As detailed in [27], (2.2) is imposed to ensure uniform L^1 Lipschitz continuity in time for the numerical solution when the discretization parameters tend to zero. The continuous version of (2.2) states that the total variation of $(A_\varepsilon(u_0))_x$ on the interval I must

be uniformly bounded with respect to ε, where $\varepsilon > 0$ is a regularization parameter of a smooth regularization $A_\varepsilon(\cdot)$ of $A(\cdot)$. In the continuous case, this condition was introduced in [29] to achieve a uniform estimate of the spatial variation of the time derivative of a viscous regularization of Problem A. Both (2.2) and the continuous n condition are satisfied, for example, if u_0 is constant. Problem A is discretized in space with classical finite volumes. The computational domain I is decomposed into cells $\{I_j\}_{j=1}^{2^L}$. The initial-boundary value problem (IBVP) is then integrated over each cell I_j, where the volume of each cell is denoted by $|I_j|$. Hence we get

$$\frac{du_j}{dt} = \bar{\mathcal{D}}_j\big(U(t)\big), \quad j = 1, \dots, 2^L,$$

where $U(t) = (u_i(t))_{i=1,\dots,2^L}$ contains the cell averages of the numerical solution at time t, such that

$$u_j(t) \approx \frac{1}{|I_j|} \int_{I_j} u(x,t)\, dx, \quad j = 1, \dots, 2^L,$$

and $\bar{\mathcal{D}}_j(U(t))$ is the numerical divergence of cell I_j at time t. In the one-dimensional case, I_j is an interval (the cell $[x_{j-1/2}, x_{j+1/2}]$) with step size $\Delta x_j := x_{j+1/2} - x_{j-1/2}$, and we may simply write

$$\bar{\mathcal{D}}_j(U(t)) \approx -\frac{1}{|I_j|}\Big(\big(b(u) - A(u)_x\big)\big|_{x_{j+1/2}} - \big(b(u) - A(u)_x\big)\big|_{x_{j-1/2}}\Big), \quad j = 1, \dots, 2^L.$$

If $\bar{F}_{j+1/2}$ and $\bar{F}_{j-1/2}$ are the numerical fluxes associated with the left and right cell boundaries, respectively, then we may write

$$\bar{\mathcal{D}}_j = -\frac{1}{\Delta x_j}\left(\bar{F}_{j+1/2} - \bar{F}_{j-1/2}\right), \quad j = 1, \dots, 2^L.$$

Available discretization methods differ by the definition of the numerical flux that approximates $\bar{F}_{j\pm 1/2}$.

In addition to the notation introduced previously, we let $N \in \mathbb{N}$ be the number of time steps, $\Delta t := T/N$, and $I^n := [t_n, t_{n+1})$, where $t_n = n\Delta t$ for $n = 0, \dots, N$. We denote by u_j^n the numerical solution at (x_j, t_n), assume that the values for $n = 0$ are given by (2.1), and approximate the entropy solution of Problem A by a three-point finite difference scheme, which is defined by an "interior" formula for $u_1^n, \dots, u_{J-1}^n$ and two "boundary" formulas for u_0^n and u_J^n, respectively. Defining $\nu := \Delta t/\Delta x^2$ and $\lambda := \Delta t/\Delta x$, we employ the following discretization, where $h_{j+1/2}^n := h(u_j^n, u_{j+1}^n)$ and $d_{j+1/2}^n := A(u_{j+1}^n) - A(u_j^n)$ for $j = 0, \dots, J-1$:

$$u_0^{n+1} = u_0^n - \lambda h_{1/2}^n + \nu d_{1/2}^n, \tag{2.3a}$$

$$u_j^{n+1} = u_j^n - \lambda\big(h_{j+1/2}^n - h_{j-1/2}^n\big) + \nu\big(d_{j+1/2}^n - d_{j-1/2}^n\big), \quad j = 1, \dots, J-1, \tag{2.3b}$$

$$u_J^{n+1} = u_J^n + \lambda h_{J-1/2}^n - \nu d_{J-1/2}^n, \tag{2.3c}$$

We use the Engquist-Osher flux function [73]

$$h(u,v) \ := b(0) + \int_0^u \max\big\{b'(s), 0\big\}\, ds + \int_0^v \min\big\{b'(s), 0\big\}\, ds. \tag{2.4}$$

In [28] it is shown that the scheme (2.3), (2.4), which is the first-order version of the basic scheme used herein, converges to the entropy solution of Problem A, provided that the following CFL condition is satisfied:

$$\mathsf{CFL} := \lambda\|b'\|_\infty + \nu\|a\|_\infty \le 1/2 \tag{2.5}$$

Convergence of a semi-implicit variant of (2.3), (2.4) is shown in [27] under the milder CFL condition $\lambda\|b'\|_\infty \le 1/2$. In both cases, the convergence proof relies on the monotonicity of the first-order scheme.

In order to upgrade the spatial discretization to second order, we use a MUSCL (variable extrapolation) scheme. We introduce a piecewise linear function $u^n(x)$ defined by

$$u^n(x) := u_j^n + s_j^n(x - x_j), \quad x \in (x_{j-1/2}, x_{j+1/2}),$$

where s_j^n denotes a suitable slope constructed from u^n. For smooth solutions, in regions where s_j^n is an $\mathcal{O}(\Delta x)$ approximation of $u_x(x_j, t_n)$, the reconstruction is linear and the truncation error is $\mathcal{O}(\Delta x^2)$. In regions where $s_j^n = 0$, the reconstruction is piecewise constant and the truncation error is $\mathcal{O}(\Delta x)$. For Cauchy problems, the slopes are limited to enforce the Total Variation Diminishing (TVD) property of the scheme. In our case, we use the $\theta-$*limiter* [82]

$$s_j^n = \hat{M}\left(\theta\frac{u_j^n - u_{j-1}^n}{\Delta x}, \frac{u_{j+1}^n - u_{j-1}^n}{2\Delta x}, \theta\frac{u_{j+1}^n - u_j^n}{\Delta x}\right), \quad \theta \in [0, 2], \tag{2.6}$$

where we choose $\theta = 0.5$ as in [31], and $\hat{M}$ is the minmod function

$$\hat{M}(a, b, c) := \begin{cases} \min\{a, b, c\} & \text{if } a, b, c > 0, \\ \max\{a, b, c\} & \text{if } a, b, c < 0, \\ 0 & \text{otherwise.} \end{cases}$$

Then we extrapolate the data to the boundaries of each cell and form the corresponding second order scheme. (An alternative "order upgrading" method would be to use a second-order essentially non-oscillatory (ENO) reconstruction [138], as done in [134].) For Problem A (with zero-flux boundary conditions), (2.6) is used for $j = 2, \ldots, J-2$, and we set

$$s_0^n = s_1^n = s_{J-1}^n = s_J^n = 0. \tag{2.7}$$

Experience in previous work [31] shows that the boundary formulas properly approximate the zero-flux boundary conditions (1.3) only if the first-order version (2.3a) and (2.3c) is utilized, that is, if condition (2.7) is imposed. Early numerical experiments showed that dropping this condition and calculating boundary slopes according to (2.6) produces oscillatory solutions.

For Problem B, the basic scheme is defined by formula (2.3b) for $j = 0, \ldots, J$, provided that the space index is taken modulo J. In the same sense, (2.6) is used for all j.

The analysis of numerical schemes for (1.1) exhibits several difficulties; most notably, due to the involved nonlinear structure of (1.1), it is usually difficult to construct an exact solution, the convergence rate is not known, and numerical experimentation is necessary to identify the best suited parameters for a numerical scheme, for example the threshold parameters in a multiresolution scheme [38].

A case with discontinuous flux.- The numerical scheme for the solution of (1.9) is essentially described in [36]. As in the previous case, we begin the definition of the base algorithm discretizing $\mathbb{R}$ into cells $I_j := [x_{j-1/2}, x_{j+1/2})$, where $x_{j+1/2} = (j + 1/2)\Delta x$ with $j \in \mathbb{Z}$. Let $\lambda = \Delta t/\Delta x$, $\mu = \Delta t/(\Delta x)^2$ and $U_j^0 = u_0(x_j)$. For $n > 0$ we define the approximations according to

$$U_j^{n+1} = U_j^n - \lambda\Delta_- h(\boldsymbol{\gamma}_{j+1/2}, U_{j+1}^n, U_j^n) + \mu\Delta_-\left(\gamma_{1,j+1/2}\Delta_+ A(U_j^n)\right),$$

where

$$\boldsymbol{\gamma}_{j+1/2} := \boldsymbol{\gamma}\big(x_{j+1/2}^-\big), \quad \gamma_{1,j+1/2} := \gamma_1\big(x_{j+1/2}^-\big). \tag{2.8}$$

The symbols $\Delta_\pm$ are spatial difference operators: $\Delta_- V_j := V_j - V_{j-1}$ and $\Delta_+ V_j := V_{j+1} - V_j$, and we use the Engquist-Osher flux [73] for the discontinuous case

$$h(\boldsymbol{\gamma}, v, u) := \frac{1}{2}\left[f(\boldsymbol{\gamma}, u) + f(\boldsymbol{\gamma}, v) - \int_u^v |f_u(\boldsymbol{\gamma}, w)|\, dw\right]. \tag{2.9}$$

Note that our pointwise discretization of $\boldsymbol{\gamma}$, (2.8), follows the usage of [32, 36, 101, 99], but differs from that of [35], where $\boldsymbol{\gamma}$ is discretized by cell averages taken over the cells $[x_j, x_{j+1})$, where $x_j := j\Delta x$, $j \in \mathbb{Z}$. The important point is that in both cases, the discretization of $\boldsymbol{\gamma}$ is *staggered* with respect to that of the conserved quantity u, and this property greatly facilitates the convergence analysis of the numerical schemes. If the discretizations were aligned (i.e., not staggered), we would have to deal with more complicated 2×2 Riemann problems at cell boundaries. Further discussion of this point is provided e.g. in [99]. Our particular choice of (2.8) (as opposed to forming cell averages) is basically its simplicity.

The space-time parameters are chosen in such way that we have the following CFL condition (see [36]):

$$\lambda \max_{u\in[0,1],x\in\mathbb{R}} |f_u(\boldsymbol{\gamma}(x), u)| + \mu \max_{u\in[0,1]} |A'(u)| \leqslant \frac{1}{2}. \tag{2.10}$$

which means that $\Delta t/(\Delta x)^2$ must be bounded. On the other hand, when the diffusion term is not considered (as in the first Example of Section 5.2.2), the CFL condition is less restrictive than (2.13), that is

$$\lambda \max_{u\in[0,1],x\in\mathbb{R}} |f_u(\boldsymbol{\gamma}(x), u)| \leqslant \frac{1}{2}. \tag{2.11}$$

which means that only $\Delta t/\Delta x$ must be bounded.

Let us mention that the scheme also admits a semi-implicit variant, in which the diffusion terms are evaluated at the time level t_{n+1}. This variant has been used for numerical examples in [36], and its convergence for a similar equation with a convective flux that does not depend on x, but which is supplemented by boundary conditions, has been proved in [27]. The advantage of a semi-implicit scheme is that it is stable under the CFL condition (2.11), which is milder than (2.10), so that much larger time step Δt could be used. However, a semi-implicit version involves the solution of systems of nonlinear equations for each time step, and these equations have to be solved iteratively by appropriate linearization.

We stress that equation (1.1) admits a rigorous convergence analysis for suitable numerical schemes. Evje and Karlsen [75] show that explicit monotone finite difference schemes [61] converge to BV entropy solutions for the Cauchy problem for (1.1). These results are extended to several space dimensions in [97]. The convergence of finite volume schemes for initial-boundary value problems is proved in [113, 27]. The monotone scheme used for numerical experiments in [35, 36] is the robust Engquist-Osher scheme [73].

A nonconservative case.- The numerical scheme for the solution of (1.19) is described in detail in [30]. The base finite volume method is defined by discretizing $I\!R$ into cells $I_j := [x_{j-1/2}, x_{j+1/2})$, where $x_{j+1/2} = (j + 1/2)\Delta x$ with $j \in \mathbb{Z}$. Let $\lambda = \Delta t/\Delta x$ and $U_j^0 = u_0(x_j)$. Therefore, for $n > 0$ the corresponding scheme is given by

$$U_j^{n+1} = U_j^n - \lambda\Delta_- h(\boldsymbol{\gamma}_{j+1/2}, U_{j+1}^n, U_j^n) + \lambda\gamma_j^3\Delta_+ U_j^n., \tag{2.12}$$

where $\boldsymbol{\gamma}_{j+1/2} = \gamma(x_{j+1/2}-)$, $\gamma_{1,j+1/2} = \gamma_1(x_{j+1/2}-)$ and $\gamma_j^3 = \gamma^3(x_j-)$. The difference operators $\Delta_\pm$ are $\Delta_- V_j = V_j - V_{j-1}$, $\Delta_+ V_j = V_{j+1} - V_j$, and $h(\boldsymbol{\gamma}, v, u)$ is the Engquist-Osher numerical flux for the discontinuous case, obtained as in (2.9). The time-space parameters are chosen in such a way that the following CFL condition holds ([30]):

$$\lambda \max_{u\in[0,1],x\in I\!R} |f_u(\boldsymbol{\gamma}(x), u)| + \lambda \max_{x\in I\!R} \lambda^3(x) \leqslant \frac{1}{2}. \tag{2.13}$$

2.2 A class of degenerate reaction-diffusion systems

We employ a standard finite volume scheme to discretize a reaction-diffusion equation, which is described here for a Cartesian mesh. The rectangular spatial domain $\Omega \subset \mathbb{R}^2$ is partitioned into control volumes $(\Omega_{ij})_{(i,j)\in\Lambda}$, where Λ is an index set, defining
$\Omega_{ij} := [x_{i-1/2}, x_{i+1/2}] \times [y_{j-1/2}, y_{j+1/2}]$, $\Delta x := x_{i+1/2} - x_{i-1/2}$, $\Delta y := y_{j+1/2} - y_{j-1/2}$, for all $(i,j) \in \Lambda$, and $\widetilde{\Delta x} := \min\{\Delta x, \Delta y\}$. The cell average of a quantity q at time t is defined by

$$\bar{q}_{ij}(t) = \frac{1}{|\Omega_{ij}|} \iint_{\Omega_{ij}} q(\mathbf{x}, t)\, d\mathbf{x}.$$

Discretization of the Turing model (1.23).- The finite volume scheme is described here for (1.20) and as it applies to the first equation of (1.23); for the second equation of (1.23), we replace u by v, $f(u,v)$ by $g(u,v)$, and $A(u)$ by $dB(v)$. Integrating the respective equation and averaging over Ω_{ij} yields

$$\frac{1}{|\Omega_{ij}|} \iint_{\Omega_{ij}} u_t(\mathbf{x}, t)\, d\mathbf{x} = \frac{1}{|\Omega_{ij}|} \iint_{\Omega_{ij}} \mathcal{D}\Big(u(\mathbf{x}, t), \nabla A\big(u(\mathbf{x}, t)\big)\Big)\, d\mathbf{x} \; + \frac{1}{|\Omega_{ij}|} \iint_{\Omega_{ij}} f(u(\mathbf{x}, t))\, d\mathbf{x},$$

where $\mathcal{D}$ denotes the right-hand side of the PDE under consideration except for the reaction term. For the two-dimensional case and on a cartesian grid, $\mathcal{D}$ is discretized via

$$\bar{\mathcal{D}}_{ij} := -\frac{1}{\Delta x}\left(\bar{F}_{i+1/2,j} - \bar{F}_{i-1/2,j}\right) - \frac{1}{\Delta y}\big(\bar{F}_{i,j+1/2} - \bar{F}_{i,j-1/2}\big),$$
$$\bar{F}_{i+1/2,j} := -\frac{1}{\Delta x}\big(A(\bar{u}_{i+1,j}) - A(\bar{u}_{ij})\big), \quad \bar{F}_{i,j+1/2} := -\frac{1}{\Delta y}\big(A(\bar{u}_{i,j+1}) - A(\bar{u}_{ij})\big).$$

The reaction term is approximated by $\bar{f}_{ij} \approx f(\bar{u}_{ij}, \bar{v}_{ij})$. If we incorporate a first-order Euler time integration for both components, then the corresponding interior marching formula for Model 2 is

$$\bar{u}_{ij}^{n+1} = \bar{u}_{ij}^n + \Delta t \gamma \bar{f}_{ij} + \Delta t \bar{\mathcal{D}}_{ij}\big(\mathcal{S}(\bar{u}_{ij}^n), \widetilde{\Delta x}\big), \quad \bar{v}_{ij}^{n+1} = \bar{v}_{ij}^n + \Delta t \gamma \bar{g}_{ij} + d\Delta t \bar{\mathcal{D}}_{ij}\big(\mathcal{S}(\bar{v}_{ij}^n), \widetilde{\Delta x}\big), \tag{2.14}$$

where $\mathcal{S}(\cdot)$ denotes the stencil utilized for computing $\bar{\mathcal{D}}_{ij}$. According to [49, 92], this scheme is stable under the CFL condition

$$\lambda\gamma\big(\|f_u\|_\infty + \|f_v\|_\infty + \|g_u\|_\infty + \|g_v\|_\infty\big) + 4\mu d\big(\|A'\|_\infty + \|B'\|_\infty\big) \leqslant 1. \tag{2.15}$$

Here $\lambda := \Delta t/\widetilde{\Delta x}$, $\mu := \Delta t/\widetilde{\Delta x}^2$.

Discretization of the chemotaxis model (1.30).- We define the difference operators $\delta_x^\pm V_{ij} := \pm(V_{i\pm1,j} - V_{ij})$ and $\delta_y^\pm V_{ij} := \pm(V_{i,j\pm1} - V_{ij})$. Then a suitable second order difference operator for a general term $\nabla\cdot(Q\nabla u)$ is

$$\nabla\cdot(Q\nabla u) \approx \frac{1}{\Delta x^2}\delta_x^+\big(Q_{i+1/2,j}\delta_x^- u_{ij}\big) + \frac{1}{\Delta y^2}\delta_y^+\big(Q_{i,j+1/2}\delta_y^- u_{ij}\big).$$

Integrating the corresponding equations, averaging over Ω_{ij} and discretizing yields the following interior marching formula:

$$\begin{aligned}
\bar{u}_{ij}^{n+1} =& \bar{u}_{ij}^n + \frac{\sigma\Delta t}{\Delta x^2}\delta_x^+\delta_x^-\bar{u}_{ij}^n + \frac{\sigma\Delta t}{\Delta y^2}\delta_y^+\delta_y^-\bar{u}_{ij}^n + \frac{\Delta t}{\Delta x^2}\big(\delta_x^+\big(Q_{i-1/2,j}^n\delta_x^-\bar{v}_{ij}^n\big)\big) \\
&+ \frac{\Delta t}{\Delta y^2}\big(\delta_y^+\big(Q_{i,j-1/2}^n\delta_y^-\bar{v}_{ij}^n\big)\big) + g\big(\bar{u}_{ij}^n\big), \\
\bar{v}_{ij}^{n+1} =& \bar{v}_{ij}^n + \Delta t h\big(\bar{u}_{ij}^n, \bar{v}_{ij}^n\big) + \frac{d\Delta t}{\Delta x^2}\delta_x^+\delta_x^-\bar{v}_{ij}^n + \frac{d\Delta t}{\Delta y^2}\delta_y^+\delta_y^-\bar{v}_{ij}^n, \\
Q_{i,j+1/2}^n :=& \frac{1}{2}\big(\chi'\big(\bar{v}_{ij}^n\big)\bar{u}_{ij}^n + \chi'\big(\bar{v}_{i,j+1}^n\big)\bar{u}_{i,j+1}^n\big), \quad Q_{i+1/2,j}^n := \frac{1}{2}\big(\chi'\big(\bar{v}_{ij}^n\big)\bar{u}_{ij}^n + \chi'\big(\bar{v}_{i+1,j}^n\big)\bar{u}_{i+1,j}^n\big).
\end{aligned} \tag{2.16}$$

Analogously to (2.15), the scheme (2.16) is stable under the corresponding CFL condition

$$\lambda\big(\|h_u\|_\infty + \|h_v\|_\infty + \|g'\|_\infty\big) + 4\mu d\big(\sigma + \|\chi'\|_\infty\big) \leqslant 1. \tag{2.17}$$

The left-hand sides of (2.15) and (2.17) obviously evolve in time, so in practice, at each time step we obtain Δt from these conditions, and λ and μ are not constants; rather, they are adjusted in each time step.

2.3 The monodomain and bidomain equations

2.3.1 An explicit scheme on uniform meshes

To approximate solutions to the bidomain equations (1.37), we employ a standard FV scheme, which is described here for a uniform grid. The square spatial domain $\Omega \subset \mathbb{R}^2$ is partitioned into control volumes $(\Omega_{ij})_{1\le i,j\le N}$, defining $\Omega_{ij} := [x_{i-1/2}, x_{i+1/2}] \times [y_{j-1/2}, y_{j+1/2}]$, $h = x_{i+1/2} - x_{i-1/2} = y_{j+1/2} - y_{j-1/2}$, for all $1 \le i, j \le N$. We define cell averages of the unknowns $H(v, w)$ and $I_{\text{ion}}(v, w)$:

$$H_{ij}^{n+1} := \frac{1}{h^2\Delta t}\int_{t^n}^{t^{n+1}}\int_{\Omega_{ij}} H\big(v(x,t), w(x,t)\big)\,dx\,dt,$$
$$I_{\text{ion},(i,j)}^{n+1} := \frac{1}{h^2\Delta t}\int_{t^n}^{t^{n+1}}\int_{\Omega_{ij}} I_{\text{ion}}\big(v(x,t), w(x,t)\big)\,dx\,dt,$$

and of the given function I_{app}:

$$I_{\text{app},(i,j)}^{n+1} := \frac{1}{h^2\Delta t}\int_{t^n}^{t^{n+1}}\int_{\Omega_{ij}} I_{\text{app}}(x,t)\,dx\,dt.$$

Notice that if we denote by θ the angle of alignment of the fibers, then we may recast $\mathbf{M}_k(x)$ explicitly in the form (see e.g. [95])

$$\mathbf{M}_k = \begin{bmatrix} \sigma_k^{\text{t}} + (\sigma_k^{\text{l}} - \sigma_k^{\text{t}})\sin^2(\theta) & (\sigma_k^{\text{l}} - \sigma_k^{\text{t}})\sin(\theta)\cos(\theta) \\ (\sigma_k^{\text{l}} - \sigma_k^{\text{t}})\sin(\theta)\cos(\theta) & \sigma_k^{\text{t}} + (\sigma_k^{\text{l}} - \sigma_k^{\text{t}})\cos^2(\theta) \end{bmatrix} \quad \text{for } k \in \{\text{e}, \text{i}\}.$$

Therefore, defining the difference operators $\delta_x^s V_{ij} := V_{i+s,j} - V_{ij}$ and $\delta_y^s V_{ij} := V_{i,j+s} - V_{ij}$, the corresponding diffusive term may be approximated by

$$\begin{aligned}\nabla\cdot(\mathbf{M}_k\nabla u)_{i,j} &\approx \mathcal{D}_h(\mathbf{M}_k, u_{ij}) \\ &:= \frac{1}{h^2}\sum_{s\in\{-1,1\}} M_k^{11}\delta_x^s u_{ij} + M_k^{12}u_{i+s,j+s} + M_k^{21}u_{i+s,j-s} + M_k^{22}\delta_y^s u_{ij},\end{aligned}$$

for all $1 \le i, j \le N$ and $k \in \{\text{e}, \text{i}\}$. We now describe the finite volume scheme employed to advance the numerical solution from t^n to t^{n+1}, which is based on a simple explicit Euler time discretization. The computation starts from the initial cell averages

$$v_{ij}^0 = \frac{1}{h^2}\int_{\Omega_{ij}} v_0(x)\,dx, \quad w_{ij}^0 = \frac{1}{h^2}\int_{\Omega_{ij}} w_0(x)\,dx. \tag{2.18}$$

Now, we first integrate the corresponding equations, average over Ω_{ij} and discretize. Then, assuming that at $t = t^n$ the quantities $u_{k,(i,j)}^n$, $k \in \{\text{e}, \text{i}\}$, $v_{ij}^n = (u_{\text{i},(i,j)}^n - u_{\text{e},(i,j)}^n)$, and w_{ij}^n are known for all Ω_{ij}, we compute

the values of these cell averages $u^{n+1}_{k,(i,j)}$, $k \in \{\mathrm{e},\mathrm{i}\}$, $v^{n+1}_{ij} = (u^{n+1}_{\mathrm{i},(i,j)} - u^{n+1}_{\mathrm{e},(i,j)})$ and w^{n+1}_{ij} at $t = t^{n+1}$ from

$$\beta c_{\mathrm{m}} h \frac{v^{n+1}_{ij} - v^n_{ij}}{\Delta t} + \mathcal{D}_h\big(\mathbf{M}_{\mathrm{e}}, u^n_{\mathrm{e},(i,j)}\big) + \beta h^2 I^n_{\mathrm{ion},(i,j)} = h^2 I^{n+1}_{\mathrm{app},(i,j)}, \tag{2.19}$$

$$\mathcal{D}_h\big((\mathbf{M}_{\mathrm{e}} + \mathbf{M}_{\mathrm{i}}), u^{n+1}_{\mathrm{e},(i,j)}\big) + \mathcal{D}_h\big(\mathbf{M}_{\mathrm{i}}, v^{n+1}_{ij}\big) = h^2 I^{n+1}_{\mathrm{app},(i,j)}, \tag{2.20}$$

$$h^2 \frac{w^{n+1}_{ij} - w^n_{ij}}{\Delta t} - h^2 H^n_{ij} = 0. \tag{2.21}$$

The order in which these equations are used to advance the solution is explicitly stated in Algorithm 2.3.1:

Algorithm 2.3.1 *General method*

1. *Assume that u^n_{i}, u^n_{e}, v^n and w^n are known (at time t^n).*
2. *Solve the ODE*
$$\partial_t w - H(v,w) = 0, \quad x \in \Omega,$$
approximately for $t^n < t \le t^{n+1}$ with initial condition w^n and data v^n, i.e., compute w^{n+1} using (2.21).
3. *Solve the parabolic PDE*
$$\beta c_{\mathrm{m}} \partial_t v + \operatorname{div}\big(\mathbf{M}_{\mathrm{e}}(x)\nabla u_{\mathrm{e}}\big) + \beta I_{\mathrm{ion}}(v,w) = I_{\mathrm{app}}, \quad x \in \Omega,$$
$$\big(\mathbf{M}_{\mathrm{e}}(x)\nabla u_{\mathrm{e}}\big)\cdot \mathbf{n} = 0 \quad \text{on } \partial\Omega$$
approximately for $t^n < t \le t^{n+1}$, with $v(t^n) = v^n$ and $w(t^n) = w^n$, i.e., calculate v^{n+1} using (2.19).
4. *Solve the elliptic problem*
$$\operatorname{div}\big((\mathbf{M}_{\mathrm{i}}(x) + \mathbf{M}_{\mathrm{e}}(x))\nabla u_{\mathrm{e}}\big) + \operatorname{div}\big(\mathbf{M}_{\mathrm{i}}(x)\nabla v\big) = I_{\mathrm{app}}, \quad x \in \Omega$$
$$\big(\mathbf{M}_j(x)\nabla u_j\big)\cdot \mathbf{n} = 0 \quad \text{on } \partial\Omega,\ j \in \{\mathrm{e},\mathrm{i}\}$$
approximately for $t^n < t \le t^{n+1}$ with $v(t^n) = v^n$ and $u_{\mathrm{e}}(t^n) = u^n_{\mathrm{e}}$, i.e., determine u^{n+1}_{e} by solving the linear system (2.20).

This algorithm structure is usually preferred for systems involving parabolic and elliptic equation, since it explicitly isolates the solution of the elliptic problem from the rest of the computations [126].

The boundary condition (1.38) is taken into account by imposing zero fluxes on the external edges and the compatibility condition (1.40) is discretized via

$$\sum_{i,j=1}^{N} h^2 u^n_{\mathrm{e},ij} = 0, \quad n = 0,1,2,\ldots.$$

Analogously, a FV method for the monodomain model (1.41) is given by determining v^{n+1}_{ij} and w^{n+1}_{ij} for $1 \le i,j \le N$ and $n = 0,1,2,\ldots$ such that we start from the initial data and use the following formulas to advance the solution over one time step:

$$\beta c_{\mathrm{m}} h^2 \frac{v^{n+1}_{ij} - v^n_{ij}}{\Delta t} + \mathcal{D}_h\left(\frac{1}{1+\lambda}\mathbf{M}_{\mathrm{i}}, v^n_{ij}\right) + \beta h^2 I^n_{\mathrm{ion},(i,j)} = \frac{\lambda}{1+\lambda} h^2 I^{n+1}_{\mathrm{app},(i,j)},$$

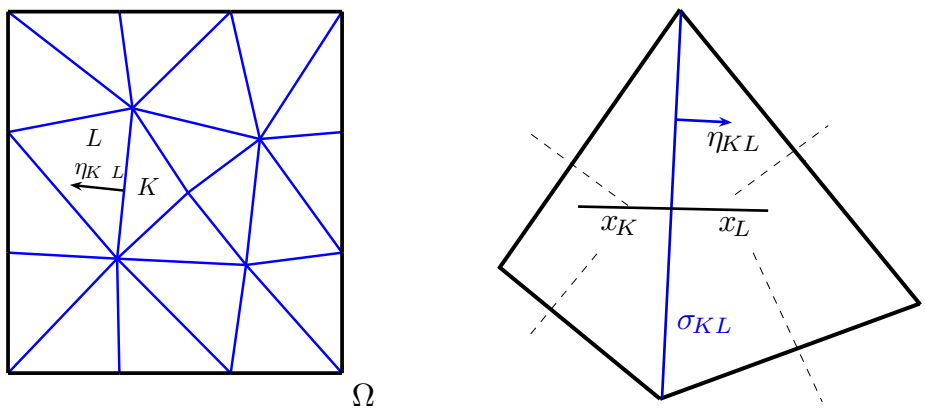

Figure 2.1: *Representation of a two–dimensional mesh and centers.*

$$h^2 \frac{w_{ij}^{n+1} - w_{ij}^n}{\Delta t} - h^2 H_{ij}^n = 0.$$

As in [9], we may deduce that the previously detailed FV method (2.18)–(2.21), is stable under the CFL condition

$$\Delta t \leqslant h\Big(2 \max_{1\leq i,j\leq N}\big(|I^n_{\mathrm{ion},(i,j)}| + |I^n_{\mathrm{app},(i,j)}|\big) + 4h^{-1} \max_{1\leq i,j\leq N}\big(|M_{\mathrm{i},(i,j)}| + |M_{\mathrm{e},(i,j)}|\big)\Big)^{-1}. \tag{2.22}$$

Notice that the values of $I^n_{\mathrm{ion},(i,j)}$ and $I^n_{\mathrm{app},(i,j)}$ depend on time. However, while I_{app} is a given control function for our model and therefore $\max_{1\leq i,j\leq N} |I^n_{\mathrm{app},(i,j)}|$ can assumed to be bounded, the quantity $I^n_{\mathrm{ion},(i,j)}$ is not bounded a priori for arbitrarily large times. Consequently, in our computations, we evaluate the right-hand side of (2.22) after each iteration at $t = t^n$, and use (2.22) to *define* the time step size Δt to advance the solution from t^n to $t^{n+1} = t^n + \Delta t$.

2.3.2 An implicit scheme on unstructured meshes

Now we give a definition of our FV scheme for approximate the solutions to the bidomain equations (1.37). This description follows the framework of [76]. An admissible mesh for Ω is formed by a family $\mathcal{T}$ of control volumes (open and convex polygons) of maximum diameter h. For all $K \in \mathcal{T}$, x_K denotes the center of K, $N(K)$ the set of neighbors of K, $\mathcal{E}_{\mathrm{int}}(K)$ is the set of edges of K in the interior of $\mathcal{T}$ and $\mathcal{E}_{\mathrm{ext}}(K)$ the set of edges of K on the boundary $\partial\Omega$. For all $L \in N(K)$ $d(K, L)$ denotes the distance between x_K and x_L, $\sigma_{K,L}$ is the interface between K and L and $\eta_{K,L}$ ($\eta_{K,\sigma}$ respectively) is the unit normal vector to $\sigma_{K,L}$ ($\sigma \in \mathcal{E}_{\mathrm{ext}}(K)$ respectively) oriented from K to L (from K to $\partial\Omega$ respectively). For all $K \in \mathcal{T}$, $|K|$ stands for the measure of the cell K. From the admissibility of $\mathcal{T}$ we have that $\overline{\Omega} = \cup_{K\in\mathcal{T}}\overline{K}$, $K \cap L = \emptyset$ if $K, L \in \mathcal{T}$ and $K \neq L$, and there exists a finite sequence $(x_K)_{K\in\mathcal{T}}$ for which $\overline{x_K x_L}$ is orthogonal to $\sigma_{K,L}$ (see Figure 2.1).

Now, consider $K \in \mathcal{T}$ and $L \in N(K)$ with common vertices $(a_{\ell,K,L})_{1\leq\ell\leq I}$ with $I \in \mathbb{N}\backslash\{0\}$ and let $T_{K,L}$ (respectively $T^{\mathrm{ext}}_{K,\sigma}$ for $\sigma \in \mathcal{E}_{\mathrm{ext}}(K)$) be the open and convex polygon with vertexes (x_K, x_L) (x_K respectively) and $(a_{\ell,K,L})_{1\leq\ell\leq I}$. Notice that Ω can be decomposed into $\overline{\Omega} = \cup_{K\in\mathcal{T}}((\cup_{L\in N(K)}\overline{T}_{K,L}) \cup (\cup_{\sigma\in\mathcal{E}_{\mathrm{ext}}(K)}\overline{T}^{\mathrm{ext}}_{K,\sigma}))$.

For all $K \in \mathcal{T}$, the approximation $\nabla_h u_h$ of ∇u is defined by

$$\nabla_h u_h(x) = \begin{cases} \frac{|\sigma_{K,L}|}{|T_{K,L}|}(u_L - u_K)\eta_{K,L}, & \text{if } x \in T_{K,L}, \\ 0, & \text{if } x \in T^{\text{ext}}_{K,\sigma}. \end{cases}$$

To discretize (1.37)–(1.39), we choose an admissible discretization of Q_T, consisting of an admissible mesh of Ω and a time step size $\Delta t > 0$. We could choose $N > 0$ as the smallest integer such that $N\Delta t \geq T$, and set $t^n := n\Delta t$ for $n \in \{0, \dots, N\}$.

On each cell $K \in \mathcal{T}$, (positive definite) conductivity tensors are defined by

$$\mathbf{M}_{\mathrm{j},K} = \frac{1}{|K|}\int_\Omega \mathbf{M}_{\mathrm{j}}(x)\,dx, \quad \mathrm{j} \in \{\mathrm{e}, \mathrm{i}\}.$$

Let $F_{j,K,L}$ be an approximation of $\int_{\sigma_{K,L}} \mathbf{M}_{\mathrm{j}}(x)\nabla u_{\mathrm{j}} \cdot \eta_{K,L} d\gamma$ for $\mathrm{j} \in \{\mathrm{e}, \mathrm{i}\}$, and for $K \in \Omega_R$, $L \in N(K)$ let

$$M_{\mathrm{j},K,L} = \left| \frac{1}{|K|}\int_K \mathbf{M}_{\mathrm{j}}(x)\,dx\,\eta_{K,L} \right| := |M_{\mathrm{j},K}\,\eta_{K,L}|\,, \quad \mathrm{j} \in \{\mathrm{e}, \mathrm{i}\}.$$

The diffusive fluxes $M_{\mathrm{j}}(x)\nabla u_j \cdot \eta_{K,L}$ on $\sigma_{K,L}$ are approximated by

$$\begin{aligned} &\int_{\sigma_{K,L}} (\mathbf{M}_{\mathrm{j}}(x)\nabla u_{\mathrm{j}}) \cdot \eta_{K,L} d\gamma \\ &\approx |\sigma_{K,L}|\nabla u_{\mathrm{j}}(y_\sigma) \cdot (M_{\mathrm{j},K}\,\eta_{K,L}) = |\sigma_{K,L}| M_{\mathrm{j},K,L}\nabla u_{\mathrm{j}}(y_\sigma) \cdot \frac{y_\sigma - x_K}{d(K, \sigma_{K,L})} \\ &\approx |\sigma_{K,L}| M_{\mathrm{j},K,L}\frac{u_{\mathrm{j},\sigma} - u_{\mathrm{j},K}}{d(K, \sigma_{K,L})}, \end{aligned} \tag{2.23}$$

where y_σ is the center of $\sigma_{K,L}$ and $u_{\mathrm{j},\sigma}$ is an approximation of $u_{\mathrm{j}}(y_\sigma)$, $\mathrm{j} \in \{\mathrm{e}, \mathrm{i}\}$. This flux computation is not consistent in the general anisotropic case (see Remark 2.3.1 by the end of this section, for further details). However, for the isotropic case, or more generally when $\mathbf{M}_{\mathrm{i}}$ and $\mathbf{M}_{\mathrm{e}}$ have the axes of the mesh as eigenvectors, the resulting approximation of fluxes is consistent (see [76]). This is also true for discretizations using uniform meshes. In addition, the scheme should be conservative. This property enables us to determine the additional unknowns $u_{\mathrm{j},\sigma}$, and to compute the numerical fluxes on internal edges:

$$F_{j,K,L} = d^*_{j,K,L}\frac{|\sigma_{K,L}|}{d(K,L)}(u_{\mathrm{j},L} - u_{\mathrm{j},K}) \text{ if } L \in N(K),$$

where we define

$$d^*_{\mathrm{j},K,L} = \frac{M_{\mathrm{j},K,L}M_{\mathrm{j},L,K}}{d(K, \sigma_{K,L})M_{\mathrm{j},K,L} + d(L, \sigma_{K,L})M_{\mathrm{j},L,K}} d(K,L),$$

while we discretize the zero-flux boundary condition by setting $F_{\mathrm{j},K,\sigma} = 0$. We define cell averages of the unknowns $H(v,w)$ and $I_{\text{ion}}(v,w)$:

$$\begin{aligned} H^{n+1}_K &:= \frac{1}{\Delta t|K|}\int_{t^n}^{t^{n+1}}\int_K H\big(v(x,t), w(x,t)\big)\,dx\,dt, \\ I^{n+1}_{\text{ion},K} &:= \frac{1}{\Delta t|K|}\int_{t^n}^{t^{n+1}}\int_K I_{\text{ion}}\big(v(x,t), w(x,t)\big)\,dx\,dt, \end{aligned}$$

and of the given function I_{app}:

$$I^{n+1}_{\text{app},K} := \frac{1}{\Delta t|K|}\int_{t^n}^{t^{n+1}}\int_K I_{\text{app}}(x,t)\,dx\,dt.$$

The computation starts from the initial cell averages

$$v_K^0 = \frac{1}{|K|}\int_K v_0(x)\,dx, \quad w_K^0 = \frac{1}{|K|}\int_K w_0(x)\,dx. \tag{2.24}$$

To advance the numerical solution from t^n to t^{n+1}, we use the following implicit FV scheme: Determine $(u_{\mathrm{j},K}^n)_{K\in\mathcal{T}}$ for $\mathrm{j}\in\{\mathrm{e},\mathrm{i}\}$ and $n\in\{0,\dots,N\}$, $(v_K^n)_{K\in\mathcal{T}} = (u_{\mathrm{i},K}^n - u_{\mathrm{e},K}^n)_{K\in\mathcal{T}}$ for $n\in\{0,\dots,N\}$, and $(w_K^n)_{K\in\mathcal{T}}$ for $n\in\{0,\dots,N\}$, such that for all $K\in\mathcal{T}$ and $n\in\{0,\dots,N-1\}$

$$\beta c_{\mathrm{m}}|K|\frac{v_K^{n+1}-v_K^n}{\Delta t} + \sum_{L\in N(K)} d_{\mathrm{e},K,L}^*\frac{|\sigma_{K,L}|}{d(K,L)}(u_{\mathrm{e},L}^{n+1}-u_{\mathrm{e},K}^{n+1}) + \beta|K|I_{\mathrm{ion},K}^n = |K|I_{\mathrm{app},K}^n, \tag{2.25}$$

$$\sum_{L\in N(K)}\frac{|\sigma_{K,L}|}{d(K,L)}\left\{\left(d_{\mathrm{i},K,L}^* + d_{\mathrm{e},K,L}^*\right)\left(u_{\mathrm{e},L}^{n+1}-u_{\mathrm{e},K}^{n+1}\right) + d_{\mathrm{i},K,L}^*\left(v_L^{n+1}-v_K^{n+1}\right)\right\} = |K|I_{\mathrm{app},K}^n, \tag{2.26}$$

$$|K|\frac{w_K^{n+1}-w_K^n}{\Delta t} - |K|H_K^n = 0. \tag{2.27}$$

The boundary condition (1.38) is taken into account by imposing zero–fluxes on external edges:

$$d_{\mathrm{j},K,\sigma}^*\frac{|\sigma_{K,L}|}{d(K,L)}(u_{\mathrm{j},L}^n - u_{\mathrm{j},K}^n) = 0 \quad \text{for } \sigma\in\mathcal{E}_{\mathrm{ext}}(K), \quad \mathrm{j}\in\{\mathrm{e},\mathrm{i}\}, \tag{2.28}$$

and the compatibility condition (1.40) is discretized via $\sum_{K\in\mathcal{T}}|K|u_{\mathrm{e},K}^n = 0$, for all $n\in\{1,\dots,N-1\}$.

In order to prove existence and uniqueness of solution to (2.24)-(2.28) we will assume that the following mild time step condition is satisfied:

$$\Delta t < \frac{\beta c_m}{\left(2\beta C_I + \frac{\beta^2\lambda^2}{b} + \frac{a^2}{b}\right)}. \tag{2.29}$$

Finally, we introduce the "piecewise constant" functions

$$u_{\mathrm{j},h}(t,x) = u_{\mathrm{j},K}^{n+1} \text{ and } w_h(t,x) = w_K^{n+1}, v_h(t,x) = v_K^{n+1}, \quad \mathrm{j}\in\{\mathrm{i},\mathrm{e}\}$$

for all $(t,x)\in(n\Delta t,(n+1)\Delta t]\times K$, with $K\in\mathcal{T}$ and $n\in\{0,\dots,N-1\}$, and for simplicity of notation, we define $\mathbf{u} := (v, u_{\mathrm{e}}, w)$ and $\mathbf{u}_h := (v_h, u_{\mathrm{e},h}, w_h)$.

Analogously, a FV method for the monodomain model (1.41) is given by determining vectors $(v_K^n)_{K\in\mathcal{T}}$ for $n\in\{0,\dots,N\}$, and $(w_K^n)_{K\in\mathcal{T}}$ for $n\in\{0,\dots,N\}$, such that for all $K\in\mathcal{T}$ and $n\in\{0,\dots,N-1\}$, we have (2.18) and

$$\begin{aligned}\beta c_{\mathrm{m}}|K|\frac{v_K^{n+1}-v_K^n}{\Delta t} &+ \sum_{L\in N(K)}\frac{d_{\mathrm{e},K,L}^* d_{\mathrm{i},K,L}^*}{d_{\mathrm{e},K,L}^* + d_{\mathrm{i},K,L}^*}\frac{|\sigma_{K,L}|}{d(K,L)}(v_L^n - v_K^n) + \beta|K|I_{\mathrm{ion},K}^n \\ &= \frac{\sigma_{\mathrm{i}}^{\mathrm{l}}}{\sigma_{\mathrm{e}}^{\mathrm{l}}+\sigma_{\mathrm{i}}^{\mathrm{l}}}|K|I_{\mathrm{app},K}^n,\end{aligned}$$

$$|K|\frac{w_K^{n+1}-w_K^n}{\Delta t} - |K|H_K^{n+1} = 0.$$

The convergence of the FV method given above is established by our main result, formulated as follows.

Theorem 2.3.1 *Suppose that $v_0 \in L^2(\Omega)$, $w_0 \in L^2(\Omega)$ and $I_{\text{ion}} \in L^2(Q_T)$, $I_{\text{app}} \in L^2(Q_T)$. Then the FV solution $\mathbf{u}_h$, generated by (2.24)-(2.28), converges along a subsequence to $\mathbf{u}$ as $h \to 0$, where $\mathbf{u}$ is a weak solution of (1.37)-(1.39). The convergence is understood in the following sense:*

$$\begin{aligned}
&v_h \to v \text{ strongly in } L^2(Q_T) \text{ and a.e. in } Q_T,\\
&\nabla_h u_{\mathrm{e},h} \to \nabla u_{\mathrm{e}} \text{ weakly in } (L^2(Q_T))^3,\ \mathrm{j} \in \{\mathrm{i}, \mathrm{e}\},\\
&w_h \to w \text{ weakly in } L^2(Q_T).
\end{aligned}$$

A FV method for another version of the bidomain equations is analyzed in [13]. The authors prove existence and uniqueness of solutions to the FV scheme, and provide convergence results. In [59] the authors give stability conditions for two time-stepping methods in different settings, and they prove convergence of an implicit FV approximation to the monodomain equations. A discrete duality FV method (DDFV) to solve the fully coupled heart and torso problem is presented in [60]. In that paper the authors prove wellposedness of the problem and show different numerical tests using preconditioning. From the applications viewpoint, in [89] the authors give one of the first approaches of FV methods for cardiac problems, and in [145] a FV scheme is introduced for the bidomain equations but representing physical discontinuities without the implicit removal of intracellular volume, yielding to linear instead of nonlinear systems.

Remark 2.3.1 *Note that the FV scheme used herein has the disadvantage of not being consistent except in the case where the diffusion matrices are both isotropic, as for example in the monodomain model. Specifically, we stress that the first equality in (2.23) is not true in general but only if $M_{\mathrm{j},K}\eta_{K,L} = |M_{\mathrm{j},K}\eta_{K,L}|\eta_{K,L}$, which is not the case except if $\eta_{K,L}$ is an eigenvector of $M_{\mathrm{j},K}$. Furthermore, the underlying scheme cannot be modified in a simple manner to be consistent in general for the bidomain equations. To overcome this difficulty, several variants of the proposed FV method have been recently proposed, as the diamond scheme, or the DDFV method (see e.g. [60]).*

Remark 2.3.2 *We also emphasize that since the proof of Theorem 2.3.1 is based on a compactness argument, we do not provide error estimates. Nevertheless, the numerical results given in Section 5.4 yield information about the experimental rate of convergence of the method.*

2.3.3 Wellposedness of the scheme

This section is devoted to the proof of existence and uniqueness of solution to the FV method (2.25)-(2.27). Although the analysis is based on the same lines that the one in [13], we detail herein the main steps for the sake of completeness and convenience of the reader.

Let $H_h(\Omega) \subset L^2(\Omega)$ be the space of piecewise constant functions on each $K \in \mathcal{T}$. For all $u_h \in H_h(\Omega)$ and for all $K \in \mathcal{T}$, u_K denotes the constant value of u_h in K. For $(u_h, v_h) \in (H_h(\Omega))^2$, we define:

$$\langle u_h, v_h \rangle_{H_h} = \frac{1}{2} \sum_{K \in \mathcal{T}} \sum_{L \in N(K)} \frac{|\sigma_{K,L}|}{d(K,L)} (u_L - u_K)(v_L - v_K),$$

and $\|u_h\|_{H_h(\Omega)} = (\langle u_h, u_h \rangle_{H_h})^{1/2}$. We also define $L_h(\Omega) \subset L^2(\Omega)$ as the space of piecewise constant functions on each $K \in \mathcal{T}$ with the norm

$$(u_h, v_h)_{L_h(\Omega)} = \sum_{K \in \mathcal{T}} |K| u_K v_K, \qquad \|u_h\|^2_{L_h(\Omega)} = \sum_{K \in \mathcal{T}} |K| \, |u_K|^2,$$

for $u_h, v_h \in L_h(\Omega)$. In the sequel we will drop the time step superscript whenever is not needed. For the existence part, we will make use of the following lemma provided in [111].

Lemma 2.3.2 *Let $(\mathcal{A}, [\cdot,\cdot], \|\cdot\|)$ be a finite dimensional Hilbert space, and let $\mathcal{P}$ be a continuous mapping from $\mathcal{A}$ into itself such that*

$$[\mathcal{P}(\xi), \xi] > 0 \quad \text{for all } \xi,\ \|\xi\| = r > 0.$$

Then there exists $\xi \in \mathcal{A}$ such that

$$\mathcal{P}(\xi) = 0.$$

Lemma 2.3.3 (Discrete Sobolev inequality) *Let u be a function such that $\frac{1}{|\Omega|}\int_\Omega u(x)\,dx = 0$ and it is constant on each cell of $\mathcal{T}$, that is, $u(x) = u_K$ if $x \in K$, $K \in \mathcal{T}$. Then there exists a constant $C_p > 0$, depending on Ω, such that*

$$\|u\|^2_{L^2(\Omega)} \le C_p \|u\|^2_{H_h(\Omega)}.$$

Proposition 2.1 *Let $\mathcal{D}$ be an admissible discretization of Ω_T. Then the FV scheme (2.25)-(2.27) admits a unique solution $(v_K^n, u_{\mathrm{e},K}^n, w_K^n)$ for all $K \in \mathcal{T}$ and $n \in \{0,\dots,N\}$.*

Proof. Let $E_h := H_h(\Omega) \times H_h(\Omega) \times L_h(\Omega)$ be a Hilbert space endowed with the obvious norm, let $\Phi_h = (\varphi_h, \psi_h, \xi_h) \in E_h$ and define the bilinear forms

$$\begin{aligned}
A_h(\mathbf{u}_h^n, \Phi_h) &:= (\beta c_m v_h^n, -\psi_h)_{L_h(\Omega)} + (w_h^n, \xi_h)_{L_h(\Omega)},\\
B_h(\mathbf{u}_h^{n+1}, \Phi_h) &:= \sum_{K\in\mathcal{T}} \sum_{L\in N(K)} \frac{|\sigma_{K,L}|}{d(K,L)} \Big(d^*_{\mathrm{e},K,L}(u^n_{\mathrm{e},L} - u^n_{\mathrm{e},K})(\psi_L - \psi_K) + [(d^*_{\mathrm{i},K,L}\\
&\qquad + d^*_{\mathrm{e},K,L})(u^{n+1}_{\mathrm{e},L} - u^{n+1}_{\mathrm{e},K}) + d^*_{\mathrm{i},K,L}(v_L^{n+1} - v_K^{n+1})][(\varphi_L + \psi_L) - (\varphi_K + \psi_K)]\Big),
\end{aligned}$$

and the operator $\mathbf{C}^n$

$$(\mathbf{C}^{n+1}, \Phi_h)_h := \sum_{K\in\mathcal{T}} |K| \Big(-\beta I^{n+1}_{\mathrm{ion},K}\psi_K - I^{n+1}_{\mathrm{app},K}\psi_K - I^{n+1}_{\mathrm{app},K}(\varphi_K + \psi_K) - H_K^{n+1}\xi_K \Big).$$

We proceed to multiply (2.25) by φ_K, (2.26) by ψ_K, (2.27) by ξ_K and summing the resulting system, we obtain

$$\frac{1}{\Delta t}\Big(A_h(\mathbf{u}_h^{n+1}, \Phi_h) - A_h(\mathbf{u}_h^n, \Phi_h) \Big) + B_h(\mathbf{u}_h^{n+1}, \Phi_h) + (\mathbf{C}^{n+1}, \Phi_h)_h = 0.$$

Now, let us define the mapping $\mathcal{P} : E_h \to E_h$, by

$$[\mathcal{P}(\mathbf{u}_h^{n+1}), \Phi_h] = \frac{1}{\Delta t}\Big(A_h(\mathbf{u}_h^{n+1}, \Phi_h) - A_h(\mathbf{u}_h^n, \Phi_h) \Big) + B_h(\mathbf{u}_h^{n+1}, \Phi_h) + (\mathbf{C}^{n+1}, \Phi_h)_h,$$

for all $\Phi_h \in E_h$; and the strategy consists in applying Lemma 2.3.2 to obtain the existence of $\mathbf{u}_K^n = (v_K^n, u^n_{\mathrm{e},K}, w_K^n)$ for all $K \in \mathcal{T}$, $n \in \{0,\dots,N\}$. Using the discrete Hölder inequality, we deduce the continuity of A_h, B_h. The continuity of the discrete form $(\mathbf{C}^{n+1}, \cdot)_h$ is also easy to verify. We then conclude that $\mathcal{P}$ is continuous and the task is now to show that

$$[\mathcal{P}(\mathbf{u}_h^{n+1}), \mathbf{u}_h^{n+1}] > 0, \qquad \text{for } \|\mathbf{u}_h^{n+1}\|_{E_h} = r > 0,$$

for a sufficiently large r. To this end, firstly observe that

$$
\begin{aligned}
&[\mathcal{P}(\mathbf{u}_h^{n+1}), \mathbf{u}_h^{n+1}] = \\
&\quad - \frac{\beta c_m}{\Delta t} \sum_{K\in\mathcal{T}} |K|(v_K^{n+1} - v_K^n) u_{\mathrm{e},L}^{n+1} + \frac{1}{\Delta t} \sum_{K\in\mathcal{T}} |K||w_K^{n+1}|^2 \\
&\quad + \sum_{K\in\mathcal{T}} \sum_{L\in N(K)} \frac{|\sigma_{K,L}|}{d(K,L)} \Big(d^*_{\mathrm{e},K,L}(u_{\mathrm{e},L}^{n+1} - u_{\mathrm{e},K}^{n+1})^2 + [(d^*_{\mathrm{i},K,L} \\
&\quad + d^*_{\mathrm{e},K,L})(u_{\mathrm{e},L}^{n+1} - u_{\mathrm{e},K}^{n+1}) + d^*_{\mathrm{i},K,L}(v_L^{n+1} - v_K^{n+1})][(v_L^{n+1} + u_{\mathrm{e},L}^{n+1}) - (v_K^{n+1} + u_{\mathrm{e},K}^{n+1})] \Big) \\
&\quad - \frac{1}{\Delta t} \sum_{K\in\mathcal{T}} |K| w_K^n w_K^{n+1} - \beta \sum_{K\in\mathcal{T}} |K| I_{\mathrm{ion},K}^{n+1} u_{\mathrm{e},K}^{n+1} - \sum_{K\in\mathcal{T}} |K| I_{\mathrm{app},K}^{n+1} u_{\mathrm{e},K}^{n+1} \\
&\quad - \sum_{K\in\mathcal{T}} |K| I_{\mathrm{app},K}^{n+1} (v_K^{n+1} + u_{\mathrm{e},K}^{n+1}) - \sum_{K\in\mathcal{T}} |K| H_K^{n+1} \\
&= - \frac{\beta c_m}{\Delta t} \sum_{K\in\mathcal{T}} |K|(v_K^{n+1} - v_K^n) u_{\mathrm{e},L}^{n+1} + \frac{1}{\Delta t} \sum_{K\in\mathcal{T}} |K||w_K^{n+1}|^2 \\
&\quad + \sum_{K\in\mathcal{T}} \sum_{L\in N(K)} \frac{|\sigma_{K,L}|}{d(K,L)} \Big(d^*_{\mathrm{e},K,L}(u_{\mathrm{e},L}^{n+1} - u_{\mathrm{e},K}^{n+1})^2 + d^*_{\mathrm{i},K,L}[(v_L^{n+1} + u_{\mathrm{e},L}^{n+1}) - (v_K^{n+1} + u_{\mathrm{e},K}^{n+1})]^2 \\
&\quad + d^*_{\mathrm{e},K,L}(u_{\mathrm{e},L}^{n+1} - u_{\mathrm{e},K}^{n+1})[(v_L^{n+1} + u_{\mathrm{e},L}^{n+1}) - (v_K^{n+1} + u_{\mathrm{e},K}^{n+1})] \Big) \\
&\quad - \frac{1}{\Delta t} \sum_{K\in\mathcal{T}} |K| w_K^n w_K^{n+1} - \beta \sum_{K\in\mathcal{T}} |K| I_{\mathrm{ion},K}^{n+1} u_{\mathrm{e},K}^{n+1} - \sum_{K\in\mathcal{T}} |K| I_{\mathrm{app},K}^{n+1} u_{\mathrm{e},K}^{n+1} \\
&\quad - \sum_{K\in\mathcal{T}} |K| I_{\mathrm{app},K}^{n+1} (v_K^{n+1} + u_{\mathrm{e},K}^{n+1}) - \sum_{K\in\mathcal{T}} |K| H_K^{n+1}.
\end{aligned}
\tag{2.30}
$$

Multiplying (2.25) by $(v_K^{n+1} + u_{\mathrm{e},K}^{n+1})$ and summing over all $K \in \mathcal{T}$ we arrive at

$$
\begin{aligned}
&\frac{\beta c_m}{\Delta t} \sum_{K\in\mathcal{T}} |K|(v_K^{n+1} - v_K^n)(v_K^{n+1} + u_{\mathrm{e},K}^{n+1}) + \beta \sum_{K\in\mathcal{T}} |K| I_{\mathrm{ion},K}^{n+1} (v_K^{n+1} + u_{\mathrm{e},K}^{n+1}) \\
&\quad + \sum_{K\in\mathcal{T}} |K| I_{\mathrm{app},K}^{n+1} (v_K^{n+1} + u_{\mathrm{e},K}^{n+1}) \\
&\qquad = \sum_{K\in\mathcal{T}} \sum_{L\in N(K)} d^*_{\mathrm{e},K,L} \frac{|\sigma_{K,L}|}{d(K,L)} (u_{\mathrm{e},L}^{n+1} - u_{\mathrm{e},K}^{n+1})[(v_L^{n+1} + u_{\mathrm{e},L}^{n+1}) - (v_K^{n+1} + u_{\mathrm{e},K}^{n+1})].
\end{aligned}
\tag{2.31}
$$

Next, exploiting (2.31) we deduce from (2.30) that

$$
\begin{aligned}
&[\mathcal{P}(\mathbf{u}_h^{n+1}), \mathbf{u}_h^{n+1}] = \\
&\quad \frac{\beta c_m}{\Delta t} \sum_{K\in\mathcal{T}} |K||v_K^{n+1}|^2 + \frac{1}{\Delta t} \sum_{K\in\mathcal{T}} |K||w_K^{n+1}|^2 - \frac{\beta c_m}{\Delta t} \sum_{K\in\mathcal{T}} |K| v_K^n v_K^{n+1} - \frac{1}{\Delta t} \sum_{K\in\mathcal{T}} |K| w_K^n w_K^{n+1} \\
&\quad + \sum_{K\in\mathcal{T}} \sum_{L\in N(K)} \frac{|\sigma_{K,L}|}{d(K,L)} \Big(d^*_{\mathrm{e},K,L}(u_{\mathrm{e},L}^{n+1} - u_{\mathrm{e},K}^{n+1})^2 + d^*_{\mathrm{i},K,L}[(v_L^{n+1} + u_{\mathrm{e},L}^{n+1}) - (v_K^{n+1} + u_{\mathrm{e},K}^{n+1})]^2 \Big) \\
&\quad - \sum_{K\in\mathcal{T}} |K| I_{\mathrm{app},K}^{n+1} u_{\mathrm{e},L}^{n+1} - \sum_{K\in\mathcal{T}} |K| H_K^{n+1} w_K^{n+1} + \beta \sum_{K\in\mathcal{T}} |K| I_{\mathrm{ion},K}^{n+1} v_K^{n+1}.
\end{aligned}
$$

Given (1.42) and Young's inequality, it follows that

$$
[\mathcal{P}(\mathbf{u}_h^{n+1}), \mathbf{u}_h^{n+1}] \geqslant
$$

$$
\begin{aligned}
&\frac{\beta c_m}{\Delta t}\sum_{K\in\mathcal{T}}|K||v_K^{n+1}|^2+\frac{1}{\Delta t}\sum_{K\in\mathcal{T}}|K||w_K^{n+1}|^2+C_M(\|v_h^{n+1}+u_{\mathrm{e},h}^{n+1}\|^2_{H_h(\Omega)}+\|u_{\mathrm{e},h}^{n+1}\|^2_{H_h(\Omega)})\\
&-\beta C_I\sum_{K\in\mathcal{T}}|K|\left|v_K^{n+1}\right|^2-\frac{b}{2}\sum_{K\in\mathcal{T}}|K|\left|w_K^{n+1}\right|^2-\frac{\beta^2\lambda^2}{2b}\sum_{K\in\mathcal{T}}|K|\left|v_K^{n+1}\right|^2+b\sum_{K\in\mathcal{T}}|K|\left|w_K^{n+1}\right|^2\\
&-\frac{a^2}{2b}\sum_{K\in\mathcal{T}}|K|\left|v_K^{n+1}\right|^2-\frac{b}{2}\sum_{K\in\mathcal{T}}|K|\left|w_K^{n+1}\right|^2-\frac{C_M}{2C_p^2}\sum_{K\in\mathcal{T}}|K|\left|u_{\mathrm{e},h}^{n+1}\right|^2\\
&\quad-C(C_M,C_p)\sum_{K\in\mathcal{T}}|K|\left|I_{\mathrm{app},K}^{n+1}\right|^2-\frac{\beta c_m}{2\Delta t}\sum_{K\in\mathcal{T}}|K|\left|v_K^{n+1}\right|^2\\
&\quad-C(c_m,\beta,\Delta t)\sum_{K\in\mathcal{T}}|K|\left|v_K^{n}\right|^2-\frac{1}{2\Delta t}\sum_{K\in\mathcal{T}}|K|\left|w_K^{n+1}\right|^2-C(\Delta t)\sum_{K\in\mathcal{T}}|K|\left|w_K^{n}\right|^2,
\end{aligned}
$$

and therefore, from Lemma 2.3.3 we get

$$
\begin{aligned}
[\mathcal{P}(\mathbf{u}_h^{n+1}),\mathbf{u}_h^{n+1}]\geqslant\ &\left(\frac{\beta c_m}{2\Delta t}-\beta C_I-\frac{\beta^2\lambda^2}{2b}-\frac{a^2}{2b}\right)\sum_{K\in\mathcal{T}}|K||v_K^{n+1}|^2+\frac{1}{2\Delta t}\sum_{K\in\mathcal{T}}|K||w_K^{n+1}|^2\\
&+\frac{C_M}{2}(\|v_h^{n+1}+u_{\mathrm{e},h}^{n+1}\|^2_{H_h(\Omega)}+\|u_{\mathrm{e},h}^{n+1}\|^2_{H_h(\Omega)})\\
&-C(C_M,C_p)\sum_{K\in\mathcal{T}}|K|\left|I_{\mathrm{app},K}^{n+1}\right|^2-C(c_m,\beta,\Delta t)\sum_{K\in\mathcal{T}}|K|\left|v_K^{n}\right|^2\\
&-C(\Delta t)\sum_{K\in\mathcal{T}}|K|\left|w_K^{n}\right|^2.
\end{aligned}
$$

Finally, if we use (2.29), then, for a given $\mathbf{u}_h^n$ we can choose $\mathbf{u}_h^{n+1}$ with norm large enough to conclude that Lemma 2.3.2 holds, and thus we have the existence of at least one solution to the scheme (2.25)-(2.27).

It remains to prove the uniqueness. Let us first assume that there exists $n\in\{0,\dots,N\}$ such that $v_K^n=\tilde{v}_K^n$, $u_{\mathrm{e},K}^n=\tilde{u}_{\mathrm{e},K}^n$, and $w_K^n=\tilde{w}_K^n$ for all $K\in\mathcal{T}$, but $v_K^{n+1}\neq\tilde{v}_K^{n+1}$, $u_{\mathrm{e},K}^{n+1}\neq\tilde{u}_{\mathrm{e},K}^{n+1}$, and $w_K^{n+1}\neq\tilde{w}_K^{n+1}$ for some $K\in\mathcal{T}$, all of these functions satisfying (2.25)-(2.27). Substracting the schemes for $\{v_K^n,u_{\mathrm{e},K}^n,w_K^n\}$ and $\{\tilde{v}_K^n,\tilde{u}_{\mathrm{e},K}^n,\tilde{w}_K^n\}$, multiplying the resulting scheme by $(w_K^{n+1}-\tilde{w}_K^{n+1})$, $(v_K^{n+1}-\tilde{v}_K^{n+1})$ and $[(u_{\mathrm{e},L}^{n+1}-\tilde{u}_{\mathrm{e},L}^{n+1})-(u_{\mathrm{e},K}^{n+1}-\tilde{u}_{\mathrm{e},K}^{n+1})]$ respectively, and summing over all $K\in\mathcal{T}$, gives

$$
\begin{aligned}
&\beta c_m|K|\frac{v_K^{n+1}-\tilde{v}_K^{n+1}}{\Delta t}+\sum_{L\in N(K)}d^*_{\mathrm{e},K,L}\frac{|\sigma_{K,L}|}{d(K,L)}\Big((u_{\mathrm{e},L}^{n+1}-\tilde{u}_{\mathrm{e},L}^{n+1})-(u_{\mathrm{e},K}^{n+1}-\tilde{u}_{\mathrm{e},K}^{n+1})\Big)\\
&\quad+\beta|K|(I_{1,\mathrm{ion}}(v_K^{n+1})-(I_{1,\mathrm{ion}}(\tilde{v}_K^{n+1}))-\lambda\beta|K|(w_K^{n+1}-\tilde{w}_K^{n+1})=0,
\end{aligned}
\tag{2.32}
$$

$$
\begin{aligned}
&-\sum_{L\in N(K)}(d^*_{\mathrm{i},K,L}+d^*_{\mathrm{e},K,L})\frac{|\sigma_{K,L}|}{d(K,L)}\Big((u_{\mathrm{e},L}^{n+1}-\tilde{u}_{\mathrm{e},L}^{n+1})-(u_{\mathrm{e},K}^{n+1}-\tilde{u}_{\mathrm{e},K}^{n+1})\Big)=\\
&\qquad\sum_{L\in N(K)}d^*_{\mathrm{i},K,L}\frac{|\sigma_{K,L}|}{d(K,L)}\Big((v_L^{n+1}-\tilde{v}_L^{n+1})-(v_K^{n+1}-\tilde{v}_K^{n+1})\Big)
\end{aligned}
\tag{2.33}
$$

$$
|K|\frac{w_K^{n+1}-\tilde{w}_K^{n+1}}{\Delta t}+b\,|K|(w_K^{n+1}-\tilde{w}_K^{n+1})-a\,|K|(v^{n+1}-\tilde{v}_K^{n+1})=0. \tag{2.34}
$$

Next, multiplying (2.32), (2.33), and (2.34) by $-\Delta t(u_{\mathrm{e},K}^{n+1}-\tilde{u}_{\mathrm{e},K}^{n+1})$, $\Delta t((v_K^{n+1}-\tilde{v}_K^{n+1})+(u_{\mathrm{e},K}^{n+1}-\tilde{u}_{\mathrm{e},K}^{n+1})$ and $\Delta t(w_K^{n+1}-\tilde{w}_K^{n+1})$ respectively and summing the resulting over K and $n\in\{0,\dots,N-1\}$ yields $E_1+E_2+E_3=$

0, where

$$E_1 := -\sum_{n=0}^{N-1}\sum_{K\in\mathcal{T}} \beta c_m |K|(v_K^{n+1}-\tilde{v}_K^{n+1})(u_{\mathrm{e},K}^{n+1}-\tilde{u}_{\mathrm{e},K}^{n+1}) + \sum_{n=0}^{N-1}\sum_{K\in\mathcal{T}} |K|\left|w_K^{n+1}-\tilde{w}_K^{n+1}\right|^2,$$

$$\begin{aligned}E_2 := \sum_{n=0}^{N-1}\Delta t \sum_{K\in\mathcal{T}}\sum_{L\in N(K)} \frac{|\sigma_{K,L}|}{d(K,L)}\Big(&d^*_{\mathrm{e},K,L}((u_{\mathrm{e},L}^{n+1}-\tilde{u}_{\mathrm{e},L}^{n+1})-(u_{\mathrm{e},K}^{n+1}-\tilde{u}_{\mathrm{e},K}^{n+1}))^2 + [(d^*_{\mathrm{i},K,L}\\ &+ d^*_{\mathrm{e},K,L})((u_{\mathrm{e},L}^{n+1}-\tilde{u}_{\mathrm{e},L}^{n+1})-(u_{\mathrm{e},K}^{n+1}-\tilde{u}_{\mathrm{e},K}^{n+1})) + d^*_{\mathrm{i},K,L}((v_L^{n+1}-\tilde{v}_L^{n+1})-(v_L^{n+1}-\tilde{v}_K^{n+1}))]\\ &\times[(v_L^{n+1}+u_{\mathrm{e},L}^{n+1})-(v_K^{n+1}+u_{\mathrm{e},K}^{n+1})]\Big),\end{aligned}$$

and

$$\begin{aligned}E_3 := &-\sum_{n=0}^{N-1}\Delta t\sum_{K\in\mathcal{T}}\beta|K|(I_{1,\mathrm{ion}}(v_K^{n+1})-(I_{1,\mathrm{ion}}(\tilde{v}_K^{n+1}))(u_{\mathrm{e},K}^{n+1}-\tilde{u}_{\mathrm{e},K}^{n+1})\\ &+\sum_{n=0}^{N-1}\Delta t\sum_{K\in\mathcal{T}}\lambda\beta|K|(w_K^{n+1}-\tilde{w}_K^{n+1})(u_{\mathrm{e},K}^{n+1}-\tilde{u}_{\mathrm{e},K}^{n+1})\\ &+\sum_{n=0}^{N-1}\Delta t\sum_{K\in\mathcal{T}} b\,|K|(w_K^{n+1}-\tilde{w}_K^{n+1})^2 - \sum_{n=0}^{N-1}\Delta t\sum_{K\in\mathcal{T}} a\,|K|(v_K^{n+1}-\tilde{v}_K^{n+1})(w_K^{n+1}-\tilde{w}_K^{n+1}).\end{aligned}$$

Multiplying (2.33) by $\Delta t((v_K^{n+1}-\tilde{v}_K^{n+1})+(u_{\mathrm{e},K}^{n+1}-\tilde{u}_{\mathrm{e},K}^{n+1}))$ and summing over all $K\in\mathcal{T}$ and $n\in\{0,\dots,N-1\}$, we get

$$\begin{aligned}&\beta c_m\sum_{n=0}^{N-1}\sum_{K\in\mathcal{T}}|K|(v_K^{n+1}-\tilde{v}_K^{n+1})((v_K^{n+1}-\tilde{v}_K^{n+1})+(u_{\mathrm{e},K}^{n+1}-\tilde{u}_{\mathrm{e},K}^{n+1}))\\ &+\sum_{n=0}^{N-1}\Delta t\sum_{K\in\mathcal{T}}\beta|K|(I_{1,\mathrm{ion}}(v_K^{n+1})-(I_{1,\mathrm{ion}}(\tilde{v}_K^{n+1}))((v_K^{n+1}-\tilde{v}_K^{n+1})+(u_{\mathrm{e},K}^{n+1}-\tilde{u}_{\mathrm{e},K}^{n+1}))\\ &-\sum_{n=0}^{N-1}\Delta t\sum_{K\in\mathcal{T}}\lambda\beta|K|(w_K^{n+1}-\tilde{w}_K^{n+1})((v_K^{n+1}-\tilde{v}_K^{n+1})+(u_{\mathrm{e},K}^{n+1}-\tilde{u}_{\mathrm{e},K}^{n+1}))\\ &\qquad=\sum_{n=0}^{N-1}\Delta t\sum_{K\in\mathcal{T}}\sum_{L\in N(K)} d^*_{\mathrm{e},K,L}\frac{|\sigma_{K,L}|}{d(K,L)}((u_{\mathrm{e},L}^{n+1}-\tilde{u}_{\mathrm{e},L}^{n+1})-(u_{\mathrm{e},K}^{n+1}-\tilde{u}_{\mathrm{e},K}^{n+1}))\\ &\qquad\qquad\times[((v_L^{n+1}-\tilde{v}_L^{n+1})+(u_{\mathrm{e},L}^{n+1}-\tilde{u}_{\mathrm{e},L}^{n+1}))-((v_K^{n+1}-\tilde{v}_K^{n+1})+(u_{\mathrm{e},K}^{n+1}-\tilde{u}_{\mathrm{e},K}^{n+1}))].\end{aligned}$$

From this it follows that

$$\begin{aligned}E_1+E_2+E_3 \geq &\sum_{n=0}^{N-1}\sum_{K\in\mathcal{T}}|K|\Big\{\beta c_m(v_K^{n+1}-\tilde{v}_K^{n+1})^2+\left|w_K^{n+1}-\tilde{w}_K^{n+1}\right|^2-\Delta t\lambda\beta(w_K^{n+1}-\tilde{w}_K^{n+1})(v_K^{n+1}-\tilde{v}_K^{n+1})\\ &+\Delta t\beta[I_{1,\mathrm{ion}}(v_K^{n+1})-I_{1,\mathrm{ion}}(\tilde{v}_K^{n+1})](v_K^{n+1}-\tilde{v}_K^{n+1})+\Delta t b\,(w_K^{n+1}-\tilde{w}_K^{n+1})^2\\ &-\Delta t a\,(v^{n+1}-\tilde{v}_K^{n+1})(w_K^{n+1}-\tilde{w}_K^{n+1})\Big\}\\ \geq &\sum_{n=0}^{N-1}\sum_{K\in\mathcal{T}}|K|\Big\{\beta c_m(v_K^{n+1}-\tilde{v}_K^{n+1})^2-\beta C_I\Delta t\left|v_K^{n+1}-\tilde{v}_K^{n+1}\right|^2-\frac{b}{2}\Delta t\left|w_K^{n+1}-\tilde{w}_K^{n+1}\right|^2\end{aligned}$$

$$-\frac{\beta^2\lambda^2}{2b}\Delta t\left|v_K^{n+1}-\tilde{v}_K^{n+1}\right|^2+\frac{b}{N}\left|w_K^{n+1}-\tilde{w}_K^{n+1}\right|^2-\frac{a^2}{2b}\Delta t\left|v_K^{n+1}-\tilde{v}_K^{n+1}\right|^2\Bigg\}.$$

Consequently, putting all the previous inequalities together, we end up with

$$\beta c_m\sum_{n=0}^{N-1}\sum_{K\in\mathcal{T}}|K|\left|v_K^{n+1}-\tilde{v}_K^{n+1}\right|^2\leq\left(\beta C_I+\frac{\beta^2\lambda^2}{2b}+\frac{a^2}{2b}\right)\sum_{n=0}^{N-1}\Delta t\sum_{K\in\mathcal{T}}|K|\left|v_K^{n+1}-\tilde{v}_K^{n+1}\right|^2, \tag{2.35}$$

and since $\sum_{K\in\mathcal{T}}|K|\left|v_K^{n+1}-\tilde{v}_K^{n+1}\right|\neq 0$, from (2.35) we get

$$\frac{\beta c_m}{\left(2\beta C_I+\frac{\beta^2\lambda^2}{b}+\frac{a^2}{b}\right)}\leq\frac{\beta c_m}{\left(\beta C_I+\frac{\beta^2\lambda^2}{2b}+\frac{a^2}{2b}\right)}\leq\Delta t,$$

which contradicts (2.29).

2.3.4 A priori estimates and convergence of the scheme

First we need to establish several a priori estimates for the FV scheme, which eventually will imply the desired convergence results.

Lemma 2.3.4 *Let $(v_K^n,u_{\mathrm{e},K}^n,w_K^n)_{K\in\mathcal{T},n\in\{0,\dots,N\}}$ be a solution of the FV scheme (2.24)-(2.28). Then there exist constants $C_1,C_2,C_3>0$, depending on Ω, T, v_0, w_0, I_{app}, and α, such that*

$$\max_{n\in\{1,\dots,N\}}\sum_{K\in\mathcal{T}}|K|\left(|v_K^n|^2+|w_K^n|^2\right)\leq C_1, \tag{2.36}$$

$$\sum_{n=0}^{N-1}\Delta t\sum_{K\in\mathcal{T}}\sum_{L\in N(K)}\frac{|\sigma_{K,L}|}{d(K,L)}\left(\left|u_{\mathrm{e},K}^{n+1}-u_{\mathrm{e},L}^{n+1}\right|^2+\left|(v_K^{n+1}+u_{\mathrm{e},K}^{n+1})-(v_L^{n+1}+u_{\mathrm{e},L}^{n+1})\right|^2\right)\leq C_2, \tag{2.37}$$

and

$$\sum_{n=0}^{N-1}\Delta t\sum_{K\in\mathcal{T}}|K|\left(\left|v_K^{n+1}\right|^4+\left|I_{1,\mathrm{ion}}(v_K^{n+1})\right|^r\right)\leq C_3, \tag{2.38}$$

for all $1\leq r\leq 4/3$.

Proof. We multiply (2.25), (2.26) and (2.27) by $-\Delta t u_{\mathrm{e},K}^{n+1}$, $\Delta t(v_K^{n+1}+u_{\mathrm{e},K}^{n+1})$ and $\Delta t w_K^{n+1}$, respectively, and add together the outcomes. Summing the resulting equation over K,n and gathering by edges yields $F_1+F_2+F_3=0$, where

$$F_1:=-\beta c_m\sum_{n=0}^{N-1}\sum_{K\in\mathcal{T}}|K|(v_K^{n+1}-v_K^n)u_{\mathrm{e},K}^{n+1}+\sum_{n=0}^{N-1}\sum_{K\in\mathcal{T}}|K|(w_K^{n+1}-w_K^n)w_K^{n+1},$$

$$F_2:=\sum_{n=0}^{N-1}\Delta t\sum_{K\in\mathcal{T}}\sum_{L\in N(K)}\frac{|\sigma_{K,L}|}{d(K,L)}\Bigg(d_{\mathrm{e},K,L}^*(u_{\mathrm{e},L}^{n+1}-u_{\mathrm{e},K}^{n+1})^2+[(d_{\mathrm{i},K,L}^*$$

$$+ d^*_{\mathrm{e},K,L})(u^{n+1}_{\mathrm{e},L} - u^{n+1}_{\mathrm{e},K}) + d^*_{\mathrm{i},K,L}(v^{n+1}_L - v^{n+1}_K)][(v^{n+1}_L + u^{n+1}_{\mathrm{e},L}) - (v^{n+1}_K + u^{n+1}_{\mathrm{e},K})]\Big),$$

and

$$\begin{aligned} F_3 := &- \beta \sum_{n=0}^{N-1} \Delta t \sum_{K\in\mathcal{T}} |K| I^{n+1}_{\mathrm{ion},K} u^{n+1}_{\mathrm{e},K} - \sum_{n=0}^{N-1} \Delta t \sum_{K\in\mathcal{T}} |K| I^{n+1}_{\mathrm{app},K} u^{n+1}_{\mathrm{e},K} \\ &- \sum_{n=0}^{N-1} \Delta t \sum_{K\in\mathcal{T}} |K| I^{n+1}_{\mathrm{app},K} (v^{n+1}_K + u^{n+1}_{\mathrm{e},K}) - \sum_{n=0}^{N-1} \Delta t \sum_{K\in\mathcal{T}} |K| H^{n+1}_K w^{n+1}_K. \end{aligned}$$

Multiplying (2.25) by $\Delta t(v^{n+1}_K + u^{n+1}_{\mathrm{e},K})$, summing over K, n and gathering by edges leads to

$$\begin{aligned} &\beta c_m \sum_{n=0}^{N-1} \Delta t \sum_{K\in\mathcal{T}} |K| (v^{n+1}_K - v^n_K)(v^{n+1}_K + u^{n+1}_{\mathrm{e},K}) + \beta \sum_{n=0}^{N-1} \Delta t \sum_{K\in\mathcal{T}} |K| I^{n+1}_{\mathrm{ion},K} (v^{n+1}_K + u^{n+1}_{\mathrm{e},K}) \\ &+ \sum_{n=0}^{N-1} \Delta t \sum_{K\in\mathcal{T}} |K| I^{n+1}_{\mathrm{app},K} (v^{n+1}_K + u^{n+1}_{\mathrm{e},K}) \\ &\quad = \sum_{n=0}^{N-1} \Delta t \sum_{K\in\mathcal{T}} \sum_{L\in N(K)} d^*_{\mathrm{e},K,L} \frac{|\sigma_{K,L}|}{d(K,L)} (u^{n+1}_{\mathrm{e},L} - u^{n+1}_{\mathrm{e},K})[(v^{n+1}_L + u^{n+1}_{\mathrm{e},L}) - (v^{n+1}_K + u^{n+1}_{\mathrm{e},K})]. \end{aligned}$$

From the inequality "$a(a-b) \geq \frac{1}{2}(a^2 - b^2)$", we obtain

$$\begin{aligned} F_1 &= \beta c_m \sum_{n=0}^{N-1} \sum_{K\in\mathcal{T}} |K| (v^{n+1}_K - v^n_K) v^{n+1}_K + \sum_{n=0}^{N-1} \sum_{K\in\mathcal{T}} |K| (w^{n+1}_K - w^n_K) w^{n+1}_K \\ &\geq \frac{\beta c_m}{2} \sum_{n=0}^{N-1} \sum_{K\in\mathcal{T}} |K| \left(\left|v^{n+1}_K\right|^2 - |v^n_K|^2 \right) + \frac{1}{2} \sum_{n=0}^{N-1} \sum_{K\in\mathcal{T}} |K| \left(\left|w^{n+1}_K\right|^2 - |w^n_K|^2 \right) \\ &= \frac{\beta c_m}{2} \sum_{K\in\mathcal{T}} |K| \left(\left|v^N_K\right|^2 - \left|v^0_K\right|^2 \right) + \frac{1}{2} \sum_{K\in\mathcal{T}} |K| \left(\left|w^N_K\right|^2 - \left|w^0_K\right|^2 \right). \end{aligned}$$

Then we obtain

$$
\begin{aligned}
&\frac{\beta c_m}{2}\sum_{K\in\mathcal{T}}|K|\left(\left|v_K^N\right|^2-\left|v_K^0\right|^2\right)+\frac{1}{2}\sum_{K\in\mathcal{T}}|K|\left(\left|w_K^N\right|^2-\left|w_K^0\right|^2\right)\\
&\quad+\sum_{K\in\mathcal{T}}\sum_{L\in N(K)}\frac{|\sigma_{K,L}|}{d(K,L)}\left(d^*_{\mathrm{e},K,L}(u^{n+1}_{\mathrm{e},L}-u^{n+1}_{\mathrm{e},K})^2+d^*_{\mathrm{i},K,L}[(v^{n+1}_L+u^{n+1}_{\mathrm{e},L})-(v^{n+1}_K+u^{n+1}_{\mathrm{e},K})]^2\right)\\
&=-\beta\sum_{K\in\mathcal{T}}|K|I^{n+1}_{\mathrm{ion},K}v^{n+1}_K+\sum_{K\in\mathcal{T}}|K|I^{n+1}_{\mathrm{app},K}u^{n+1}_{\mathrm{e},L}+\sum_{K\in\mathcal{T}}|K|H^{n+1}_K w^{n+1}_K\\
&\le\beta C_I\sum_{K\in\mathcal{T}}|K|\left|v_K^{n+1}\right|^2+\frac{C_M}{2C_p^2}\sum_{K\in\mathcal{T}}|K|\left|u^{n+1}_{\mathrm{e},h}\right|^2+C(C_M,C_p)\sum_{K\in\mathcal{T}}|K|\left|I^{n+1}_{\mathrm{app},K}\right|^2\\
&\quad+\frac{b}{2}\sum_{K\in\mathcal{T}}|K|\left|w_K^{n+1}\right|^2+\frac{\beta^2\lambda^2}{2b}\sum_{K\in\mathcal{T}}|K|\left|v_K^{n+1}\right|^2-b\sum_{K\in\mathcal{T}}|K|\left|w_K^{n+1}\right|^2\\
&\quad+\frac{a^2}{2b}\sum_{K\in\mathcal{T}}|K|\left|v_K^{n+1}\right|^2+\frac{b}{2}\sum_{K\in\mathcal{T}}|K|\left|w_K^{n+1}\right|^2\\
&\le(\beta C_I+\frac{\beta^2\lambda^2}{2b}+\frac{a^2}{2b})\sum_{K\in\mathcal{T}}|K|\left|v_K^{n+1}\right|^2+\frac{C_M}{2}\sum_{K\in\mathcal{T}}\sum_{L\in N(K)}\frac{|\sigma_{K,L}|}{d(K,L)}d^*_{\mathrm{e},K,L}(u^{n+1}_{\mathrm{e},L}-u^{n+1}_{\mathrm{e},K})^2\\
&\quad+C(C_M,C_p)\sum_{K\in\mathcal{T}}|K|\left|I^{n+1}_{\mathrm{app},K}\right|^2,
\end{aligned}
\tag{2.39}
$$

which implies

$$
\begin{aligned}
&\frac{\beta c_m}{2}\sum_{K\in\mathcal{T}}|K|\left|v_K^N\right|^2+\frac{1}{2}\sum_{K\in\mathcal{T}}|K|\left|w_K^N\right|^2\\
&\quad\le C(C_M,C_p)\sum_{n=0}^{N-1}\Delta t\sum_{K\in\mathcal{T}}|K|\left|I^{n+1}_{\mathrm{app},K}\right|^2+\sum_{K\in\mathcal{T}}|K|\Big(\frac{\beta c_m}{2}\left|v_K^0\right|^2+\frac{1}{2}\left|w_K^0\right|^2\Big)\\
&\qquad+\Big(\beta C_I+\frac{\beta^2\lambda^2}{2b}+\frac{a^2}{2b}\Big)\sum_{n=0}^{N-1}\Delta t\sum_{K\in\mathcal{T}}|K|\left|v_K^{n+1}\right|^2.
\end{aligned}
\tag{2.40}
$$

Clearly,

$$
\sum_{n=0}^{N-1}\Delta t\sum_{K\in\mathcal{T}}|K|\left|I^{n+1}_{\mathrm{app},K}\right|^2\le\|I_{\mathrm{app}}\|^2_{L^2(Q_T)},
$$

and

$$
\sum_{K\in\mathcal{T}}|K|\Big(\frac{\beta c_m}{2}\left|v_K^0\right|^2+\frac{1}{2}\left|w_K^0\right|^2\Big)\le\frac{\beta c_m}{2}\|v_0\|^2_{L^2(\Omega)}+\frac{1}{2}\|w_0\|^2_{L^2(\Omega)}.
$$

In view of (2.40), this implies the existence of constants $C_4, C_5>0$ such that

$$
\sum_{K\in\mathcal{T}}|K|\left|v_K^N\right|^2\le C_4+C_5\sum_{n=0}^{N-1}\Delta t\sum_{K\in\mathcal{T}}|K|\left|v_K^{n+1}\right|^2.
\tag{2.41}
$$

Note that (2.41) is also true if we replace N by $n_0\in\{1,\dots,N\}$, so we have established

$$
\sum_{K\in\mathcal{T}}|K|\left|v_K^{n_0}\right|^2\le C_4+C_5\sum_{n=0}^{n_0-1}\Delta t\sum_{K\in\mathcal{T}}|K|\left|v_K^{n+1}\right|^2.
\tag{2.42}
$$

By a discrete Gronwall inequality, we obtain from (2.42)

$$\sum_{K\in\mathcal{T}} |K|\,|v_K^{n_0}|^2 \le C_6, \tag{2.43}$$

for any $n_0 \in \{1,\dots,N\}$ and some constant $C_6 > 0$. Then

$$\max_{n\in\{1,\dots,N\}} \sum_{K\in\mathcal{T}} |K|\,|v_K^n|^2 \le C_6.$$

Finally, from (2.40) and (2.43), there exist constants $C_7, C_8 > 0$ such that

$$\max_{n\in\{1,\dots,N\}} \sum_{K\in\mathcal{T}} |K|\,|w_K^n|^2 \le C_7,$$

$$\sum_{n=0}^{N-1} \Delta t \sum_{K\in\mathcal{T}} \Bigg(\sum_{L\in N(K)} \frac{|\sigma_{K,L}|}{d(K,L)} \left| u_{\mathrm{e},K}^{n+1} - u_{\mathrm{e},L}^{n+1} \right|^2 + \sum_{L\in N(K)} \frac{|\sigma_{K,L}|}{d(K,L)} \left| (v_K^{n+1} + u_{\mathrm{e},K}^{n+1}) - (v_L^{n+1} + u_{\mathrm{e},\sigma}^{n+1}) \right|^2 \Bigg) \le C_8.$$

From the previous inequalities it easily follows that

$$0 \le \sum_{n=0}^{N-1} \Delta t \sum_{K\in\mathcal{T}} |K| I_{1,\mathrm{ion}}(v_K^{n+1}) v_K^{n+1} + C_I \sum_{n=0}^{N-1} \Delta t \sum_{K\in\mathcal{T}} |K|\,\left|v_K^{n+1}\right|^2 \le C,$$

for some constant $C > 0$. Using this and (2.36), we get

$$\sum_{n=0}^{N-1} \Delta t \sum_{K\in\mathcal{T}} |K|\,\left| I_{1,\mathrm{ion}}(v_K^{n+1}) v_K^{n+1} \right| \le C', \tag{2.44}$$

for some constant $C' > 0$. Finally, from (1.43) and (2.44), there exists a constant $C_9' > 0$ such that

$$\|v_h\|_{L^4(Q_T)} + \|I_{1,\mathrm{ion}}(v_h)\|_{L^r(Q_T)} \le C_9' \text{ for all } 1 \le r \le 4/3.$$

Before passing to the limit, we derive space and time translation estimates implying that the sequence v_h is relatively compact in $L^2(Q_T)$.

Lemma 2.3.5 *There exists positive a constant $C > 0$ depending on Ω, T, v_0, I_{app} and C_g such that*

$$\iint_{\Omega'\times(0,T)} |v_h(t,x+y) - v_h(t,x)|^2 \, dx\, dt \le C\,|y|\,(|y| + 2h),$$

for all $y \in I\!R^3$ with $\Omega' = \{x \in \Omega,\ [x, x+y] \subset \Omega\}$, and

$$\iint_{\Omega\times(0,T-\tau)} |v_h(t+\tau,x) - v_h(t,x)|^2 \, dx\, dt \le C\tau.$$

for all $\tau \in (0,T)$.

The proof of Lemma (2.3.5) will be omitted since it is similar to that of Lemma 4.3 and Lemma 4.6 in [76] (see also Lemma 6.1 in [13]). The next lemma is a consequence of previously established a priori estimates.

Lemma 2.3.6 *There exists a subsequence of* $\mathbf{u}_h$*, not relabeled, such that, as* $h \to 0$*,*

$$\begin{aligned} &(i)\ \mathbf{u}_h \to \mathbf{u} \text{ weakly in } L^2(Q_T),\\ &(ii)\ v_h \to v \text{ strongly in } L^2(Q_T) \text{ and a.e. in } Q_T,\\ &(iii)\ \nabla_h u_{\mathrm{e},h} \to \nabla u_{\mathrm{e}} \text{ weakly in } (L^2(Q_T))^3. \end{aligned} \tag{2.45}$$

Proof. Claims (i) and (ii) in (2.45) follow from Lemmas 2.3.4 and 2.3.5, for (ii) we also use Kolmogorov's compactness criterion (see, e.g., [24, Theorem IV.25]). The proof of claim (iii) is omitted since it is similar to that of Lemma 4.4 in [44].

Our final goal is to prove that the limit functions v, u_{e}, w constructed in Lemma 2.3.6 constitute a weak solution of (1.37)-(1.39). Let T $\varphi_{\mathrm{e}}, \psi \in \mathcal{D}([0,T)\times\overline{\Omega})$ be such that φ_{e} belong to $(0,T)\times\{x \in \Omega : d(x,\partial\Omega) > h\}$ for a sufficiently small $h > 0$. Observe that

$$\varphi_{\mathrm{e}}(x) = 0 \text{ if } x \in T^{\mathrm{ext}}_{K,\sigma}, \tag{2.46}$$

for all $\sigma \in N_{\mathrm{ext}}(K)$ and $K \in \Omega_h$. We multiply (2.25) by $\Delta t \varphi_{\mathrm{e}}(t^n, x_K)$. Summing the result over K and n yields $c_m T_1 + T_2 + T_3 + T_4 = T_5$, where

$$\begin{aligned} T_1 &:= \sum_{n=0}^{N-1} \sum_{K\in\mathcal{T}} |K|(v_K^{n+1} - v_K^n)\varphi_{\mathrm{e}}(t^n, x_K),\\ T_2 &:= -\sum_{n=0}^{N-1} \Delta t \sum_{K\in\mathcal{T}} \sum_{L\in N(K)} d^*_{\mathrm{e},K,L} \frac{|\sigma_{K,L}|}{d(K,L)} (u^{n+1}_{\mathrm{e},L} - u^{n+1}_{\mathrm{e},K})\varphi_{\mathrm{e}}(t^n, x_K),\\ T_3 &:= \sum_{n=0}^{N-1} \Delta t \sum_{K\in\mathcal{T}} |K| I_{1,\mathrm{ion}}(v_K^{n+1})\varphi_{\mathrm{e}}(t^n, x_K), \quad T_4 := \delta \sum_{n=0}^{N-1} \Delta t \sum_{K\in\mathcal{T}} |K| w_K^{n+1} \varphi_{\mathrm{e}}(t^n, x_K),\\ T_5 &:= \sum_{n=0}^{N-1} \Delta t \sum_{K\in\mathcal{T}} |K| I^{n+1}_{\mathrm{app},K} \varphi_{\mathrm{e}}(t^n, x_K). \end{aligned}$$

To obtain T_2 we have used (2.46). Performing integration-by-parts and keeping in mind that $\varphi_{\mathrm{e}}(T, x_K) = 0$ for all $K \in \mathcal{T}$, we obtain

$$\begin{aligned} T_1 &= -\sum_{n=0}^{N-1} \sum_{K\in\mathcal{T}} |K| v_K^{n+1} (\varphi_{\mathrm{e}}(t^{n+1}, x_K) - \varphi_{\mathrm{e}}(t^n, x_K)) - \sum_{K\in\mathcal{T}} |K| v_K^0 \varphi_{\mathrm{e}}(0, x_K)\\ &= -\sum_{n=0}^{N-1} \sum_{K\in\mathcal{T}} \int_{t^n}^{t^{n+1}} \int_K v_K^{n+1} \partial_t \varphi_{\mathrm{e}}(t, x_K)\, dx\, dt - \sum_{K\in\mathcal{T}} \int_K v_0(x)\varphi_{\mathrm{e}}(0, x_K)\, dx =: -T_{1,1} - T_{1,2}. \end{aligned}$$

Let us also introduce

$$T_1^* = -\sum_{n=0}^{N-1} \sum_{K\in\mathcal{T}} \int_{t^n}^{t^{n+1}} \int_K v_K^{n+1} \partial_t \varphi_{\mathrm{e}}(t, x)\, dx\, dt - \int_\Omega v_0(x)\varphi_{\mathrm{e}}(0, x)\, dx =: -T^*_{1,1} - T^*_{1,2}.$$

Then

$$T_{1,2} - T^*_{1,2} = \sum_{K\in\mathcal{T}} \int_K v_0(x)(\varphi_{\mathrm{e}}(0, x_K) - \varphi_{\mathrm{e}}(0, x))\, dx.$$

By the regularity of φ_{e}, there exists a positive constant C such that $|\varphi_{\mathrm{e}}(0,x_K)-\varphi_{\mathrm{e}}(0,x)|\le Ch$. This implies

$$\left|T_{1,2}-T_{1,2}^*\right|\le Ch\sum_{K\in\mathcal{T}}\int_K|v_0(x)|\,dx. \tag{2.47}$$

Sending $h\to 0$ in (2.47) we arrive at $\lim_{h\to 0}\left|T_{1,2}-T_{1,2}^*\right|=0$. Next, note that

$$T_{1,1}-T_{1,1}^*=\sum_{n=0}^{N-1}\sum_{K\in\mathcal{T}}v_K^{n+1}\int_{t^n}^{t^{n+1}}\int_K\Big(\partial_t\varphi_{\mathrm{e}}(t,x_K)-\partial_t\varphi_{\mathrm{e}}(t,x)\Big)\,dx\,dt,$$

and hence from the regularity of $\partial_t\varphi_{\mathrm{e}}$ and Hölder's inequality, we obtain

$$\left|T_{1,1}-T_{1,1}^*\right|\le C(h)\left(\sum_{n=0}^{N-1}\Delta t\sum_{K\in\mathcal{T}}|K|\left|v_K^{n+1}\right|^2\right)^{1/2},$$

where $C(h)>0$ is a function satisfying $C(h)\to 0$ as $h\to 0$. In view of (2.3.4), we conclude that $\lim_{h\to 0}\left|T_{1,1}-T_{1,1}^*\right|=0$. Continuing, we define I_D and T_2^* by

$$I_D:=\int_0^T\int_\Omega\mathbf{M}_{\mathrm{e}}(x)\nabla u_{\mathrm{e}}\cdot\nabla\varphi_{\mathrm{e}}\,dx\,dt,\quad T_2^*:=\int_0^T\int_\Omega u_{\mathrm{e},h}\mathrm{div}\,(\mathbf{M}_{\mathrm{e}}(x)\nabla\varphi_{\mathrm{e}})\,dx\,dt.$$

Integration by parts yields

$$I_D=-\int_0^T\int_\Omega u_{\mathrm{e}}\mathrm{div}\,(\mathbf{M}_{\mathrm{e}}\nabla\varphi_{\mathrm{e}})\,dx\,dt,$$

and then we see that $T_2^*\to -I_D\quad$ as $h\to 0$. Now, notice that

$$\begin{aligned}T_2^*&=\sum_{n=0}^{N-1}\sum_{K\in\mathcal{T}}\sum_{L\in N(K)}u_{\mathrm{e},K}^{n+1}\int_{t_n}^{t_{n+1}}\int_{\sigma_{K,L}}\mathbf{M}_{\mathrm{e}}(x)\nabla\varphi_{\mathrm{e}}\cdot\eta_{K,L}d\gamma\\&=-\frac{1}{2}\sum_{n=0}^{N-1}\sum_{K\in\mathcal{T}}\sum_{L\in N(K)}(u_{\mathrm{e},L}^{n+1}-u_{\mathrm{e},K}^{n+1})\int_{t_n}^{t_{n+1}}\int_{\sigma_{K,L}}\mathbf{M}_{\mathrm{e}}(x)\nabla\varphi_{\mathrm{e}}\cdot\eta_{K,L}d\gamma,\end{aligned}$$

and

$$\begin{aligned}T_2&=-\sum_{n=0}^{N-1}\Delta t\sum_{K\in\mathcal{T}}\sum_{L\in N(K)}d_{\mathrm{e},K,L}^*|\sigma_{K,L}|\frac{u_{\mathrm{e},L}^{n+1}-u_{\mathrm{e},K}^{n+1}}{d(K,L)}\varphi_{\mathrm{e}}(t^n,x_K)\\&=\frac{1}{2}\sum_{n=0}^{N-1}\Delta t\sum_{K\in\mathcal{T}}\sum_{L\in N(K)}d_{\mathrm{e},K,L}^*\frac{|\sigma_{K,L}|}{d(K,L)}(u_{\mathrm{e},L}^{n+1}-u_{\mathrm{e},K}^{n+1})(\varphi_{\mathrm{e}}(t^n,x_L)-\varphi_{\mathrm{e}}(t^n,x_K)).\end{aligned}$$

Therefore

$$\begin{aligned}T_2+T_2^*&=\frac{1}{2}\sum_{n=0}^{N-1}\sum_{K\in\mathcal{T}}\sum_{L\in N(K)}|\sigma_{K,L}|(u_{\mathrm{e},L}^{n+1}-u_{\mathrm{e},K}^{n+1})\\&\times\left(\int_{t_n}^{t_{n+1}}d_{\mathrm{e},K,L}^*\frac{\varphi_{\mathrm{e}}(t^n,x_L)-\varphi_{\mathrm{e}}(t^n,x_K)}{d(K,L)}-\frac{1}{|\sigma_{K,L}|}\int_{t_n}^{t_{n+1}}\int_{\sigma_{K,L}}\mathbf{M}_{\mathrm{e}}(x)\nabla\varphi_{\mathrm{e}}\cdot\eta_{K,L}d\gamma\right).\end{aligned}$$

Since the line $[x_K, x_L]$ is orthogonal to $\sigma_{K,L}$, we have $x_K - x_L = d(K,L)\eta_{K,L}$. This implies from the regularity of φ_{e} that

$$\frac{\varphi_{\mathrm{e}}(t^n, x_L) - \varphi_{\mathrm{e}}(t^n, x_K)}{d(K,L)} \equiv \nabla\varphi_{\mathrm{e}}(t^n, x) \cdot \eta_{K,L},$$

for some $x \in [x_K, x_L]$, and then

$$\left| \int_{t_n}^{t_{n+1}} d^*_{\mathrm{e},K,L} \frac{\varphi_{\mathrm{e}}(t^n, x_L) - \varphi_{\mathrm{e}}(t^n, x_K)}{d(K,L)} - \frac{1}{|\sigma_{K,L}|} \int_{t_n}^{t_{n+1}} \int_{\sigma_{K,L}} \mathbf{M}_{\mathrm{e}}(x) \nabla\varphi_{\mathrm{e}} \cdot \eta_{K,L} d\gamma \right| \leq C\Delta t\, h, \tag{2.48}$$

for some constant $C > 0$. Using (2.48) and (2.37), we deduce

$$\lim_{h\to 0} T_2 = -\int_0^T \int_\Omega u_{\mathrm{e}} \mathrm{div}\,(\mathbf{M}_{\mathrm{e}}(x)\nabla\varphi_{\mathrm{e}})\, dx\, dt = \int_0^T \int_\Omega \mathbf{M}_{\mathrm{e}}(x)\nabla u_{\mathrm{e}} \cdot \nabla\varphi_{\mathrm{e}}\, dx\, dt.$$

Next, we would like to show that

$$\lim_{h\to 0} T_3 = \int_0^T \int_\Omega I_{1,\mathrm{ion}}(v)\varphi_{\mathrm{e}}\, dx\, dt.$$

For this purpose, we introduce

$$T_{3,1} := \sum_{n=0}^{N-1} \sum_{K\in\mathcal{T}} I_{1,\mathrm{ion}}(v_K^{n+1}) \int_{t^n}^{t^{n+1}} \int_K \Big(\varphi_{\mathrm{e}}(t^n, x_K) - \varphi_{\mathrm{e}}(t,x)\Big)\, dx\, dt,$$

and

$$T_{3,2} := \sum_{n=0}^{N-1} \sum_{K\in\mathcal{T}} \int_{t^n}^{t^{n+1}} \int_K \Big(I_{1,\mathrm{ion}}(v_K^{n+1}) - I_{1,\mathrm{ion}}(v)\Big)\varphi_{\mathrm{e}}(t,x)\, dx\, dt.$$

We have for all $x \in K$ and $t \in [t^n, t^{n+1}]$ that

$$|\varphi_{\mathrm{e}}(t^n, x_K) - \varphi_{\mathrm{e}}(t,x)| \leq C(\Delta t + h), \tag{2.49}$$

and thus, thanks to (2.38),

$$|T_{3,1}| \leq C(\Delta t + h) \sum_{n=0}^{N-1} \Delta t \sum_{K\in\mathcal{T}} |K| \left|I_{1,\mathrm{ion}}(v_K^{n+1})\right| \leq C(\Delta t + h).$$

Hence, $T_{3,1} \to 0$ as $h \to 0$. We also have

$$|T_{3,2}| \leq C \int_0^T \int_\Omega |I_{1,\mathrm{ion}}(v_h) - I_{1,\mathrm{ion}}(v)|\, dx\, dt.$$

By Lemma 2.3.4, $I_{1,\mathrm{ion}}(v_h)$ is bounded in $L^{4/3}(Q_T)$, so

$$I_{1,\mathrm{ion}}(v_h) \to I_{1,\mathrm{ion}}(v) \text{ strongly in } L^q(Q_T) \text{ for } q \in [1, 4/3),$$

and therefore $|T_{3,2}|$ tends to zero as $h \to 0$.

Let

$$T_{4,1} := \delta \sum_{n=0}^{N-1} \sum_{K\in\mathcal{T}} w_K^{n+1} \int_{t^n}^{t^{n+1}} \int_K \Big(\varphi_{\mathrm{e}}(t^n, x_K) - \varphi_{\mathrm{e}}(t,x)\Big)\, dx\, dt,$$

and

$$T_{4,2} := \delta \sum_{n=0}^{N-1} \sum_{K\in\mathcal{T}} \int_{t^n}^{t^{n+1}} \int_K \Big(w_K^{n+1} - w\Big)\varphi_{\mathrm{e}}(t,x)\,dx\,dt.$$

From (2.36), we have

$$|T_{4,1}| \le C(\Delta t + h) \sum_{n=0}^{N-1} \Delta t \sum_{K\in\mathcal{T}} |K| \left|w_K^{n+1}\right| \le C(\Delta t + h),$$

and

$$|T_{4,2}| := \delta \int_0^T \int_\Omega \Big(w_K^{n+1} - w\Big)\varphi_{\mathrm{e}}(t,x)\,dx\,dt.$$

Since $w_h \to w$ weakly in $L^2(Q_T)$ as $h \to 0$,

$$\lim_{h\to 0} T_4 = \int_0^T \int_\Omega w\varphi_{\mathrm{e}}\,dx\,dt.$$

It remains to prove that

$$\lim_{h\to 0} T_5 = \int_0^T \int_\Omega I_{\mathrm{app}}\varphi_{\mathrm{e}}\,dx\,dt.$$

To this end, we set

$$T_{5,1} = \sum_{n=0}^{N-1} \sum_{K\in\mathcal{T}} I_{\mathrm{app},K}^{n+1} \int_{t^n}^{t^{n+1}} \int_K \Big(\varphi_{\mathrm{e}}(t^n, x_K) - \varphi_{\mathrm{e}}(t,x)\Big)\,dx\,dt,$$

and

$$T_{5,2} := \sum_{n=0}^{N-1} \sum_{K\in\mathcal{T}} \int_{t^n}^{t^{n+1}} \int_K \Big(I_{\mathrm{app},K}^{n+1} - I_{\mathrm{app}}\Big)\varphi_{\mathrm{e}}(t,x)\,dx\,dt.$$

Since $I_{\mathrm{app}} \in L^2(Q_T)$, we deduce from (2.49) and the L^1 convergence of the piecewise constant $I_{\mathrm{app},K}^{n+1}$ to I_{app} that

$$\lim_{h\to 0} T_{5,1} = 0, \qquad \lim_{h\to 0} T_{5,2} = 0.$$

Reasoning along the same as above, we conclude that (1.44) holds and this proves the theorem.

2.4 A doubly nonlinear chemotaxis model

Firstly we describe a finite volume method using Cartesian meshes. If we integrate the corresponding equations, average over Ω_{ij} and discretize, we obtain the following interior marching formula:

$$\begin{aligned}
\bar{u}_{ij}^{n+1} &= \bar{u}_{ij}^n + \frac{\Delta t}{\Delta x_i^2}\big(\delta_x^+(P_{i-1/2,j}\delta_x^-\bar{u}_{ij})\big) + \frac{\Delta t}{\Delta y_j^2}\big(\delta_y^+(P_{i,j-1/2}\delta_y^-\bar{u}_{ij})\big) \\
&\quad + \frac{\Delta t}{\Delta x_i^2}\big(\delta_x^+(Q_{i-1/2,j}\delta_x^-\bar{v}_{ij})\big) + \frac{\Delta t}{\Delta y_j^2}\big(\delta_y^+ Q_{i,j-1/2}\delta_y^-\bar{v}_{ij})\big), \\
\bar{v}_{ij}^{n+1} &= \bar{v}_{ij}^n + \Delta t h(\bar{u}_{ij}^n, \bar{v}_{ij}^n) + \frac{d\Delta t}{\Delta x_i^2}\delta_x^+\delta_x^-\bar{v}_{ij} + \frac{d\Delta t}{\Delta y_j^2}\delta_y^+\delta_y^-\bar{v}_{ij},
\end{aligned}$$

where $P_{l,m}$ and $Q_{l,m}$ are centered discretizations of $\hat{P}(u) := a(u)|\nabla u|^{p-2}$ and $\hat{Q}(u) := \chi(u)u\,f(u)$ respectively:

$$
\begin{aligned}
P_{i,j+1/2} &:= \frac{1}{2}\big(a(\bar{u}_{ij})R(\bar{u}_{ij},\bar{u}_{i+1,j},\bar{u}_{i,j+1}) + a(\bar{u}_{i,j+1})R(\bar{u}_{i,j+1},\bar{u}_{i+1,j+1},\bar{u}_{i,j+2})\big),\\
P_{i+1/2,j} &:= \frac{1}{2}\big(a(\bar{u}_{ij})R(\bar{u}_{ij},\bar{u}_{i+1,j},\bar{u}_{i,j+1}) + a(\bar{u}_{i+1,j})R(\bar{u}_{i+1,j},\bar{u}_{i+2,j},\bar{u}_{i+1,j+1})\big),\\
Q_{i,j+1/2} &:= \frac{1}{2}\big(\chi(\bar{u}_{ij})\bar{u}_{ij}f(\bar{u}_{ij}) + \chi(\bar{u}_{i,j+1})\bar{u}_{i,j+1}f(\bar{u}_{i,j+1})\big),\\
Q_{i+1/2,j} &:= \frac{1}{2}\big(\chi(\bar{u}_{ij})\bar{u}_{ij}f(\bar{u}_{ij}) + \chi(\bar{u}_{i+1,j})\bar{u}_{i+1,j}f(\bar{u}_{i+1,j})\big).
\end{aligned}
$$

We discretize the norm of the gradient of the solution by forward differences, which keep the stability of the scheme (see [80]):

$$
|\nabla\bar{u}|^{p-2} \approx R(\bar{u}_{ij},\bar{u}_{i+1,j},\bar{u}_{i,j+1}) := \left(\frac{(\bar{u}_{i+1,j}-\bar{u}_{ij})^2}{\Delta x_{i+1/2}^2} + \frac{(\bar{u}_{i,j+1}-\bar{u}_{ij})^2}{\Delta y_{j+1/2}^2}\right)^{(p-2)/2}.
$$

Finally we give another formulation in the more general setting of arbitrary meshes (recall the description in Section 2.3.2). We define for all $\sigma \in \mathcal{E}$, the transmissibility coefficient as

$$
\tau_\sigma = \begin{cases} \dfrac{|\sigma|}{d(x_K,x_L)} & \text{for } \sigma \in \mathcal{E}_{\text{int}}(K),\ \sigma = K|L,\\[2ex] \dfrac{|\sigma|}{d(x_K,\sigma)} & \text{for } \sigma \in \mathcal{E}_{\text{ext}}(K), \end{cases}
$$

also define cell averages of the unknowns $A(u)$, $f(u)$ and $g(u,v)$ over $K \in \mathcal{T}$:

$$
A_K^{n+1} := \frac{1}{\Delta t|K|}\int_{t^n}^{t^{n+1}}\int_K A\big(u(x,t)\big)\,dx\,dt, \quad g_K^{n+1} := \frac{1}{\Delta t|K|}\int_{t^n}^{t^{n+1}}\int_K g\big(u(x,t),v(x,t)\big)\,dx\,dt,
$$
$$
f_K^{n+1} := \frac{1}{\Delta t|K|}\int_{t^n}^{t^{n+1}}\int_K f\big(u(x,t)\big)\,dx\,dt,
$$

and the initial conditions are discretized by

$$
u_K^0 = \frac{1}{|K|}\int_K u_0(x)\,dx, \quad v_K^0 = \frac{1}{|K|}\int_K v_0(x)\,dx.
$$

We now give the finite volume scheme employed to advance the numerical solution from t^n to t^{n+1}, which is based on a simple explicit Euler time discretization. Assuming that at $t = t^n$, the pairs (u_K^n, v_K^n) are known for all $K \in \mathcal{T}$, we compute (u_K^{n+1}, v_K^{n+1}) from

$$
\begin{aligned}
|K|\frac{u_K^{n+1}-u_K^n}{\Delta t} &= \sum_{\sigma\in\mathcal{E}(K)} \tau_\sigma \left|\nabla_h A_{K,\sigma}^n\right|_h^{p-2} \nabla_h A_{K,\sigma}^n\\
&\quad + \chi \sum_{\sigma\in\mathcal{E}(K)} \tau_\sigma \left[\left(\nabla_h v_{K,\sigma}^n\right)^+ u_K^n f_K^n - \left(\nabla_h v_{K,\sigma}^n\right)^- u_L^n f_L^n\right],\\
|K|\frac{v_K^{n+1}-v_K^n}{\Delta t} &= \sum_{\sigma\in\mathcal{E}(K)} \tau_\sigma \nabla_h v_{K,\sigma}^n + |K| g_K^n.
\end{aligned}
$$

Here $|\cdot|_h$ denotes the discrete Euclidean norm. Additionally, the Neumann boundary conditions are taken into account by imposing zero fluxes on the external edges.

Chapter 3

Multiresolution and wavelets

In this Chapter we summarize the relevant material on multiresolution techniques. They were first introduced by Harten [87] to improve the performance of schemes for one-dimensional conservation laws. Later on, these original ideas were extended to several kinds of related problems leading finally to the concept of fully adaptive multiresolution schemes [53, 62, 118, 134]. The basic aim of this approach is to accelerate a given finite volume scheme on a uniform grid at the cost of an at most controllable loss of accuracy, that is, the accelerated scheme should be of the same order than the original one. The principle of the multiresolution analysis is to represent a set of data given on a fine grid as values on a coarser grid plus a series of differences, called *details*, at different levels of nested dyadic grids. These differences contain information on the local regularity of the solution. An appealing feature of this data representation is that these details are small in regions where the solution is smooth. By thresholding small details (cells whose coefficients are smaller than a prescribed tolerance are removed), a locally refined adaptive grid is defined. This threshold is chosen such that the discretization error of the reference scheme is balanced with the accumulated thresholding error introduced in each time step. Significant speed-up of the computation and data compression is achieved for long-time evolution problems, large systems, multidimensional domains, and solutions with sharp fronts.

3.1 Wavelet basis and detail coefficients

3.1.1 The one-dimensional case

The following description is based on a standard approach which for sake of completeness we outline herein. For further details on the one-dimensional theory, we refer to the fairly complete description in [118].

Let us consider the simple domain $\Omega = [-H/2, H/2]$ in which we determine a mesh hierarchy by a dyadic partition of Ω: $V_{lk} = [-H/2 + 2^{-l}k, -H/2 + 2^{-l}(k+1)]$, $k \in I_l = \{0, \ldots, 2^l - 1\}$ (a sketch is presented in Figure 3.1).

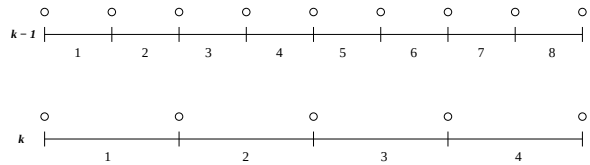

Figure 3.1: *Sequence of nested grids.*

The refinement sets are $\mathcal{M}_{lk} = \{2k, 2k+1\}$. The level box function is given by

$$\tilde{\varphi}_{lk} = 2^l \chi_{[0,1]}(2^l \cdot -k),$$

and there is a two-levels relation of the form

$$\tilde{\varphi}_{lk} = \frac{1}{2}(\tilde{\varphi}_{l+1,2k} + \tilde{\varphi}_{l+1,2k+1}), \quad \hat{u}_{lk} = \frac{1}{2}(\hat{u}_{l+1,2k} + \hat{u}_{l+1,2k+1}). \tag{3.1}$$

By introducing the wavelet function and the corresponding detail coefficients as

$$\tilde{\psi}_{lk} := \frac{1}{2}(\tilde{\varphi}_{l+1,2k} - \tilde{\varphi}_{l+1,2k+1}), \quad d_{lk} := \langle u, \tilde{\psi}_{lk}\rangle_{[0,1]} = \frac{1}{2}(\hat{u}_{l+1,2k} - \hat{u}_{l+1,2k+1}),$$

every box function on the level $l+1$ may be written in function of $\tilde{\varphi}_{lk}$ a nd $\tilde{\psi}_{lk}$ using

$$\tilde{\varphi}_{l+1,2k} = \tilde{\varphi}_{lk} + \tilde{\psi}_{lk}, \quad \tilde{\varphi}_{l+1,2k+1} = \tilde{\varphi}_{lk} - \tilde{\psi}_{lk}, \tag{3.2}$$

and in the same fashion, the relation holds for the cell averages:

$$\hat{u}_{l+1,2k} = \hat{u}_{l,k} + d_{lk}, \quad \hat{u}_{l+1,2k+1} = \hat{u}_{l,k} - d_{lk}.$$

For sake of notation, we write $\tilde{\Phi}_l := (\tilde{\varphi}_{lk})_{k\in I_l}$ and $\tilde{\Psi}_l := (\tilde{\psi}_{lk})_{k\in I_l}$. Then, for instance,

$$\tilde{\Phi}_0 = \tilde{\varphi}_{01}, \quad \tilde{\Phi}_1 = \begin{pmatrix} \tilde{\varphi}_{11} \\ \tilde{\varphi}_{12} \end{pmatrix}, \quad \tilde{\Phi}_2 = \begin{pmatrix} \tilde{\varphi}_{21} \\ \tilde{\varphi}_{22} \\ \tilde{\varphi}_{23} \\ \tilde{\varphi}_{24} \end{pmatrix}, \quad \tilde{\Phi}_3 = \begin{pmatrix} \tilde{\varphi}_{31} \\ \tilde{\varphi}_{32} \\ \vdots \\ \tilde{\varphi}_{37} \\ \tilde{\varphi}_{38} \end{pmatrix}, \text{ etc.}$$

In this notation, (3.1) reads

$$\tilde{\Phi}_l^T = \tilde{\Phi}_{l+1}^T \tilde{\mathbf{M}}_{l,0}, \quad \tilde{\Psi}_l^T = \tilde{\Phi}_{l+1}^T \tilde{\mathbf{M}}_{l,1}$$

where $\tilde{\mathbf{M}}_{l,0}$ and $\tilde{\mathbf{M}}_{l,1}$ are mask matrices formed by the coefficients in (3.1). For instance,

$$\tilde{\mathbf{M}}_{1,0} = \begin{pmatrix} \frac{1}{2} & 0 \\ \frac{1}{2} & 0 \\ 0 & \frac{1}{2} \\ 0 & \frac{1}{2} \end{pmatrix}, \quad \tilde{\mathbf{M}}_{1,1} = \begin{pmatrix} \frac{1}{2} & 0 \\ -\frac{1}{2} & 0 \\ 0 & \frac{1}{2} \\ 0 & -\frac{1}{2} \end{pmatrix}, \quad \tilde{\mathbf{M}}_{2,0} = \begin{pmatrix} \frac{1}{2} & 0 & 0 & 0 \\ \frac{1}{2} & 0 & 0 & 0 \\ 0 & \frac{1}{2} & 0 & 0 \\ 0 & \frac{1}{2} & 0 & 0 \\ 0 & 0 & \frac{1}{2} & 0 \\ 0 & 0 & \frac{1}{2} & 0 \\ 0 & 0 & 0 & \frac{1}{2} \\ 0 & 0 & 0 & \frac{1}{2} \end{pmatrix}, \text{ etc.}$$

Analogously, (3.2) reads

$$\tilde{\Phi}_{l+1}^T = \tilde{\Phi}_l^T \tilde{\mathbf{G}}_{l,0} + \tilde{\Psi}_l^T \tilde{\mathbf{G}}_{l,1},$$

where $\tilde{\mathbf{G}}_{l,i} := 2\tilde{\mathbf{M}}_{l,i}^T$, $i = 0, 1$ are the mask matrices, and for instance

$$\tilde{\mathbf{G}}_{1,0} = \begin{pmatrix} 1 & 1 & 0 & 0 \\ 0 & 0 & 1 & 1 \end{pmatrix}, \quad \tilde{\mathbf{G}}_{1,1} = \begin{pmatrix} 1 & -1 & 0 & 0 \\ 0 & 0 & 1 & -1 \end{pmatrix}, \text{ etc.}$$

Notice that the matrices

$$\tilde{\mathbf{M}}_l := [\tilde{\mathbf{M}}_{l,0}\ \tilde{\mathbf{M}}_{l,1}], \quad \tilde{\mathbf{G}}_l := [\tilde{\mathbf{G}}_{l,0}^T\ \tilde{\mathbf{G}}_{l,1}^T]^T \tag{3.3}$$

are invertible. For example,

$$\tilde{\mathbf{M}}_1 = \begin{pmatrix} \frac{1}{2} & 0 & \frac{1}{2} & 0 \\ \frac{1}{2} & 0 & -\frac{1}{2} & 0 \\ 0 & \frac{1}{2} & 0 & \frac{1}{2} \\ 0 & \frac{1}{2} & 0 & -\frac{1}{2} \end{pmatrix}, \quad \tilde{\mathbf{G}}_1 = \tilde{\mathbf{M}}_1^{-1} = \begin{pmatrix} 1 & 0 & 1 & 0 \\ 1 & 0 & -1 & 0 \\ 0 & 1 & 0 & 1 \\ 0 & 1 & 0 & -1 \end{pmatrix}, \text{etc.}$$

Therefore we have

$$\tilde{\mathbf{M}}_{l,0}\tilde{\mathbf{G}}_{l,0} + \tilde{\mathbf{M}}_{l,1}\tilde{\mathbf{G}}_{l,1} = \mathbf{I}, \quad \tilde{\mathbf{G}}_{l,i}\tilde{\mathbf{M}}_{l,i'} = \delta_{i,i'}\mathbf{I}, \quad i, i' \in \{0, 1\}.$$

Let us define the dual system

$$\varphi_{lk} := 2^{-l}\tilde{\varphi}_{lk}, \quad \psi_{lk} := 2^{-l}\tilde{\psi}_{lk},$$

or more concisely $\Phi_l := 2^{-l}\tilde{\Phi}_l$ and $\Psi_l := 2^{-l}\tilde{\Psi}_l$. These elements correspond to the L^∞-normalized counterpart of $\tilde{\varphi}_{lk}$ and $\tilde{\psi}_{lk}$ respectively; and therefore they also satisfy two-levels relations similar to (3.1)-(3.3). It can be shown that $\tilde{\Phi}_l \cup \tilde{\Psi}_l$ and $\Phi_l \cup \Psi_l$ are biorthogonal, i.e.,

$$\begin{array}{rclcl} \langle \Phi_l, \tilde{\Phi}_l \rangle_{[0,1]} & = & \langle \Psi_l, \tilde{\Psi}_l \rangle_{[0,1]} & = & \mathbf{I}, \\ \langle \Phi_l, \tilde{\Psi}_l \rangle_{[0,1]} & = & \langle \Psi_l, \tilde{\Phi}_l \rangle_{[0,1]} & = & \Theta. \end{array}$$

Let

$$u_l := \sum_{k \in I_l} \langle u, \tilde{\varphi}_{l,k} \rangle_{[0,1]} \varphi_{l,k} =: \Phi_l^T \hat{\mathbf{u}}_l,$$

be the projection of u over the constant functions at level l, or

$$u_l = \Phi_{l-1}^T \hat{\mathbf{u}}_{l-1} + \Psi_{l-1}^T \mathbf{d}_{l-1}.$$

This representation motivates the interpretation of detail coefficients as the updating when going from a coarse to a finer level.

The magnitude of the detail coefficients decrease where the solution is smooth. For constant u, we have

$$\langle 1, \tilde{\psi}_{l,k} \rangle_{[0,1]} = 0.$$

In addition, $\|\tilde{\psi}_{l,k}\|_{L^1([0,1])} = 1$ yields

$$|d_{l,k}| \leqslant \inf_{c \in \mathbb{R}} |\langle u - c, \tilde{\psi}_{l,k} \rangle_{[0,1]}| \leqslant \inf_{c \in \mathbb{R}} \|u - c\|_{L^\infty(V_{l,k})} \leqslant C 2^{-l} \|u'\|_{L^\infty(V_{l,k})}.$$

From this relation we see that details decrease at a rate greater than 2^{-l} (in the case that u is differentiable) and this fact motivates the discarding of information corresponding to sufficiently small details in order to compress data. In our particular case we have a biorthogonal system of higher order, which allows to write

$$\langle p, \tilde{\psi}_{l,k}\rangle_{[0,1]} = 0, \quad p \in \mathbb{P}^k.$$

Now we transform a vector with cell averages over the finest level, into *something else* in order to obtain data compression. Therefore, using the mask matrices (3.3), we obtain

$$\hat{\mathbf{u}}_{l+1} = \mathbf{G}_l \begin{pmatrix} \hat{\mathbf{u}}_l \\ \mathbf{d}_l \end{pmatrix}, \quad \begin{pmatrix} \hat{\mathbf{u}}_l \\ \mathbf{d}_l \end{pmatrix} = \mathbf{M}_l \hat{\mathbf{u}}_{l+1}.$$

By applying this relations iteratively, $hat\mathbf{u}_L$ may be decomposed into a sequence of cell averages over coarse levels and the corresponding detail coefficients.

3.1.2 A two-dimensional extension

The extension of the standard one-dimensional multiresolution analysis to the two-dimensional case is carried out by using a tensorial product approach in Cartesian meshes. Consider a rectangle which after a change of variables can be regarded as $\Omega = [0,1]^2$. We determine a nested mesh hierarchy $\Lambda_0 \subset \cdots \subset \Lambda_L$, using an uniform dyadic partition of Ω. Here each grid $\Lambda_l := \{V_{(i,j),l}\}_{(i,j)}$, with (i,j) to be defined, is formed by the control volumes in each level $V_{(i,j),l} := 2^{-l}[i,i+1] \times [j,j+1]$, $i,j \in I_l = \{0,\ldots,2^l-1\}$, $l = 0,\ldots,L$. Here, $l = 0$ corresponds to the coarsest and $l = L$ to the finest level. The nestedness of the grid hierarchy is determined by the refinement sets $\mathcal{M}_{(i,j),l} = \{2(i,j) + \mathbf{e}\}$, $\mathbf{e} \in E := \{0,1\}^2$ and $\#\mathcal{M}_{(i,j),l} = 4$. For each level $l = 0,\ldots,L$, the *level box function* is defined as

$$\tilde{\varphi}_{(i,j),l}(x) := \frac{1}{|V_{(i,j),l}|}\chi_{V_{(i,j),l}}(x) = 2^{2l}\chi_{[0,1]^2}(2^l x_1 - i, 2^l x_2 - j),$$

and the averages of any function $u(\cdot,t) \in L^1(\Omega)$ for the cell (i,j) at level l can be expressed equivalently as in (2.18) as the inner product

$$\bar{u}_{(i,j),l} := \left\langle u, \tilde{\varphi}_{(i,j),l}\right\rangle_{L^1(\Omega)}$$

After these preliminaries, we can define a two–levels relation for cell averages and box functions

$$\begin{aligned}
\tilde{\varphi}_{(i,j),l} &= \sum_{\mathbf{r}\in\mathcal{M}_{(i,j),l}} \frac{|V_{\mathbf{r},l+1}|}{|V_{(i,j),l}|}\tilde{\varphi}_{\mathbf{r},l+1} \\
&= \frac{1}{4}\left(\tilde{\varphi}_{2(i,j),l+1} + \tilde{\varphi}_{(2i,2j+1),l+1} + \tilde{\varphi}_{(2i+1,2j),l+1} + \tilde{\varphi}_{(2i+1,2j+1),l+1}\right), \\
\bar{u}_{(i,j),l} &= \sum_{\mathbf{r}\in\mathcal{M}_{(i,j),l}} \frac{|V_{\mathbf{r},l+1}|}{|V_{(i,j),l}|}\bar{u}_{\mathbf{r},l+1} \\
&= \frac{1}{4}(\bar{u}_{2(i,j),l+1} + \bar{u}_{(2i,2j+1),l+1} + \bar{u}_{(2i+1,2j),l+1} + \bar{u}_{(2i+1,2j+1),l+1}).
\end{aligned} \tag{3.4a}$$

This relation defines a *projection* operator, which allows us to move from finer to coarser levels. For $x \in V_{2(i,j)+\mathbf{r}a,l+1}$ with $\mathbf{r}a \in E$, we define the *wavelet function* depending on the box functions on a finer level

$$\tilde{\psi}_{(i,j),\mathbf{e},l}(x) := 2^2\tilde{\varphi}_{2(i,j)+\mathbf{r}a,l+1}(x).$$

Therefore

$$\begin{aligned}\tilde{\psi}_{(i,j),\mathbf{e},l} &= \sum_{\mathbf{r}a\in E} 2^{-2}(-1)^{\mathbf{r}a\cdot\mathbf{e}}\tilde{\varphi}_{2(i,j)+\mathbf{r}a,l+1}\\ &= \sum_{\mathbf{r}\in\mathcal{M}_{(i,j),l}} \frac{|V_{\mathbf{r}=2(i,j)+\mathbf{r}a,l+1}|}{|V_{(i,j),l}|}(-1)^{\mathbf{r}a\cdot\mathbf{e}}\tilde{\varphi}_{\mathbf{r},l+1}.\end{aligned}$$

In contrast to the one-dimensional case, the number of related wavelets is $\#\mathcal{M}_{(i,j),l}-1=3$. Furthermore, since $\mathbf{r}\cdot\mathbf{e}\in\{0,1,2\}$ for $\mathbf{r},\mathbf{e}\in E$, we have for instance that

$$\tilde{\psi}_{(i,j),(1,0),l} = \frac{1}{4}\left(\tilde{\varphi}_{2(i,j),l+1}+\tilde{\varphi}_{2(i,j)+(0,1),l+1}-\tilde{\varphi}_{2(i,j)+(1,0),l+1}-\tilde{\varphi}_{2(i,j)+(1,1),l+1}\right).$$

Repeating the same relation for all $\mathbf{e}\in E^* := E\setminus\{(0,0)\}$, we end up with the system

$$\begin{pmatrix} \frac14 & -\frac14 & \frac14 & -\frac14\\ \frac14 & \frac14 & -\frac14 & -\frac14\\ \frac14 & -\frac14 & -\frac14 & \frac14\\ \frac14 & \frac14 & \frac14 & \frac14\end{pmatrix}\begin{pmatrix}\tilde{\varphi}_{l+1,2(i,j)}\\ \tilde{\varphi}_{l+1,2(i,j)+(0,1)}\\ \tilde{\varphi}_{l+1,2(i,j)+(1,0)}\\ \tilde{\varphi}_{l+1,2(i,j)+(1,1)}\end{pmatrix} = \begin{pmatrix}\tilde{\psi}_{l,(i,j),(0,1)}\\ \tilde{\psi}_{l,(i,j),(1,0)}\\ \tilde{\psi}_{l,(i,j),(1,1)}\\ \tilde{\varphi}_{l,(i,j)}\end{pmatrix},$$

where the solution

$$\begin{pmatrix}\tilde{\varphi}_{l+1,2(i,j)}\\ \tilde{\varphi}_{l+1,2(i,j)+(0,1)}\\ \tilde{\varphi}_{l+1,2(i,j)+(1,0)}\\ \tilde{\varphi}_{l+1,2(i,j)+(1,1)}\end{pmatrix} = \begin{pmatrix} 1 & 1 & 1 & 1\\ -1 & 1 & -1 & 1\\ 1 & -1 & -1 & 1\\ -1 & -1 & 1 & 1\end{pmatrix}\begin{pmatrix}\tilde{\psi}_{l,(i,j),(0,1)}\\ \tilde{\psi}_{l,(i,j),(1,0)}\\ \tilde{\psi}_{l,(i,j),(1,1)}\\ \tilde{\varphi}_{l,(i,j)}\end{pmatrix},$$

corresponds to the inverse two–levels relation deduced in [83]

$$\tilde{\varphi}_{2(i,j)+\mathbf{r}a,l+1} = \sum_{\mathbf{e}\in E}(-1)^{\mathbf{r}a\cdot\mathbf{e}}\tilde{\psi}_{(i,j),\mathbf{e},l}, \quad \mathbf{r}a\in E.$$

This equation is related to the concept of *stable completions* (see [118]). Roughly speaking, the L^∞-counterparts of the wavelet functions $\{\tilde{\psi}_{(i,j),l}\}_{i,j\in I_l}$ form a completion of the L^∞-counterpart of the basis system $\{\tilde{\varphi}_{(i,j),l}\}_{i,j\in I_l}$, and this determines the existence of a biorthogonal system. For $\mathbf{e}\in E^*$, we introduce the *details*, which will be crucial to detect zones with steep gradients:

$$d_{(i,j),\mathbf{e},l} := \langle u, \tilde{\psi}_{(i,j),\mathbf{e},l}\rangle.$$

These detail coefficients also satisfy a two–levels relation, namely

$$d_{(i,j),\mathbf{e},l} = \frac{1}{4}\sum_{2(i,j)+\mathbf{r}a\in\mathcal{M}_{(i,j),l}}(-1)^{\mathbf{r}a\cdot\mathbf{e}}\bar{u}_{2(i,j)+\mathbf{r}a,l+1}. \tag{3.5}$$

An appealing feature is that we can determine a transformation between the cell averages on level L and the cell averages on level 0 plus a series of details. This can be achieved by applying recursively the two–levels relations (3.4a) and (3.5); but we also require this transformation to be reversible:

$$\hat{u}_{(i,j),l+1} = \sum_{\mathbf{r}\in\bar{S}^l_{(i,j)}} g^l_{(i,j),\mathbf{r}}\bar{u}_{\mathbf{r},l}, \tag{3.6}$$

where we denote by

$$\bar{S}^l_{(i,j)} := \left\{V_{([i/2]+r_1,[j/2]+r_2),l}\right\}_{r_1,r_2\in\{-s,\dots,0,\dots,s\}}$$

the stencil of interpolation, $g^l_{(i,j),\mathbf{r}}$ are coefficients and the hat over u in the left-hand side of (3.6) means that this corresponds to a predicted value.

Relation (3.6) defines the so called *prediction* operator, which allow us to move from coarser to finer resolution levels. In contrast with the projection, the prediction operator is not unique, but we will impose two constraints: To be consistent with the projection, in the sense that it is the *right inverse* of the projection, and to be local, in the sense that the predicted value depends only on $\bar{S}^l_{(i,j)}$.

From the two–level relation (3.4a) we may easily deduce the value of the coefficients $g^l_{(i,j),\mathbf{r}}$, however, in order to determine the remaining coefficients, a prediction operator is needed. Notice that each term of the right-hand side of (3.4a) can be expressed in terms of $\hat{u}_{l,(i,j)}$ and the remaining terms. Thus we determine the prediction only for three of these terms:

$$\tilde{u}_{l+1,2(i,j)+\mathbf{e}} = \sum_{\mathbf{r}\in\bar{S}^l_{(i,j)}} a^l_{(i,j),\mathbf{r},\mathbf{e}}\hat{u}_{l,\mathbf{r}}, \quad \mathbf{e}\in E^*.$$

The detail coefficients represent the error induced by the prediction operator, therefore we may write

$$d_{l,(i,j),\mathbf{e}} = \hat{u}_{l+1,2(i,j)+\mathbf{e}} - \tilde{u}_{l+1,2(i,j)+\mathbf{e}}. \tag{3.7}$$

From (3.6)-(3.7), we have

$$\begin{aligned}\hat{u}_{l+1,2(i,j)+\mathbf{e}} &= \tilde{u}_{l+1,2(i,j)+\mathbf{e}} + d_{l,(i,j),\mathbf{e}}\\ &= \sum_{\mathbf{r}\in\bar{S}^l_{(i,j)}} a^l_{(i,j),\mathbf{r},\mathbf{e}}\hat{u}_{l,\mathbf{r}} + d_{l,(i,j),\mathbf{e}}, \quad \mathbf{e}\in E^*,\end{aligned} \tag{3.8}$$

and using (3.4a), (3.7), and (3.8) we arrive at

$$\begin{aligned}\hat{u}_{l+1,2(i,j)} &= 4\hat{u}_{l,(i,j)} - \sum_{\mathbf{e}\in E^*}\hat{u}_{l+1,(i,j)+\mathbf{e}}\\
&= 4\hat{u}_{l,(i,j)} - \sum_{\mathbf{e}\in E^*}\left(\sum_{\mathbf{r}\in\bar{S}^l_{(i,j)}} a^l_{(i,j),\mathbf{r},\mathbf{e}}\hat{u}_{l,\mathbf{r}} + d_{l,\mathbf{r},\mathbf{e}}\right),\\
&= 4\hat{u}_{l,(i,j)} - \Bigg(\sum_{\mathbf{r}\in\bar{S}^l_{(i,j)}} a^l_{(i,j),\mathbf{r},\mathbf{e}_1}\hat{u}_{l,\mathbf{r}} + \sum_{\mathbf{r}\in\bar{S}^l_{(i,j)}} a^l_{(i,j),\mathbf{r},\mathbf{e}_2}\hat{u}_{l,\mathbf{r}}\\
&\qquad + \sum_{\mathbf{r}\in\bar{S}^l_{(i,j)}} a^l_{(i,j),\mathbf{r},\mathbf{e}_3}\hat{u}_{l,\mathbf{r}}\Bigg) - \sum_{\mathbf{e}\in E^*}\sum_{\mathbf{r}\in\bar{S}^l_{(i,j)}} d_{l,\mathbf{r},\mathbf{e}},\\
&= 4\hat{u}_{l,(i,j)} - \sum_{\mathbf{r}\in\bar{S}^l_{(i,j)}}\sum_{\mathbf{e}\in E^*} a^l_{(i,j),\mathbf{r},\mathbf{e}}\hat{u}_{l,\mathbf{r}} - \sum_{\mathbf{e}\in E^*}\sum_{\mathbf{r}\in\bar{S}^l_{(i,j)}} d_{l,\mathbf{r},\mathbf{e}},\\
&= \sum_{\mathbf{r}\in\bar{S}^l_{(i,j)}} 4\delta_{\mathbf{r},(i,j)}\hat{u}_{l,(i,j)} - \sum_{\mathbf{r}\in\bar{S}^l_{(i,j)}}\sum_{\mathbf{e}\in E^*} a^l_{(i,j),\mathbf{r},\mathbf{e}}\hat{u}_{l,\mathbf{r}} - \sum_{\mathbf{e}\in E^*}\sum_{\mathbf{r}\in\bar{S}^l_{(i,j)}} d_{l,\mathbf{r},\mathbf{e}},\\
&= \sum_{\mathbf{r}\in\bar{S}^l_{(i,j)}}\left(4\delta_{\mathbf{r},(i,j)} - \sum_{\mathbf{e}\in E^*} a^l_{(i,j),\mathbf{r},\mathbf{e}}\right)\hat{u}_{l,\mathbf{r}} - \sum_{\mathbf{r}\in\bar{S}^l_{(i,j)}}\left(\sum_{\mathbf{e}\in E^*} d_{l,\mathbf{r},\mathbf{e}}\right),\end{aligned} \tag{3.9}$$

therefore, from (3.9) we get

$$m^l_{(i,j),\mathbf{r}} = 4\delta_{\mathbf{r},(i,j)} - \sum_{\mathbf{e}\in E^*} a^l_{(i,j),\mathbf{r},\mathbf{e}}, \quad \text{and} \quad \tilde{m}^l_{(i,j),\mathbf{r}} = -1.$$

Analogously, we determine the remaining coefficients

$$\begin{aligned}
\hat{u}_{l+1,2(i,j)+\mathbf{e}} &= \sum_{\mathbf{r}\in\bar{S}^l_{(i,j)}} m^l_{(i,j),\mathbf{r},\mathbf{e}}\hat{u}_{l,\mathbf{r}} + \sum_{\mathbf{i}\in E^*}\sum_{\mathbf{r}\in\bar{S}^l_{(i,j)}} \tilde{m}^l_{(i,j),\mathbf{r},\mathbf{e},\mathbf{i}} d_{l,\mathbf{r},\mathbf{i}} \\
&= \sum_{\mathbf{r}\in\bar{S}^l_{(i,j)}} a^l_{(i,j),\mathbf{r},\mathbf{e}}\hat{u}_{l,\mathbf{r}} + d_{l,\mathbf{r},\mathbf{e}} \\
&= \sum_{\mathbf{r}\in\bar{S}^l_{(i,j)}} a^l_{(i,j),\mathbf{r},\mathbf{e}}\hat{u}_{l,\mathbf{r}} + \sum_{\mathbf{r}\in\bar{S}^l_{(i,j)}} \delta_{\mathbf{r},(i,j)} d_{l,\mathbf{r},\mathbf{e}} \\
&= \sum_{\mathbf{r}\in\bar{S}^l_{(i,j)}} a^l_{(i,j),\mathbf{r},\mathbf{e}}\hat{u}_{l,\mathbf{r}} + \sum_{\mathbf{i}\in E^*}\sum_{\mathbf{r}\in\bar{S}^l_{(i,j)}} \delta_{\mathbf{r},(i,j)}\delta_{\mathbf{e},\mathbf{i}} d_{l,\mathbf{r},\mathbf{i}},
\end{aligned}$$

and this implies

$$m^l_{(i,j),\mathbf{r},\mathbf{e}} = a^l_{(i,j),\mathbf{r},\mathbf{e}}, \quad \text{and} \quad \tilde{m}^l_{(i,j),\mathbf{r},\mathbf{e},\mathbf{i}} = \delta_{\mathbf{r},(i,j)}\delta_{\mathbf{e},\mathbf{i}}.$$

Now we want to determine $\tilde{g}^j_{(i,j),\mathbf{r}}$. Using (3.7) and (3.4a) we have

$$\begin{aligned}
d_{l,(i,j),\mathbf{e}} &= \hat{u}_{l+1,2(i,j)+\mathbf{e}} - \sum_{\mathbf{r}\in\bar{S}^l_{(i,j)}} a^l_{(i,j),\mathbf{r},\mathbf{e}}\hat{u}_{l,\mathbf{r}} \\
&= \hat{u}_{l+1,2(i,j)+\mathbf{e}} - \frac{1}{4}\sum_{\mathbf{r}\in\bar{S}^l_{(i,j)}} a^l_{(i,j),\mathbf{r},\mathbf{e}}\left(\sum_{\mathbf{i}\in E^*}\hat{u}_{l+1,2\mathbf{r}+\mathbf{i}}\right) \\
&= \sum_{\mathbf{r}\in\bar{S}^l_{(i,j)}} \delta_{\mathbf{r},(i,j)}\hat{u}_{l+1,2(i,j)+\mathbf{e}} - \frac{1}{4}\sum_{\mathbf{r}\in\bar{S}^l_{(i,j)}} a^l_{(i,j),\mathbf{r},\mathbf{e}}\left(\sum_{\mathbf{i}\in E^*}\hat{u}_{l+1,2\mathbf{r}+\mathbf{i}}\right) \\
&= \sum_{\mathbf{i}\in E^*}\sum_{\mathbf{r}\in\bar{S}^l_{(i,j)}} \left(\delta_{\mathbf{r},(i,j)}\delta_{\mathbf{e},\mathbf{i}} - \frac{1}{4}a^l_{(i,j),\mathbf{r},\mathbf{i}}\right)\hat{u}_{l+1,2\mathbf{r}+\mathbf{i}}.
\end{aligned}$$

And from this, we finally get

$$\tilde{g}^l_{(i,j),\mathbf{r},\mathbf{e},\mathbf{i}} = \delta_{\mathbf{r},(i,j)}\delta_{\mathbf{e},\mathbf{i}} - \frac{1}{4}a^l_{(i,j),\mathbf{r},\mathbf{i}}.$$

For sake of notation, in our case we may write (3.6) as

$$\hat{u}_{(2i+e_1,2j+e_2),l+1} = \bar{u}_{(i,j),l} - (-1)^{e_1}Q_x - (-1)^{e_2}Q_y + (-1)^{e_1e_2}Q_{xy},$$

where $e_1, e_2 \in \{0,1\}$ and

$$Q_x := \sum_{n=1}^{s}\tilde{\gamma}_n\big(\bar{u}_{(i+n,j),l} - \bar{u}_{(i-n,j),l}\big), \quad Q_y := \sum_{p=1}^{s}\tilde{\gamma}_p\big(\bar{u}_{(i,j+p),l} - \bar{u}_{(i,j-p),l}\big),$$

$$Q_{xy} := \sum_{n=1}^{s}\tilde{\gamma}_n\sum_{p=1}^{s}\tilde{\gamma}_p\big(\bar{u}_{(i+n,j+p),l} - \bar{u}_{(i+n,j-p),l} - \bar{u}_{(i-n,j+p),l} + \bar{u}_{(i-n,j-p),l}\big).$$

Here the corresponding coefficients are $\tilde{\gamma}_1 = -\frac{22}{128}$ and $\tilde{\gamma}_2 = \frac{3}{128}$ (see [19]).

In practice, the details are simply the differences between the exact and the predicted value

$$\bar{d}^u_{(i,j),l} := \bar{u}_{(i,j),l} - \hat{u}_{(i,j),l}.$$

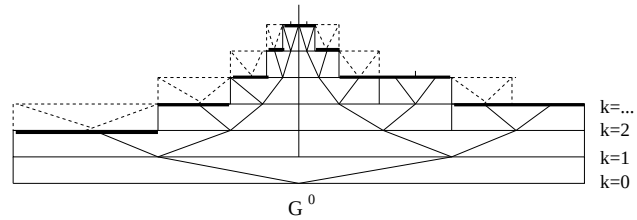

Figure 3.2: *One-dimensional graded tree data structure.*

The following lemma (see e.g. [53]) gives a notion of the relation between details and the regularity of a given function.

Theorem 3.1 *If u is sufficiently smooth, then detail coefficients decrease when going from coarser to finer levels:*

$$\left|\bar{d}^{u}_{(i,j),l}\right| \leqslant C2^{-2lr}\|u^{(r)}\|_{L^\infty(V_{(i,j),l})},$$

where $r = 2s + 1$ is the number of vanishing moments of the wavelets.

This means that the more regular u is over $V_{(i,j),l}$, the smaller is the corresponding detail coefficient. In view of this property, it is natural to think that we could discard the information corresponding to small details. This is called *thresholding*. Basically, we discard all the elements corresponding to details below a level-dependent tolerance given by

$$\varepsilon_l = 2^{2(l-L)}\varepsilon_{\mathrm{R}}, \tag{3.10}$$

where ε_{R} is a reference tolerance selected by means of an error analysis (see Section 3.3). Notice that this tolerance is smaller when going to coarser levels. This choice guarantees that we keep only the most significant L^1 contributions $\|d_{(i,j),l}\psi_{(i,j),l}\|_{L^1}$ (see [53]).

For multicomponent solutions, there are many possible definitions for a scalar detail $\bar{d}_{(i,j),l}$ that is calculated from the details of the components (see a brief discussion in [40]). In order to guarantee that the refinement and coarsening procedures are always on the safe side, in the sense that we always prefer to keep a position with a detail triple containing at least one component above the threshold (3.10), we will use

$$\bar{d}_{(i,j),l} = \min\{\bar{d}^{v}_{(i,j),l}, \bar{d}^{u_{\mathrm{e}}}_{(i,j),l}, \bar{d}^{w}_{(i,j),l}\}$$

for the refinement procedure and

$$\bar{d}_{(i,j),l} = \max\{\bar{d}^{v}_{(i,j),l}, \bar{d}^{u_{\mathrm{e}}}_{(i,j),l}, \bar{d}^{w}_{(i,j),l}\}$$

for the coarsening procedure.

3.2 Graded tree data structure

We organize the cell averages and corresponding details at different levels, in a *dynamic graded tree structure*: this means that neighboring cells will differ in at most one refinement level. The following are the basic elements of the tree structure.

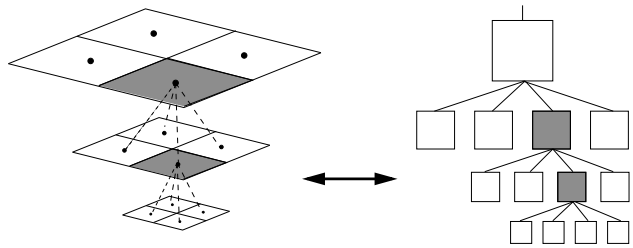

Figure 3.3: *Graded tree data structure ("quadtree"), after [118].*

- We denote by *root* the basis of the tree.
- A *node* is an element of the tree. Each control volume coincides with a node.
- In two space dimensions, a parent node has four *sons*, and the sons of the same parent are called *brothers*.
- A node without sons is called a *leaf*.
- The leaves of the tree are the control volumes forming the adaptive mesh. We denote by $\mathcal{L}(\Lambda)$ the restriction of Λ to the leaves.

The tree structure evolves in time. Therefore, in order to remain graded, the following conditions should be taken into account by the structure:

- Whenever an element is included in the tree, all other elements corresponding to the same spatial region in coarser resolution levels are also included.
- A given node has $s' = 2$ nearest neighbors in each spatial direction, called *nearest cousins*, needed for the computation of the fluxes of leaves; if these nearest cousins do not exist, we create them as *virtual leaves*.
- A given node can be removed only if all its brothers are also removed and only if the node is not the nearest cousin of an existing node.

These choices guarantee the stability of the multilevel operations (see [53]). Moreover, by construction, the graded tree structure ensures the connectivity between the nodes of the tree. We also stress that although the graduation of the tree structure is responsible for a slight increment in the size of the set of non-discarded nodes, this fact does not affect significantly the achieved memory compression.

Figures 3.2,3.3 illustrate the graded tree structure for one dimensional and two dimensional domains.

We apply this MR reconstruction to the spatial part of the function $\mathbf{u} = (v, u_e, w)$ which corresponds to the numerical solution of the underlying problem for each time step, so we need to update the tree structure for the proper representation of the solution during the evolution. To this end, we apply a thresholding strategy, but always keep the graded tree structure of the data. Once the thresholding is performed, we add to the tree a *safety zone*, so the new tree may contain the possible adaptive mesh for the next time step. Our safety zone will be formed by adding one finer level to the tree in all possible positions without violating the graded tree data structure. This device, first proposed e.g. in [87], ensures that the graded tree will

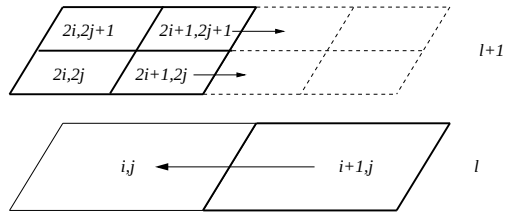

Figure 3.4: *Conservative flux computation for coarser levels.*

represent adequately the solution in the next time step, and depends strongly on the assumption of finite propagation speed of the singularities. Possible appearance of singularities may be also taken into account by testing the details against $2^{2s}\varepsilon$, where s is the degree of the reconstruction polynomial. By using this strategy, one can decide whether to include a finer level or not.

Notice that we compute only the fluxes at level $l+1$ and we set the ingoing flux on the leaf at level l equal to the sum of the outgoing fluxes on the leaves of level $l+1$ sharing the same edge (see Figure 3.4)

$$F_{(i+1,j),l\to(i,j),l} = F_{(2i+1,2j),l+1\to(2i+2,2j),l+1} + F_{(2i+1,2j+1),l+1\to(2i+2,2j+1),l+1}. \tag{3.11}$$

This choice decreases the number of costly flux evaluations without loosing the conservativity in the flux computation.

It is important to remark that in the case of systems, since we are dealing with reaction-diffusion systems where species tend to attract each other, we manage the multiresolution framework and the data structure as one unified mesh with two components per element. This means that we construct only one graded tree and apply only one thresholding strategy for both species; however, there are other cases where is preferable to organize the different species in separate adaptive meshes, for example when the species segregate spatially, as in systems of conservation laws modelling traffic flow and polydisperse sedimentation [37].

To measure the improvement in data compression, we use the *data compression rate* [40, 41]

$$\eta := \frac{\mathcal{N}}{2^{-(L+1)}\mathcal{N} + \#\mathcal{L}(\Lambda)},$$

Here, $\mathcal{N}$ is the number of elements in the full finest grid at level L, and $\#\mathcal{L}(\Lambda)$ is the size of the set of leaves. We measure the *speed-up* between the CPU time of the numerical solution obtained by the FV method and the CPU time of the numerical solution obtained by the MR method:

$$\mathcal{V} := \frac{\text{CPU time}_{\text{FV}}}{\text{CPU time}_{\text{MR}}}.$$

As an observation of a practical nature for readers who may wish to implement the method presented herein, we mention that in order to obtain data compression, not only the tree data structure is essential, but also the way of navigating inside the data structure, as proposed in [134]. Each node should be represented by a triple (i, j, l) corresponding to the spatial position (i, j) on the level l. The children nodes need to be connected to its parent node for example by using pointers, so that the maximum number of steps required to get to any node is L because we move recursively between children nodes and its parent.

3.3 Choice of the threshold parameter

3.3.1 Error analysis for conservation laws and parabolic equations

We briefly recall here the error analysis conducted first in [53] and then in [134] for scalar, one-dimensional conservation laws and strictly parabolic equations, respectively. Based on the main properties of the respective reference finite volume scheme on a uniform grid at the finest level L, such as the contraction property in L^1 norm, the CFL stability condition and order of approximation in space, the authors of both papers decompose the global error between the cell average values of the exact solution vector at the level L, denoted here by u^L_{ex}, and those of the multiresolution computation with a maximal level L, denoted by $\bar{u}^L_{\text{MR}}$, into two errors

$$\left\|\bar{u}^L_{\text{ex}} - \bar{u}^L_{\text{MR}}\right\| \leq \left\|\bar{u}^L_{\text{ex}} - \bar{u}^L_{\text{FV}}\right\| + \left\|\bar{u}^L_{\text{FV}} - \bar{u}^L_{\text{MR}}\right\|.$$

The first error on the right-hand side, called *discretization error*, is that of the reference finite volume scheme on a uniform grid at the finest level L. For both a scalar, one-dimensional conservation law [53] and a strictly parabolic equation [134], the order of convergence, denoted $\tilde{\alpha}$, of the corresponding reference finite volume scheme is known (the classical approach of Kuznetsov [106] yields $\tilde{\alpha} = 1/2$ and $\tilde{\alpha} = 2$, respectively), which permits to bound the discretization error by

$$\left\|\bar{u}^L_{\text{ex}} - \bar{u}^L_{\text{FV}}\right\| \leqslant C_1 2^{-\tilde{\alpha}L} \tag{3.12}$$

for a constant $C_1 > 0$. For the second error, called *perturbation error*, Cohen et al. [53] assume that the details on a level l are deleted when they are smaller than a prescribed tolerance ϵ_l. Under this assumption, they show that if the discrete time evolution operator is contractive in the chosen norm, and if ϵ_l is given by (3.10), then the perturbation error accumulates in time and satisfies $\|\bar{u}^L_{\text{FV}} - \bar{u}^L_{\text{MR}}\| \leq C_2 n\epsilon$, where $C_2 > 0$ and n denotes the number of time steps. At a fixed time $T = n\Delta t$, this gives

$$\left\|\bar{u}^L_{\text{FV}} - \bar{u}^L_{\text{MR}}\right\| \leq C_2 \frac{T}{\Delta t}\epsilon, \quad C_2 > 0. \tag{3.13}$$

For the equations considered in [53, 134], the reference (explicit) finite volume scheme is convergent provided that a CFL-type condition

$$\Delta t \leqslant \frac{\Delta x^2}{a\Delta x + b} \tag{3.14}$$

is satisfied, where the constants a and b depend on the coefficients of the equation under consideration, and Δx is the meshwidth of the finest grid, i.e. $\Delta x = \tilde{C}(\Omega)2^{-L}$, where $\tilde{C}$ depends on the dimension and shape of the computational domain. Consequently, if Δt denotes the largest time step possible, then this quantity can be expressed in terms of 2^{-L} if we consider equality in (3.14), i.e.,

$$\Delta t = \frac{[\tilde{C}(\Omega)]^2 2^{-2L}}{\tilde{C}(\Omega)2^{-L}a + b}. \tag{3.15}$$

The main idea of the adaptive multiresolution scheme is to perturb the solution given by a finite volume scheme on a uniform discretization (reference mesh) in such a way that the total error, i.e., the error between the exact solution and the adaptive solution that is projected to the reference fine mesh, is of the same order as the discretization error. For this purpose, one has to balance the discretization error and the perturbation error, which means that the discretization and perturbation errors should be of the same order as Δx, or

equivalently, L varies. To derive an expression for ε from this requirement, we observe that the right-hand sides of (3.12) and (3.13) must be proportional, or equivalently,

$$\varepsilon \propto 2^{-\tilde{\alpha}L}\Delta t. \tag{3.16}$$

In light of (3.14), this yields a proportionality of the type

$$\varepsilon = \hat{C}2^{-\tilde{\alpha}L}\frac{[\tilde{C}(\Omega)]^2 2^{-2L}}{\tilde{C}(\Omega)2^{-L}a+b}, \tag{3.17}$$

from which one may deduce a value of the reference tolerance $\varepsilon_{\mathrm{R}} = \varepsilon$, provided that the factor of proportionality $\hat{C}$ can be determined, for example from suitable experiments, as is done in [134].

3.3.2 Reference tolerance for degenerate reaction-diffusion systems

The derivation of the reference tolerance by the preceding method is supported by a rigorous analysis only in those cases where the order of convergence $\tilde{\alpha}$ is known, and the discrete time evolution operator is contractive in the chosen norm. These properties hold for a scalar, one-dimensional first-order conservation law and a second-order parabolic equation studied in [53] and [134], respectively. For finite volume discretizations of strongly degenerate parabolic equations, and in particular of the degenerate reaction-diffusion systems studied herein, an exact rate of convergence has not yet been derived. However, in [40, 41] it is demonstrated that also for these equations, an equation of the type (3.17) may be employed to determine the reference tolerance ε_{R} if $\tilde{\alpha}$ is replaced by a rate of convergence determined by numerical experiments on a sequence of uniform grids, and the corresponding coefficient $\hat{C}$ is selected after a series of preliminary computations, with the final result that the total error of the multiresolution scheme is of the same order as that of the reference finite volume scheme.

In light of these results, we apply the same methodology to determine a reference tolerance for the problems at hand. We first give the corresponding reference tolerance for the numerical schemes in Section 2.1:

$$\epsilon_{\mathrm{R}} = C\frac{2^{-(\alpha+1)L}}{|I|\|b'\|_\infty + 2^L\|a\|_\infty}. \tag{3.18}$$

For the hyperbolic case, i.e. $\|a\|_\infty = 0$, choosing the reference tolerance as in (3.18) is equivalent to the result $\epsilon \propto 2^{-(\alpha+1)L}$ obtained by Cohen et al. [53]. For the discontinuous flux case,

$$\varepsilon_{\mathrm{R}} = C\frac{2^{-(\alpha+1)L}}{|I|\max\limits_{u\in[0,1],x\in\mathbb{R}}|f_u(\boldsymbol{\gamma}(x),u)| + 2^{-L}\max\limits_{u\in[0,1]}|A'(u)|},$$

and for the case $A(u) = 0$, the reference tolerance must be taken as

$$\varepsilon_{\mathrm{R}} = C2^{-\alpha L}\left(\max_{u\in[0,1],x\in\mathbb{R}}\left|f_u\big(\boldsymbol{\gamma}(x),u\big)\right|\right)^{-1},$$

because of the less restrictive CFL condition.

Based on preliminary numerical experiments (obtained in a similar fashion as in [40]), for the Turing model and combustion examples we obtain the approximate value $\tilde{\alpha} = 2.18$. The global CFL condition (2.15) of the reference finite volume scheme defined for the discretization of the Turing model (1.23) implies that

$$\Delta t \leqslant \frac{\widetilde{\Delta x}^2}{\|f_u\|_\infty + \|f_v\|_\infty + \|g_u\|_\infty + \|g_v\|_\infty + \widetilde{\Delta x}4d(\|A'\|_\infty + \|B'\|_\infty)}.$$

Now, if we write $\widetilde{\Delta x} = \sqrt{|\Omega|}2^{-L}$ (i.e., $\tilde{C}(\Omega) = \sqrt{|\Omega|}$), we obtain the following analogue of (3.15):

$$\Delta t = C_3 \frac{|\Omega| 2^{-2L}}{\|f_u\|_\infty + \|f_v\|_\infty + \|g_u\|_\infty + \|g_v\|_\infty + \sqrt{|\Omega|}2^{-L} 4d(\|A'\|_\infty + \|B'\|_\infty)}, \quad 0 < C_3 \leqslant 1.$$

If we require that the proportionality (3.16) holds, we arrive at the following expression for the reference tolerance ε_{R} for the numerical computations of the Turing model (1.23), which is a version of (3.17):

$$\epsilon_{\mathrm{R}} = C \frac{2^{-(\tilde{\alpha}+2)L}}{|\Omega|(\|f_u\|_\infty + \|f_v\|_\infty + \|g_u\|_\infty + \|g_v\|_\infty) + |\Omega|^{3/2} 2^L\, 4d(\|A'\|_\infty + \|B'\|_\infty)}. \tag{3.19}$$

For the chemotaxis model (1.30), the reference tolerance may be set to

$$\epsilon_{\mathrm{R}} = C \frac{2^{-(\tilde{\alpha}_1+2)L}}{|\Omega|(\|h_u\|_\infty + \|h_v\|_\infty + \|g'\|_\infty) + |\Omega|^{3/2} 2^L\, 4d(\sigma + \|\chi'\|_\infty)}, \tag{3.20}$$

where $\tilde{\alpha}_1$ is a value of the corresponding convergence rate.

We proceed in the same fashion to obtain the reference tolerance for the bidomain system

$$\varepsilon_{\mathrm{R}} = C \frac{2^{-(\tilde{\alpha}+2)L}}{|\Omega| \max\limits_{(i,j,l)\in\mathcal{L}(\Lambda)} \Big(|I_{\mathrm{ion},(i,j)}| + 2|I_{\mathrm{app},(i,j)}| \Big) + |\Omega|^{3/2} 2^{2+L} \max\limits_{(i,j,l)\in\mathcal{L}(\Lambda)} \Big(|\mathbf{M}_{\mathrm{i},(i,j,l)}| + |\mathbf{M}_{\mathrm{e},(i,j,l)}| \Big)}.$$

Note that all the L^∞ norms in (3.19) and (3.20) are computed numerically. To determine an acceptable value for the factor C (which, of course, depends on T, C_1, C_2 and C_3), a series of computations with different tolerances are needed in each case, prior to final computations. Essentially, we select the largest available candidate value for C such that the same order of accuracy (same slopes for the error computation) as that of the reference finite volume scheme is maintained. This procedure basically generalizes the treatment in [41] of spatially one-dimensional strongly degenerate parabolic equations. In [69] the authors prove for scalar, one-dimensional nonlinear conservation laws, that the threshold error is stable in the sense that the constant C is uniformly bounded and, in particular, does not depend on the threshold value ϵ_{R}, the number of refinement levels L and the number of time steps n. In our case, even when a rigorous proof is still missing for the systems considered in the present work, from the previous deduction we see a similar behavior for C.

We also mention that as in previous works [40, 41, 53], here the reference tolerance remains fixed for all times, though it is certainly possible to recompute the reference tolerance at each time step.

To measure errors between a reference solution u_{ex} and an approximate solution u_{MR}, we will use L^p-errors: $e_p = \|u^n_{\mathrm{ex}} - u^n_{\mathrm{MR}}\|_p$, $p = 1, 2, \infty$, where

$$e_\infty = \max_{(i,j,l)\in\mathcal{L}(\Lambda)} \big| u^n_{\mathrm{ex}\,i,j,l} - u^n_{\mathrm{MR}\,i,j,l} \big|,$$

$$e_p = \left(\frac{1}{|\mathcal{L}(\Lambda)|} \sum_{(i,j,l)\in\mathcal{L}(\Lambda)} \big| u^n_{\mathrm{ex}\,i,j,l} - u^n_{\mathrm{MR}\,i,j,l} \big|^p \right)^{1/p}, \quad p = 1, 2.$$

Here $u^n_{\mathrm{ex}\,i,j,l}$ stands for the projection of the reference solution over the leaf (i, j, l).

Chapter 4

Time-step accelerating methods and algorithms

This Chapter is devoted to the study of two strategies for advancing the time evolution of the space adaptive MR scheme presented in the previous section. One of these strategies is based on using the same time step to advance the solution on all parts of the computational domain, and controlling the time step through an embedded pair of Runge-Kutta schemes (known as Runge-Kutta-Fehlberg schemes). In these procedures, one compares the numerical solution after each time step with an (approximate) reference solution, and adjusts the time step if the discrepancy is unacceptable. The other strategy consist in an adaptation of the locally varying time stepping strategy recently introduced for multiresolution schemes for conservation laws and multidimensional systems in [108, 119]. This strategy is not precisely (time-)adaptive for scalar equations, since the time step for each level remains the same for all times, but the idea is to enforce a local CFL condition by using the same CFL number for all resolution levels, and then evolving all leaves using a local time step. We also present a general algorithm to accurately describe the multiresolution procedures.

4.1 Local time stepping

We utilize a version of the locally varying time stepping strategy advanced by Müller and Stiriba [119], and summarize here its principles. The basic idea is to enforce a local CFL condition by using the same CFL number for all scales, and the strategy consists in evolving all leaves on level l using the local time step

$$\Delta t_l = 2^{L-l}\Delta t, \quad l = L-1, \ldots, 0, \tag{4.1}$$

where $\Delta t = \Delta t_L$ corresponds to the time step on the finest level L. This strategy allows to increase the time step for the major part of the adaptive mesh without violating the CFL stability condition.

Clearly, portions of the solution lying on different resolution levels need to be synchronized to obtain a conservative scheme. This will be achieved after 2^l time steps using Δt_l: all leaves forming the adaptive mesh are synchronized in time, so one time step with Δt_0 is equivalent to 2^L intermediate time steps with

Δt_L. In order to additionally save computational effort, we update the tree structure (refinement and coarsening) only each odd intermediate time step $1, 3, \ldots, 2^L - 1$ (as suggested in [16]), and furthermore, the projection and prediction operators are performed only on the scales occupied by the leaves of the current tree, i.e., we do not update the tree structure by prediction from the root cell, but from the coarsest leaves (we refer to this as *partial grid adaptation*). For the rest of the intermediate time steps, we use the current tree structure. For the sake of synchronization and conservativity of the flux computation, for coarse levels (scales without leaves), we employ *the same* fluxes ($\bar{\mathcal{D}}_{ij,l}$ and $\bar{f}_{ij,l}$) computed in the previous intermediate time step, because the cell averages on these scales are the same that in the previous intermediate time step. Only for finer levels (scales containing leaves), we compute fluxes, and do so in the following way: if there is a leaf at the corresponding cell edge and at the same resolution level l, we simply perform a flux computation using the brother leaves, and the virtual leaves at the same level if necessary; and if there is a leaf at the corresponding cell edge but on a finer resolution level $l+1$ (in this case we refer to this edge as an *interface edge*), the flux will be determined as in (3.11), that is, we compute the fluxes at a level $l+1$ on the same edge, and we set the ingoing flux on the corresponding edge at level l equal to the sum of the outgoing fluxes of the son cells of level $l+1$ (for the same edge). Notice that the graded tree structure ensures that the elements of the adaptive mesh do not differ for more than one resolution level. In order to always have at hand the computed fluxes as in (3.11), we need to perform the locally varying time stepping recursively from fine to coarse levels. If at any instance of the procedure there is a missing value, we can project the value from the sons nodes or we can predict this value from the parent nodes. For illustrative purposes, we give an example of an interior first-order flux calculation for Model 2, to complete a full macro time step, by the following algorithm:

Algorithm 4.1.1 (Locally varying intermediate time stepping)

1. *Grid adaptation (provided the former sets of leaves and virtual leaves).*
2. **do** $k = 1, \ldots, 2^L$ *(and therefore the local time steps are* $n + 2^{-L}, n + 2 \cdot 2^{-L}, n + 3 \cdot 2^{-L}, \ldots, n + 1$*)*
   (a) *Synchronization:*

   do $l = L, \ldots, 1$
   do $i = 1, \ldots, |\tilde{\Lambda}|_x(l)$, $j = 1, \ldots, |\tilde{\Lambda}|_y(l)$
   if $1 \leqslant l \leqslant \tilde{l}_{k-1}$ **then**
   if (i, j, l) *is a virtual leaf* **then**

$$\bar{F}^{n+k2^{-L}}_{(i,j,l)\to(i+1,j,l)} \leftarrow \bar{F}^{n+(k-1)2^{-L}}_{(i,j,l)\to(i+1,j,l)}$$

$$\bar{f}^{n+k2^{-L}}_{ij,l} \leftarrow \bar{f}^{n+(k-1)2^{-L}}_{ij,l}, \quad \bar{g}^{n+k2^{-L}}_{ij,l} \leftarrow \bar{g}^{n+(k-1)2^{-L}}_{ij,l}$$

   endif
   else
   if (i, j, l) *is a leaf* **then**

$$\bar{f}^{n+k2^{-L}}_{ij,l} \leftarrow f\big(\bar{u}^{n+k2^{-L}}_{ij,l}, \bar{v}^{n+k2^{-L}}_{ij,l}\big), \quad \bar{g}^{n+k2^{-L}}_{ij,l} \leftarrow g\big(\bar{u}^{n+k2^{-L}}_{ij,l}, \bar{v}^{n+k2^{-L}}_{ij,l}\big)$$

   if $(i+1, j, l)$ *is a leaf* **then** *compute fluxes by*

$$\bar{F}_{(i,j,l)\to(i+1,j,l)} \leftarrow -\frac{1}{h(l)}\big(A(\bar{u}_{i+1,j,l}) - A(\bar{u}_{i,j,l})\big)$$

$$\bar{F}_{(i,j,l)\to(i,j+1,l)} \leftarrow -\frac{1}{h(l)}\big(A(\bar{u}_{i,j+1,l}) - A(\bar{u}_{i,j,l})\big)$$

endif

if $(2i+2, 2j, l+1)$, $(2i+2, 2j+1, l+1)$ *are leaves (interface edges)* **then** *compute fluxes by*

$$\bar{F}_{(i,j,l)\to(i+1,j,l)} \leftarrow \bar{F}_{(2i+2,2j,l+1)\to(2i+1,2j,l+1)} + \bar{F}_{(2i+2,2j+1,l+1)\to(2i+1,2j+1,l+1)}$$

$$\bar{F}_{(i,j,l)\to(i,j+1,l)} \leftarrow \bar{F}_{(2i,2j+2,l+1)\to(2i,2j+1,l+1)} + \bar{F}_{(2i+1,2j+2,l+1)\to(2i+1,2j+1,l+1)}$$

endif

endif

endif

enddo

enddo

(b) *Time evolution:*

do $l = 1, \ldots, L$, $i = 1, \ldots, |\tilde{\Lambda}|_x(l)$, $j = 1, \ldots, |\tilde{\Lambda}|_y(l)$

if $1 \leqslant l \leqslant \tilde{l}_{k-1}$ **then** *there is no evolution:*

$$\bar{u}_{ij,l}^{n+(k+1)2^{-L}} \leftarrow \bar{u}_{ij,l}^{n+k2^{-L}}, \quad \bar{v}_{ij,l}^{n+(k+1)2^{-L}} \leftarrow \bar{v}_{ij,l}^{n+k2^{-L}}$$

else

Interior marching formula only for the leaves (i, j, l)*:*

$$\bar{u}_{ij,l}^{n+(k+1)2^{-L}} \leftarrow \bar{u}_{ij,l}^{n+k2^{-L}} + \gamma\Delta t_l \bar{f}_{ij,l}^{n+k2^{-L}} + \Delta t_l \bar{\mathcal{D}}_{ij,l}\big(\mathcal{S}\big(\bar{u}_{ij,l}^{n+k2^{-L}}\big), h(l)\big)$$

$$\bar{v}_{ij,l}^{n+(k+1)2^{-L}} \leftarrow \bar{v}_{ij,l}^{n+k2^{-L}} + \gamma\Delta t_l \bar{g}_{ij,l}^{n+k2^{-L}} + d\Delta t_l \bar{\mathcal{D}}_{ij,l}\big(\mathcal{S}\big(\bar{v}_{ij,l}^{n+k2^{-L}}\big), h(l)\big)$$

endif

enddo

(c) *Partial grid adaptation each odd intermediate time step:*

do $l = L, \ldots, \tilde{l}_k + 1$

Projection from the leaves.

enddo

do $l = \tilde{l}_k, \ldots, L$

Thresholding, prediction, and addition of the safety zone.

enddo

enddo

Here, $\tilde{l}_k$ denotes the coarsest level containing leaves in the intermediate step k (as introduced in [119]), $h(l)$ is the mesh size on level l, and $|\tilde{\Lambda}|_z(l)$ is the size of the set formed by leaves and virtual leaves per resolution level l in the direction z. The interior marching formula is the modified marching formula (2.14) for Model 2, for the intermediate time steps $k = 1, \ldots, 2^L$, for the leaf in the position (i, j) at level l.

Our scheme is formulated for a first-order, explicit Euler time discretization. Generalizations for higher order schemes are given in [119] for Crank-Nicolson schemes and in [70] for Runge-Kutta schemes, respectively.

4.2 A Runge-Kutta-Fehlberg method

Most of the basic FV schemes described in Chapter 2 are only first order in time, and should be upgraded to at least second order so that the second-order spatial accuracy is effective. This can be achieved if the time integration is done, for example, by a standard second or higher order Runge-Kutta (RK) scheme. However, we herein utilize a particular class of so-called embedded RK schemes [63, 77, 86], which, apart from providing the necessary accuracy, also allow for an adaptive control of the time step. Specifically, we utilize a simple version of a so-called Runge-Kutta-Fehlberg (RKF) method. RKF schemes are based on the observation that by varying the vector b of weights for the stages calculated in the course of a Runge-Kutta step, pairs of schemes with different orders of accuracy can be generated. This allows to estimate the approximation error in time, and the time step can be automatically adjusted to control the error in time. The additional computational effort is moderate, since both schemes utilize the same nodes and interior weights of the quadrature formula.

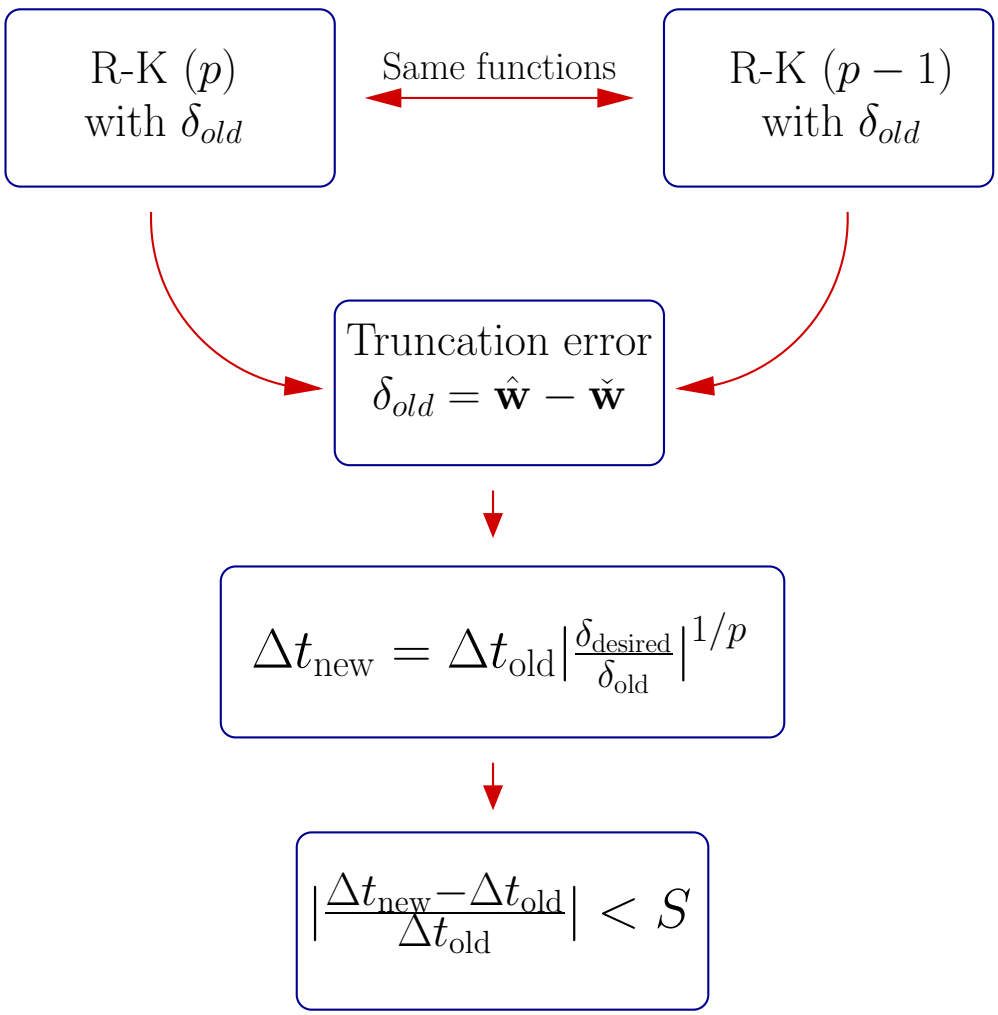

Figure 4.1: *Runge-Kutta-Fehlberg (RKF) time stepping schematic chart, after [131].*

In the case of multi-species variables (with N species), we will consider naturally a vector valued RKF time

stepping, i.e., $\mathbf{u} = (u_i)_{i=1}^N$, and for ease of discussion assume that the problem is written as $\mathbf{u}_t = \mathcal{A}(t, \mathbf{u})$.

We use two Runge-Kutta methods, of orders $p = 3$ and $p - 1 = 2$

$$\hat{\mathbf{u}}^{m+1} = \bar{\mathbf{u}}^m + \hat{b}_1\bar{\kappa}_1 + \hat{b}_2\bar{\kappa}_2 + \hat{b}_3\bar{\kappa}_3, \quad \check{\mathbf{u}}^{m+1} = \bar{\mathbf{u}}^m + \check{b}_1\bar{\kappa}_1 + \check{b}_2\bar{\kappa}_2 + \check{b}_3\bar{\kappa}_3, \tag{4.2}$$

where

$$\begin{aligned} &\bar{\kappa}_1 = \Delta t\mathcal{A}(t^m, \bar{\mathbf{u}}^m),\ \bar{\kappa}_2 = \Delta t\mathcal{A}(t^m + c_2\Delta t, \bar{\mathbf{u}}^m + a_{21}\bar{\kappa}_1), \\ &\bar{\kappa}_3 = \Delta t\mathcal{A}(t^m + c_3\Delta t, \bar{\mathbf{u}}^m + a_{31}\bar{\kappa}_1 + a_{32}\bar{\kappa}_2), \end{aligned} \tag{4.3}$$

and the corresponding coefficients for the RK3(2) method are given in the following Butcher tableau:

$$\begin{array}{c|ccc} c_1 = 0 & & & \\ c_2 = 1 & a_{21} = 1 & & \\ c_3 = 1/2 & a_{31} = 1/4 & a_{32} = 1/4 & \\ \hline & \hat{b}_1 = 1/6 & \hat{b}_2 = 1/6 & \hat{b}_3 = 2/3 \\ \hline & \check{b}_1 = 1/2 & \check{b}_2 = 1/2 & \check{b}_3 = 0 \end{array}. \tag{4.4}$$

These specific coefficients define an optimal pair of embedded TVD-RK methods of orders two and three [138].

The truncation error between the two approximations for $\bar{\mathbf{u}}^{m+1}$ is estimated by

$$\bar{\delta}_{\text{old}} := \hat{\mathbf{u}}^{m+1} - \check{\mathbf{u}}^{m+1} = \sum_{i=1}^{p}(\hat{b}_i - \check{b}_i)\bar{\kappa}_i \sim (\Delta t)^p, \quad \delta_{\text{old}} := \|\bar{\delta}_{\text{old}}\|_\infty \tag{4.5}$$

Then we can adjust the step size in order to achieve prescribed accuracy δ_{desired} in time. We have

$$\Delta t_{\text{new}} = \Delta t_{\text{old}}|\delta_{\text{desired}}/\delta_{\text{old}}|^{1/p},$$

with $p = 3$. We could adjust Δt to maintain prescribed accuracy δ_{desired} in time by using

$$\Delta t_{\text{new}} = \Delta t_{\text{old}}|\delta_{\text{desired}}/\delta_{\text{old}}|^{1/p}$$

with $p = 3$, but to avoid excessively large time steps, a limiter function $\mathcal{S}$ is defined as

$$\mathcal{S}(t) = (\mathcal{S}_0 - \mathcal{S}_{\min})\exp(-t/\Delta t) + \mathcal{S}_{\min},$$

where $\mathcal{S}_0 = 0.1$ y $\mathcal{S}_{min} = 0.01$. This implies that we initially allow 10% of variation in the time step, and after a few iterations, we allow only 1%.

The new time step Δt_{new} is then defined as

$$\Delta t_{\text{new}} = \begin{cases} \Delta t_{\text{old}}|\delta_{\text{desired}}/\delta_{\text{old}}|^{1/p} & \text{if } |(\Delta t_{\text{new}} - \Delta t_{\text{old}})/\Delta t_{\text{old}}| \le \dfrac{1}{2}\mathcal{S}(t, \Delta t_{\text{old}}), \\ \dfrac{1}{2}\mathcal{S}(t, \Delta t_{\text{old}})\Delta t_{\text{old}} + \Delta t_{\text{old}} & \text{otherwise,} \end{cases} \tag{4.6}$$

In Figure 4.1 we present a schematic flowchart of the RKF method. Notice that Δt_{new} is the time step for computing $\bar{u}^{m+2}$. The nomenclature of "RKF method" for the embedded Runge-Kutta scheme used herein is widespread in the literature (see e.g. [141]). However, this scheme does *not* utilize what has become known as the "Fehlberg trick" [63] (i.e., κ_p equals κ_1 of the next time step).

Both the second- and third-order TVD-RK schemes presented herein are optimal in the sense that if the first-order explicit Euler time discretization $u^{m+1} = u^m + \Delta t \mathcal{L}(t_m, u^m)$ is stable in a certain norm, i.e., $\|u^{m+1}\| \leq \|u^m\|$ under a condition $\Delta t \leq \Delta t_1$, then both schemes are stable under the same condition $\Delta t \leq \Delta t_1$, see [138] for details. This means that even though these TVD-RK schemes are of second-order or third-order accuracy, the CFL condition for the resulting FV scheme is still the CFL condition imposed on the first-order version of the scheme, which limits $\Delta t/\Delta x^2$.

4.3 A general multiresolution algorithm

Now we give a brief description of the general MR procedure.

Algorithm 4.3.1 (Multiresolution procedure)

1. *Initialization of parameters.*
2. *Creation of the initial tree:*
   (a) *Create the root and compute its cell average value.*
   (b) *Split the cell, compute the cell average values in the sons and compute details.*
   (c) *Apply thresholding for the splitting of the new sons.*
   (d) *Repeat this until all sons have details below the required tolerance ε_l.*
3. **do** $n = 1, \ldots, total_time_steps$
   (a) *Determination of the leaves and virtual leaves sets.*
   (b) *Time evolution with global time step: Compute the discretized space operator $\mathcal{A}$ for all the leaves.*
   (c) *Updating the tree structure:*
      - *Recalculate the values on the nodes by projection from the leaves. Compute the details for all nodes $(\cdot, \cdot, l)$ for $l \geqslant \tilde{l}_k$. If the detail in a node and in its brothers is smaller than the prescribed tolerance, then the cell and its brothers are* deletable.
      - *If some node and all its sons are deletable, and the sons are leaves without virtual sons, then delete sons. If this node has no sons and it is not deletable and it is not at level $l = L$, then create sons.*
      - *Update the values in the new sons by prediction from the former leaves.*

   enddo
4. *Output: Save meshes, leaves and cell averages.*

Here *total_time_steps* is the total time steps needed to reach T_{final} using Δt as the maximum time step allowed by the CFL condition using the finest space step.

When using a RKF strategy for the time evolution, replace step (3b) by the new step

(3)
- *Compute the discretized space operator $\mathcal{A}$ for all the leaves as in* (4.3).
- *Compute the difference between the two solutions obtained as in* (4.5).

- *Apply the limiter for the time step variation and compute the new time step by* (4.6).

When using a LTS strategy, replace step (3b) by the new step

(3) **do** $n = 1, \ldots, total_time_steps$

(a) *Determination of the leaves and virtual leaves sets.*

(b) *Time evolution with local time stepping: Compute the discretized space operator $\mathcal{A}$ for all the leaves and virtual leaves*

(c) **do** $k = 1, \ldots, 2^L$ *(k counts intermediate time steps)*

- *Compute the intermediate time steps depending on the position of the leaf as explained in Section 4.1.*
- **if** k is odd **then** *update the tree structure:*
  - *Recalculate the values on the nodes and the virtual nodes by projection from the leaves. Compute the details in the whole tree. If the detail in a node is smaller than the prescribed tolerance, then the cell and its brothers are* deletable.
  - *If some node and all its sons are deletable, and the sons are leaves without virtual sons, then delete sons. If this node has no sons and it is not deletable and it is not at level $l = L$, then create sons.*
  - *Update the values in the new sons by prediction from the former leaves.*

  endif

enddo

(Now, after 2^L intermediate steps, all the control volumes are synchronized.)

enddo

Here *total_time_steps* is the total time steps needed to reach T_{final}, with Δt_0 as the maximum time step allowed by the CFL condition using the coarsest space step.

Chapter 5

Numerical simulations

In this Chapter we present a variety of numerical examples where we test the good performance of the finite volume schemes and the fully adaptive multiresolution method. We detail these findings by displaying the corresponding approximate solutions, errors in different norms, convergence rates, data compression rates, CPU speed-up rates and choice of the threshold parameters. Or results demonstrate the advantage of the multiresolution approach compared with standard finite volume schemes. In our experiments, we have obtained a considerable speed-up on the computations and also a substantial memory compression, while keeping the same accuracy order as in the reference schemes.

5.1 Strongly degenerate parabolic equations

5.1.1 Numerical results for batch sedimentation

As in [36, 135], we consider a suspension characterized by the functions (1.4) with $v_\infty = 1.0 \times 10^{-4}\,\mathrm{m/s}$, $K = 5$ and $u_{\max} = 1.0$, and (1.5) with $\sigma_0 = 1.0\,\mathrm{Pa}$, $u_{\mathrm{c}} = 0.1$ and $\beta = 6$, respectively. The remaining parameters are $\Delta_\varrho = 1660\,\mathrm{kg/m^3}$ and $g = 9.81\,\mathrm{m/s^2}$. Note that for (1.4) and $\beta \in \mathbb{N}$, the function $A(u)$ has a closed algebraic form [31]. In Figure 5.2 we show the model functions $b(u)$ and $A(u)$. In the batch sedimentation example, we consider an initially homogeneous suspension with $u_0 \equiv 0.08$ in a column of depth $H = 1\,\mathrm{m}$.

Before discussing in detail the performance of the scheme for this case, we display in Figure 5.1 the complete numerical solution until $t = 20000\,\mathrm{s}$ obtained by the fully adaptive multiresolution scheme in order to illustrate the physics of the model. Figure 5.1 illustrates that the suspension-clear liquid interface propagates as a sharp shock and the transition between the region of initial concentration and the sediment rising from below is sharp. We can also note the formation of a stationary sediment. In Figure 5.1 the visual grid used to represent the numerical solution is much coarser than the computational.

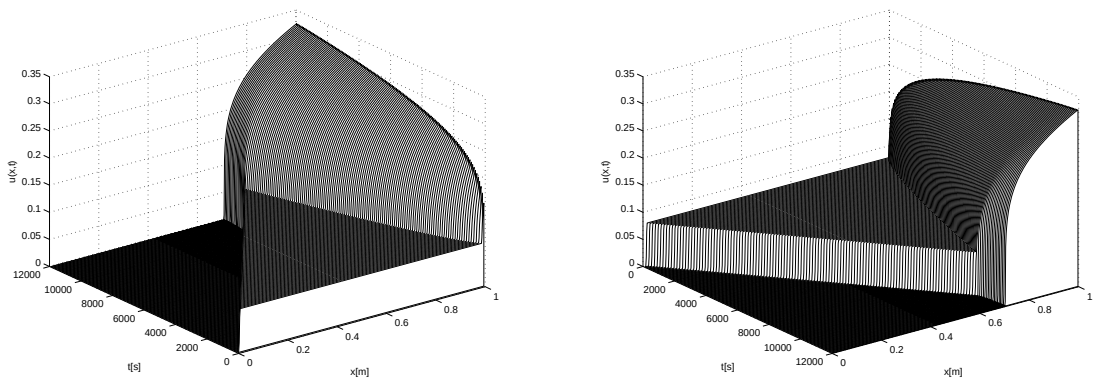

Figure 5.1: *Batch sedimentation: time-space representation of the solution.*

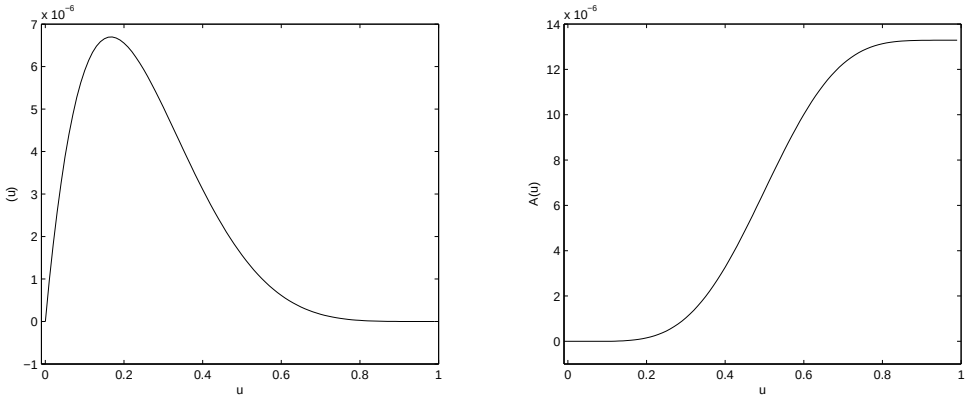

Figure 5.2: *Batch sedimentation: model functions $b(u)$ (left) and $A(u)$ (right).*

Computations on uniform fine meshes.-

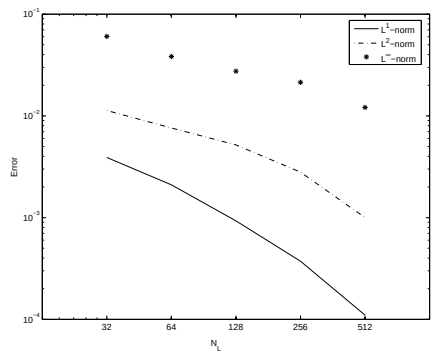

Figure 5.3: *Batch sedimentation: errors for different degrees of freedom.*

To estimate the convergence rate of the FV scheme detailed in Section 2.1, we performed numerical experiments using a fixed time step (with the third-order, three-step RK scheme defined by (4.2), (4.4) instead of an adaptive RKF time discretization) for all computations. We calculated a reference solution on a fine mesh with $J = 2048$ and performed computations using $J = 128$, 256, 512 and 1024. We compared errors at three different instants: before the front and back waves meet ($t = 4000\,\mathrm{s}$), near the point at which they meet ($t = 9000\,\mathrm{s}$), and after the solution has reached a steady state ($t = 12000\,\mathrm{s}$). In all cases, the errors between the FV computations with 2^l, $l = 7, \ldots, 10$ control volumes are plotted in Figure 5.3 versus the corresponding degrees of freedom in a double logarithmic graphic, where the slope corresponding to the L^1 norm of the error is $\alpha \approx 0.6$. We have also used different initial functions $u_0(x)$ (smooth functions and piecewise constants with several discontinuities). Of course, the observed convergence rate depends on the number and strength of discontinuities of the initial datum; to obtain a conservative estimate, we choose the following fairly rough initial condition, on which the results of Figure 5.3 are based:

$$u_0(x) = \begin{cases} 0 & \text{for } x \in [0, \frac{1}{8}] \cup [\frac{2}{8}, \frac{1}{4}] \cup [\frac{5}{8}, \frac{3}{4}] \cup [\frac{7}{8}, 1], \\ 0.1 & \text{otherwise,} \end{cases} \tag{5.1}$$

In Figure 5.4 we show the evolution of the time step depending on the initial CFL value, using the FV scheme on a uniform fine mesh with global adaptivity, and the RK3(2) method introduced in Section 4.2. The parameters are $N_L = 128$, $\delta_{\text{desired}} = 0.0005$ and $\mathcal{S}_0 = 0.01$. For all choices of the initial CFL number, the time step converges to the value $0.0621\,\mathrm{s}$, and Table 5.1 indicates that the adaptation of the step size reduces the computational cost. Here, the gain is substantially larger for initial CFL values above the maximum CFL number allowed by (2.5). We also note that the final error with respect to the reference solution is reduced for the time adaptive schemes compared to the FV scheme with fixed time step, even when these configurations violate (2.5).

Multiresolution examples.- For this example, we take an initial dynamic graded tree, allowing $L = 11$ multiresolution levels. We use a fixed time step determined by $\lambda = 20\,\mathrm{s/m}$, so that $\Delta t = \lambda h_L$. The prescribed tolerance ε_{R} is obtained from (3.17), where the constant C for this example corresponds to a factor $C = 500$ (see the Appendix for details) , so $\varepsilon_{\mathrm{R}} = 5.16 \times 10^{-5}$ and the threshold strategy is $\varepsilon_l = 2^{l-L}\varepsilon_{\mathrm{R}}$. The constants in the corresponding form of (3.17) are $\|b'\|_\infty = 9.0296 \times 10^{-5}\,\mathrm{m/s}$ and $\|a\|_\infty = 3.5981 \times 10^{-5}\,\mathrm{m^2/s}$.

We simulate the process until the phenomenon enters in a steady state ($t_{\text{final}} = 12000\,\mathrm{s}$). Figures 5.5 (a), (c)

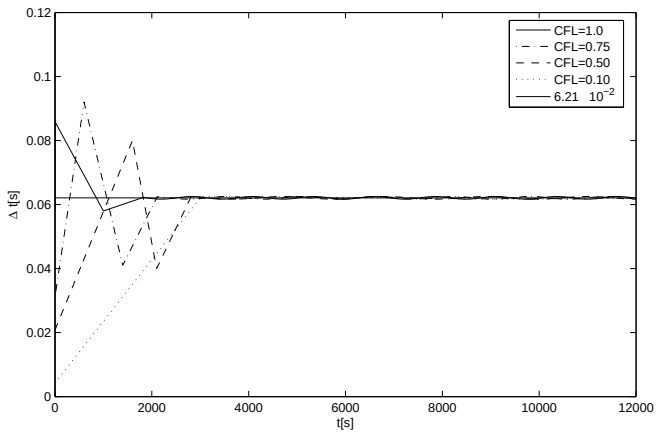

Figure 5.4: *Batch sedimentation: evolution of the time step depending on the initial CFL value for the FV scheme with global time adaptivity using the RK3(2) method.*

CFL_0	V	Initial Δt [s]	Final Δt [s]	L^∞-error	L^2-error	L^1-error
(*) 0.50	1	7.81×10^{-3}	7.81×10^{-3}	6.99×10^{-3}	5.96×10^{-3}	5.78×10^{-3}
1.00	27.22	5.09×10^{-2}	6.18×10^{-2}	3.16×10^{-3}	3.04×10^{-3}	2.17×10^{-3}
0.75	16.49	3.11×10^{-2}	6.15×10^{-2}	3.56×10^{-3}	2.79×10^{-3}	2.03×10^{-3}
0.50	10.34	7.81×10^{-3}	6.13×10^{-2}	3.21×10^{-3}	2.71×10^{-3}	2.05×10^{-3}
0.10	6.20	4.21×10^{-3}	6.12×10^{-2}	3.01×10^{-3}	2.38×10^{-3}	1.64×10^{-3}

Table 5.1: *Batch sedimentation: Initial* CFL*, speed-up factor* V*, initial and final time steps, and corresponding final errors.* $N_L = 128$*,* $\delta_{\text{desired}} = 0.0005$*,* $\mathcal{S}_0 = 0.1$*,* $\mathcal{S}_{\min} = 0.01$*. (*): Fixed time step RK3.*

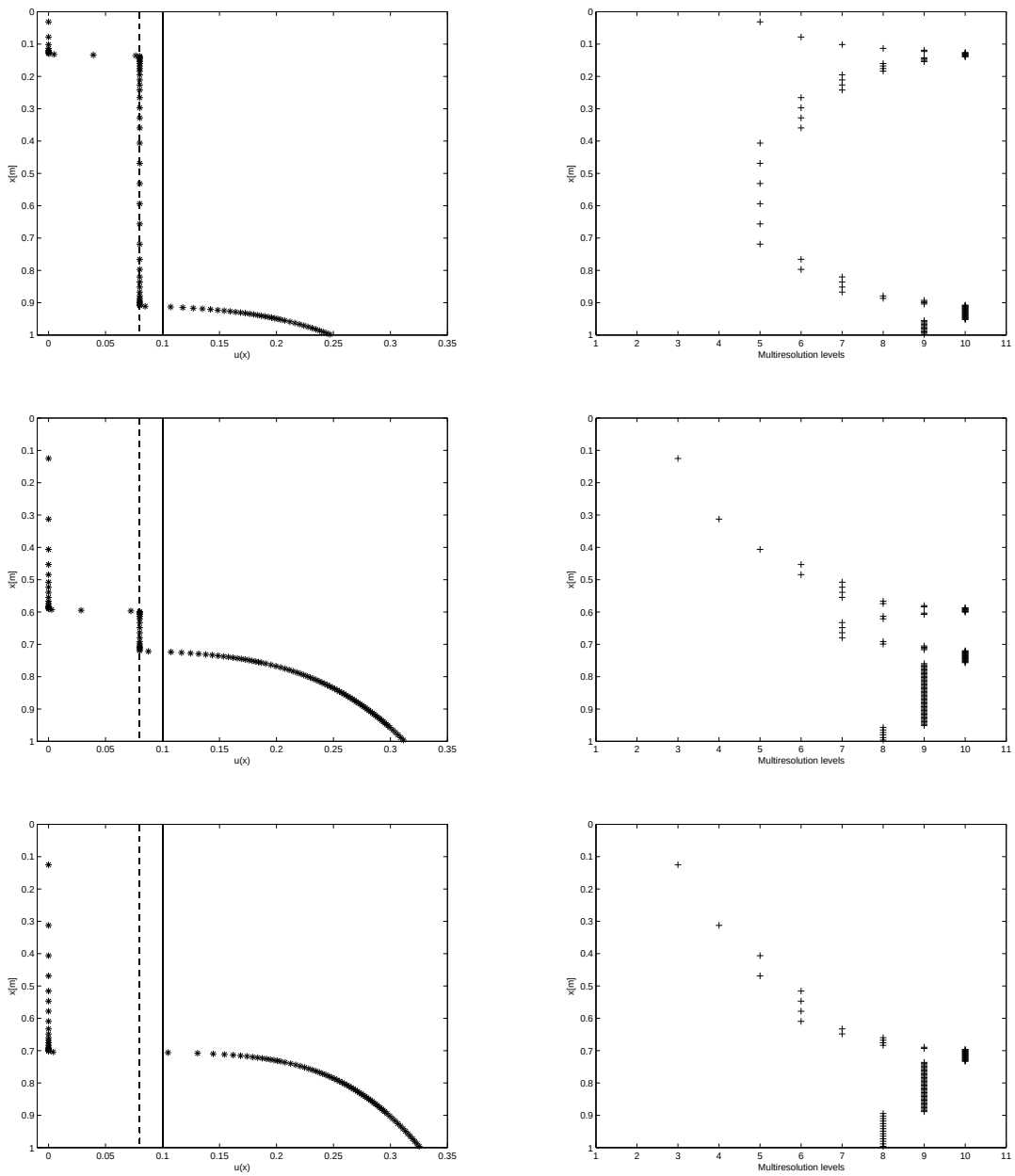

Figure 5.5: *Batch sedimentation: numerical solution (left) and positions of the leaves (right) at time instants* $t = 2000\,\mathrm{s}$, $t = 9000\,\mathrm{s}$ *and* $t = 12000\,\mathrm{s}$. *The dashed vertical line is the initial datum* $u_0 = 0.08$*; the solid vertical line marks* u_c.

and (e) show the solution before the front and back waves meet ($t = 2000\,\mathrm{s}$), near the point when these waves meet ($t = 9000\,\mathrm{s}$), and after the solution has reached a steady state ($t = 12000\,\mathrm{s}$), respectively. Figures 5.5 (b), (d) and (f) display the corresponding positions of the leaves of the tree (where a "+" marks the center of each leaf). The plotted positions indicate that the adaptation of the mesh is adapted correctly, in the sense that the multiresolution method automatically detects steep gradient regions and adds finer scales.

Method	V	μ	L^1-error	L^2-error	L^∞-error
			$t = 2000\,\mathrm{s}$		
FV	1	1	5.28×10^{-6}	1.41×10^{-6}	3.76×10^{-6}
FV + RKF	14.32	1	1.79×10^{-5}	8.91×10^{-6}	1.66×10^{-5}
MR	8.21	15.93	2.23×10^{-5}	2.35×10^{-5}	3.83×10^{-5}
MR + RKF	27.42	15.92	1.28×10^{-4}	4.57×10^{-5}	6.36×10^{-5}
			$t = 9000\,\mathrm{s}$		
FV	1	1	2.11×10^{-6}	1.28×10^{-6}	8.46×10^{-6}
FV + RKF	14.38	1	3.45×10^{-5}	8.95×10^{-6}	3.29×10^{-5}
MR	9.32	15.64	3.32×10^{-5}	3.84×10^{-5}	4.72×10^{-5}
MR + RKF	31.20	15.65	2.49×10^{-4}	4.08×10^{-5}	7.65×10^{-5}
			$t = 12000\,\mathrm{s}$		
FV	1	1	6.38×10^{-7}	4.84×10^{-7}	5.03×10^{-7}
FV + RKF	14.49	1	5.61×10^{-6}	1.27×10^{-6}	4.31×10^{-6}
MR	9.87	14.52	5.41×10^{-6}	6.79×10^{-5}	1.43×10^{-6}
MR + RKF	33.05	14.52	8.74×10^{-5}	1.82×10^{-5}	4.29×10^{-5}

Table 5.2: *Batch sedimentation: corresponding simulated time t, speed-up factor V, data compression rate μ, and normalized errors for different methods at different times. $L = 11$ multiresolution levels.*

From Table 5.2 we infer that the multiresolution computation is always cheaper in CPU time and in memory requirements than the FV method on the finest grid. The CPU time used with adaptive time stepping is roughly a third of the CPU time required with a fixed time step. The fixed time step for the MR calculation (with $\mathsf{CFL} = 1/2$) is $\Delta t_{\mathrm{fixed}} = 8.24 \times 10^{-3}\,\mathrm{s}$ and the adaptive time step for the MR (+RKF) calculation apparently converges to $\Delta t = 2.34 \times 10^{-2}\,\mathrm{s} \approx 3\Delta t_{\mathrm{fixed}}$. It is worth pointing out that the time adaptivity is global in the sense that time stepping is dominated by the time step on the finest resolution level $l = L$.

The L^1, L^2, and L^∞ norms of the error between the numerical solution obtained by multiresolution for different multiresolution levels L, and a finite volume approximation on a uniform fine grid, are depicted in Figure 5.6. In fact, we compute in practice the error between the numerical solution obtained by multiresolution and the projection of the numerical solution by FV approximation. Comparisons of speed-up factor and data compression for different maximal multiresolution levels L are displayed in Figure 5.7.

Table 5.3 summarizes the speed-up factor V, the compression rate μ and errors for the FV and multiresolution schemes using different maximal multiresolution levels. The simulated time is $t = 2000\,\mathrm{s}$. Figure 5.8 shows the corresponding L^1-errors, compared with a reference solution obtained by finite volume approximation on a uniform fine grid with 2^{13} control volumes. Note that the slope for all methods is practically the same.

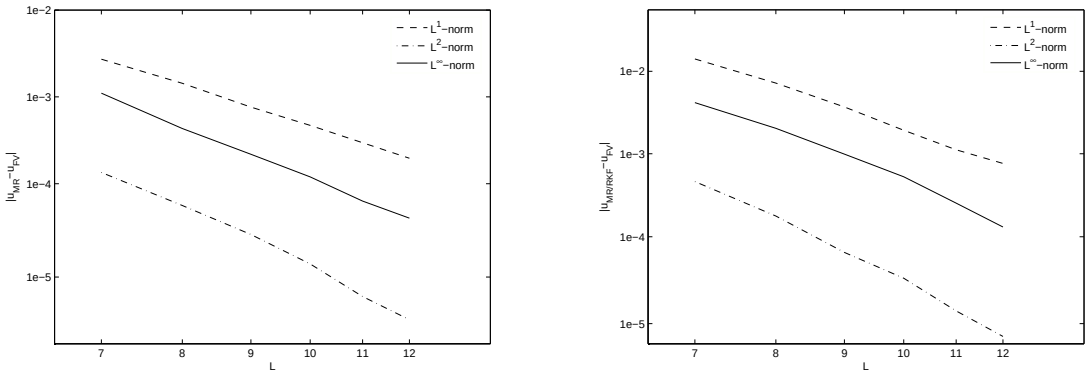

Figure 5.6: *Batch sedimentation: errors* $\|\bar{u}_{\mathrm{MR}} - \bar{u}_{\mathrm{FV}}\|_1$, $\|\bar{u}_{\mathrm{MR}} - \bar{u}_{\mathrm{FV}}\|_2$ *and* $\|\bar{u}_{\mathrm{MR}} - \bar{u}_{\mathrm{FV}}\|_\infty$ *(left) and errors* $\|\bar{u}_{\mathrm{MR/RKF}} - \bar{u}_{\mathrm{FV}}\|_1$, $\|\bar{u}_{\mathrm{MR/RKF}} - \bar{u}_{\mathrm{FV}}\|_2$ *and* $\|\bar{u}_{\mathrm{MR/RKF}} - \bar{u}_{\mathrm{FV}}\|_\infty$ *(right) for different scales* L*. The simulated time is* $t = 2000\,\mathrm{s}$.

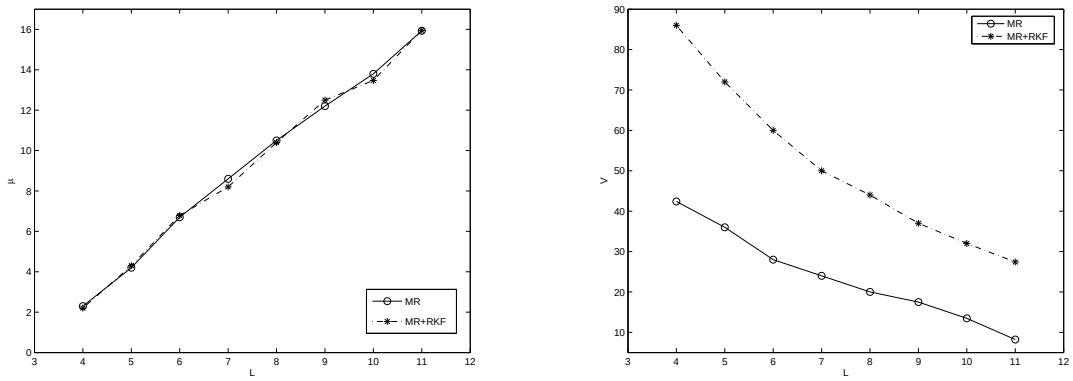

Figure 5.7: *Batch sedimentation: data compression rate* μ *(left) and speed-up factor* V *(right) for different scales* L*. Comparison between multiresolution with fixed and adaptive time stepping. The simulated time is* $t = 2000\,\mathrm{s}$.

Method	V	μ	L^1-error	L^2-error	L^∞-error
			$L = 10$		
FV	1	1	1.35×10^{-5}	8.70×10^{-4}	9.35×10^{-4}
MR	8.78	12.76	4.09×10^{-4}	1.35×10^{-4}	7.49×10^{-4}
MR+RKF	32.15	12.76	6.35×10^{-4}	2.74×10^{-4}	8.88×10^{-4}
			$L = 11$		
FV	1	1	4.37×10^{-6}	5.68×10^{-7}	1.47×10^{-5}
MR	10.46	15.93	1.23×10^{-5}	2.35×10^{-5}	3.83×10^{-5}
MR+RKF	39.19	15.95	5.34×10^{-5}	4.39×10^{-5}	6.01×10^{-5}
			$L = 12$		
FV	1	1	1.29×10^{-9}	6.37×10^{-9}	8.65×10^{-10}
MR	12.70	16.34	4.16×10^{-6}	1.01×10^{-7}	6.72×10^{-7}
MR+RKF	43.21	16.35	5.47×10^{-6}	6.44×10^{-7}	1.38×10^{-6}

Table 5.3: *Batch sedimentation: Corresponding simulated time, speed-up factor V, data compression rate μ, and errors for different methods at different maximal scales.*

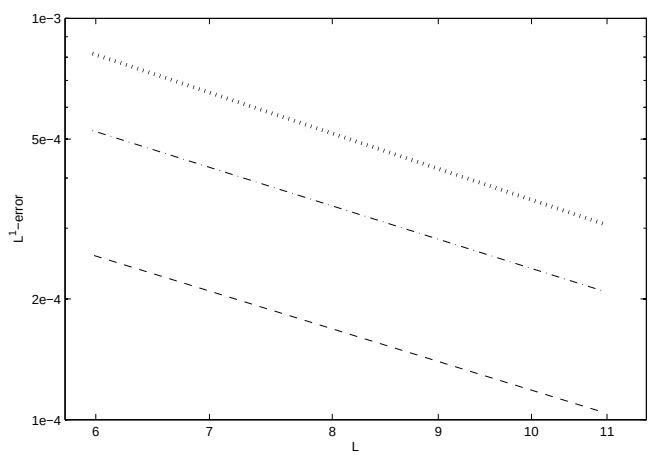

Figure 5.8: *Batch sedimentation: L^1-errors for the MR method (dash-dotted), MR+RKF method (dotted) and FV method (dashed).*

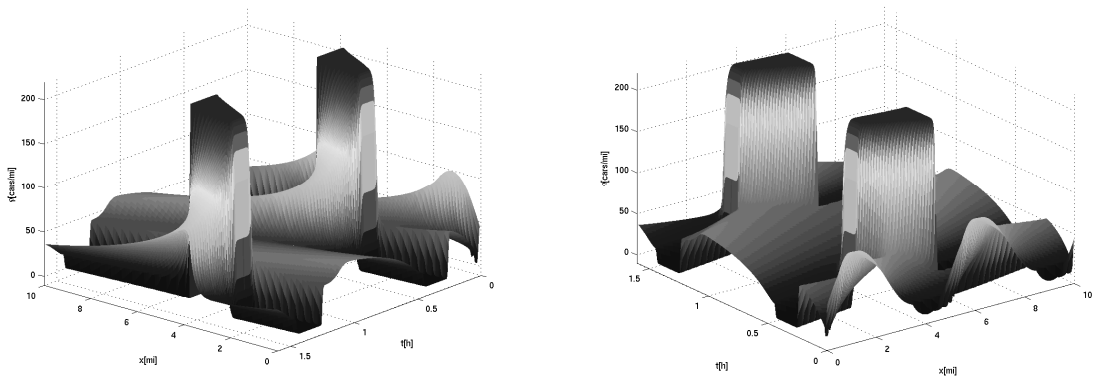

Figure 5.9: *Traffic flow: time-space representation of the solution.*

5.1.2 Traffic flow on a circular road

We consider the traffic model with driver's reaction outlined in Section 1.1, and choose the velocity function and model parameters according to [32, 123]. The velocity function is given by (1.6) with $u_{\max} = 220\,\text{cars/mi}$, $C = \mathrm{e}/7 = 0.38833$ and $v_{\max} = 70\,\text{mph}$, so that

$$b(u) = \begin{cases} v_{\max} u & \text{for } 0 \le u \le u_{\mathrm{c}} = 16.7512\,\text{cars/mi}, \\ v_{\max}(\mathrm{e}/7) u \ln(u_{\max}/u) & \text{for } u_{\mathrm{c}} < u \le u_{\max}, \\ 0 & \text{otherwise.} \end{cases}$$

For the traffic flow example, we choose the parameters $\tilde{a} = 0.1\,g$, where g is the acceleration of gravity in mi/h^2, $\tau = 2\,\text{s} = 0.000\bar{5}\,\text{h}$ and $L_{\min} = 0.05\,\text{mi}$. This yields the following integrated diffusion coefficient $A(u)$, measured in cars $\cdot$ mph, see [32] for details on its algebraic derivation:

$$A(u) = \begin{cases} 0 & \text{for } u \le u_{\mathrm{c}}, \\ 1.27099 \cdot (41.878u - 12.787u \ln u + u(\ln u)^2) & \\ \qquad -0.4105u - 286.54 & \text{for } u_{\mathrm{c}} < u \le u^*, \\ 117.9003 + 0.94864u & \text{for } u > u^*, \end{cases}$$

where $u^* := 78.2198\,\text{cars/mi}$. The model functions $b(u)$ and $A(u)$ are depicted in Figure 5.10.

We assume a circular road of length $H = 10\,\text{mi}$, so that the periodic boundary condition

$$u(H,t) = u(0,t), \quad t \in (0,T] \tag{5.2}$$

applies. We assume the smooth initial density distribution $u_0(x) = 50(1 + \sin(0.4\pi x))\,\text{cars/mi}$. In addition, at $x = 5\,\text{mi}$, a traffic light S is placed with

$$S(t) = \begin{cases} 0\ (\text{red}) & \text{for } t \in [(k + 0.125)\,\text{h}, (k + 0.375)\,\text{h}],\ k = 0, 1, 2, \ldots, \\ 1\ (\text{green}) & \text{otherwise.} \end{cases} \tag{5.3}$$

Note that this example involves periodicity both in space (due to the periodic boundary condition (5.2)), in time (due to the behavior of the traffic light), and is provided with periodic initial condition.

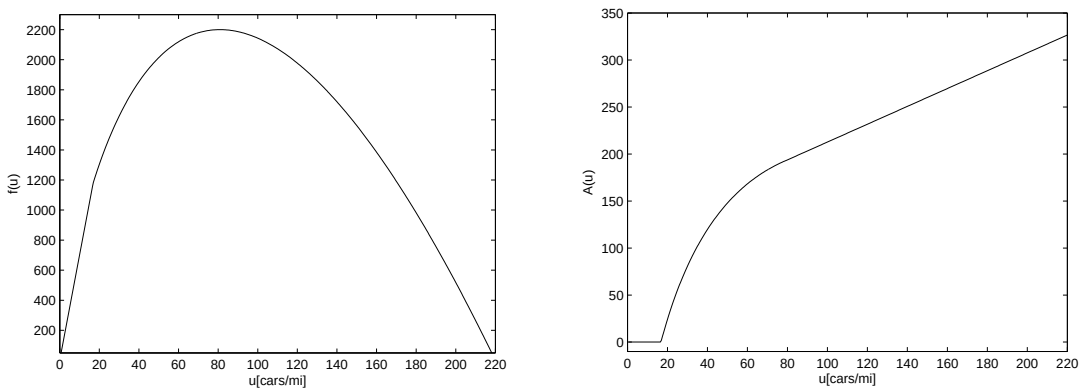

Figure 5.10: *Traffic flow: model functions $b(u)$ (left) and $A(u)$ (right).*

Before discussing the performance of the fully adaptive multiresolution scheme, we present in Figure 5.9 three-dimensional plots of the numerical solution obtained for by this scheme. It illustrates that a nearly periodic solution quickly evolves. Moreover, the depletion of the zone behind the traffic light and the queue of cars waiting in front of it periodically produces traveling type-change interfaces, i.e. jumps between the solution value zero and sub-critical values. In Figure 5.9, the visual grid used to represent the numerical solution is again much coarser than the computational one.

Finest grid computations.- In Figure 5.11 we show the time evolution of the time step depending on the initial value of CFL, using the FV scheme on a uniform fine mesh with global adaptivity and the RK3(2) method described in Section 4.2. In all cases, the time step apparently converges to the value 1.217×10^{-4} s. Here, the adaptivity of the step size reduces the computational cost, see Table 5.4.

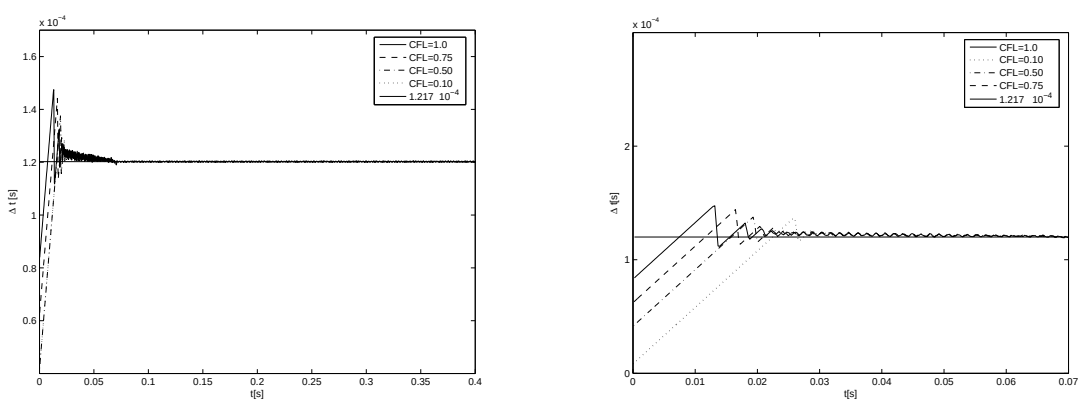

Figure 5.11: *Traffic flow: evolution of the time step depending on the initial value of* CFL *for the FV scheme with global time adaptivity using the RK3(2) method (left), and zoom until $t = 0.07$ h (right). $N_L = 256$, $\delta_{\text{desired}} = 0.001$ and $\mathcal{S}_0 = 0.01$.*

Multiresolution examples.- We take an initial dynamic graded tree, allowing $L = 10$ multiresolution levels. First we use a multiresolution procedure with fixed time step, taking CFL $= 1/2$, and we simulate the process until $t_{\text{final}} = 1.6$ h. Figure 5.12 shows the solution before the traffic light is red and during the red phase.

CFL_0	V	Initial Δt [h]	Final Δt [h]	L^∞-error	L^2-error	L^1-error
(*) 0.50	1	4.10×10^{-5}	4.10×10^{-5}	5.62×10^{-4}	1.47×10^{-4}	8.32×10^{-4}
1.00	16.32	8.22×10^{-5}	1.29×10^{-4}	8.53×10^{-3}	5.41×10^{-3}	5.06×10^{-3}
0.75	11.34	6.16×10^{-5}	1.17×10^{-4}	1.38×10^{-3}	2.77×10^{-3}	3.46×10^{-3}
0.10	8.75	8.62×10^{-5}	1.22×10^{-4}	7.51×10^{-4}	2.01×10^{-3}	8.86×10^{-4}

Table 5.4: *Traffic model: initial* CFL*, speed-up factor V, initial and final time steps, and corresponding normalized errors. $N_L = 256$, $\delta_{\text{desired}} = 0.001$, $\mathcal{S}_0 = 0.1$, $\mathcal{S}_{\min} = 0.01$. (*): Fixed time step RK3.*

Figure 5.13 shows the solution right after the *green* phase and part of the second cycle of the traffic light. For this example, the factor C in (3.17) is set to $C = 1 \times 10^6$ (see details in the Appendix), yielding a reference tolerance of $\varepsilon_{\text{R}} = 1.33 \times 10^{-5}$ for $L = 10$. Here, the Lipschitz constants in the corresponding form of (3.17) are $\|b'\|_\infty = 70\,\text{mi/h}$ and $\|a\|_\infty = 7.9177\,\text{mi}^2/\text{h}$. Errors in different norms and compression rates V and μ for different methods are displayed in Table 5.5.

Method	V	μ	L^1-error	L^2-error	L^∞-error
			$t = 0.1\text{h}$		
MR	5.12	7.93	2.31×10^{-4}	4.79×10^{-4}	5.83×10^{-5}
MR+RKF	12.47	7.93	6.18×10^{-4}	1.07×10^{-3}	6.66×10^{-5}
			$t = 0.2\,\text{h}$		
MR	5.21	5.99	1.76×10^{-4}	7.68×10^{-5}	8.39×10^{-6}
MR+RKF	16.34	5.99	3.67×10^{-4}	2.73×10^{-4}	3.00×10^{-5}
			$t = 0.3\,\text{h}$		
MR	5.23	7.58	2.24×10^{-4}	7.89×10^{-5}	9.46×10^{-6}
MR+RKF	17.34	7.58	7.47×10^{-4}	9.21×10^{-5}	3.67×10^{-5}
			$t = 0.4\,\text{h}$		
MR	7.42	5.54	1.83×10^{-4}	3.32×10^{-5}	4.36×10^{-6}
MR+RKF	19.18	5.54	4.62×10^{-4}	5.29×10^{-5}	1.08×10^{-3}
			$t = 1.3\,\text{h}$		
MR	7.78	7.36	1.55×10^{-3}	5.64×10^{-5}	2.61×10^{-5}
MR+RKF	21.62	7.37	2.31×10^{-3}	8.06×10^{-5}	3.17×10^{-5}
			$t = 1.6\,\text{h}$		
MR	7.59	9.75	6.17×10^{-3}	1.01×10^{-4}	2.94×10^{-4}
MR+RKF	19.63	9.75	8.40×10^{-3}	5.16×10^{-4}	4.55×10^{-4}

Table 5.5: *Traffic flow: corresponding simulated time, speed-up factor V, data compression rate μ, and errors for different methods. $L = 10$ multiresolution levels.*

The errors in L^1, L^2, and L^∞ norms between the numerical solution obtained by multiresolution for different multiresolution levels L, and the solution obtained by finite volume approximation in a uniform fine grid, are depicted in Figure 5.14. In fact, we compute in practice the error between the numerical solution obtained by multiresolution and the projection of the numerical solution by FV approximation. Furthermore, comparisons of speed-up factor and data compression for different maximal multiresolution levels L, are depicted in Figure 5.15. All these calculations corresponds to the "red" phase, $t = 0.2\,\text{h}$.

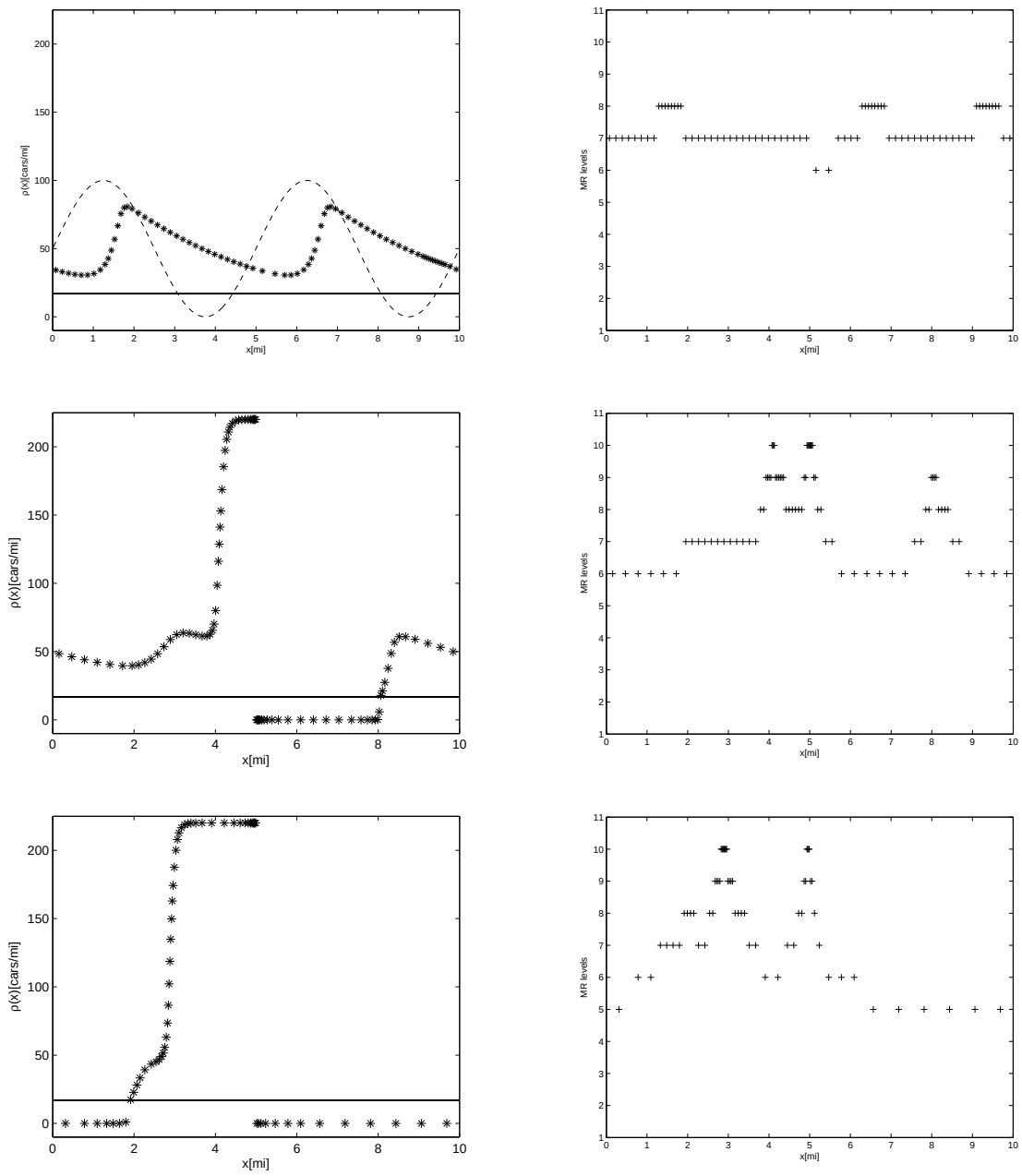

Figure 5.12: *Traffic flow: numerical solution (left) and positions of the leaves (right). The simulated times are* $t = 0.1\,\mathrm{h}$, $t = 0.2\,\mathrm{h}$ *and* $t = 0.3\,\mathrm{h}$. *The dashed curve in plot (a) is the initial datum* $u_0(x)$. *The solid horizontal line marks* u_c.

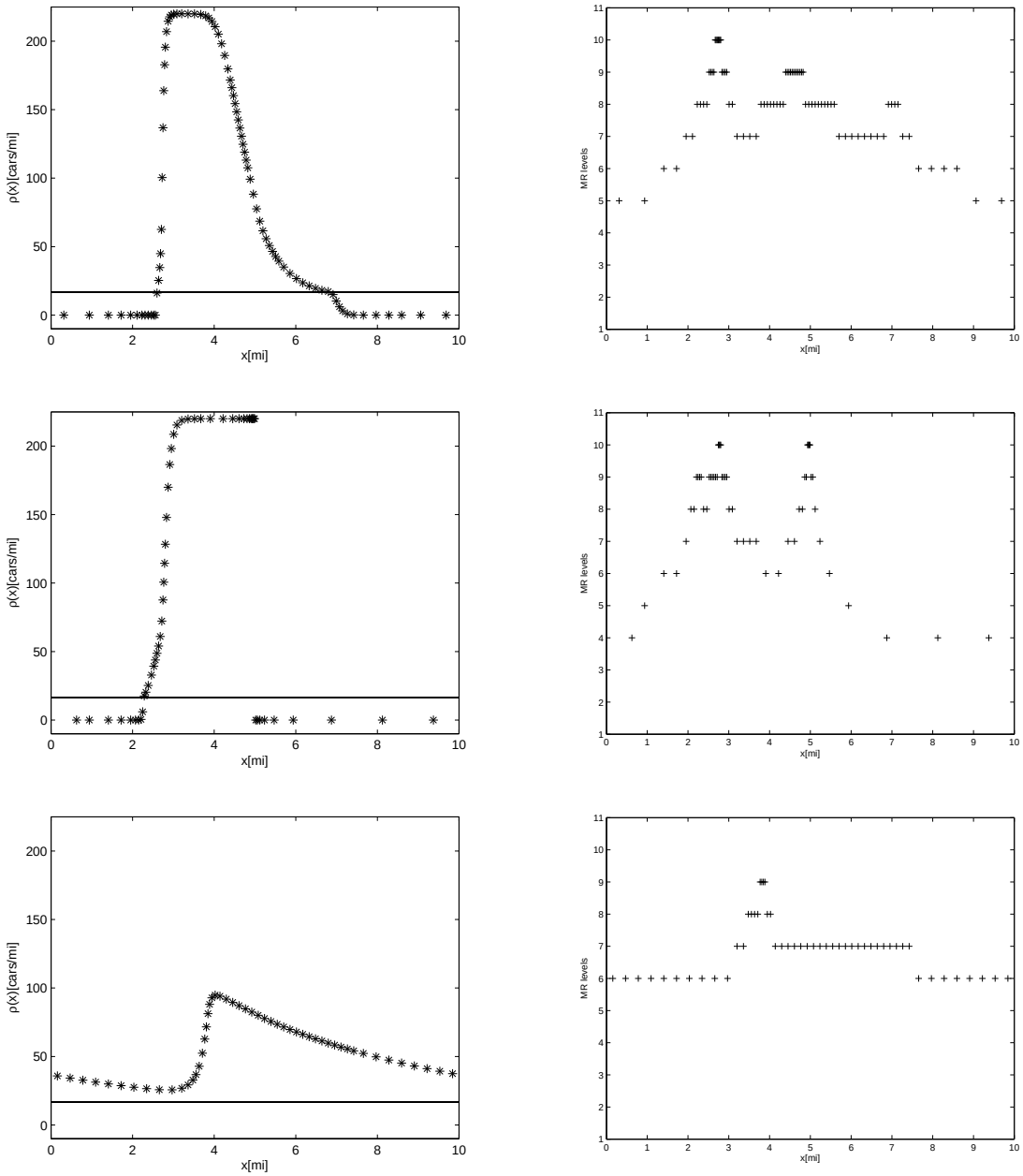

Figure 5.13: *Traffic flow: numerical solution (left) and positions of the leaves (right). The simulated times are* $t = 0.4\,\mathrm{h}$, $t = 1.3\,\mathrm{h}$ *and* $t = 1.6\,\mathrm{h}$. *The solid horizontal line marks* u_c.

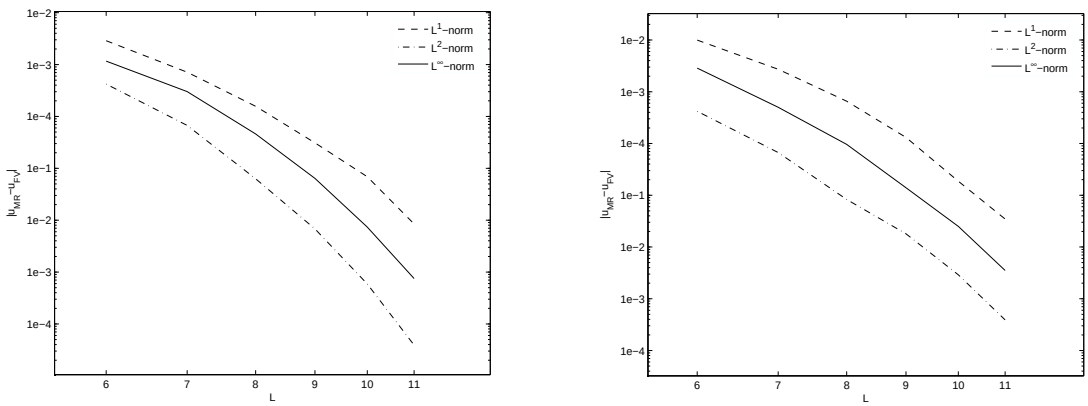

Figure 5.14: *Traffic flow: errors* $\|\bar{u}_{\mathrm{MR}} - \bar{u}_{\mathrm{FV}}\|_1$, $\|\bar{u}_{\mathrm{MR}} - \bar{u}_{\mathrm{FV}}\|_2$ *and* $\|\bar{u}_{\mathrm{MR}} - \bar{u}_{\mathrm{FV}}\|_\infty$ *(left) and errors* $\|\bar{u}_{\mathrm{MR/RKF}} - \bar{u}_{\mathrm{FV}}\|_1$, $\|\bar{u}_{\mathrm{MR/RKF}} - \bar{u}_{\mathrm{FV}}\|_2$ *and* $\|\bar{u}_{\mathrm{MR/RKF}} - \bar{u}_{\mathrm{FV}}\|_\infty$ *(right) for different scales* L*. The simulated time is* $t = 0.2\,\mathrm{h}$*.*

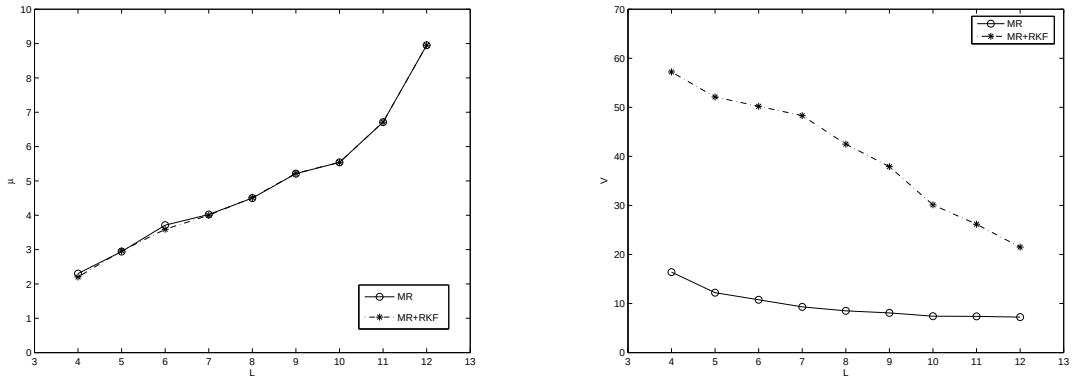

Figure 5.15: *Traffic flow on a circular road: data compression rate* μ *(left) and speed-up factor* V *(right) for different scales* L*. The simulated time is* $t = 0.2\,\mathrm{h}$*.*

Table 5.6 summarizes the CPU time, compression rate and errors for the FV method and the multiresolution scheme, using different maximal multiresolution levels. The simulated time is $t = 0.4\,\mathrm{h}$. Here we can see that the multiresolution computation is always cheaper in CPU time and in memory requirements than the finite volume method on the finest grid, and we can also notice that the gain in speed-up factor using an adaptive time stepping is about four times the speed-up factor attained by fixed time stepping, this comes clear if we also note that the fixed time step for the MR calculation, with $\mathsf{CFL} = 1/2$ is $\Delta t = 2.217 \times 10^{-5}\,\mathrm{h}$ and the adaptive time step for the MR (+RKF) calculation tends to converge to the value $\Delta t = 9.86 \times 10^{-5}\,\mathrm{h}$, which is roughly four times the above value. Figure 5.16 shows the corresponding L^1-errors, compared with a reference solution obtained on a uniform fine grid with 2^{13} control volumes.

Method	V	μ	L^1-error	L^2-error	L^∞-error
			$L = 10$		
FV	2.21	1	3.94×10^{-6}	4.77×10^{-6}	2.53×10^{-6}
MR	7.42	5.54	1.83×10^{-4}	3.32×10^{-5}	4.36×10^{-4}
MR+RKF	32.11	5.54	4.62×10^{-4}	5.29×10^{-5}	1.08×10^{-3}
			$L = 11$		
FV	1.54	1	2.11×10^{-6}	1.28×10^{-7}	8.46×10^{-7}
MR	7.38	6.31	9.07×10^{-5}	4.68×10^{-5}	5.71×10^{-5}
MR+RKF	26.16	6.31	3.27×10^{-4}	7.21×10^{-5}	2.15×10^{-6}
			$L = 12$		
FV	1	1	1.14×10^{-8}	4.29×10^{-8}	8.65×10^{-9}
MR	7.22	8.95	4.61×10^{-5}	1.21×10^{-6}	4.72×10^{-6}
MR+RKF	21.49	8.95	1.26×10^{-4}	6.89×10^{-6}	2.02×10^{-5}

Table 5.6: *Traffic flow: speed-up factor V, data compression rate μ, and normalized errors for different methods at different maximal scales for $t = 0.4\,\mathrm{h}$.*

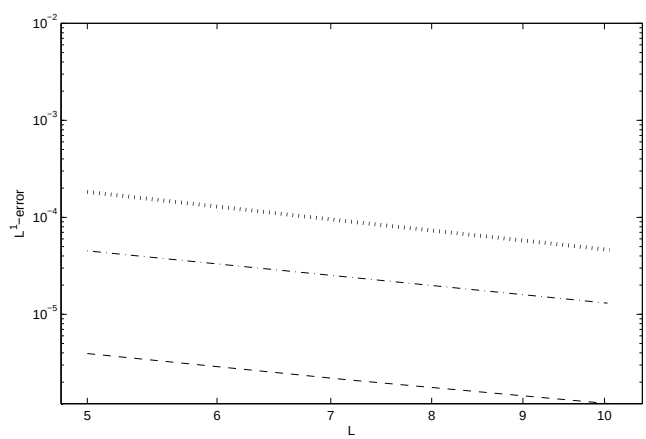

Figure 5.16: *Traffic flow: L^1-errors for the MR method (dash-dotted), MR+RKF method (dotted) and FV method (dashed).*

5.2 Degenerate parabolic equations with discontinuous flux

5.2.1 Diffusively corrected kinematic model with changing road surface conditions

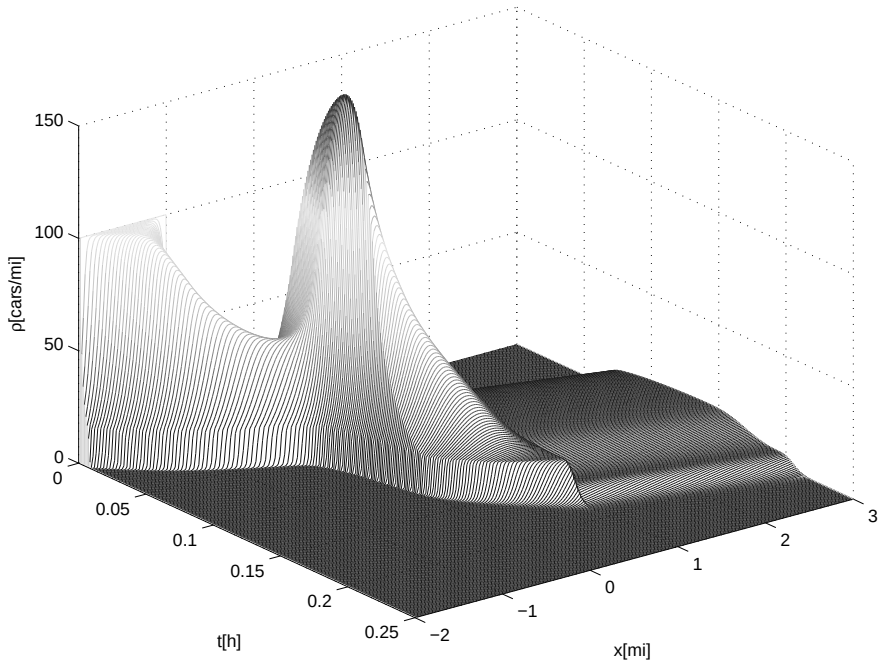

Figure 5.17: *DCK Traffic model: three-dimensional plot of the numerical solution.*

$t_{\text{final}}\,[h]$	V	η	L^1 error	L^2 error	L^∞ error
0.05	6.38	4.5511	5.16×10^{-4}	6.22×10^{-5}	5.64×10^{-5}
0.10	6.99	4.2140	4.57×10^{-4}	2.41×10^{-5}	8.16×10^{-5}
0.15	7.84	7.8168	7.21×10^{-4}	5.12×10^{-5}	7.23×10^{-4}
0.20	9.01	17.3559	1.14×10^{-3}	2.47×10^{-4}	3.86×10^{-3}

Table 5.7: *DCK Traffic model: Corresponding simulated time, speed-up factor V, compression rate, and normalized errors. $L = 10$ multiresolution levels.*

Our numerical example for this model has been chosen in such a way that results can be compared with simulations shown in Example 5 of [32]. The velocity function is given by (1.6) with $u_{\max} = 220\,\text{cars/mi}$, $C = \text{e}/7 = 0.38833$ and $v_{\max} = 70\,\text{mph}$, so that

$$f(u) = \begin{cases} v_{\max} u & \text{for } 0 \le u \le u_{\text{c}} = 16.7512\,\text{cars/mi}, \\ v_{\max}(\text{e}/7)u\ln(u_{\max}/u) & \text{for } u_{\text{c}} < u \le u_{\max}, \\ 0 & \text{otherwise.} \end{cases} \tag{5.4}$$

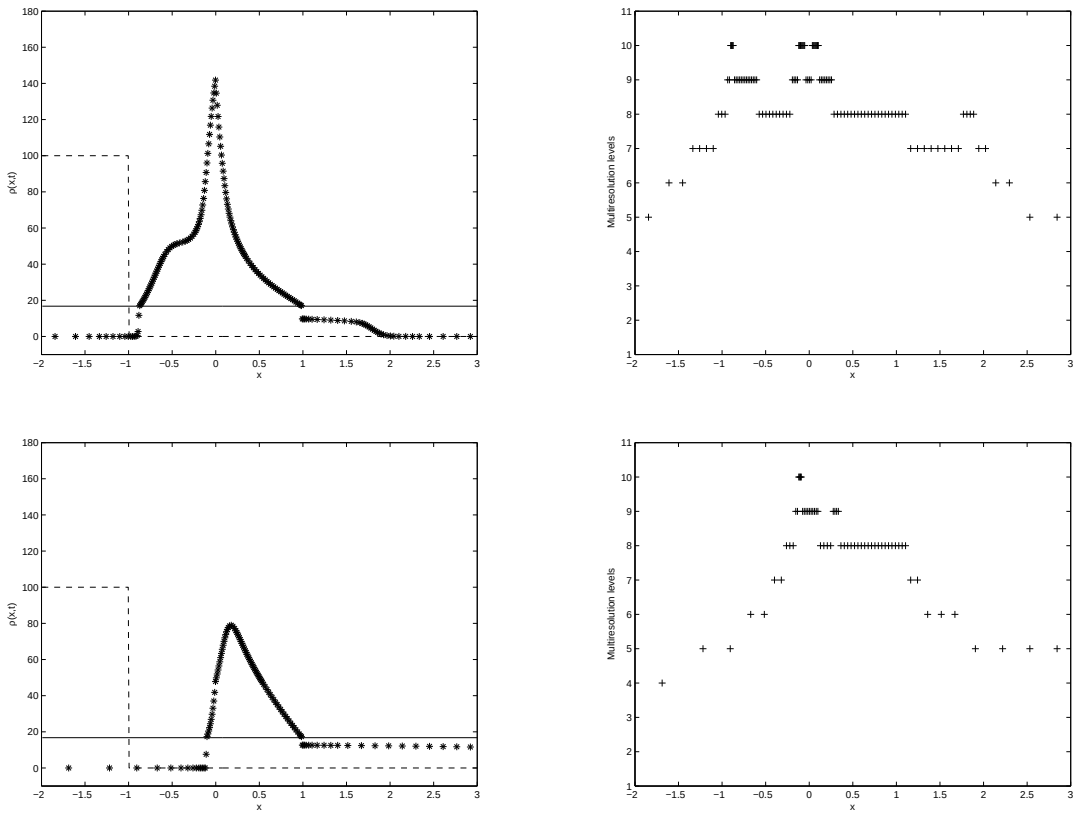

Figure 5.18: *DCK Traffic model: numerical solution (left) and positions of the leaves (right) at* $t = 0.05\,\mathrm{h}$ *and* $t = 0.1\,\mathrm{h}$.

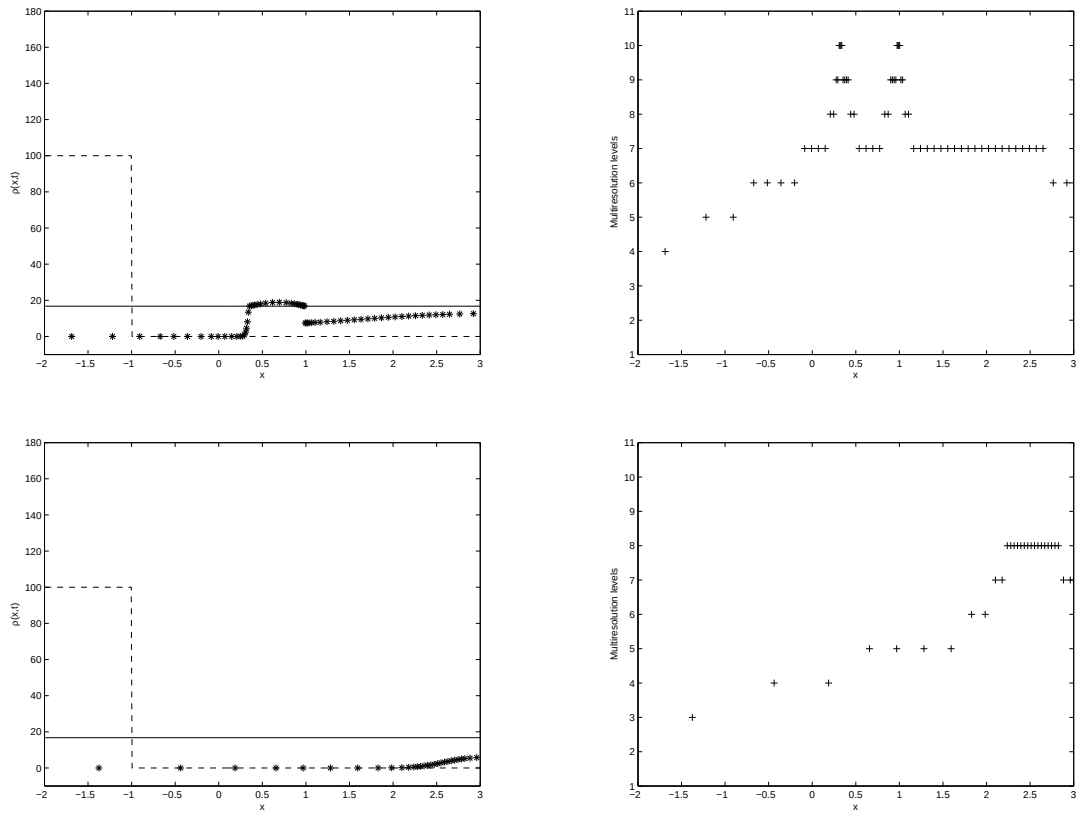

Figure 5.19: *DCK Traffic model: numerical solution (left) and positions of the leaves (right) at* $t = 0.15\,\mathrm{h}$ *and* $t = 0.2\,\mathrm{h}$.

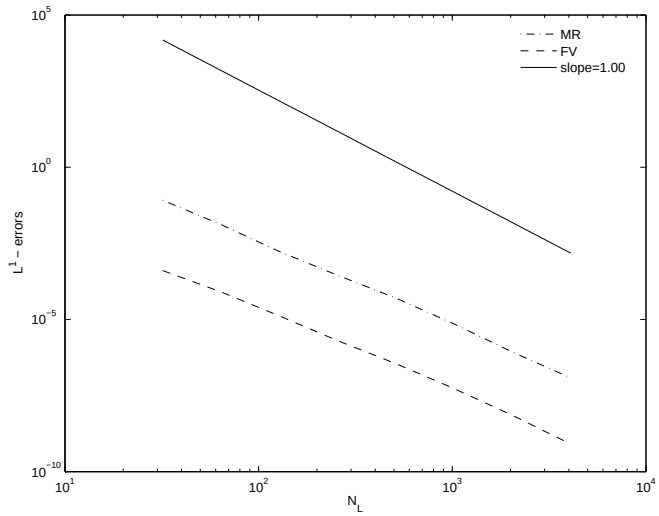

Figure 5.20: *DCK Traffic model: L^1 errors.*

We choose $v^0_{\max} = 70$ mph and $v^*_{\max} = 25$ mph. The initial density is chosen as

$$\rho_0(x) = \begin{cases} 100\,\text{cars/mi} & \text{for } -2\,\text{mi} \le x \le -1\,\text{mi}, \\ 0 & \text{otherwise.} \end{cases}$$

The integrated diffusion coefficient $A(u)$ resulting from our choice of parameters satisfies $A(u) = 0$ for $0 \le u \le u_c = 16.7512\,\text{cars/mi}$, and has an explicit algebraic representation [32, 38].

In a first example, we consider an initial convoy of cars traveling on an empty road, and wish to see how the convoy passes through the reduced speed road segment. The numerical solution obtained by our method is represented in a three-dimensional plot in Figure 5.17 and shown at four different times in Figures 5.18 and 5.19. These figures also display the corresponding position of the leaves. For these four times, Table 5.7 displays the corresponding values of the speed-up factor V, the compression rate η, and normalized approximate errors. These errors and the speed-up factor are measured with respect to a fine grid calculation (no multiresolution) with $N_L = 2^{13}$ cells. (We further comment on the behavior of V and η in the discussion of the third example.)

For this example, we take an initial dynamic graded tree, allowing $L = 10$ multiresolution levels. We use a fixed time step determined by $\lambda = 0.0003\,\text{h/mi}$, thus $\Delta t = \lambda h_L$. The prescribed tolerance ε_{R} is obtained from (3.17), where the constant C for this example corresponds to a factor $C = 10^5$, so $\varepsilon = 0.301$ and the thresholding strategy is $\varepsilon_k = 2^{k-L}\varepsilon$.

The errors in L^1 norm between the numerical solution obtained by our multiresolution scheme for different multiresolution levels L, and the numerical solution by finite volume approximation in a uniform fine grid with 2^{13} control volumes, are depicted in Fig. 5.20. In practice, we compute the error between the numerical solution obtained by multiresolution and *the projection* of the the numerical solution by finite volume approximation. We also observe the same slope ($= 0.8819$) between finite volume and multiresolution computation in the L^1 error of Figure 5.20.

5.2.2 Clarifier-thickener treating an ideal suspension ($A \equiv 0$).

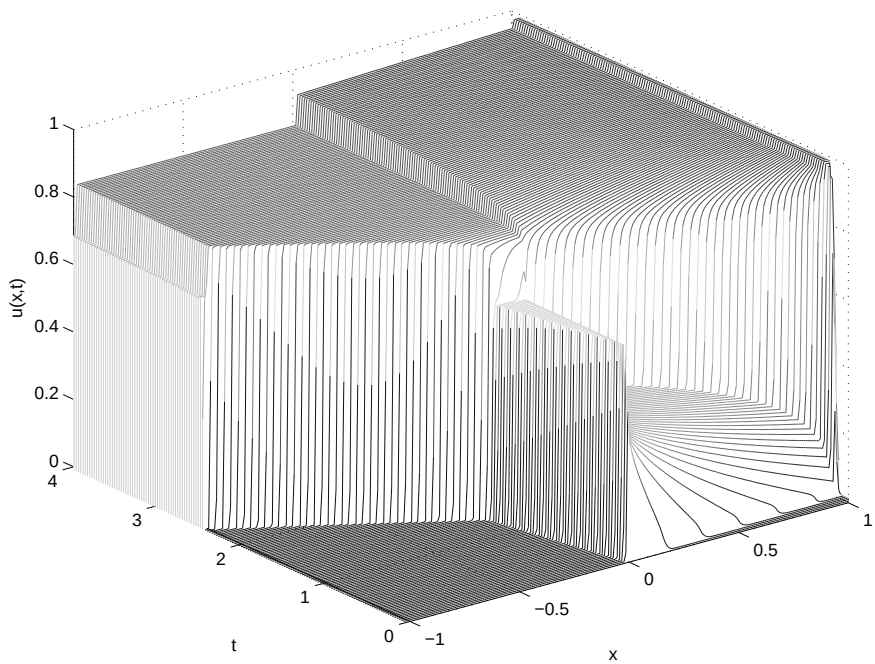

Figure 5.21: *Clarifier-thickener with $A \equiv 0$: three-dimensional plot of the numerical solution.*

t_{final}	V	η	L^1 error	L^2 error	L^∞ error
1	8.42	6.4362	2.47×10^{-4}	6.31×10^{-4}	8.49×10^{-5}
2	9.36	8.0315	4.11×10^{-4}	8.47×10^{-4}	2.40×10^{-4}
3	10.21	8.7850	3.42×10^{-4}	1.84×10^{-3}	6.74×10^{-4}
4	10.94	8.7850	4.18×10^{-4}	1.10×10^{-3}	1.26×10^{-3}

Table 5.8: *Clarifier-thickener with $A \equiv 0$: Corresponding simulated time, speed-up factor V, compression rate, and normalized errors. $L = 10$ multiresolution levels.*

For the clarifier-thickener model with $A \equiv 0$ (second example), we choose the same parameters as in [33, 34], so that results can be compared. In particular, we consider an ideal suspension that does not form compressible sediments, i.e., we set $A \equiv 0$, so that the model considered in this example actually corresponds to the first-order equation (1.10).

We consider a clarifier-thickener unit that is initially full of water by setting $u_0(x) = 0$. At $t = 0$, we start to fill up the device with feed suspension of concentration $u_{\text{F}} = 0.8$. We also consider $x_{\text{L}} = -1$ and $x_{\text{R}} = 1$ and we assume that the mixture leaving the unit at x_{L} and x_{R} is transported away at the bulk flow velocities $q_{\text{L}} = -1$ and $q_{\text{R}} = 0.6$. The suspension is characterized by the function $f(u)$ given by (1.4) with $v_\infty = 27/4$, $C = 2$ and $u_{\max} = 1$.

We use an initially graded tree with $L = 10$ multiresolution levels and a reference tolerance of $\varepsilon = 4.15\times10^{-3}$.

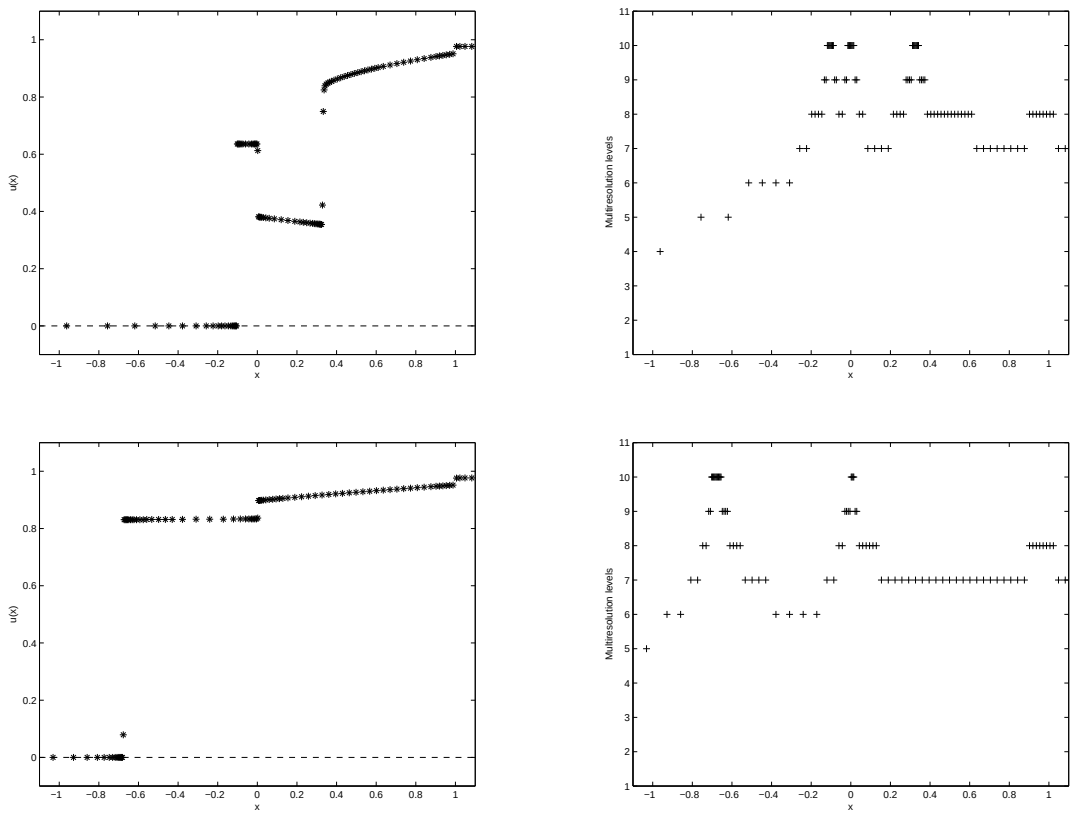

Figure 5.22: *Clarifier-thickener with $A \equiv 0$: numerical solution (left) and positions of the leaves (right) at $t = 1$ and $t = 2$.*

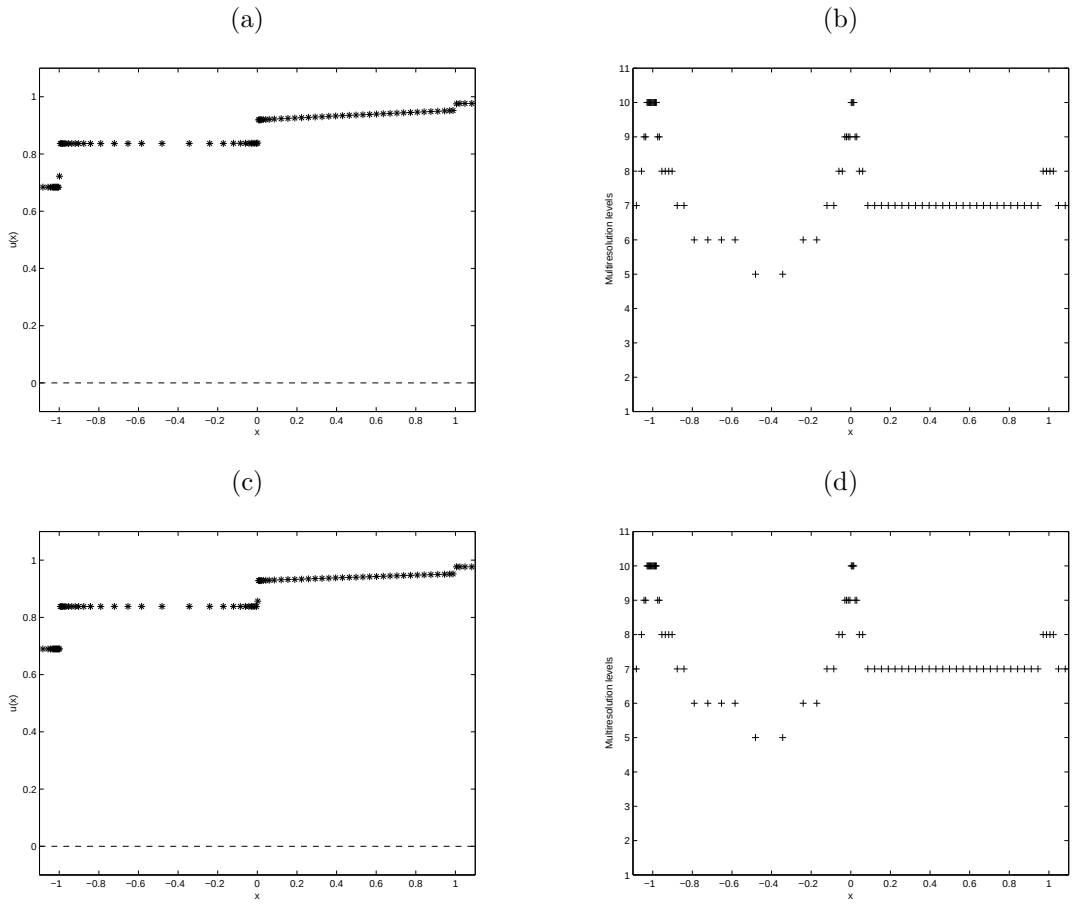

Figure 5.23: *Clarifier-thickener with $A \equiv 0$: numerical solution (left) and positions of the leaves (right) at $t = 3$ and $t = 4$.*

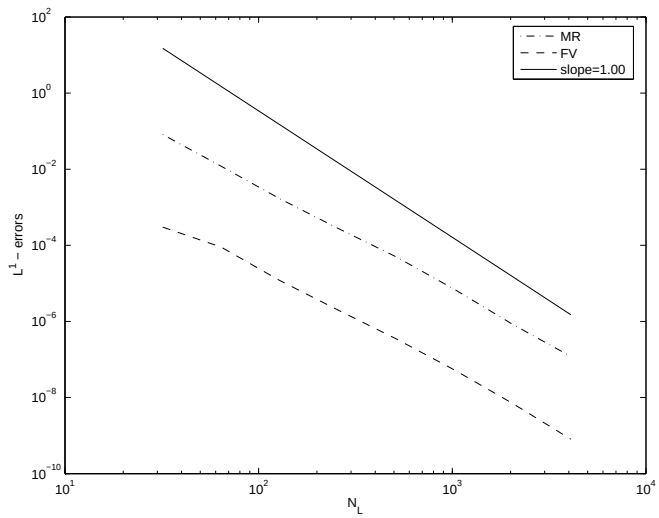

Figure 5.24: *Clarifier-thickener with $A \equiv 0$: L^1 errors.*

The finest grid has $N_L = 512$ control volumes and we choose a factor $\lambda = 1/16$. Observe that the visual grid used to display Figure 5.21 coincides with the computational grid in x direction, but in t direction, only every 50th profile is plotted.

For the clarifier-thickener model with $A \equiv 0$, we use as a reference solution a fine grid computation with 2^{13} control volumes. Table 5.8 lists the behavior of the error and the gain in computational effort and data storage for different times. Also, analogously to Example 1, we can observe in Figure 5.24 that the plots of the L^1 error, which is measured here for $t = 2$, have the same slopes.

5.2.3 Clarifier-thickener treating a flocculated suspension ($A \not\equiv 0$)

t_{final} [s]	V	η	L^1 error	L^2 error	L^∞ error
10000	7.88	4.1787	3.67×10^{-4}	8.41×10^{-5}	6.73×10^{-4}
25000	9.01	4.4265	4.82×10^{-4}	9.32×10^{-5}	8.29×10^{-4}
50000	10.74	4.4734	6.30×10^{-4}	1.24×10^{-4}	1.07×10^{-3}

Table 5.9: *Clarifier-thickener with flocculated suspension: Corresponding simulated time, speed-up factor V, compression rate, and normalized errors. $L = 9$ multiresolution levels.*

The parameter of the flux is the same as in the previous example, and the function $\sigma_{\text{e}}(u)$ is given by (1.5) with $\sigma_0 = 1.0\,\text{Pa}$, $u_{\text{c}} = 0.1$ and $\beta = 6$. The remaining parameters are $\Delta_\varrho = 1660\,\text{kg/m}^3$ and $g = 9.81\,\text{m/s}^2$. Note that for (1.4) with $\beta \in \mathbb{N}$, the function $A(u)$ has an explicit closed-form representation, see [31]. The reference numerical scheme is (2.12) with $\lambda = 40\,\text{s/m}$.

Our simulation corresponds to the choice $q_{\text{R}} = 2.5 \times 10^{-6}\,\text{m/s}$ and $q_{\text{L}} = -1.0 \times 10^{-5}\,\text{m/s}$. The feed concentration corresponds to $u_{\text{F}} = 0.086$. Figure 5.25 shows the numerical solution until $t = 50000\,\text{s}$. In

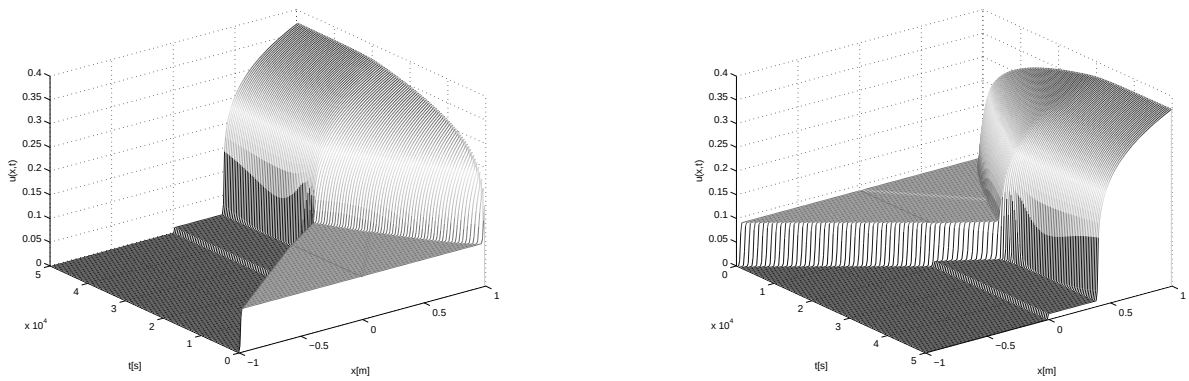

Figure 5.25: *Clarifier-thickener with flocculated suspension: two views of the time-space representation of the numerical solution.*

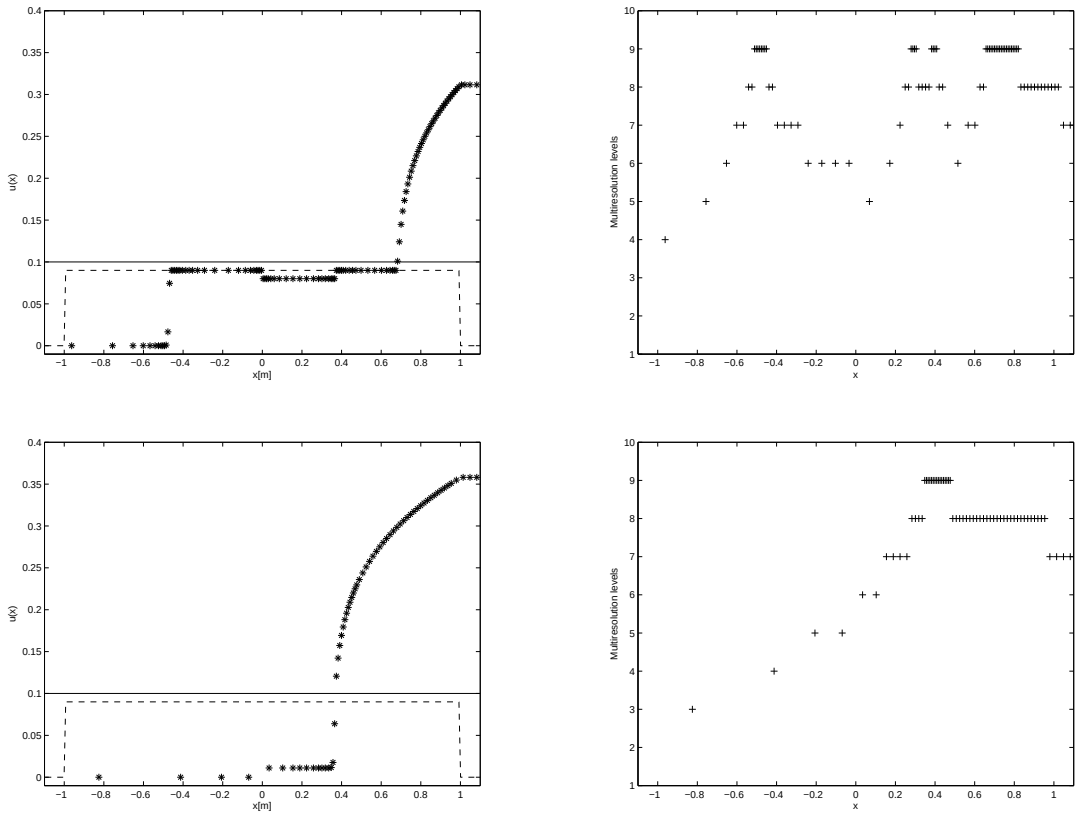

Figure 5.26: *Clarifier-thickener with flocculated suspension: numerical solution (stars) and initial condition (dashed) (left) and positions of the leaves (right) at* $t = 10000\,\mathrm{s}$, $t = 25000\,\mathrm{s}$ *for the transition to a steady state from* $u_0 = 0.09$. *The horizontal solid line in the left denotes the critical concentration* $u_\mathrm{c} = 0.1$.

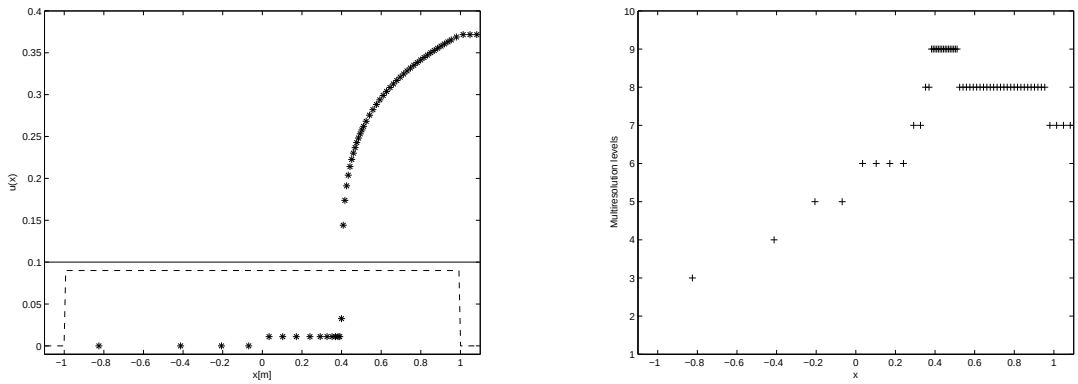

Figure 5.27: *Clarifier-thickener with flocculated suspension: numerical solution (stars) and initial condition (dashed) (left) and positions of the leaves (right) at* $t = 50000\,\mathrm{s}$ *for the transition to a steady state from* $u_0 = 0.09$. *The horizontal solid line in the left denotes the critical concentration* $u_\mathrm{c} = 0.1$.

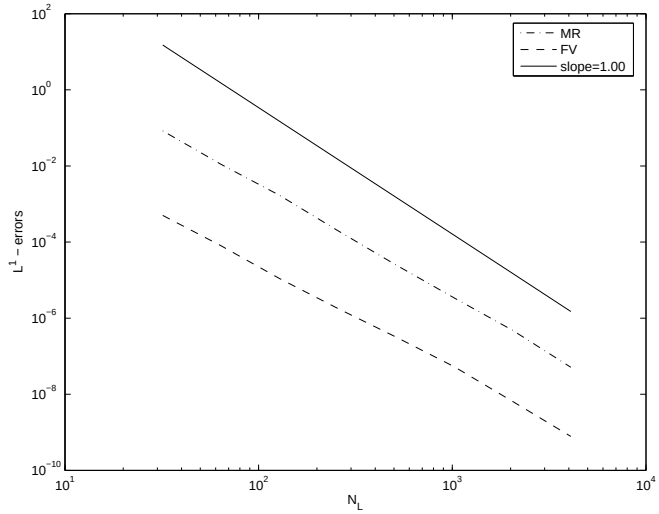

Figure 5.28: *Clarifier-thickener with flocculated suspension:* L^1 *errors.*

this case we consider the device with an initial concentration distribution of $u_0(x) = u_c$, $x \in [x_L, x_R]$ and we can observe the initial stage of the fill-up process. For this example, we take an initial dynamic graded tree, allowing $L = 8$ multiresolution levels, and for the reference tolerance we use $C = 10^{-3}$, so $\varepsilon_R = 2.24 \times 10^{-4}$.

For the clarifier-thickener model with flocculated suspension we use as a reference solution a fine grid computation with 2^{13} control volumes. Table 5.9 again displays the behavior of the error and the gain in computational effort and data storage for different times. Also, analogously to the previous examples, we observe in Figure 5.28 the same slope between the L^1 errors for the finite volume and multiresolution methods. This error is measured here at $t = 25000\,\mathrm{s}$.

Note that in all numerical examples, the speed-up factor V increases as t_{final} is increased, even if the data compression rate η remains constant, which approximately is the case in Table 5.9, or even decreases, as we see, for example, by comparing the values of η for $t_{\mathrm{final}} = 0.05\,\mathrm{h}$ and $t_{\mathrm{final}} = 0.10\,\mathrm{h}$ in Table 5.7. The explanation of this discrepancy is that while η measures the quality of performance of the multiresolution seen at the instant $t = t_{\mathrm{final}}$, the speed-up factor V is referred to the total time of simulation and also includes the "overhead" required by initializing the graded tree in step (2) of the multiresolution algorithm. The initialization requires a fixed amount of CPU time, which is independent of the number of total time steps (which is proportional to t_{final}, since we consider Δt to be fixed). On the other hand, a standard FV method on a fixed grid will always require CPU time proportional to the number of time steps. This explains why even if η does not change significantly, we observe an improvement of the speed-up factor V as t_{final} is increased.

5.2.4 An extended clarifier-thickener model

Let us consider a suspension characterized by $b(u)$ as in (1.4) with $v_\infty = 1.0 \times 10^{-4}\,\mathrm{m/s}$, $C = 5$ and $u_{\max} = 1$. Furthermore $x_L = -2\,\mathrm{m}$ and $x_R = 1\,\mathrm{m}$, the device being initially empty ($u_0 \equiv 0$). These parameters and the control variables $q_L = 0.0\,\mathrm{m/s}$, $q_R = 0.6\,\mathrm{m/s}$, $q_D = -1.0\,\mathrm{m/s}$ and $u_F = 0.7$ are chosen as in Case 5 of [30] and [42]. The reference tolerance used for this example is $\varepsilon = 4.6 \times 10^{-4}$.

Figure 5.2.4 shows the numerical solution until $t = 4$. In this case the solid material entering to the clarifying zone is fully absorbed by the singular sink term.

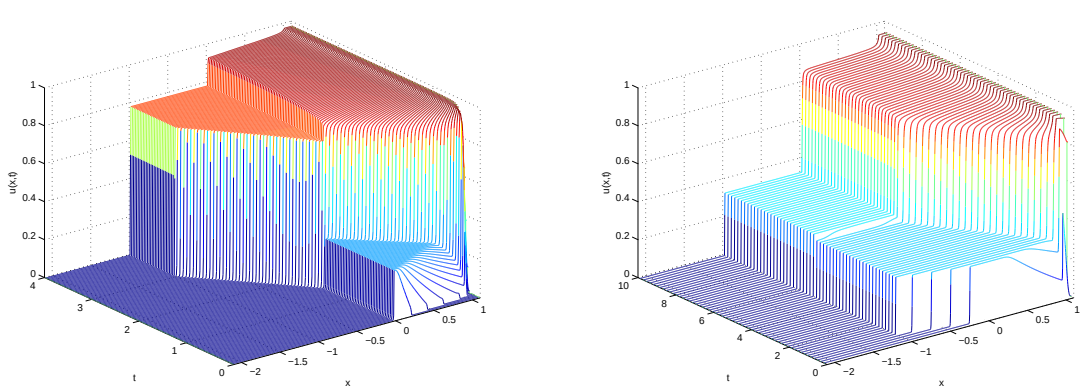

Figure 5.29: *Extended clarifier-thickener model: Time-space representation of the numerical solution. First example (left) and second example (right).*

Figures 5.30 and 5.31 show the numerical solution using multiresolution. In every case the figures on the right side show that the multiresolution effectively detects the stationary shocks corresponding to the flux discontinuities and the differences of gradients in the solution.

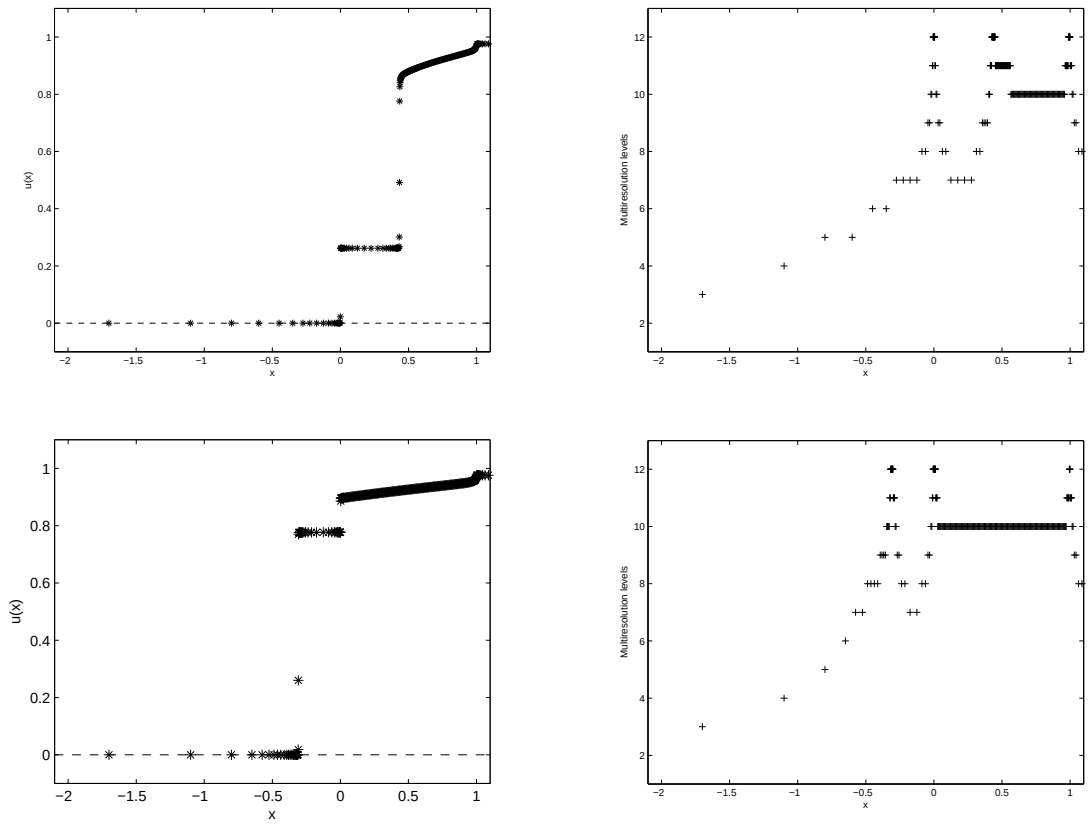

Figure 5.30: *First Example for the extended clarifier-thickener model: Numerical solution (left) and position of the leaves (right) for the clarifier–thickener model, at* $t = 1\,\mathrm{s}$ *and* $t = 2\,\mathrm{s}$.

Now we modify the control variables $q_{\mathrm{L}} = -2.25\,\mathrm{m/s}$, $q_{\mathrm{R}} = 1.35\,\mathrm{m/s}$, $q_{\mathrm{D}} = -2.25\,\mathrm{m/s}$ y $u_{\mathrm{F}} = 0.3$ to make them coincide with the ones chosen in Case 7 of [30]. The reference tolerance is $\varepsilon = 1.1 \times 10^{-3}$. Figure 5.2.4 shows the numerical solution until time $t = 10$.

Figure 5.32 shows how the multiresolution detects the higher gradient zones. It is important to mention that even when using a first order reference finite volume scheme, the high order of the multiresolution reconstruction ($r = 5$ in our case) ensures the correct representation of sharp discontinuities.

Due to the lack of an exact known solution, we use as reference solution, a numerical solution obtained with a finite volume calculation on a fine grid with $\mathcal{N} = 2^{15}$ control volumes.

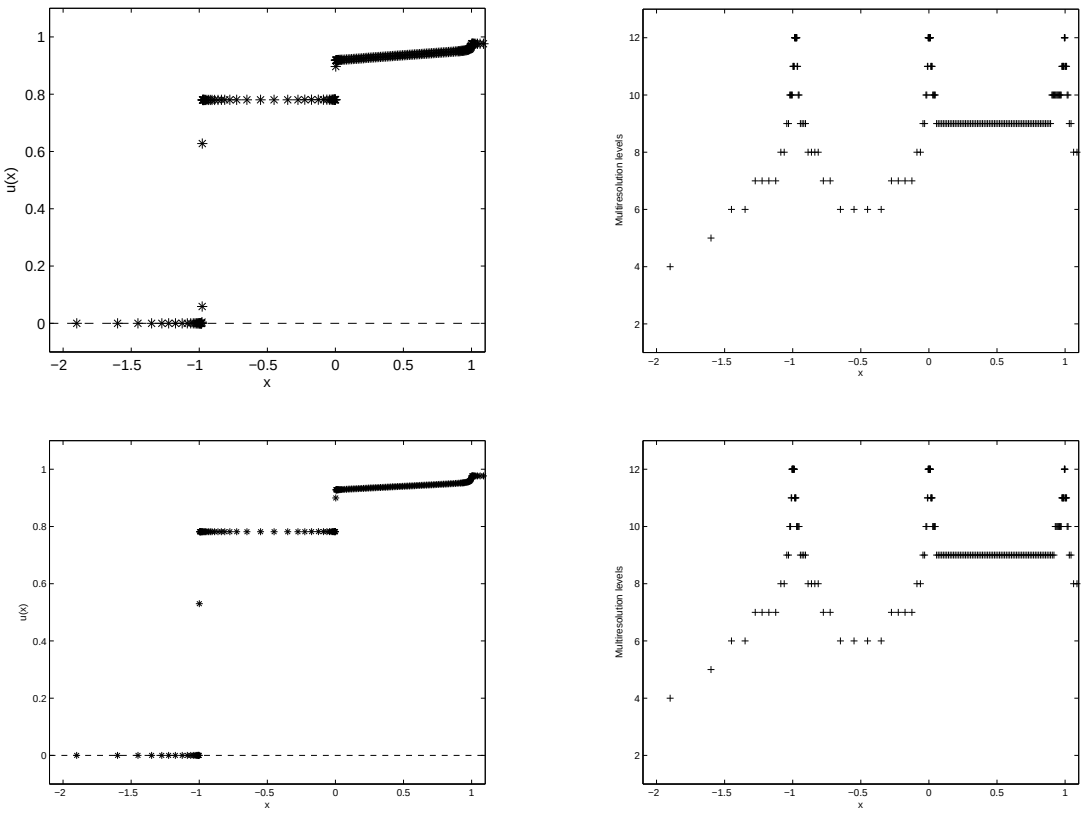

Figure 5.31: *First Example for the extended clarifier-thickener model: Numerical solution (left) and position of the leaves (right) for the clarifier–thickener model, at* $t = 3\,\mathrm{s}$ *and* $t = 4\,\mathrm{s}$.

	Accuracy	V	μ	L^1-error	L^2-error	$L^\infty-$error
$t = 1\,\mathrm{s}$						
	$r = 3$	7.46	10.6391	8.56×10^{-5}	2.35×10^{-7}	3.83×10^{-5}
	$r = 5$	7.25	10.1450	2.16×10^{-5}	7.48×10^{-8}	1.29×10^{-5}
$t = 2\,\mathrm{s}$						
	$r = 3$	8.01	8.5156	2.17×10^{-5}	3.84×10^{-5}	4.72×10^{-5}
	$r = 5$	7.89	8.5156	8.58×10^{-6}	1.10×10^{-5}	9.64×10^{-6}
$t = 3\,\mathrm{s}$						
	$r = 3$	8.06	11.2219	1.47×10^{-5}	6.79×10^{-9}	1.43×10^{-7}
	$r = 5$	7.98	11.1648	5.86×10^{-6}	2.28×10^{-9}	8.52×10^{-8}
$t = 4\,\mathrm{s}$						
	$r = 3$	8.29	11.3463	2.83×10^{-4}	5.32×10^{-9}	9.51×10^{-8}
	$r = 5$	8.01	11.2871	7.55×10^{-5}	1.39×10^{-9}	3.62×10^{-8}

Table 5.10: *First Example for the extended clarifier-thickener model: Simulation time, speed–up rate* V*, compression* r *ate* μ*, and normalized errors.* $L = 12$.

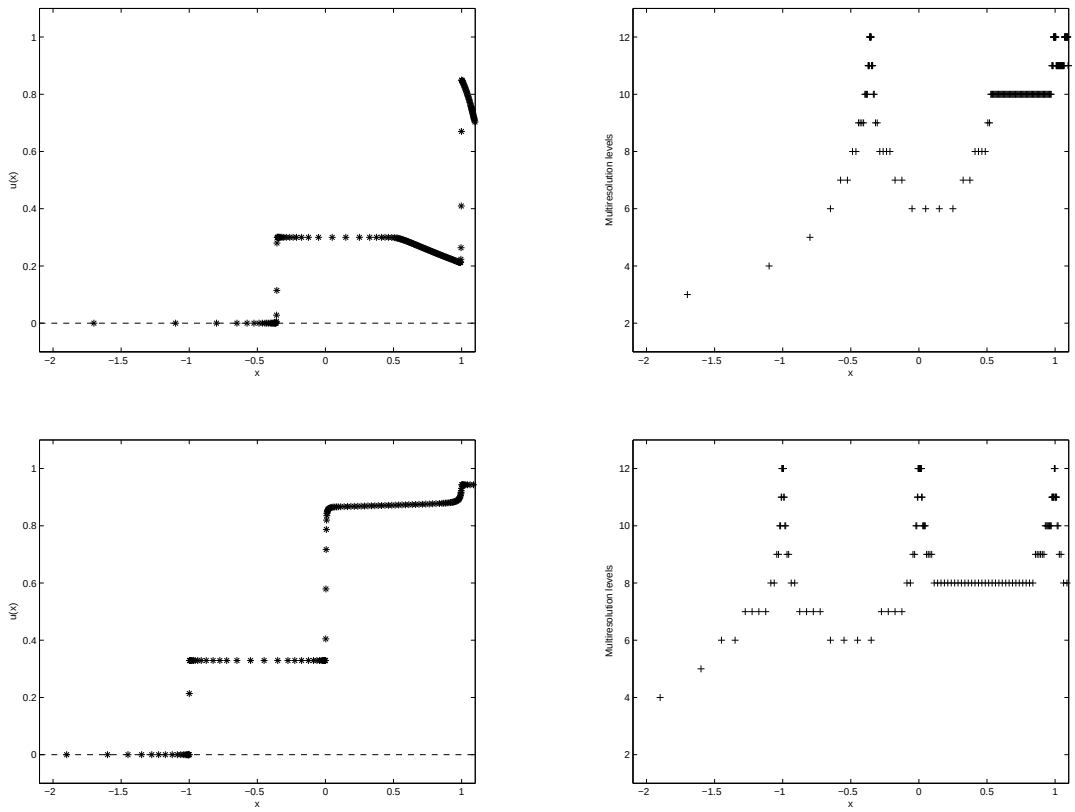

Figure 5.32: *Second Example for the extended clarifier-thickener model: Numerical solution (left) and position of the leaves (right) for the clarifier–thickener model, at* $t = 0.3\,\mathrm{s}$ *and* $t = 10\,\mathrm{s}$.

	Accuracy	V	μ	L^1-error	L^2-error	$L^\infty-$error
$t = 0.3$						
	$r = 3$	9.26	11.3915	9.52×10^{-5}	2.35×10^{-8}	3.83×10^{-5}
	$r = 5$	9.01	11.1246	2.27×10^{-5}	8.76×10^{-9}	9.79×10^{-6}
$t = 10$						
	$r = 3$	8.39	14.3719	4.98×10^{-4}	3.84×10^{-5}	4.72×10^{-5}
	$r = 5$	7.28	13.8974	1.14×10^{-4}	8.99×10^{-6}	1.02×10^{-5}

Table 5.11: *Second Example for the extended clarifier-thickener model: Simulation time, speed–up rate* V*, compression rate* μ*, and normalized errors.* $L = 12$.

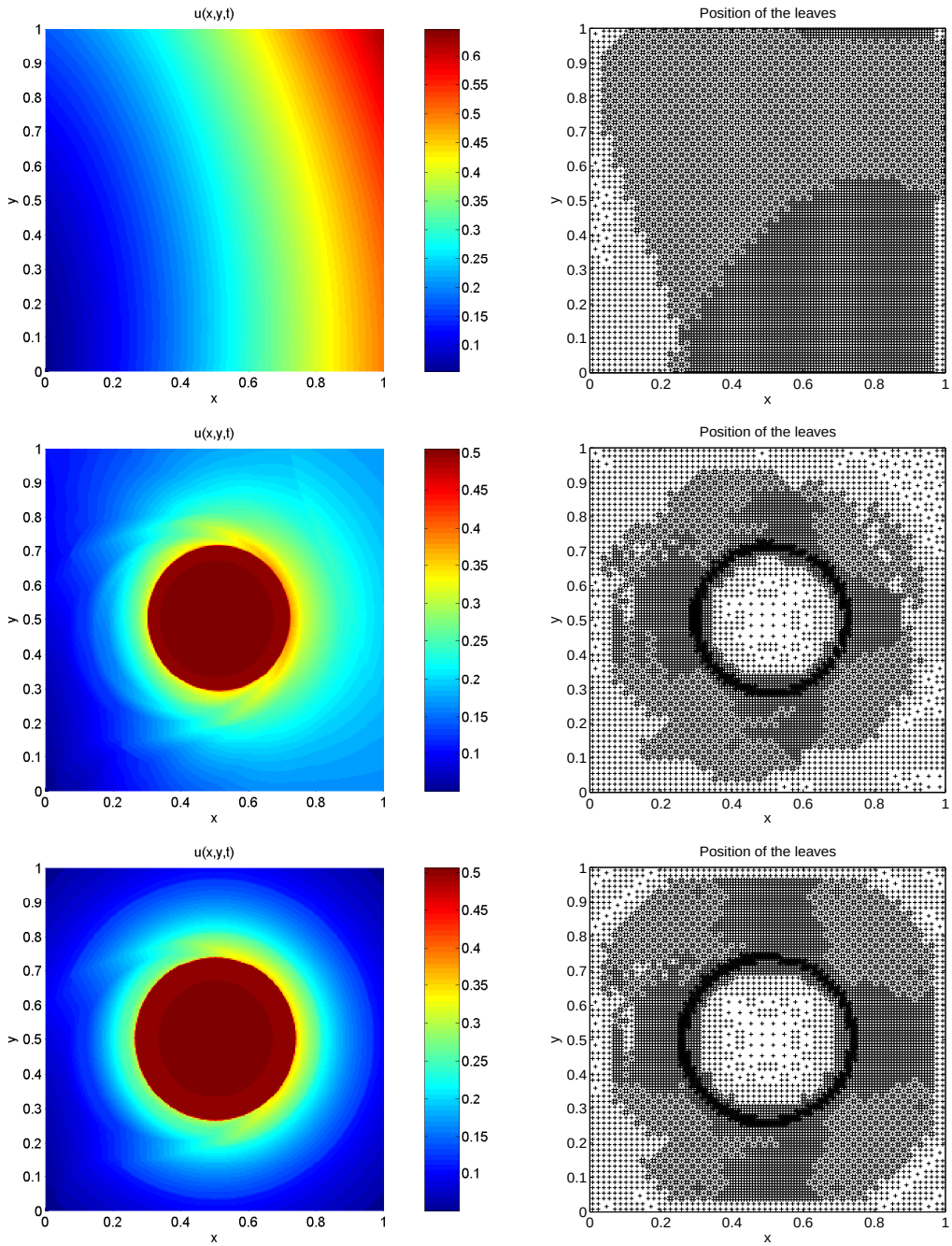

Figure 5.33: *Single-species model: Numerical solution (left) and leaves (right) of the corresponding tree data structure at times* $t = 0$ *(top),* $t = 0.5$ *(middle) and* $t = 3$ *(bottom).*

5.3 A class of reaction-diffusion systems

5.3.1 A single-species model

For this example, we consider (1.20) with a strongly degenerate diffusion term (1.22), where we choose $D := 1$ and $u_c := 0.5$, a square domain $\Omega = [0,1]^2$, and the function $f(u, \mathbf{x})$ given by (1.21). Figure 5.33 displays the numerical solution starting from the smoothly varying initial function

$$u_0(x, y) = 0.5\big(1 + \sin(1.1(x - \cos(0.7y)))\big)\cos\big(0.5(y - \sin(1.3x))\big).$$

We choose a maximal resolution level of $N_L = 256^2 = 65536$ control volumes on the finest grid. Figure 5.34 illustrates how the factor C in (3.19) is selected in our case as the optimal value from a finite selection of test values (each value giving a different value for the reference tolerance (3.19) ε_{R}).

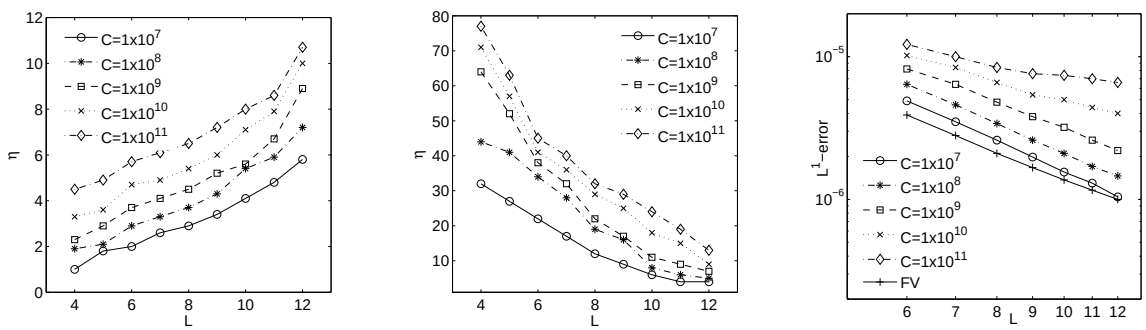

Figure 5.34: *Single-species model: data compression rate η (left), speed-up factor V (middle) and L^1-errors for different levels L and values of C (right). The simulated time is $t = 0$.*

Figures 5.34 (a) and (b) indicate that for all displayed levels, the multiresolution procedure is in every case (for different values of C) cheaper (in terms of both acceleration and memory savings) than the corresponding reference FV computation on the finest grid. Figure 5.34 (c) indicates that the computations obtained using $C = 1.0 \times 10^9$ (and hence $\varepsilon_{\mathrm{R}} = 9.43 \times 10^{-4}$) are sufficiently accurate, in the sense that with these choices, we keep the same slope for the L^1-error as the FV calculations while increasing V and η. We remark that here, as in previous works that use similar methods (see e.g. [53]), there actually exists a range of threshold parameters that preserve the same slope for errors with respect to reference solution, for which $C = 1.0 \times 10^9$ is an average value. Here, we compute errors using a reference FV solution on a fine grid with $N_L = 2048^2 = 4194304$ control volumes. (Here and in all other examples, we calculate errors in the approximate sense with respect to a reference solution.)

5.3.2 Interaction between two flame balls

We study (1.23) as a dimensionless model for the interaction between two flame balls of different sizes. We consider a square domain $\Omega = [-30, 30]^2$ and that the walls are sufficiently far from the flame balls so that their influence is negligible. Physical parameters characterizing the gaseous mixture and the combustion process are chosen as in [132, 133]. We use the parameters $\alpha = 0.64$ and $\beta = 10$. The initial data is given

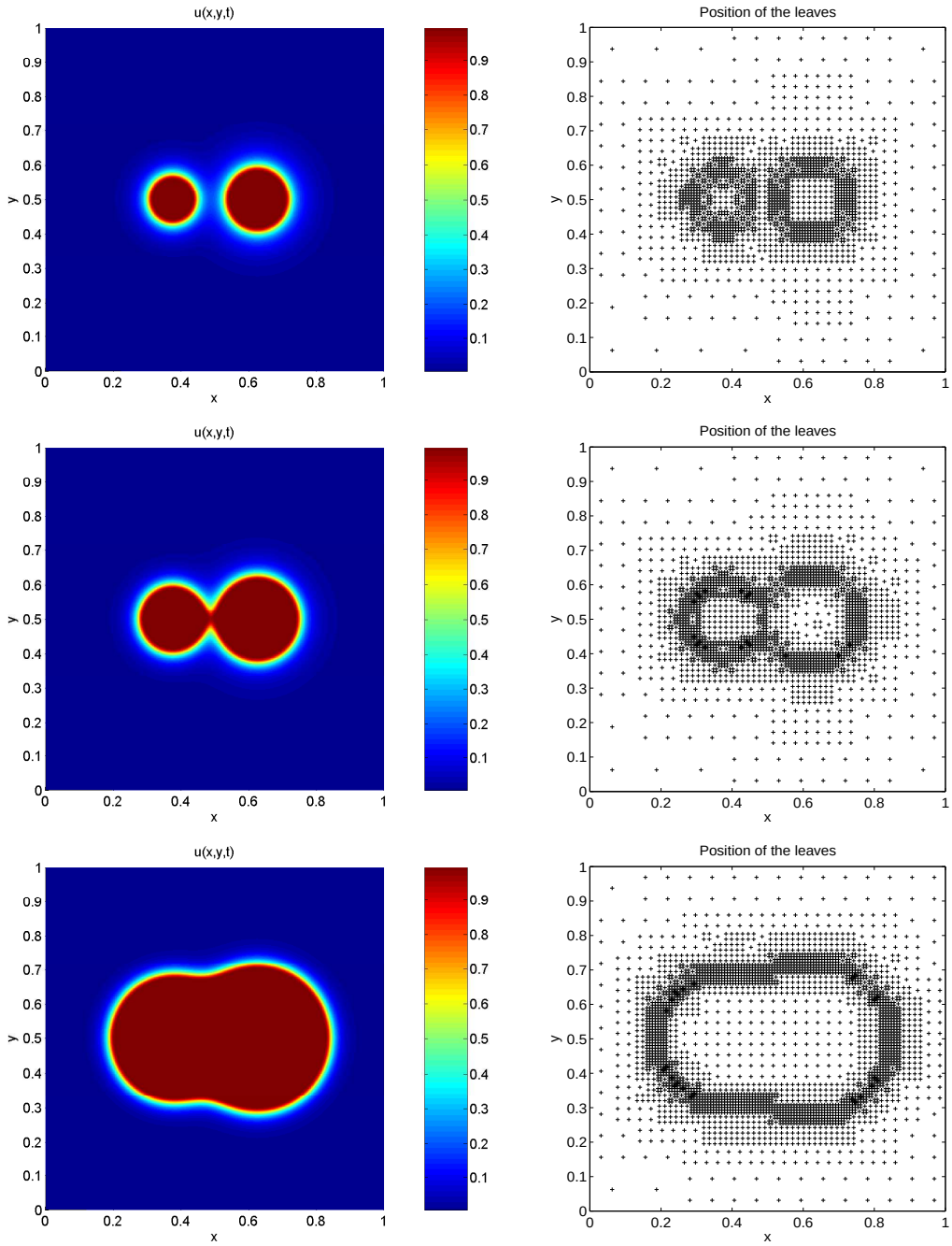

Figure 5.35: *Interaction of two flame balls without radiation: Numerical solution for species u (left) and leaves of the corresponding tree data structure (right) at times $t = 2$ (top), $t = 4$ (middle) and $t = 10$ (bottom).*

by $u(x,y,0) = u_0(r_1,r_2),\ v(x,y,0) = v_0(r_1,r_2)$ with $r_1^2 = (x-x_1)^2 + y^2,\ r_2^2 = (x-x_2)^2 + y^2$, where

$$u_0(r_1,r_2) := \begin{cases} 1 & \text{if } r_1 < a \text{ or } r_2 < b, \\ \max\{\exp(1-r_1/a), \exp(1-r_2/b)\} & \text{otherwise,} \end{cases} \qquad v_0(r_1,r_2) := 1 - u_0(r_1,r_2). \quad (5.5)$$

In this example, we simulate the process without radiation, i.e., $\rho = 0$ and hence $S(u) = 0$. We set the Lewis number to $\mathrm{Le} = 1$. Here $x_1 = -7.5$, $x_2 = 7.5$ and $a = 1.8$, $b = 2.5$ are the respective $x-$position and initial radii of the two flame balls. This choice ensures that there is no interaction between the two flame balls at $t = 0$ and that there is no extinction of the flame balls. We simulate the process until $t = 10$, and Figure 5.35 shows from left to right the temperature and reaction rate configuration obtained using the fully adaptive multiresolution scheme, and the position of the dynamic graded tree leaves, which form the corresponding adaptive mesh. The different times correspond from the top to the bottom to: before ($t = 2$), during ($t = 4$) and after ($t = 10$) direct interaction between the two flame balls, when the balls tend to create a new circular flame structure. We choose the following multiresolution parameters: the maximal resolution level $L = 10$ corresponding to $N_L = 512^2 = 262144$ control volumes in the finest grid, and the reference tolerance $\varepsilon_{\mathrm{R}} = 4.94 \times 10^{-3}$.

For comparison purposes, we introduce the global chemical reaction rate

$$R(t) := \iint_\Omega f(u,v)\, dx\, dy.$$

Errors in different norms, reaction rates, information on data compression and speed-up rate for different methods at three different times are depicted in Table 5.12. Due to the particular shape of solutions, which is nearly constant away from the combustion front, by using multiresolution, one can obtain very high rates of data compression, speed-up and low errors.

In another example, we simulate the case with radiation, i.e. we use (1.24) and (1.25), where $\rho = 0.05$ and $\mathrm{Le} = 0.3$. Now $x_1 = -5$, $x_2 = 5$ and $a = 0.5$, $b = 1$ are the respective $x-$position and initial radii of the two flame balls. We simulate the process until $t = 10$ and Figures 5.36 and 5.37 show the scenario for this case. First, the balls grow spherically, tend to create a new flame structure, and then their fronts tend to extinguish when they touch each other, while the radiation effect causes the entire flame front to split. Here the maximal resolution level is set to $L = 10$ corresponding to $N_L = 512^2 = 262144$ control volumes in the finest grid, and the reference tolerance is $\varepsilon_{\mathrm{R}} = 7.43 \times 10^{-3}$.

Notice that the multiresolution procedure automatically detects the higher gradient regions and uses this information to adaptively represent the solution by the refinement and coarsening of the mesh, i.e., by the adaptive addition and removal of control volumes on these areas.

The L^1, L^2 and L^∞ errors between the numerical solution obtained by our multiresolution scheme for different multiresolution levels L and the reference solution (obtained by finite volume approximation in a uniform fine grid with $2^{2\cdot 14}$ control volumes) for the case without radiation, are depicted in Figure 5.38 (c) and (d). The slopes indicate a rate of convergence slightly better than two.

For the case including radiation effects, we apply the locally varying time stepping (LTS) strategy detailed in Section 4.1. We choose the maximum CFL number allowed by (2.15), which is $\mathsf{CFL}_0 = 1$ for the coarsest level. For the remaining levels we use $\mathsf{CFL}_l = 2^l \mathsf{CFL}_0$, which means that we perform each macro time step with $\Delta t = \Delta t_0 = 2^L \Delta t_L$ as given by (4.1).

In Figure 5.39 we compare speed-up, data compression rate and total reaction rate for the finite volume reference scheme, the multiresolution scheme with global time step, and the multiresolution method with level-dependent time stepping. Notice that with LTS, the speed-up rate is approximately doubled for all

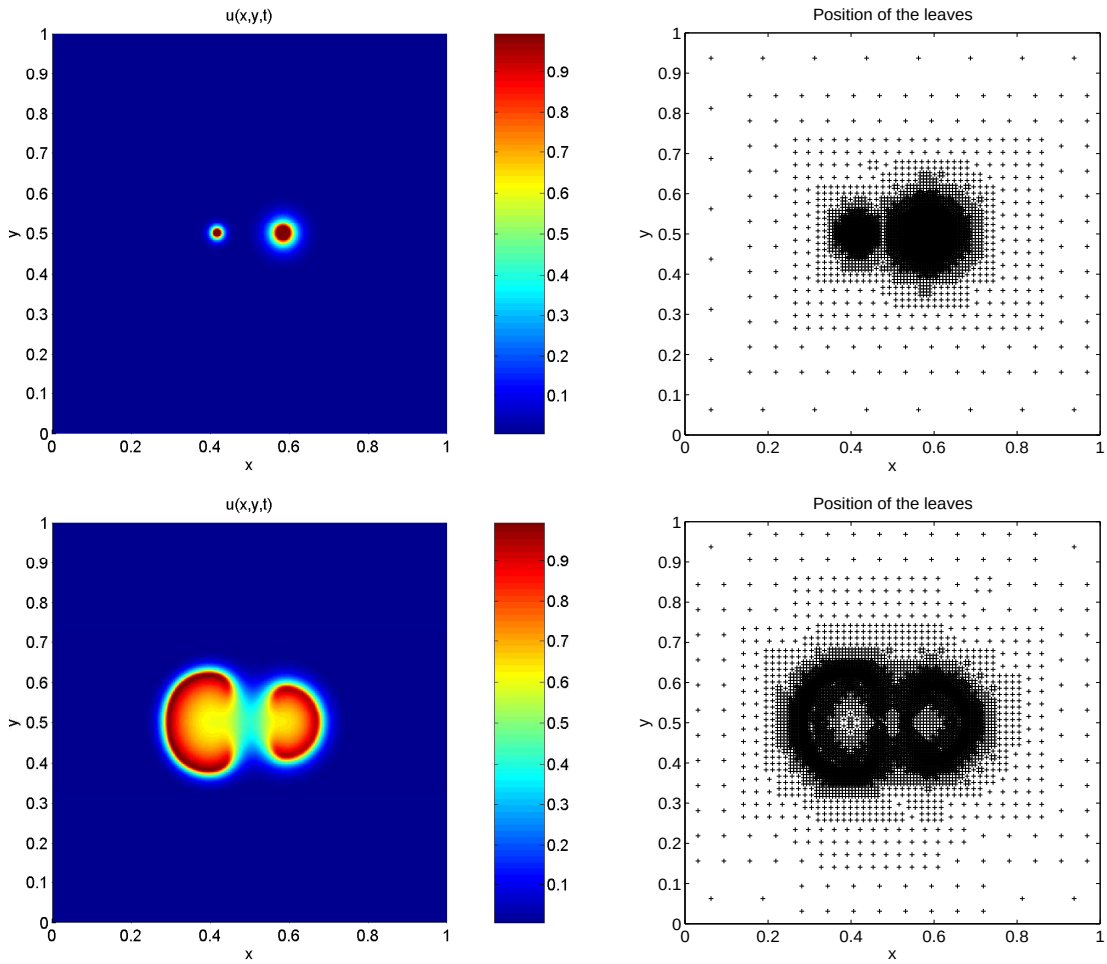

Figure 5.36: *Interaction of two flame balls with radiation: Numerical solution for species u (left) and and leaves of the corresponding tree (right) at times $t = 0$ and $t = 5$.*

Time	V	η	L^1-error	L^2-error	$L^\infty-$error	Method	$R(t)$
$t = 2.0$	12.47	138.2613	5.41×10^{-3}	5.77×10^{-3}	2.46×10^{-2}	MR	56.7230
						FV	56.0078
$t = 4.0$	20.56	113.4331	6.39×10^{-3}	8.42×10^{-4}	3.02×10^{-2}	MR	80.0374
						FV	79.5247
$t = 10.0$	34.42	83.9129	5.20×10^{-3}	4.90×10^{-3}	5.49×10^{-2}	MR	98.9210
						FV	98.7942

Table 5.12: *Interaction of two flame balls without radiation: Corresponding simulated time, speed-up rate V, compression rate η, errors, and total reaction rate $R(t)$ for the u species.*

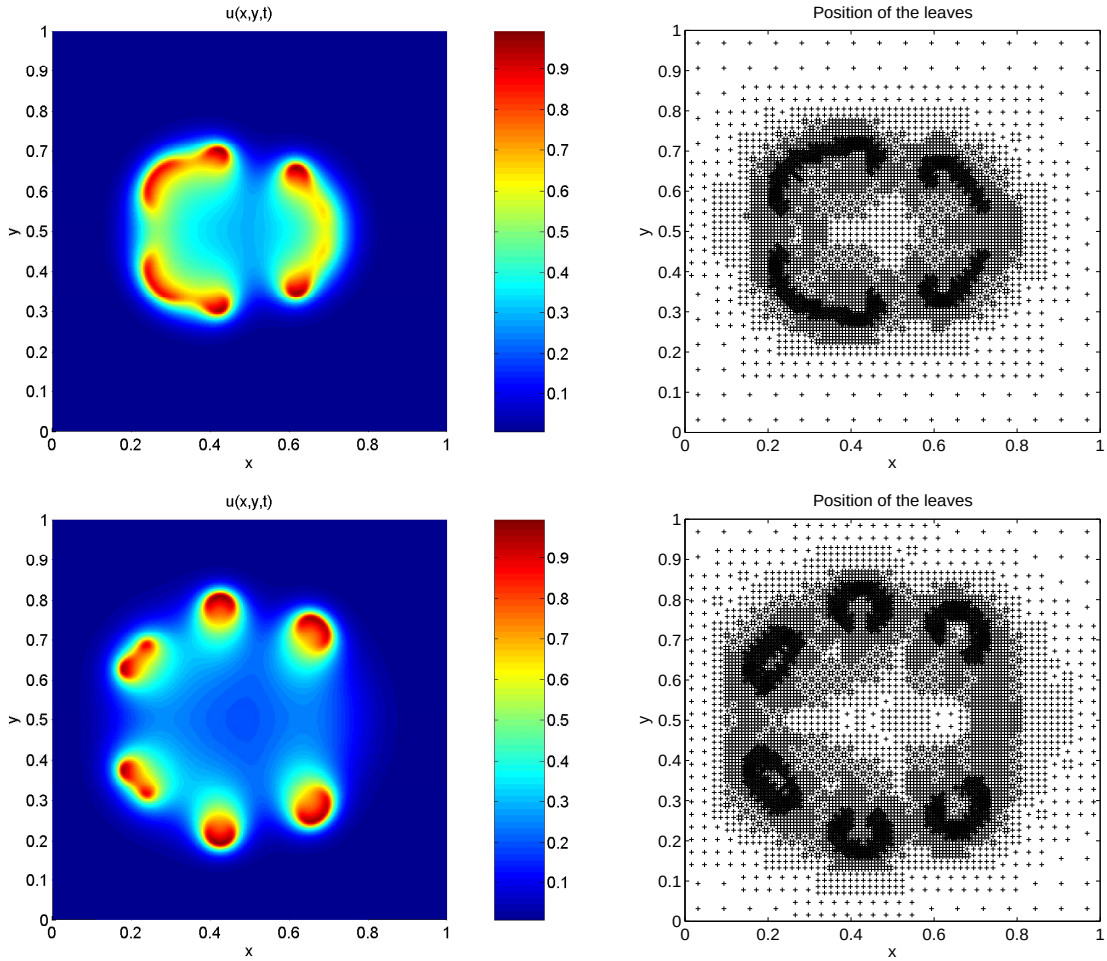

Figure 5.37: *Interaction of two flame balls with radiation: Numerical solution for species u and leaves of the corresponding tree (right) at times $t = 12$ and $t = 20$.*

times, while the compression rate and the total reaction rate remain of the same order as the multiresolution computation with global time step.

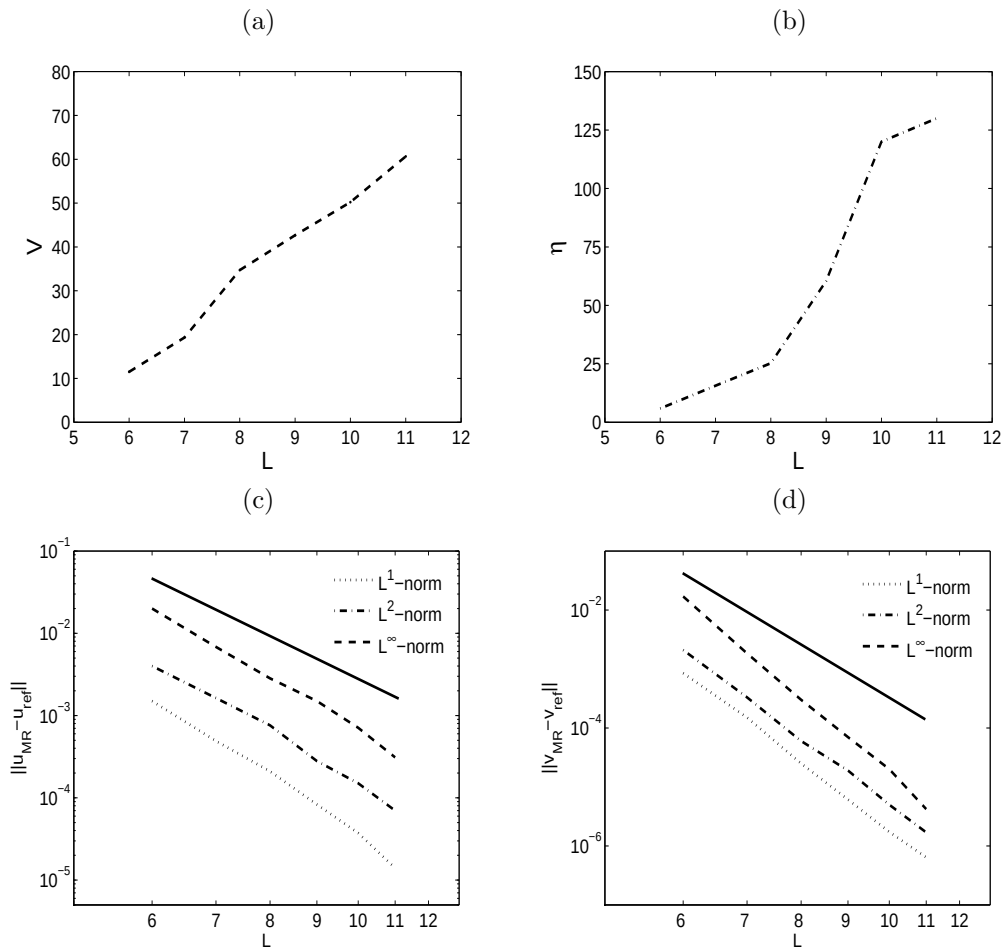

Figure 5.38: *Interaction of two flame balls without radiation: (a) speed-up rate V, (b) data compression rate η, for different levels, at time $t = 4.0$; (c) errors $\|\bar{u}_{\mathrm{MR}} - \bar{u}_{\mathrm{ref}}\|_1$, $\|\bar{u}_{\mathrm{MR}} - \bar{u}_{\mathrm{ref}}\|_2$, $\|\bar{u}_{\mathrm{MR}} - \bar{u}_{\mathrm{ref}}\|_\infty$ and (d) $\|\bar{v}_{\mathrm{MR}} - \bar{v}_{\mathrm{ref}}\|_1$, $\|\bar{v}_{\mathrm{MR}} - \bar{v}_{\mathrm{ref}}\|_2$ and $\|\bar{v}_{\mathrm{MR}} - \bar{v}_{\mathrm{ref}}\|_\infty$ respectively for different levels L, at time $t = 4$.*

5.3.3 A Turing model of pattern formation

We select the parameters $a = -0.5$, $b = 1.9$, $d = 4.8$ and $\gamma = 210$. According to the discussion of Section 1.3, these parameters allow diffusion-driven instabilities to evolve. The initial concentration distribution is a normally distributed random perturbation around the stationary state (u^0, v^0) for the non-degenerate case, with a variance lower than the amplitude of the final patterns, see Figure 5.40. For the case of non-degenerate diffusion (Example 4), we use $A(u)$ and $B(u)$ as given by (1.27). For these parameters, the steady state is $(u^0 = 1.4, v^0 = 0.96939)$.

For the first case, we choose a maximal resolution level of $N_L = 256^2 = 65536$ control volumes in the finest grid and a reference tolerance given by $\varepsilon_{\mathrm{R}} = 2.6 \times 10^{-3}$. The time step is the maximum allowed by the

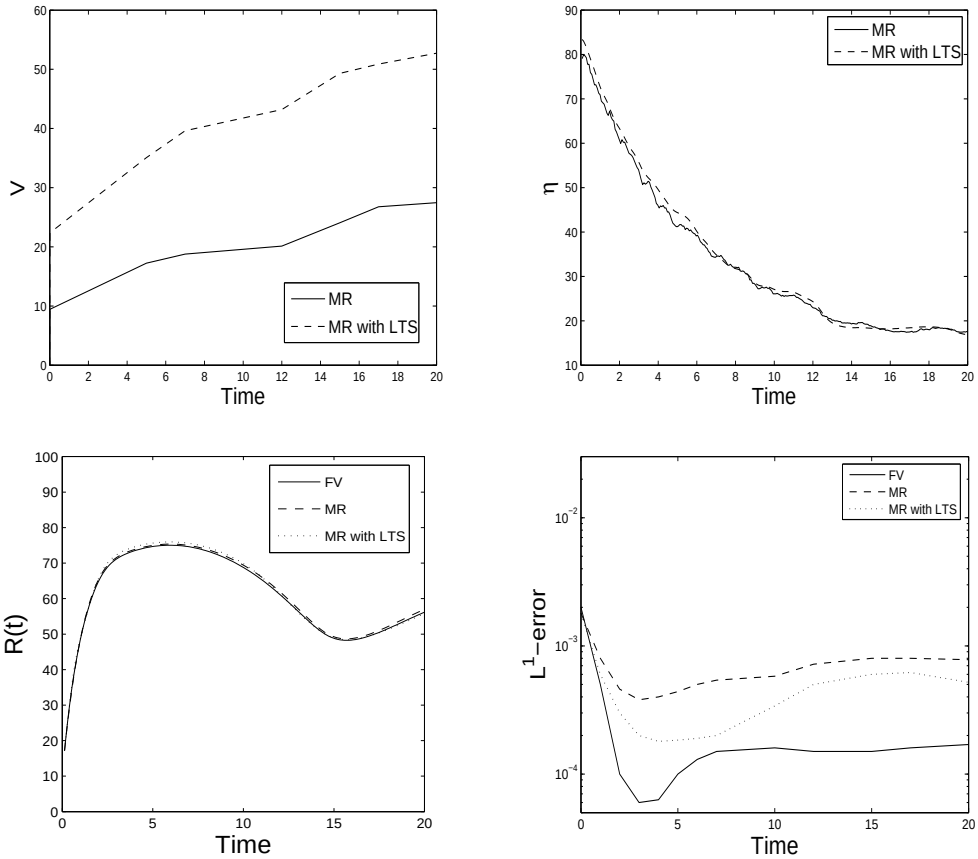

Figure 5.39: *Interaction of two flame balls with radiation: Time evolution of speed-up, data compression, and total reaction rates; and L^1-errors for different methods. $L = 10$ multiresolution levels and reference tolerance $\varepsilon_{\mathrm{R}} = 7.43 \times 10^{-3}$.*

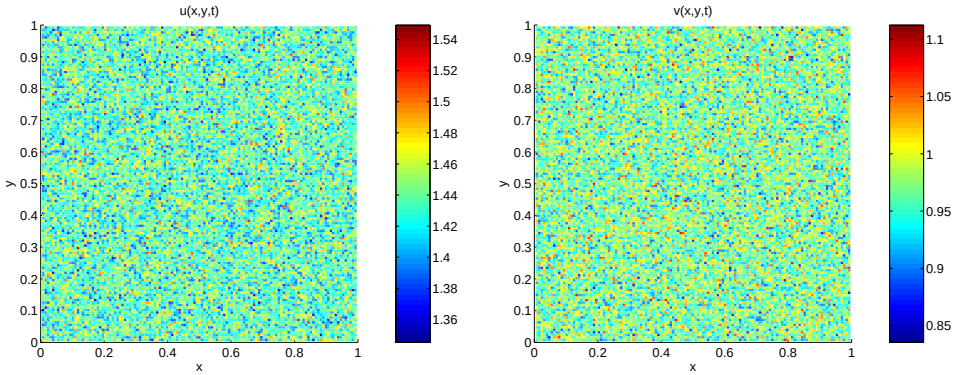

Figure 5.40: *Turing pattern-formation: Initial data $u_0(x, y)$ (left) and $v_0(x, y)$ (right).*

CFL condition (2.15). Table 5.13 summarizes the speed-up rate, compression rate and errors in different norms between the numerical solution by multiresolution and the fine-mesh finite volume reference solution for different times. We depict errors between our multiresolution scheme and a reference FV solution with $N_L = 1024^2 = 1048576$ control volumes in the finest grid, for different multiresolution levels L in Figure 5.42 (c) and (d). In this case, the slopes equally indicate a rate of convergence slightly larger than two. Concerning the computation of errors, when involving random initial conditions, the system is evolved until the "random noise", which is imposed as an initial condition on the finest grid, has been smoothed sufficiently; then, this solution is projected on coarser levels to obtain auxiliary initial conditions for all the needed levels.

Time	V	η	Species	L^1-error	L^2-error	$L^\infty-$error
$t = 0.05$	7.16	11.3783	u	6.81×10^{-4}	4.76×10^{-5}	3.46×10^{-3}
			v	4.09×10^{-4}	3.92×10^{-4}	5.38×10^{-4}
$t = 0.25$	9.29	11.9756	u	8.37×10^{-4}	6.94×10^{-5}	9.93×10^{-3}
			v	4.22×10^{-4}	5.43×10^{-4}	8.48×10^{-4}
$t = 1.50$	11.87	14.4739	u	9.26×10^{-4}	2.71×10^{-4}	2.44×10^{-2}
			v	4.30×10^{-4}	9.77×10^{-5}	8.39×10^{-3}

Table 5.13: *Turing model with non-degenerate diffusion: Corresponding simulated time, CPU ratio V, compression rate η and componentwise errors.*

For the second case, we use the degenerate diffusion coefficients (1.29) with $u_c = 1.2$ and $v_c = 0.7$, and employ again the kinetics (1.26), but this time we choose the parameters $a = -0.5$, $b = 1.9$, $d = 4.8$ and $\gamma = 395$. We select a maximal resolution level of $N_L = 256^2 = 65536$ control volumes in the finest grid, with a reference tolerance given by $\varepsilon_R = 3.59 \times 10^{-4}$. From Table 5.14 we see that the multiresolution algorithm allows significant acceleration and data compression rate are significantly increased by the multiresolution algorithm with very good accuracy. Figure 5.43 indicates that due to the degeneracy of the diffusion given by (1.29), and in contrast to the previous example, species u exhibits patterns with steeper gradients, and especially at $t = 0.25$ and $t = 1.5$, singularities appear.

Time	V	η	Species	L^1-error	L^2-error	$L^\infty-$error
$t = 0.10$	6.32	12.5438	u	6.31×10^{-4}	5.82×10^{-4}	2.72×10^{-3}
			v	4.98×10^{-4}	5.37×10^{-4}	9.46×10^{-4}
$t = 0.25$	9.79	10.3457	u	6.12×10^{-4}	2.46×10^{-5}	3.03×10^{-3}
			v	3.91×10^{-4}	9.22×10^{-4}	9.92×10^{-4}
$t = 1.50$	11.60	10.1984	u	3.42×10^{-4}	7.34×10^{-4}	3.40×10^{-3}
			v	2.63×10^{-4}	4.98×10^{-4}	2.81×10^{-3}

Table 5.14: *Turing model with degenerate diffusion: Corresponding simulated time, speed-up rate V, compression rate η and componentwise errors.*

5.3.4 A chemotaxis-growth system

For this example in (1.30) we consider a square domain $\Omega = [0, 16]^2$ and fix the parameters $\sigma = 0.0625$ and $d = 1$. The function $h(u, v)$ is given by (1.33) with $\alpha = 1$ and $\beta = 32$. The growth function $g(u)$ for the species u is given by (1.32), and the chemotactical sensitivity is given by (1.31). This configuration corresponds to the model of chemotaxis and growth presented in [114], which is further analyzed in [72]. Similarly to [72], the initial datum is $(u_0, v_0) = (1 + \epsilon(\mathbf{x}), 1/32)$, where $\epsilon(\mathbf{x})$ is a particular smooth perturbation which goes to zero near $(8, 8)$. We simulate the process until the solution reaches inhomogeneous stationary states,

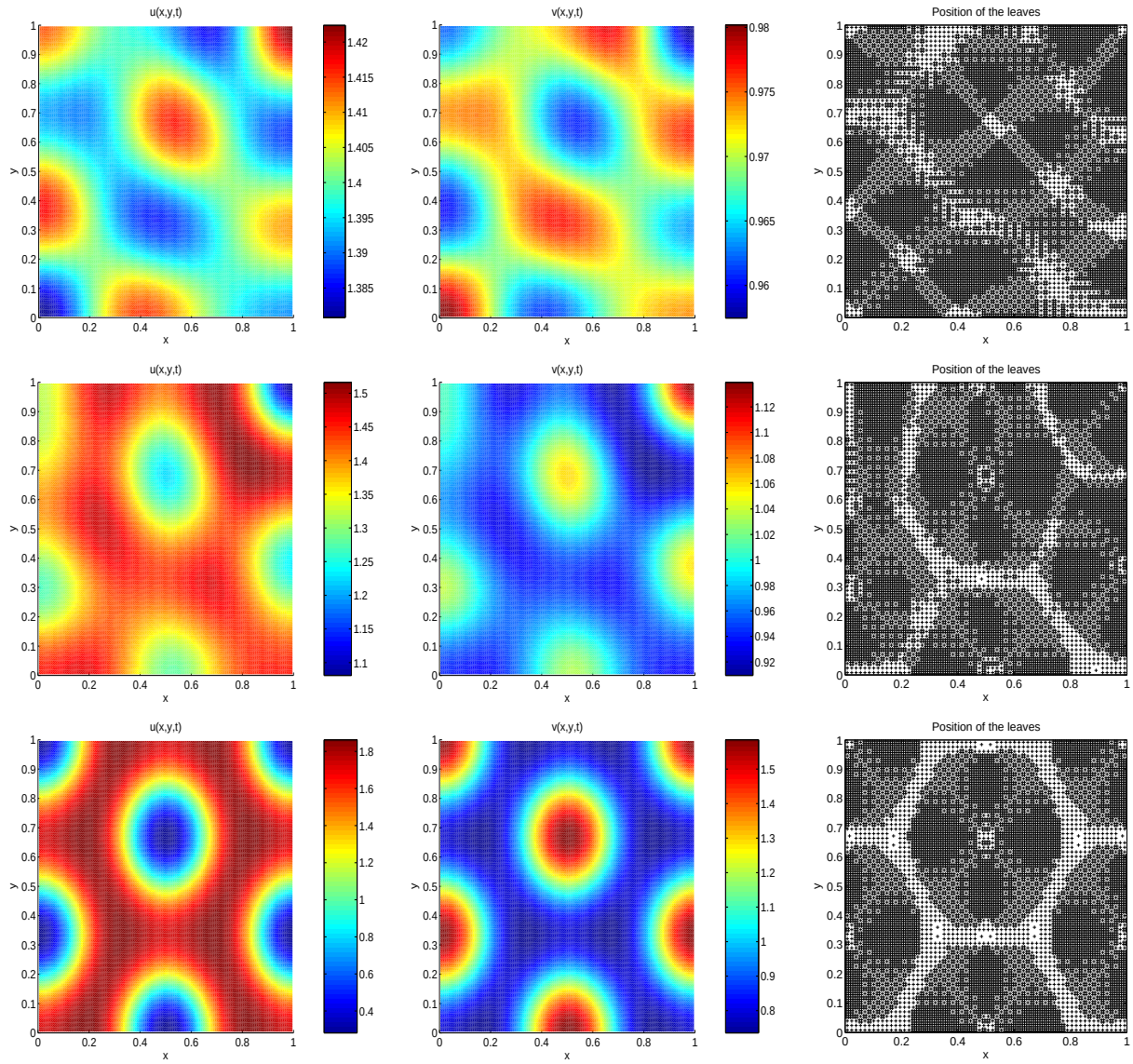

Figure 5.41: *Turing model with non-degenerate diffusion: Numerical solution for species u (left) and v (right), and leaves of the corresponding tree data structure at times $t = 0.05$ (top), $t = 0.25$ (middle) and $t = 1.5$ (bottom).*

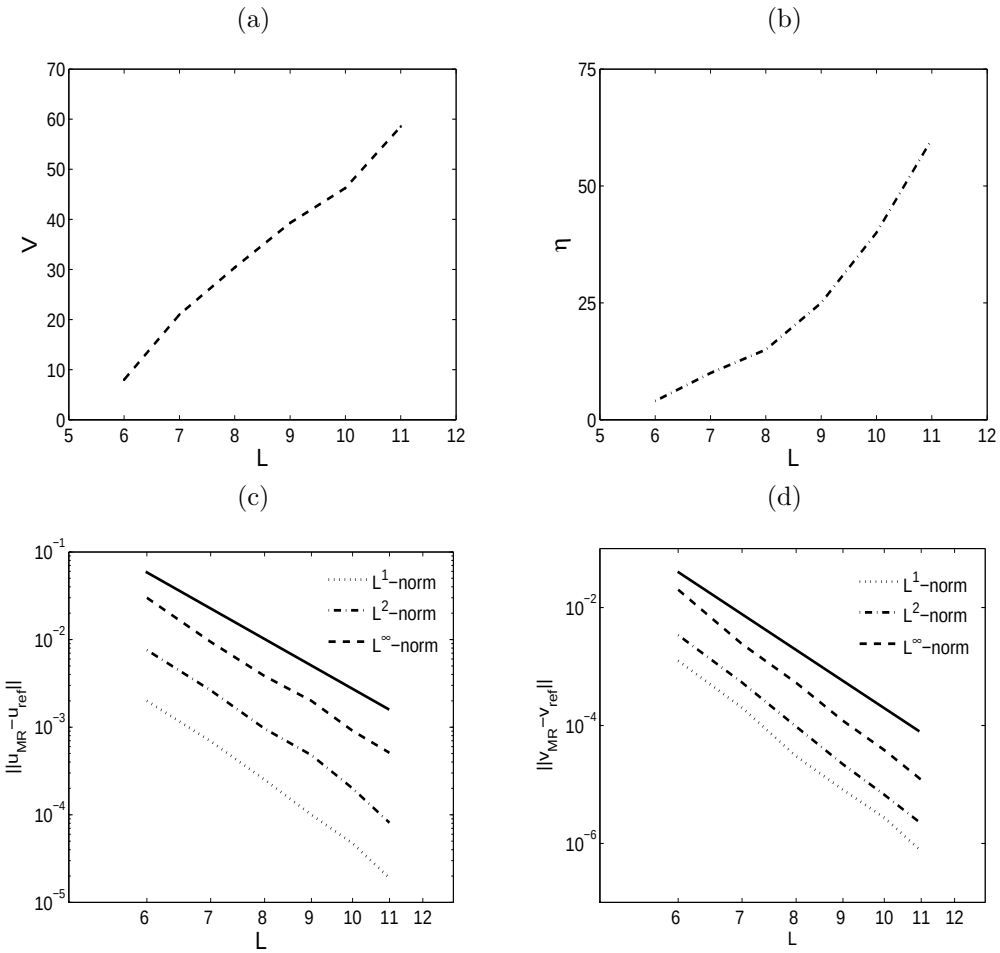

Figure 5.42: *Turing model with non-degenerate diffusion: (a) CPU acceleration V, (b) data compression rate η, for different levels, at time $t = 0.75\,\mathrm{s}$; (c) errors $\|\bar{u}_{\mathrm{MR}} - \bar{u}_{\mathrm{ref}}\|_1$, $\|\bar{u}_{\mathrm{MR}} - \bar{u}_{\mathrm{ref}}\|_2$, $\|\bar{u}_{\mathrm{MR}} - \bar{u}_{\mathrm{ref}}\|_\infty$ and (d) $\|\bar{v}_{\mathrm{MR}} - \bar{v}_{\mathrm{ref}}\|_1$, $\|\bar{v}_{\mathrm{MR}} - \bar{v}_{\mathrm{ref}}\|_2$ and $\|\bar{v}_{\mathrm{MR}} - \bar{v}_{\mathrm{ref}}\|_\infty$ respectively for different levels L, at time $t = 0.75$.*

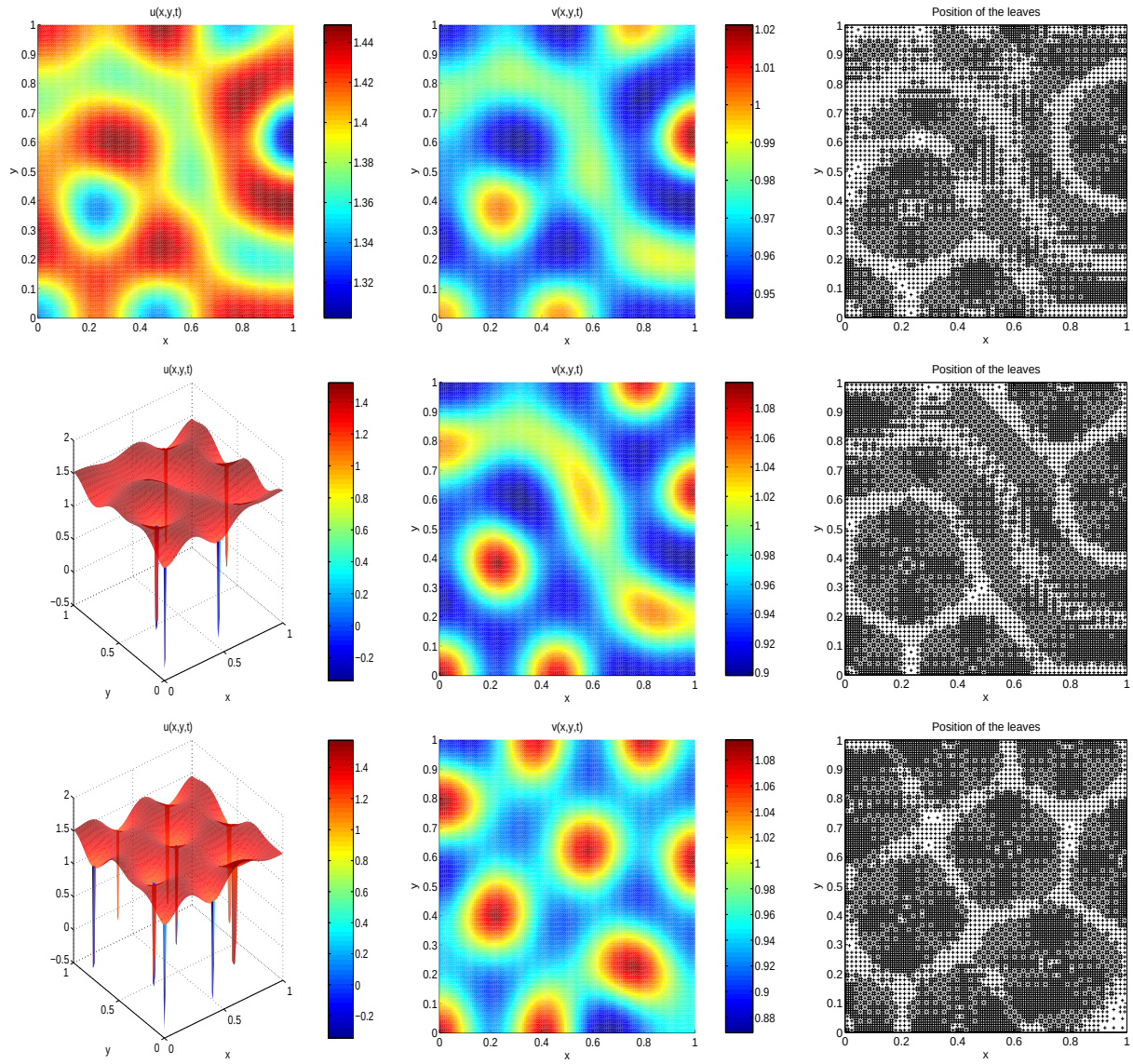

Figure 5.43: *Turing model with degenerate diffusion: Numerical solution for species u (left) and v (middle), and leaves of the corresponding tree data structure (right) at times $t = 0.1$ (top), $t = 0.25$ (middle) and $t = 1.5$ (bottom).*

and we present three cases corresponding to different values of ν, which is responsible for the complexity of the spatial patterns. For instance, for $\nu = 7$ Figure 5.44 (middle) shows labyrinth-shaped patterns and for $\nu = 10$ (bottom), single filaments and spots. The corresponding adaptive meshes were generated with $N_L = 512^2 = 262144$ control volumes in the finest grid, with $\varepsilon_{\mathrm{R}} = 8.43 \times 10^{-4}$. For all these cases we implement locally varying time stepping, so we will choose the maximum CFL number allowed by (2.17), $\mathsf{CFL}_0 = 1$ for the coarsest level and $\mathsf{CFL}_l = 2^l \mathsf{CFL}_0$ for finer levels. From Figure 5.45 and Table 5.15 we can observe that if we incorporate the local time stepping strategy, a substantial gain (a factor slightly lower than 2, which is consistent with the results by Lamby, Müller, and Stiriba [108]) is obtained in speed-up rate when comparing with a multiresolution calculation using global time stepping. The errors are computed from a reference solution in a grid with $N_L = 2048^2 = 4194304$ control volumes. We conclude that the errors are kept of the same slope that the errors obtained with a global time step. The compression rate η for both methods is lower than in the previous examples, which could be explained by the complexity and density of the spatial patterns in this particular example.

Time	Method	V	η	L^1-error	L^∞-error
$t = 1$	MR	16.79	5.37	8.41×10^{-4}	3.54×10^{-3}
	MR with LTS	34.18	5.29	5.30×10^{-4}	3.15×10^{-3}
$t = 5$	MR	16.96	6.48	7.43×10^{-4}	4.19×10^{-3}
	MR with LTS	33.51	6.23	6.14×10^{-4}	3.71×10^{-3}
$t = 10$	MR	15.44	7.87	6.20×10^{-4}	2.86×10^{-3}
	MR with LTS	31.08	7.01	4.15×10^{-4}	3.02×10^{-3}
$t = 20$	MR	17.29	5.92	7.14×10^{-4}	3.46×10^{-3}
	MR with LTS	33.87	5.50	4.99×10^{-4}	3.40×10^{-3}

Table 5.15: *Chemotaxis with growth: Time evolution for data compression, speed-up rate, and normalized errors for different methods: Multiresolution scheme with fixed global time step, and multiresolution with locally varying time step.* $\nu = 7.0$, $CFL_0 = 1$, $\varepsilon_R = 5.0 \times 10^{-4}$ *and* $L = 10$.

5.4 The monodomain and bidomain models

Time	$\mathcal{V}$	η	L^1-error	L^2-error	$L^\infty-$error
$t = 0.0\,\mathrm{ms}$		170.22	4.31×10^{-4}	2.47×10^{-4}	3.99×10^{-4}
$t = 1.5\,\mathrm{ms}$	27.81	37.56	4.97×10^{-4}	1.96×10^{-4}	4.63×10^{-4}
$t = 3.5\,\mathrm{ms}$	26.47	29.89	5.23×10^{-4}	4.05×10^{-4}	4.82×10^{-4}
$t = 4.5\,\mathrm{ms}$	31.41	28.12	7.48×10^{-4}	4.29×10^{-4}	5.31×10^{-4}
$t = 5.5\,\mathrm{ms}$	30.62	24.70	1.04×10^{-3}	6.20×10^{-4}	6.79×10^{-4}

Table 5.16: *2D monodomain model: Corresponding simulated time, CPU ratio* $\mathcal{V}$*, compression rate* η *and normalized errors for* v*, using a MR method.*

We will present test cases showing the efficiency of the previously described methods in capturing the dynamical evolution of electro-physiological waves for both the monodomain and bidomain models. Since we are dealing with multi-component solutions, it is worthy to state that we will consider a single mesh for representing the vector of relevant variables. In the bidomain model, the anisotropies, mesh structures as

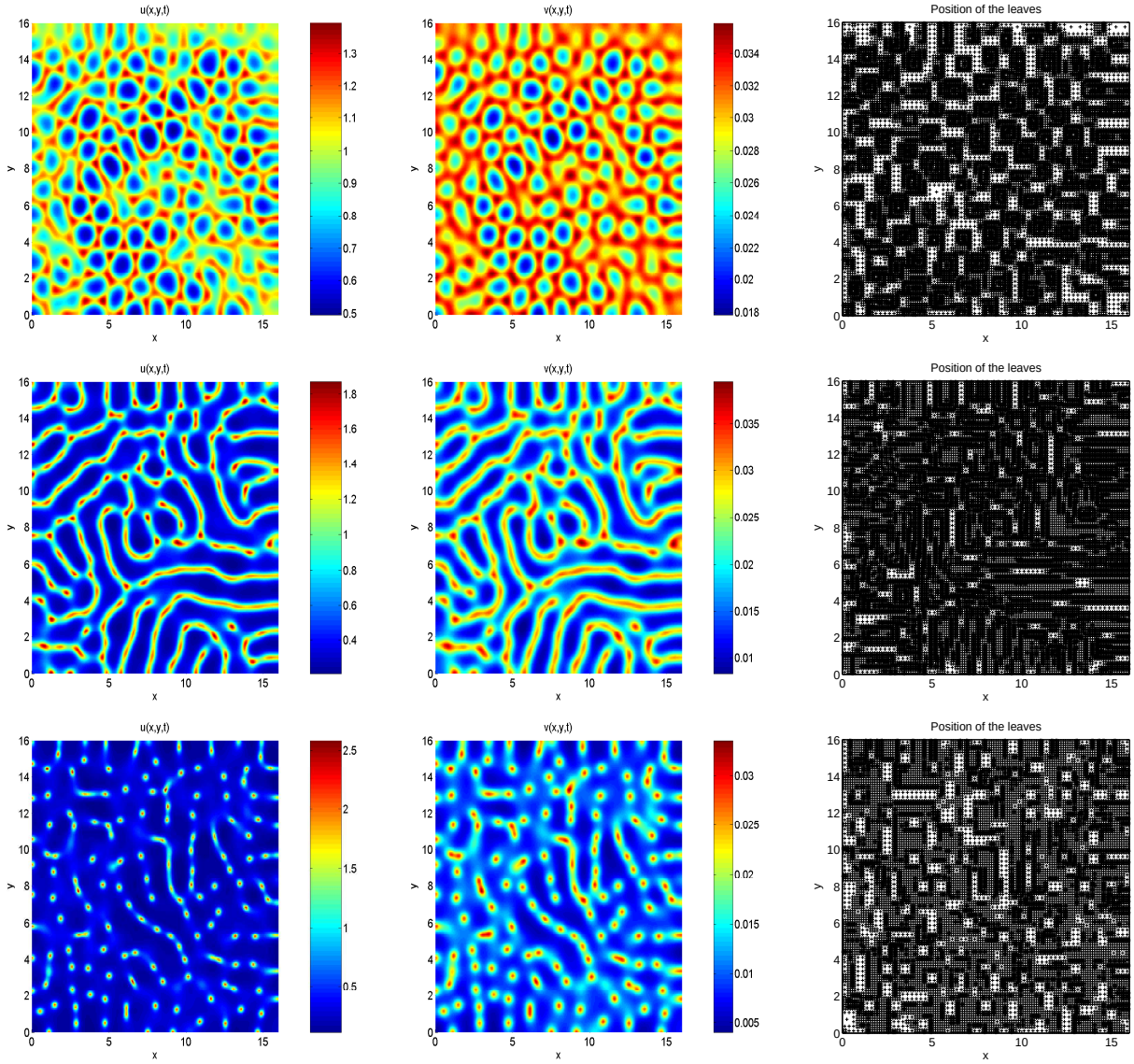

Figure 5.44: *Chemotaxis with growth: Numerical solution for species u (left) and v (middle), and leaves of the corresponding tree data structure (right) for $\nu = 6.04$ (top), $\nu = 7$ (middle) and $\nu = 10$ (bottom).*

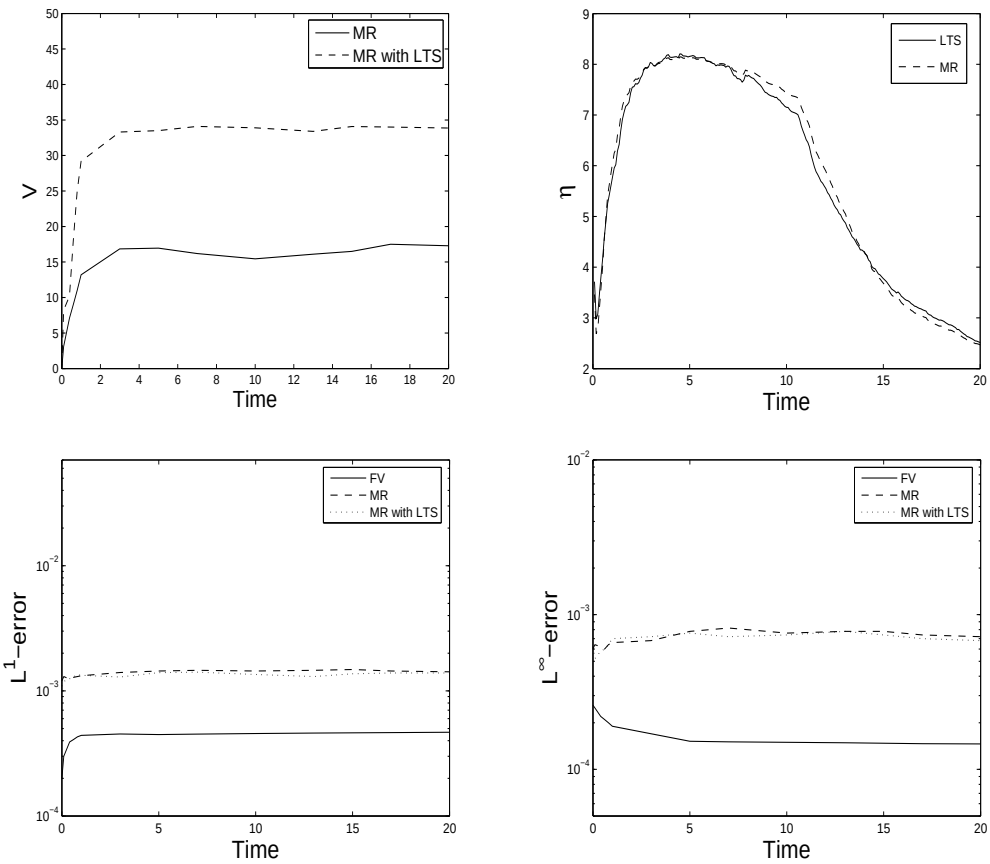

Figure 5.45: *Chemotaxis with growth, $\nu = 7$: Time evolution for speed-up rate V, data compression rate η and errors for different methods: Multiresolution scheme with global time step, and multiresolution with locally varying time step.*

well as the size of the problem cause the sparse linear system corresponding to (1.37b) to be ill-conditioned. This system needs to be solved in each time step and to this end, we use the Cholesky method.

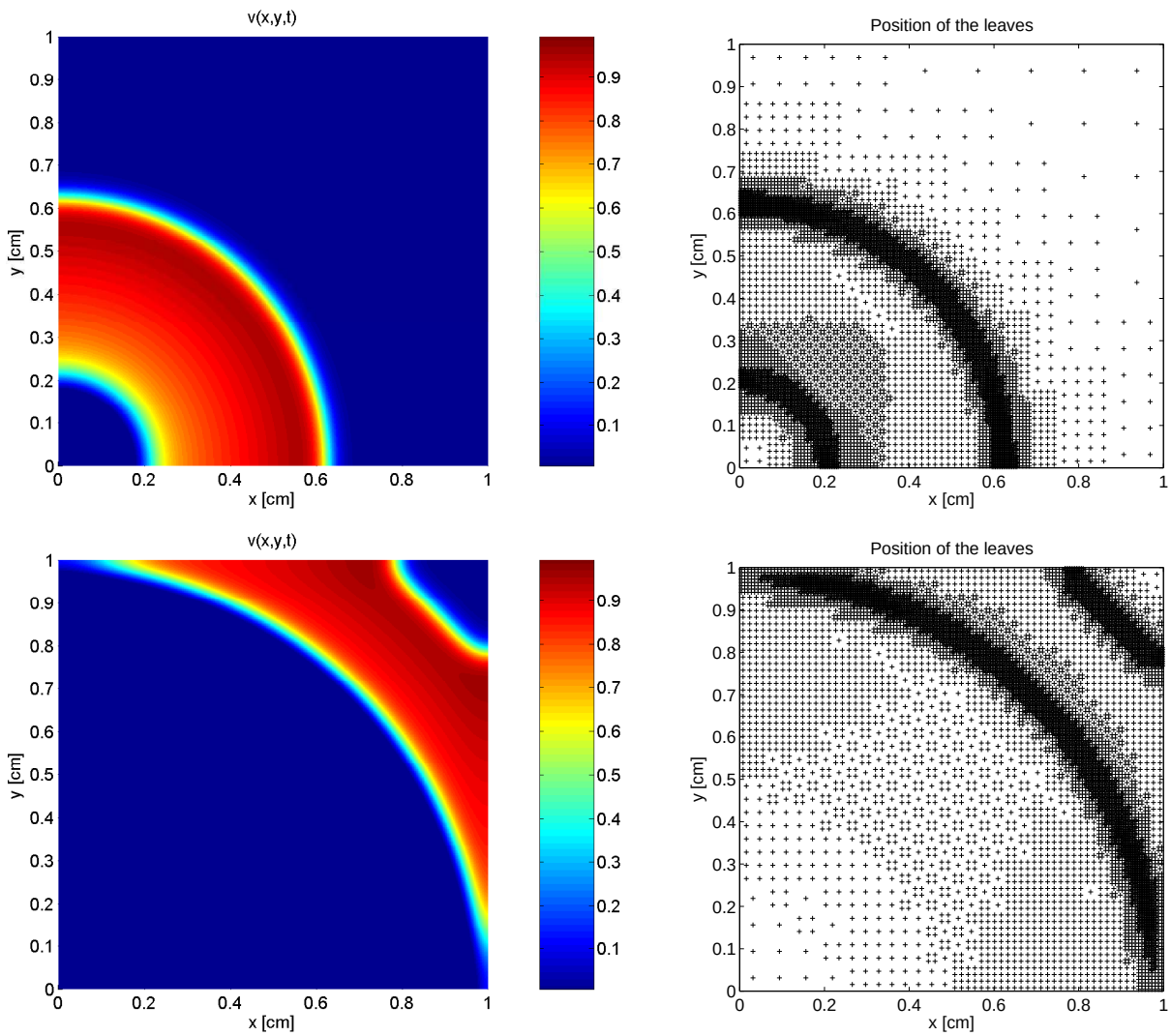

Figure 5.46: *Monodomain model: Numerical solution for v, measured in* [mV] *(left) and leaves of the corresponding tree at times (from top to bottom) $t = 1.5\,\mathrm{ms}$, $t = 3.5\,\mathrm{ms}$.*

5.4.1 2D monodomain model

For this example, we consider the simple monodomain model (1.41) with homogeneous Neumann boundary conditions. The ionic current and membrane model is determined by the FitzHugh-Nagumo membrane kinetics (1.36), with $a = 0.16875$, $b = 1.0$, $\lambda = -100$ and $\theta = 0.25$. The computational domain is the square $\Omega = [0, 1\ \mathrm{cm}]^2$, and the remaining parameters are $c_\mathrm{m} = 1.0\,\mathrm{mF/cm}^2$ and $\beta = 1.0\,\mathrm{cm}^{-1}$. The units for v, w

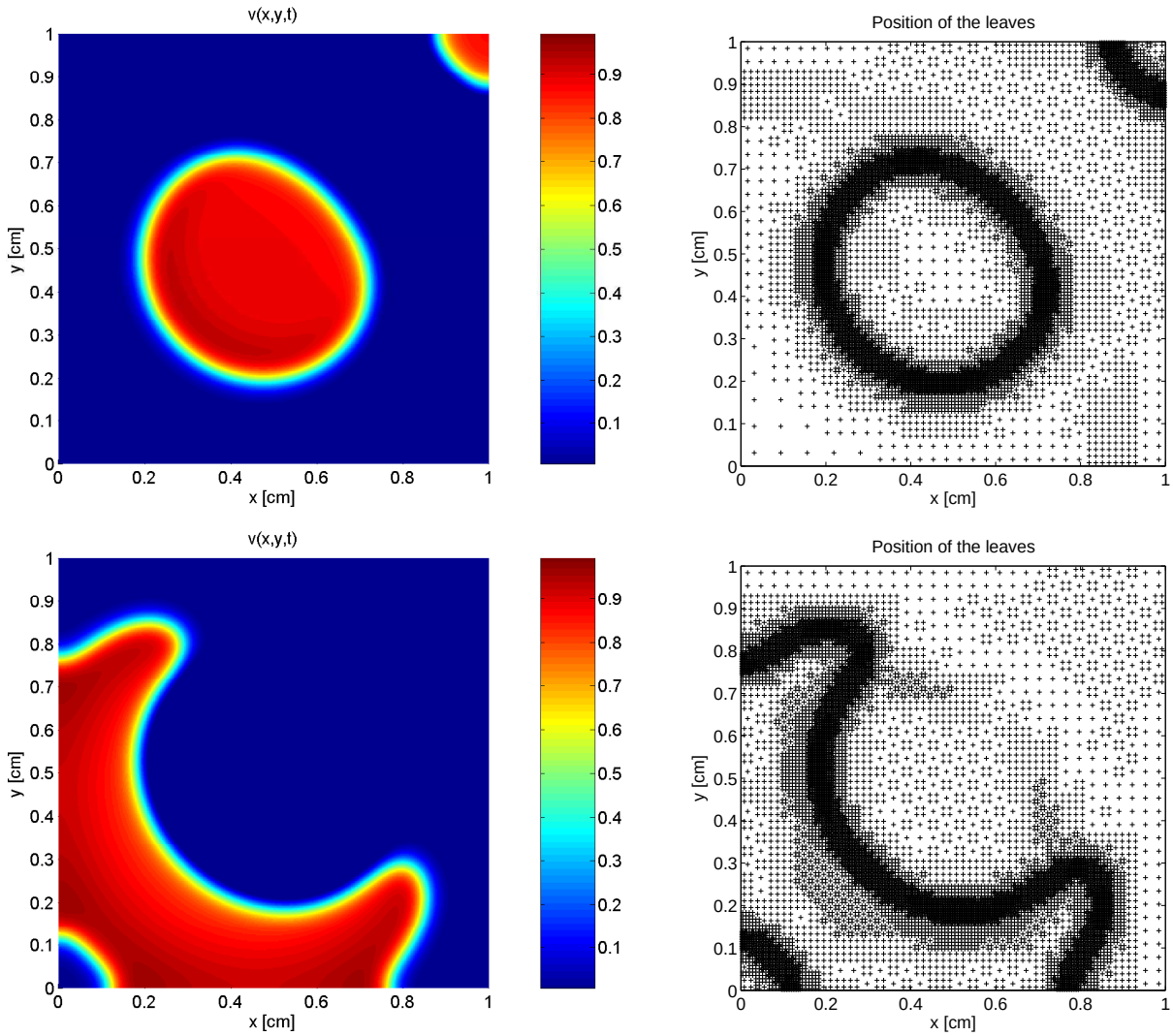

Figure 5.47: *2D monodomain model: Numerical solution for v, measured in* [mV] *(left) and leaves of the corresponding tree at times (from top to bottom)* $t = 4.5\,\mathrm{ms}$ *and* $t = 5.5\,\mathrm{ms}$.

are mV. We consider in (1.41)

$$\mathbf{M}_{\mathrm{e}}(\mathbf{M}_{\mathrm{e}}+\mathbf{M}_{\mathrm{i}})^{-1}\mathbf{M}_{\mathrm{i}} := \begin{bmatrix}\gamma & 0\\ 0 & \gamma\end{bmatrix}, \quad \gamma = 0.01.$$

The initial data for v and w are respectively

$$v^0(x,y) = \left(1 - \frac{1}{1+\exp(-50(x^2+y^2)^{1/2}-0.1)}\right)\,\mathrm{mV}, \quad w_0 = 0\,\mathrm{mV}.$$

After 4 ms, a stimulus is applied in $(x_0, y_0) = (0.5\,\mathrm{cm}, 0.5\,\mathrm{cm})$ to the membrane potential v

$$\frac{\sigma_{\mathrm{i}}^{\mathrm{l}}}{\sigma_{\mathrm{e}}^{\mathrm{l}}+\sigma_{\mathrm{i}}^{\mathrm{l}}} I_{\mathrm{app}} := \begin{cases} 1\,\mathrm{mV} & \text{if } (x-x_0)^2+(y-y_0)^2 < 0.04\,\mathrm{cm}^2, \\ 0\,\mathrm{mV} & \text{otherwise.}\end{cases}.$$

In this example, we use $L = 10$ resolution levels, $\mathcal{N} = 262144$ elements in the finest level, a tolerance of $\varepsilon_{\mathrm{R}} = 1\times 10^{-3}$ and we compute normalized errors by comparison with a reference solution obtained with a fine mesh calculation with $\mathcal{N} = 1024^2 = 1048576$ control volumes. The time evolution is made using a first order explicit Euler scheme. Plots of the numerical solution with the corresponding adaptively refined meshes at different times are shown in Figures 5.46 and 5.47.

As can be seen from Table 5.16, the normalized errors are controlled to be of the same order of the reference tolerance ε_{R}. We also see that the MR algorithm is efficient: we have high rates of memory compression and speed-up.

5.4.2 3D monodomain model

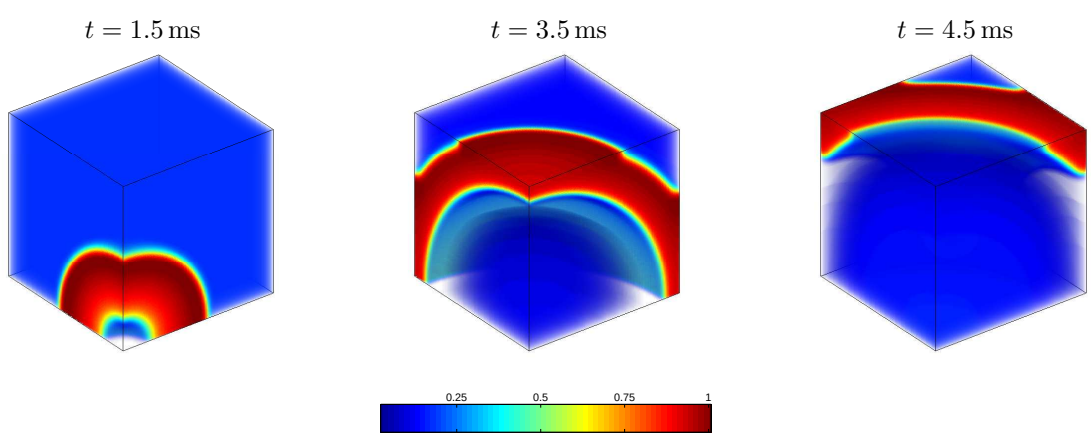

Figure 5.48: *3D monodomain model: Numerical solution v, measured in* [mV] *for the monodomain model at different times.*

We perform a simulation for the simple monodomain model described in (1.41) with homogeneous Neumann boundary conditions. The ionic current and membrane model is determined by the FitzHugh-Nagumo membrane kinetics (1.36), with $a = 0.16875$, $b = 1.0$, $\lambda = -100$ and $\theta = 0.25$. The computational domain is the cube $\bar{\Omega} = [0, 1\,\mathrm{cm}]^3$, the number of control volumes is $\mathcal{N} = 262144$ and the remaining parameters are $c_{\mathrm{m}} =$

$1.0\,\mathrm{mF/cm^2}$ and $\beta = 1.0\,\mathrm{cm}^{-1}$. The units for v, w are mV. We consider in (1.41) $(1+\lambda)^{-1}\mathbf{M}_\mathrm{i} := \mathrm{diag}(\gamma,\gamma)$ with $\gamma = 0.01$.

The respective initial data for v and w are

$$v^0(x,y) = \left(1 - \frac{1}{1+\exp(-50(x^2+y^2)^{1/2} - 0.1)}\right)\,\mathrm{mV}, \quad w_0 = 0\,\mathrm{mV}.$$

After 4 ms, an instantaneous stimulus is applied in $(x_0, y_0) = (0.5\,\mathrm{cm}, 0.5\,\mathrm{cm})$ to the membrane potential v

$$\frac{\lambda}{1+\lambda} I_\mathrm{app} := \begin{cases} 1\,\mathrm{mV} & \text{if } (x-x_0)^2 + (y-y_0)^2 < 0.04\,\mathrm{cm}^2, \\ 0\,\mathrm{mV} & \text{otherwise.} \end{cases}.$$

Time	$\mathcal{N}$	h	L^1-error	$r^1(v)$
$t = 1.5$	4096	0.0625	5.68×10^{-2}	–
	32768	0.0313	2.58×10^{-2}	1.2412
	262144	0.0156	1.21×10^{-2}	1.2356
	2097152	0.0078	5.67×10^{-3}	1.1936
$t = 3.5$	4096	0.0625	2.34×10^{-2}	–
	32768	0.0313	1.07×10^{-2}	1.2315
	262144	0.0156	4.91×10^{-3}	1.2238
	2097152	0.0078	2.28×10^{-3}	1.2067
$t = 4.5$	4096	0.0625	9.12×10^{-3}	–
	32768	0.0313	4.26×10^{-3}	1.1982
	262144	0.0156	1.89×10^{-3}	1.2725
	2097152	0.0078	8.91×10^{-4}	1.1849

Table 5.17: *3D monodomain model: Corresponding simulated time in* [ms]*, number of control volumes $\mathcal{N}$, meshsize h, approximate L^1-errors for the transmembrane potential v and convergence rates $r(v)$.*

Snapshots of the corresponding numerical solution at different times are shown in Figure 5.48. Here, due to the lack of exact solutions for these examples, we compute errors in different norms using a numerical solution on a extremely fine mesh (of 134217728 and 1048576 control volumes for the 3D and 2D models respectively) as reference. To measure errors between such a reference solution u_r and an approximate solution u_h, we will use L^p-errors: $e_p = \|u^n - u_h^n\|_p$, $p = 1, 2, \infty$, where

$$e_\infty = \max_{K\in\mathcal{T}} \left|u_{r,K}^n - u_{h\,K}^n\right|; \quad e_p = \left(\frac{1}{|K|}\sum_{K\in\mathcal{T}} \left|u_{r,K}^n - u_{h\,K}^n\right|^p\right)^{1/p}, \quad p = 1, 2.$$

Here $u_{r,K}^n$ stands for the projection of the reference solution onto the control volume K. The corresponding convergence history for Example 1 is given in Table 5.17. From this information we point out that the method provides a rate of convergence around 1.2. By rate of convergence we mean

$$r(u) = \frac{\log\left(\frac{e(u)}{e^*(u)}\right)}{\log(h/h^*)},$$

where $e(u)$ and $e^*(u)$ denote the corresponding errors computed for two consecutive meshes of sizes h and h^* respectively.

5.4.3 A 2D bidomain model

Now in the first example for the bidomain model, consider a two-dimensional domain $\bar{\Omega} = [0, 1\text{ cm}]^2$, and the bidomain model (1.37) with rotational anisotropy and $c_{\mathrm{m}} = 1.0\,\mathrm{mF/cm^2}$, $\sigma_{\mathrm{i}}^{\mathrm{l}} = 3.0 \times 10^{-3}\,\Omega^{-1}\mathrm{cm}^{-1}$, $\sigma_{\mathrm{i}}^{\mathrm{t}} = 3.1525 \times 10^{-4}\,\Omega^{-1}\mathrm{cm}^{-1}$ $\sigma_{\mathrm{e}}^{\mathrm{l}} = 2.0 \times 10^{-3}\,\Omega^{-1}\mathrm{cm}^{-1}$, $\sigma_{\mathrm{e}}^{\mathrm{t}} = 1.3514 \times 10^{-3}\,\Omega^{-1}\mathrm{cm}^{-1}$, $\beta = 100\,\mathrm{cm}^{-1}$, $R_{\mathrm{m}} = 2.5 \times 10^3\,\Omega\,\mathrm{cm}^2$, $v_p = 100\,\mathrm{mV}$, $\eta_1 = 0.0044$, $\eta_2 = 0.12$, $\eta_3 = 1$, $\eta_4 = 13$ and $\eta_5 = 0.15$. The initial data is given by

$$u_{\mathrm{e}}^0(x, y) = \begin{cases} 1\,\mathrm{mV} & \text{if } \|(x - 0.5, y - 0.5)\| \leq 0.1 \\ 0 & \text{otherwise} \end{cases}, \quad w_0(x, y) = \sin^2(x) + \cos^2(y)\,\mathrm{mV}, \quad v_0 = \sin(w_0).$$

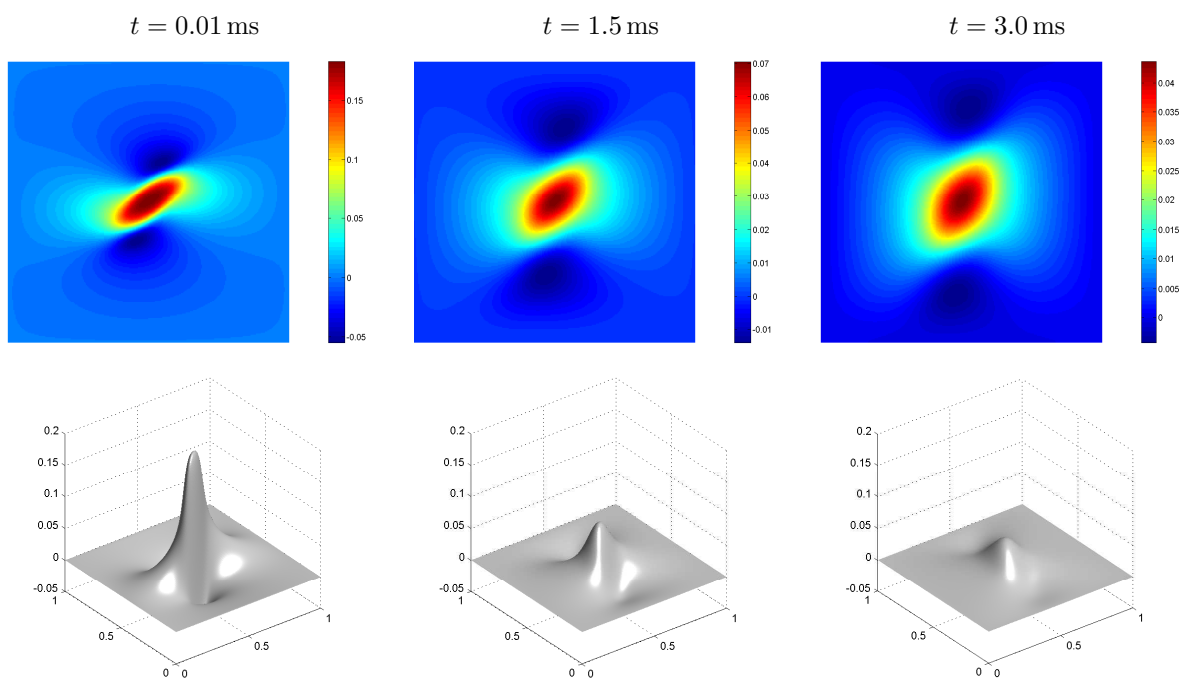

Figure 5.49: *First example for the bidomain model: Transmembrane potential v, measured in* [mV] *for the bidomain model at different times.*

We use a regular mesh of $\mathcal{N} = 65536$ control volumes to obtain the series of plots of the numerical solution for the extracellular potential that we depict in Figure 5.49. Due to the lack of exact solutions for these examples, we will compute errors in different norms using a numerical solution on a extremely fine mesh (of 1048576 control volumes) as reference. In addition, from Table 5.18 we observe that the rate of convergence provided by the method is a bit higher than $O(h)$, but still lower than the rates obtained for the monodomain case. This behavior of the experimental rates of convergence can be also observed from Figure 5.50, where we show the meshsize and errors in different norms plotted in a log-log fashion against the number of control volumes.

Now for a second example, the simulations use a computational domain $\Omega = [0, 5\,\mathrm{cm}]^2$ and the parameters in (1.37) and (1.35) (after [74, 140, 157, 158]) are given by the membrane capacitance $c_{\mathrm{m}} = 1.0\,\mathrm{mF/cm^2}$, the intracellular conductivity in the principal axis $\sigma_{\mathrm{i}}^{\mathrm{l}} = 6\,\Omega^{-1}\mathrm{cm}^{-1}$, the remaining intracellular conductivity $\sigma_{\mathrm{i}}^{\mathrm{t}} = 0.6\,\Omega^{-1}\mathrm{cm}^{-1}$ (corresponding to an anisotropy ratio of 10), the extracellular conductivities $\sigma_{\mathrm{e}}^{\mathrm{l}} = 24\,\Omega^{-1}\mathrm{cm}^{-1}$

Time	$\mathcal{N}$	L^1-error	$r^1(v)$	L^2-error	$r^2(v)$	$L^\infty-$error	$r^\infty(v)$
$t = 0.01$	1024	7.68×10^{-3}	–	4.79×10^{-3}	–	6.51×10^{-3}	–
	4096	3.81×10^{-3}	1.0135	2.28×10^{-3}	1.0253	3.13×10^{-3}	1.0378
	16384	1.12×10^{-3}	1.0904	9.85×10^{-4}	1.0831	1.26×10^{-3}	1.0903
	65536	5.87×10^{-4}	1.0812	4.69×10^{-4}	1.0982	6.07×10^{-4}	1.0894
$t = 1.5$	1024	3.15×10^{-3}	–	3.01×10^{-4}	–	7.14×10^{-3}	–
	4096	1.28×10^{-3}	1.0187	1.21×10^{-4}	0.9804	3.54×10^{-3}	1.0953
	16384	5.89×10^{-4}	1.0712	5.72×10^{-5}	1.1034	1.63×10^{-4}	1.0937
	65536	2.61×10^{-4}	1.1106	2.43×10^{-5}	1.0267	7.58×10^{-5}	1.0881
$t = 3.0$	1024	1.64×10^{-3}	–	2.92×10^{-3}	–	1.05×10^{-2}	–
	4096	7.39×10^{-4}	1.1053	1.40×10^{-3}	0.9659	4.67×10^{-3}	0.9896
	16384	3.28×10^{-4}	1.0972	6.82×10^{-4}	1.0024	2.13×10^{-3}	1.0480
	65536	1.57×10^{-4}	1.0835	2.97×10^{-4}	1.1321	9.72×10^{-4}	1.0875

Table 5.18: *First example for the bidomain example: Corresponding simulated time in* [ms]*, number of control volumes* $\mathcal{N}$*, approximate errors in different norms for the transmembrane potential* v *and convergence rates* $r(v)$*.*

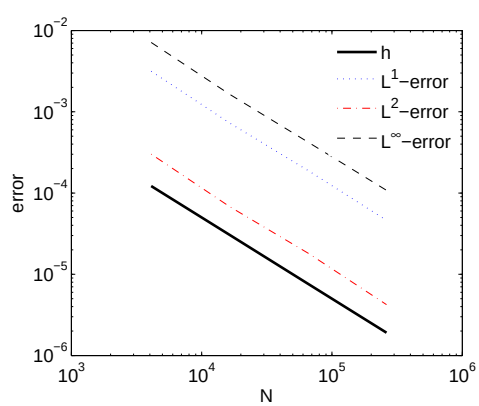

Figure 5.50: *First example for the bidomain model: Meshsize* h *and errors in different norms for the transmembrane potential* v *versus the number of control volumes* $\mathcal{N}$*. The simulated time is* $t = 1.5\,\mathrm{ms}$*.*

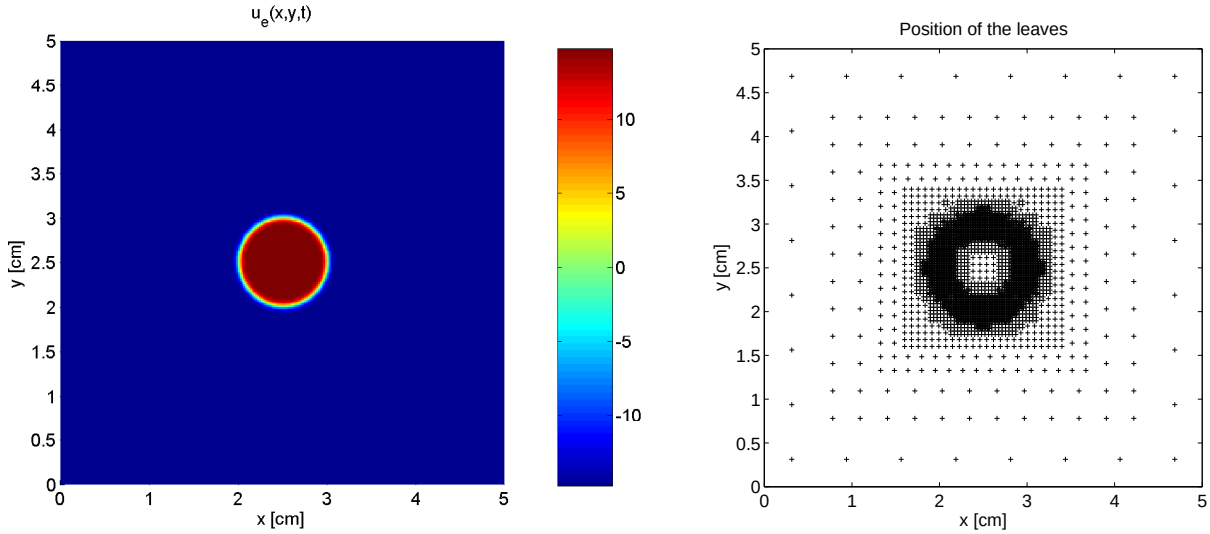

Figure 5.51: *Second example for the bidomain model: Initial condition for the extracellular potential* u_{e}*, and leaves of the corresponding tree data structure.*

and $\sigma_{\mathrm{e}}^{\mathrm{t}} = 12\,\Omega^{-1}\mathrm{cm}^{-1}$ (corresponding to an anisotropy ratio of 2), the surface-to-volume ratio $\beta = 2000\,\mathrm{cm}^{-1}$, the surface resistivity $R_{\mathrm{m}} = 2 \times 10^4\,\Omega\,\mathrm{cm}^2$, $v_p = 100\,\mathrm{mV}$, $\eta_1 = 0.005$, $\eta_2 = 0.1$, $\eta_3 = 1.5$, $\eta_4 = 7.5$, and $\eta_5 = 0.1$. The fibers form an angle of $\pi/4$ with the x-axis and the initial datum is given by a stimulus applied on the extracellular potential u_{e} in the center of the domain, while both v and the gating variable w are initially set to zero (see Figure 5.51). The units for v, u_e and w are mV.

The following MR setting is chosen. We utilize wavelets with $r = 3$ vanishing moments, a maximal resolution level $L = 9$, and therefore a finest mesh with $\mathcal{N} = 65536$ elements. The reference tolerance given by $\varepsilon_{\mathrm{R}} = 5.0 \times 10^{-4}$.

We show in Figures 5.52 and 5.53 a sequence of snapshots after an initial stimulus applied to the center of the domain, corresponding to transmembrane potential v, extracellular potential u_{e} and adaptive mesh.

Table 5.19 illustrates the efficiency and accuracy of the base MR method by tabulating CPU ratio $\mathcal{V}$, compression rate η and normalized errors. By using MR, we obtain an average data compression rate of 17 and an increasing speed-up rate up to 26.09. Moreover, the errors in three different norms remain of the order of ε_{R}. Here we have computed normalized errors using a reference FV solution on a grid with $\mathcal{N} = 1024^2 = 1048576$ control volumes.

For the time integration using the LTS method, we choose the maximum CFL number allowed by (2.22), $\mathrm{CFL}_{l=0} = 0.5$ for the coarsest level and $\mathrm{CFL}_l = 2^l \mathrm{CFL}_{l=0}$ for finer levels. For the RKF computations, we use $\delta_{\mathrm{desired}} = 1 \times 10^{-4}$, $\mathcal{S}_0 = 0.1$, $\mathcal{S}_{\mathrm{min}} = 0.01$, and the initial CFL condition $\mathrm{CFL}_{t=0} = 0.5$.

We select this example for a detailed comparison of the performance of the FV and MR methods with a global time step, the MR method with RKF adaptive global time stepping (MR-RKF), and the MR method with local time stepping (MR-LTS). The evolution of the speed-up factor $\mathcal{V}$ the and data compression rate η for the MR versions and of the normalized L^1 and L^∞ errors for all these methods are displayed in Figure 5.55. From these plots it is observed that with RKF and LTS, the data compression rate is of the same order during

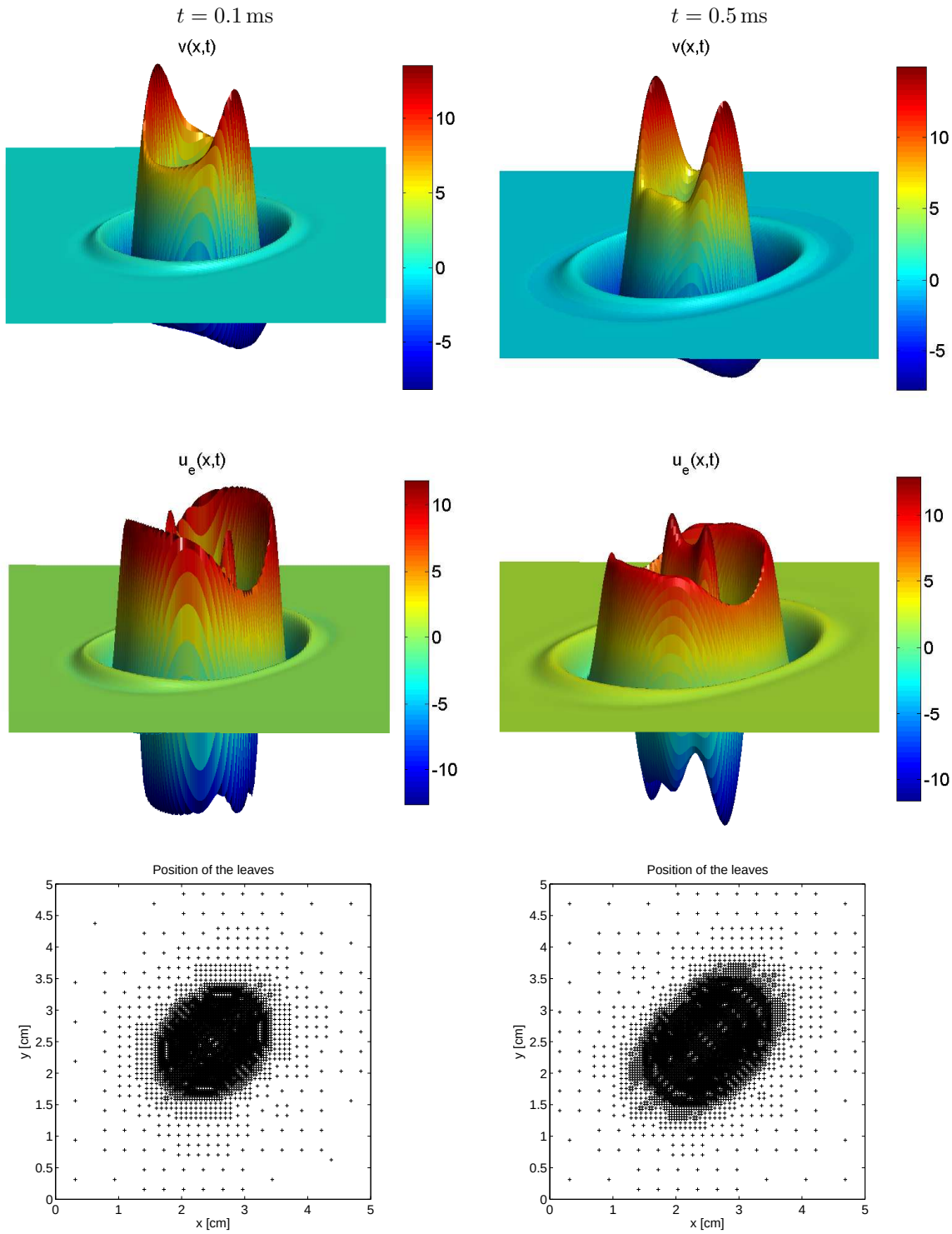

Figure 5.52: *Second example for the bidomain model: Numerical solution for transmembrane potential v and extracellular potential u_e in* [mV]*, and leaves of the corresponding tree data structure at times $t = 0.1\,\mathrm{ms}$ and $t = 0.5\,\mathrm{ms}$.*

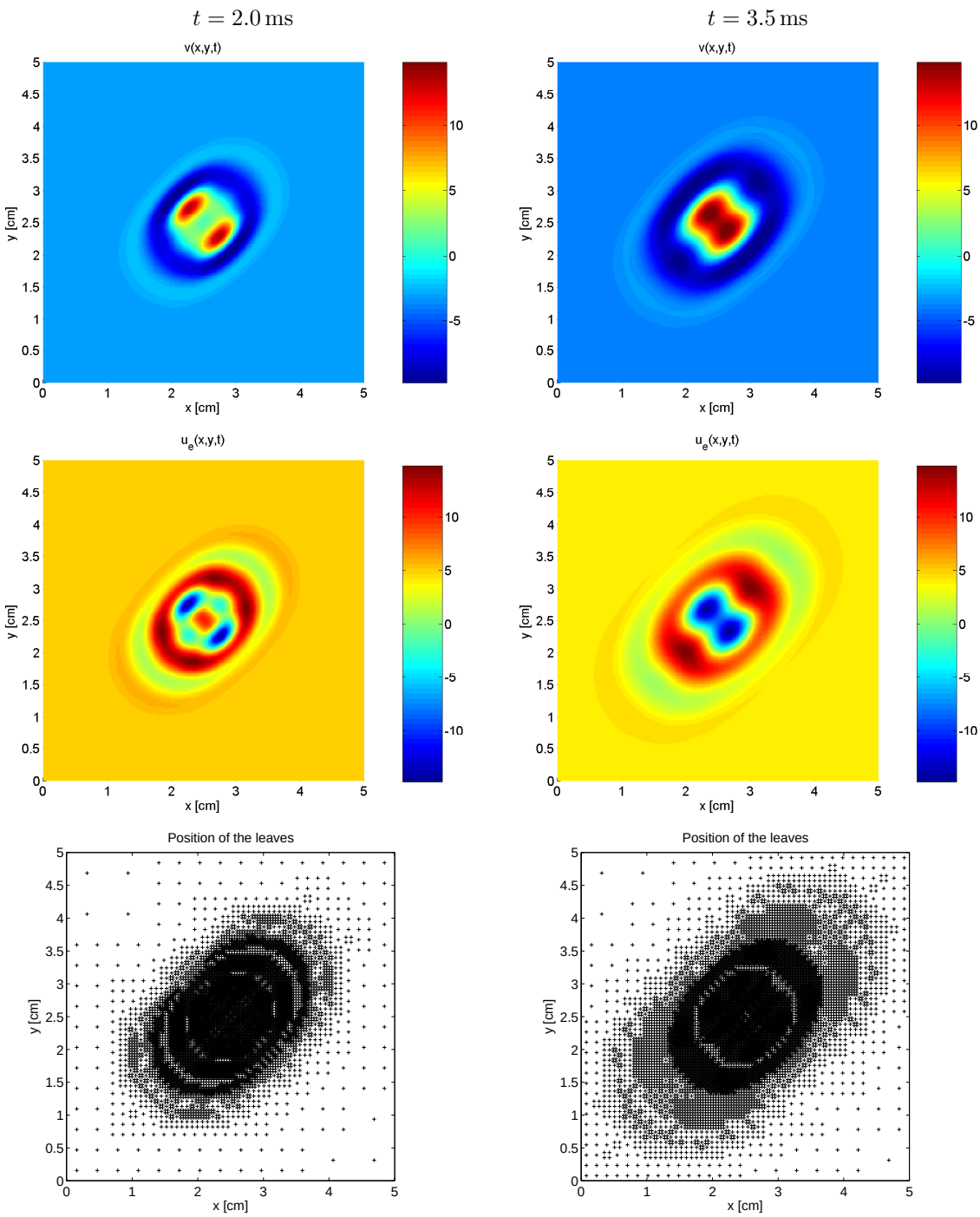

Figure 5.53: *Second example for the bidomain model: Numerical solution for transmembrane potential v and extracellular potential u_e in* [mV], *and leaves of the corresponding tree data structure at times $t = 2.0\,\mathrm{ms}$ and $t = 3.5\,\mathrm{ms}$.*

Time	$\mathcal{V}$	η	Pot.	L^1-error	L^2-error	$L^\infty-$error
$t = 0.1$	13.74	19.39	v	3.68×10^{-4}	8.79×10^{-5}	6.51×10^{-4}
			u_e	2.01×10^{-4}	6.54×10^{-5}	5.22×10^{-4}
$t = 0.5$	21.40	17.63	v	4.06×10^{-4}	9.26×10^{-5}	6.83×10^{-4}
			u_e	2.79×10^{-4}	8.72×10^{-5}	5.49×10^{-4}
$t = 2.0$	25.23	17.74	v	4.37×10^{-4}	1.25×10^{-4}	6.88×10^{-4}
			u_e	3.48×10^{-4}	9.44×10^{-5}	6.11×10^{-4}
$t = 5.0$	26.09	16.35	v	5.29×10^{-4}	1.94×10^{-4}	7.20×10^{-4}
			u_e	4.15×10^{-4}	1.06×10^{-4}	6.32×10^{-4}

Table 5.19: *Second example for the bidomain model: Corresponding simulated time, CPU ratio $\mathcal{V}$, compression rate η and normalized errors.*

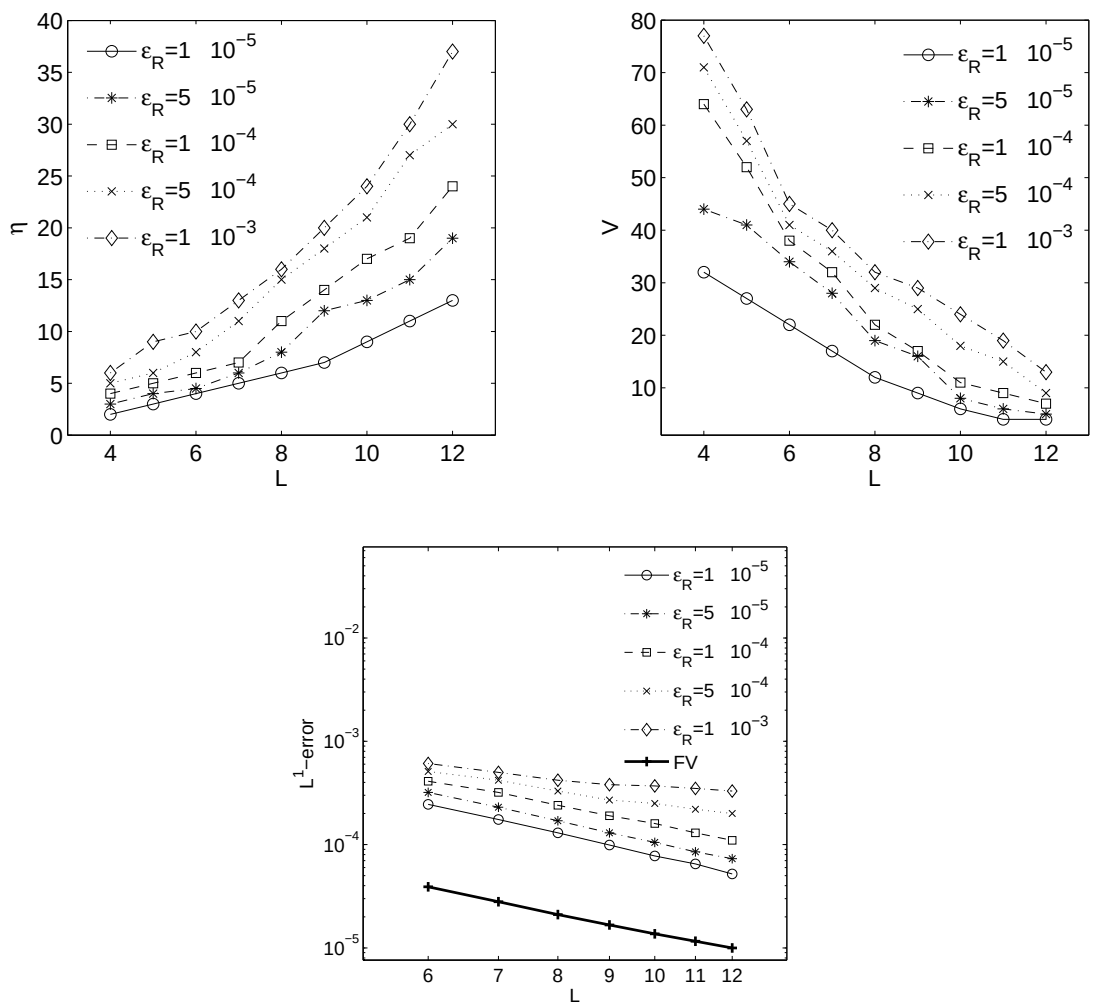

Figure 5.54: *Second example for the bidomain model: data compression rate η (top left), speed-up factor $\mathcal{V}$ (top right) and L^1-errors for different scales L and values of ε_R (bottom). The simulated time is $t = 2.0\,\mathrm{ms}$.*

the time evolution, which means that the adaptive meshes are not too different from method to method. Also, a substantial additional gain is obtained in speed-up rate when comparing with a MR calculation using global time stepping: The MR-LTS method gives us an additional speed-up factor of about 2, while with the RKF alternative we obtain an additional speed-up of about 4. This effect could be explained in part from the fact that there is no need of a synchronization procedure for the RKF computations and the fact that the CFL condition (2.22) is not imposed during the time evolution with the MR-RKF method, allowing larger time steps. (Related to this fact, it should be noted that although condition (2.22) guarantees numerical stability of the solutions, in practice this is observed to be a too strict estimate). We can also conclude that the errors of the MR-LTS computations are kept of the same order that the errors obtained with a global time stepping, while the incurred errors by using the MR-RKF method are larger during the whole time evolution.

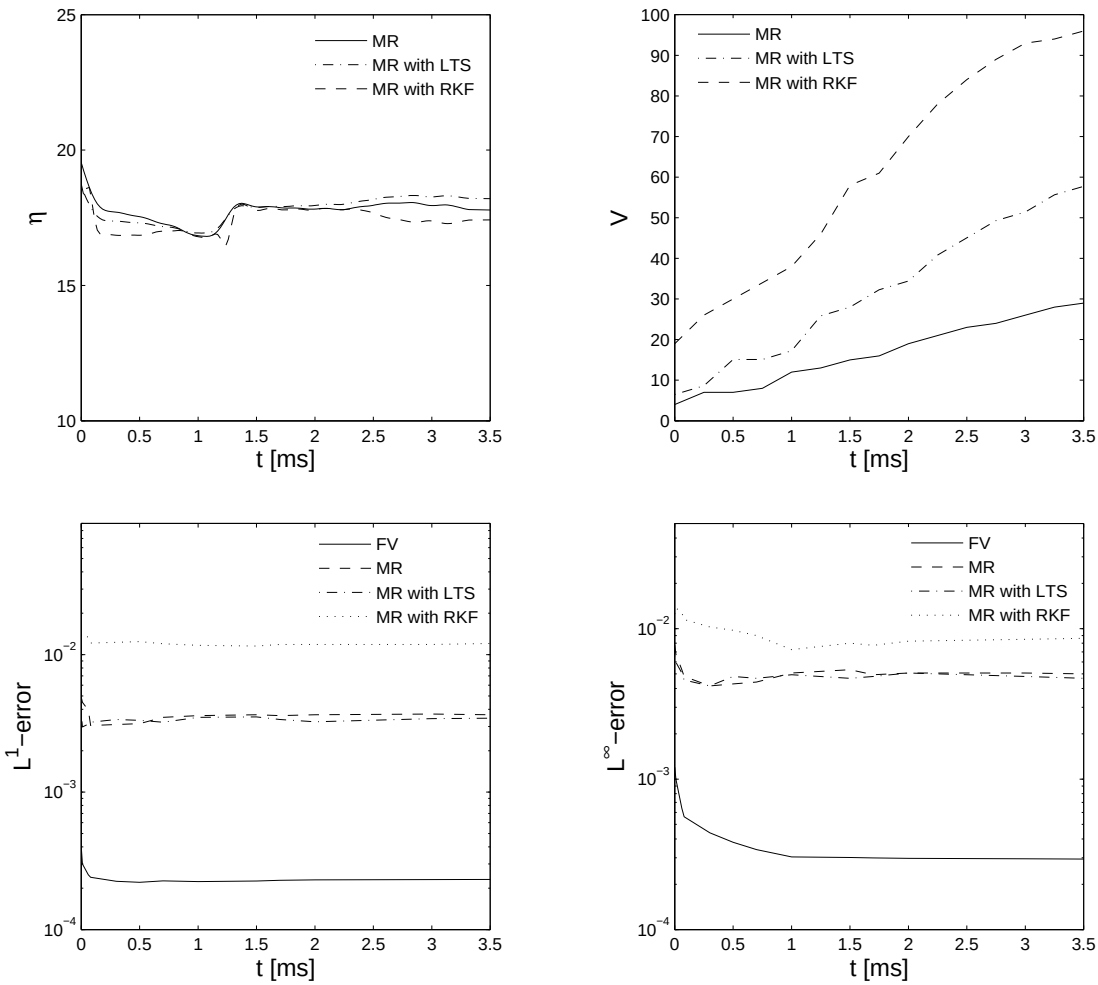

Figure 5.55: *Second example for the bidomain model: Time evolution for data compression rate η, speed-up rate $\mathcal{V}$, and normalized errors for different methods: MR scheme with global time step, MR with locally varying time stepping and MR with RKF time stepping.*

As a third example for the bidomain model, let us consider a slightly different setting. First we apply an initial stimulus at the center of the domain, later in $t = 0.2\,\text{ms}$ we apply another stimulus to the northwest

corner of the domain, and then in $t = 1.0$ ms we apply a third stimulus of the same magnitude to the northeast and southwest corners. The system is evolved and we show snapshots of the numerical solution for v, u_{e} and the adaptive mesh. We use the MR-RKF method with $\mathcal{N} = 65536$, $\varepsilon_{\mathrm{R}} = 2.5 \times 10^{-3}$, $\delta_{\mathrm{desired}} = 1 \times 10^{-3}$ and the remaining parameters are considered as in the previous subsection. From Figures 5.56 and 5.57 we clearly notice the anisotropic orientation of the fibers.

5.5 A doubly nonlinear diffusion model of chemotaxis

In this section, we provide numerical examples to illustrate how the approximate solutions of the simple chemotaxis model (1.45) vary when changing the parameter p from standard nonlinear diffusion ($p = 2$), to doubly nonlinear diffusion ($p > 2$). For the discretization of the examples, a standard first order finite volume method (see Section 2.4 for details on the numerical scheme) on a regular mesh of 262144 control volumes is used. We choose a simple square domain $\Omega = [-1, 1]^2$ and use the functions $a(u) = \epsilon u(1 - u)$, $f(u) = (1 - u)^2$ and $g(u, v) = \alpha u - \beta v$ along with parameters that are stated separately in each case.

For the first chemotaxis example, we choose $\epsilon = 0.01$, $\alpha = 40$, $\beta = 160$, $\chi = 0.2$ and $d = 0.05$. The initial condition for the species density is given by

$$u_0(x) = \begin{cases} 1 & \text{for } \|x\| \leq 0.2 \\ 0 & \text{otherwise,} \end{cases},$$

and the concentration for the chemoattractant is assumed to have uniform distribution $v_0(x) = 4.5$. In a first simulation, we consider the simple case of $p = 2$ and we compare the result with an analogous experiment with $p = 6$. We evolve the system until $t = 1.0$, and show in Figure 5.58 a snapshot of the cell density at this instant for both cases. Note that the special form of the functions $a(u)$ and $f(u)$ (they include the factor $(1-u)$), in the species diffusion and chemotactical cross diffusion, takes into account the volume filling effect: these terms vanish at $u = 0$ and $u = u_{\mathrm{m}} = 1$.

As a second chemotaxis example we now choose the parameters $\epsilon = 0.5$, $\alpha = 5$, $\beta = 0.5$, $\chi = 1$ and $d = 0.25$. The initial condition for the species density is given by

$$u_0(x) = \begin{cases} 1 & \text{for } \|x - (-0.25, 0.25)\| \leq 0.2 \text{ or } \|x - (0.25, -0.25)\| \leq 0.2 \\ 0 & \text{otherwise,} \end{cases}$$

and for the chemoattractant

$$v_0(x) = \begin{cases} 4.5 & \text{for } \|x - (0.25, 0.25)\| \leq 0.2 \text{ or } \|x + (0.25, 0.25)\| \leq 0.2 \\ 0 & \text{otherwise.} \end{cases}$$

The behavior of the system for the cases $p = 2$ and $p = 6$ is presented in the left and right plots, respectively, of Figures 5.59, 5.60 and 5.61.

For the third chemotaxis example, we use a model for chemotactic bacterial patterns in a liquid medium (see [148]) and to conciliate this model with the general framework of (1.45), we may rewrite (1.45) in the particular form:

$$\begin{aligned} \partial_t u &= D_u \mathrm{div}\,(|\nabla u|^{p-2}\nabla u) - \mathrm{div}\,(\chi u f(v)\nabla v) \quad \text{in } Q_T, \\ \partial_t v &= D_v \Delta v + g(u) \quad \text{in } Q_T, \end{aligned}$$

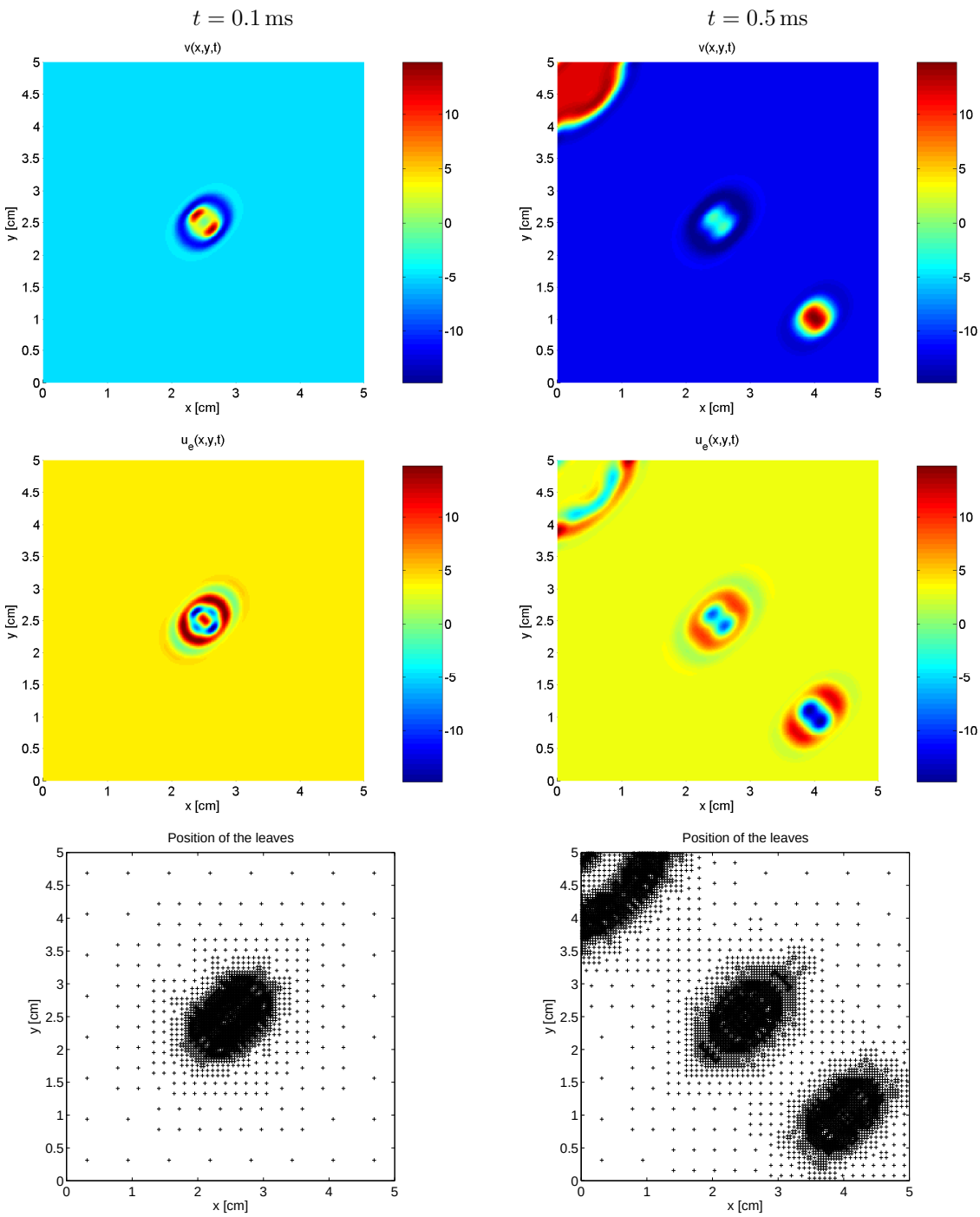

Figure 5.56: *Third example for the bidomain model: Numerical solution for transmembrane potential v and extracellular potential u_e in* [mV]*, and leaves of the corresponding tree data structure at times $t = 0.1\,\mathrm{ms}$ and $t = 0.5\,\mathrm{ms}$.*

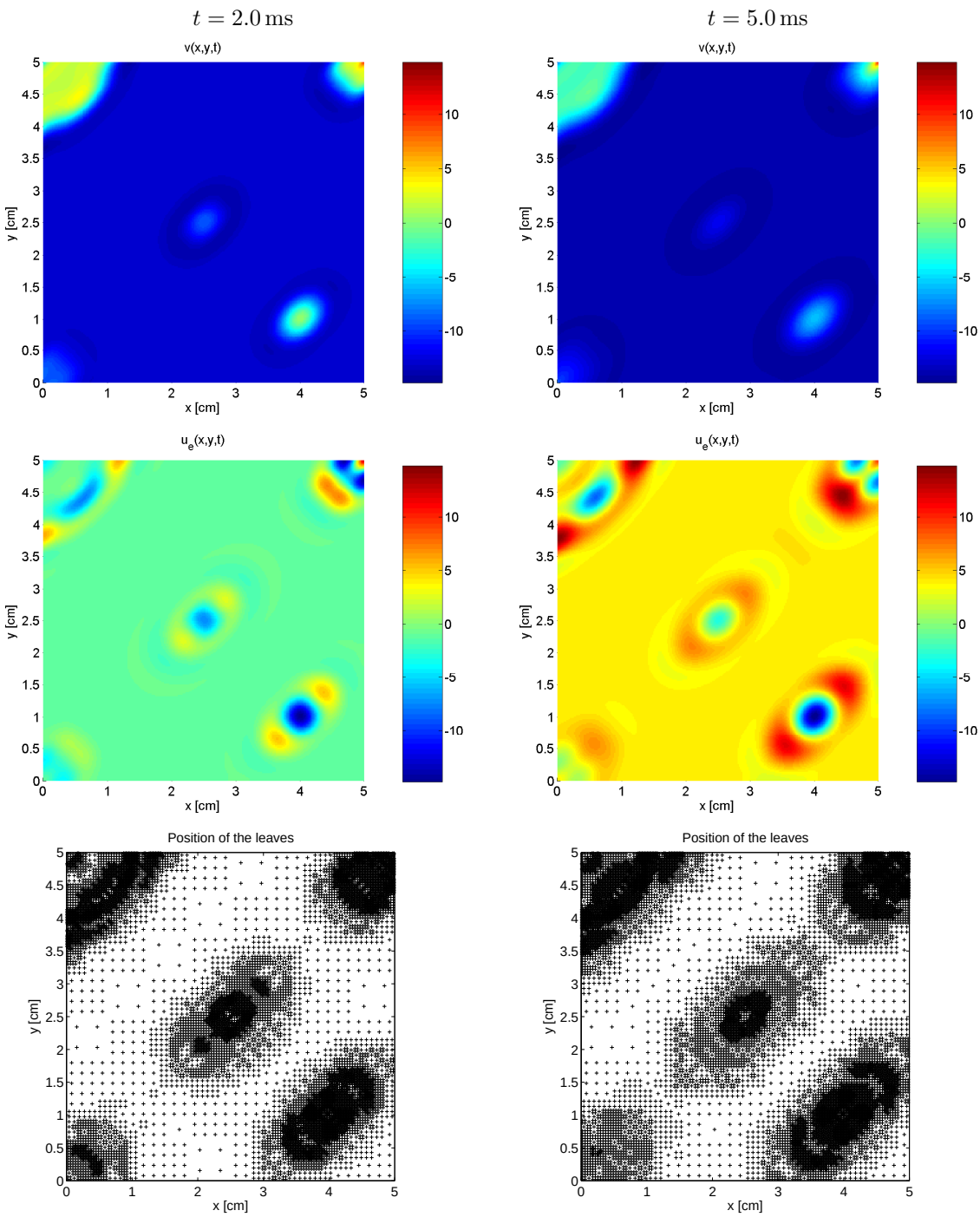

Figure 5.57: *Third example for the bidomain model: Numerical solution for transmembrane potential v and extracellular potential u_e in* [mV]*, and leaves of the corresponding tree data structure at times $t = 2.0\,\mathrm{ms}$ and $t = 5.0\,\mathrm{ms}$.*

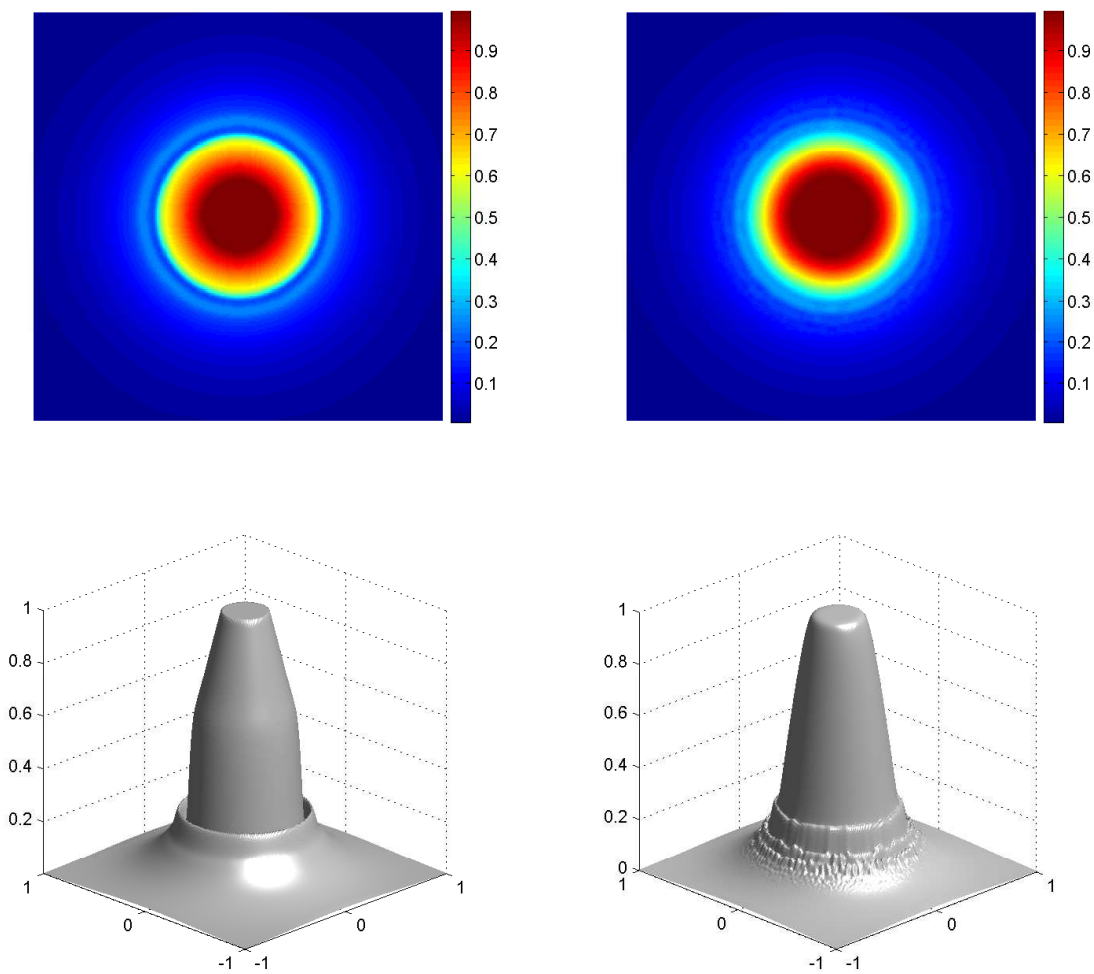

Figure 5.58: *First chemotaxis example: Numerical solution for species u, at $t = 1.0$ for $p = 2$ (left), and $p = 6$ (right).*

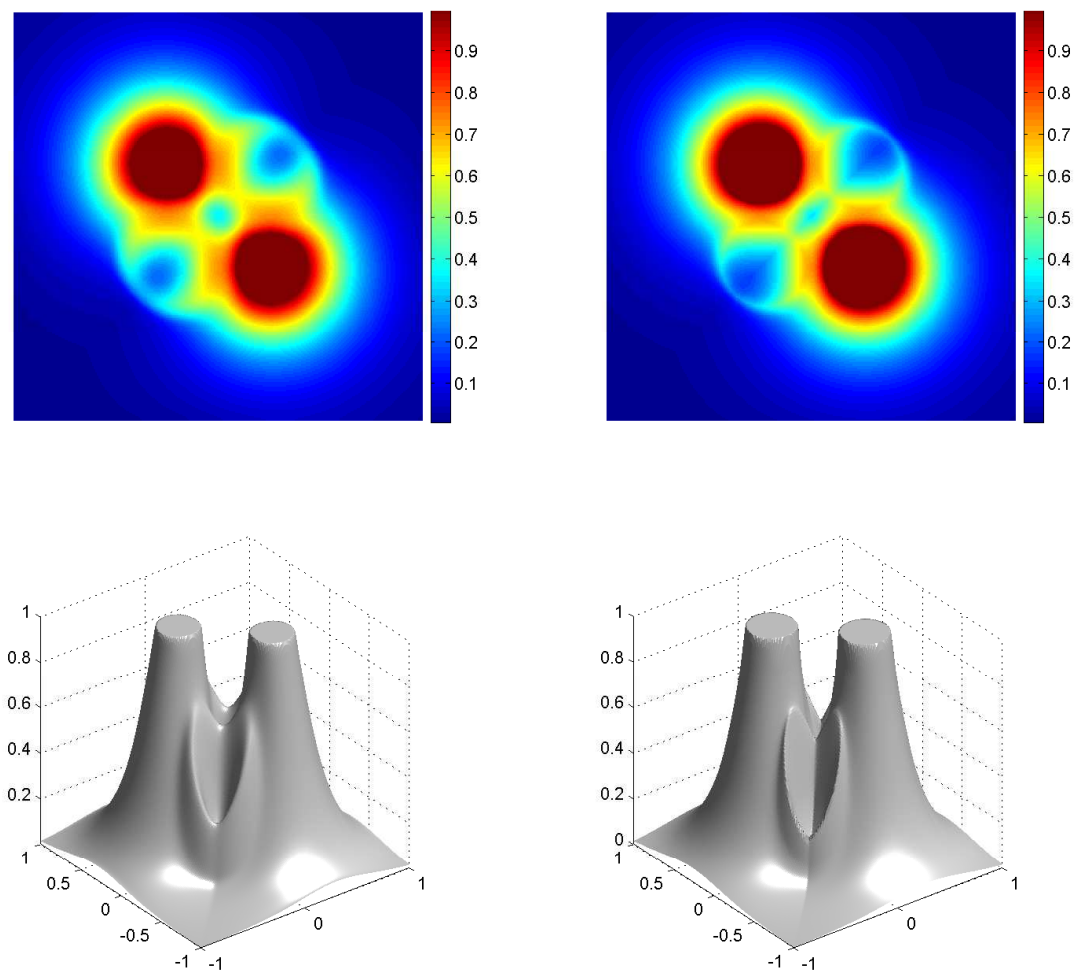

Figure 5.59: *Second chemotaxis example: Numerical solution for species u, at $t = 0.1$ for $p = 2$ (left), and $p = 6$ (right).*

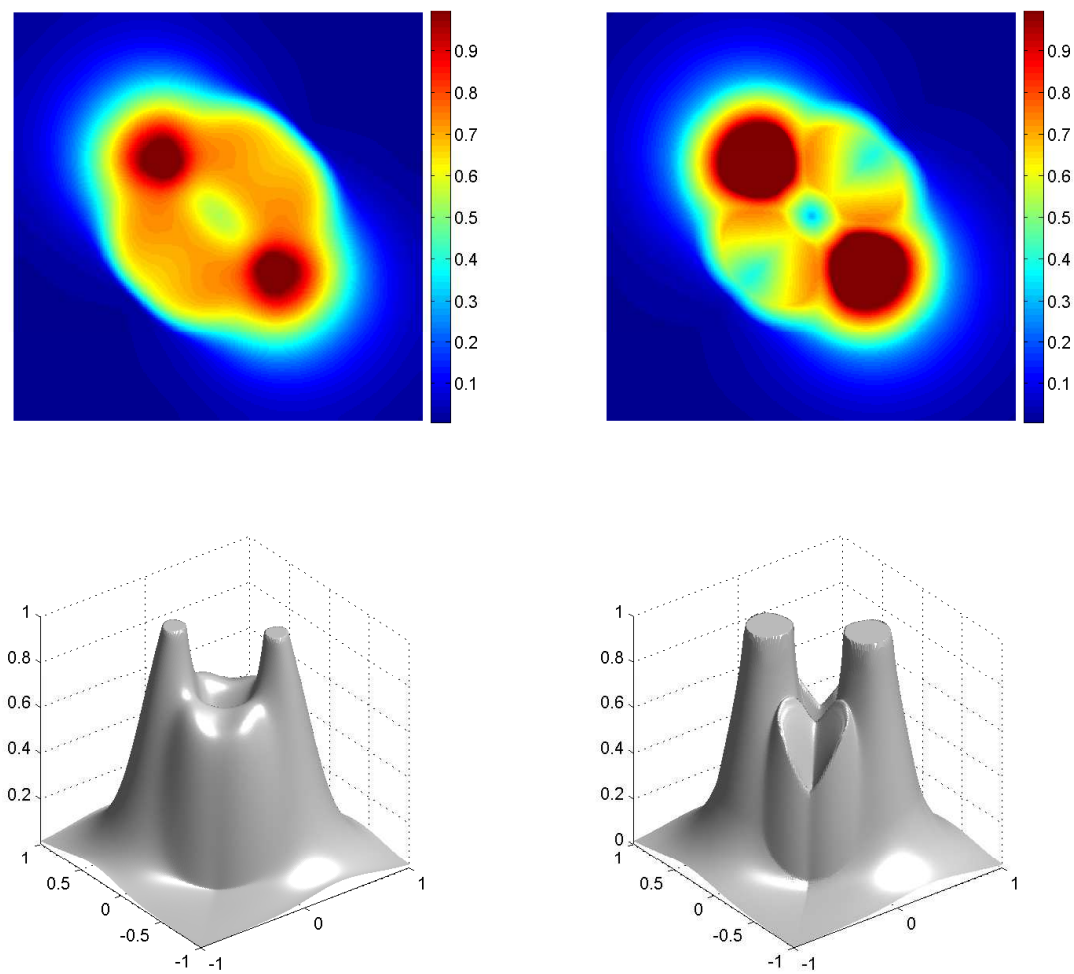

Figure 5.60: *Second chemotaxis example: Numerical solution for species u, at $t = 0.5$ for $p = 2$ (left), and $p = 6$ (right).*

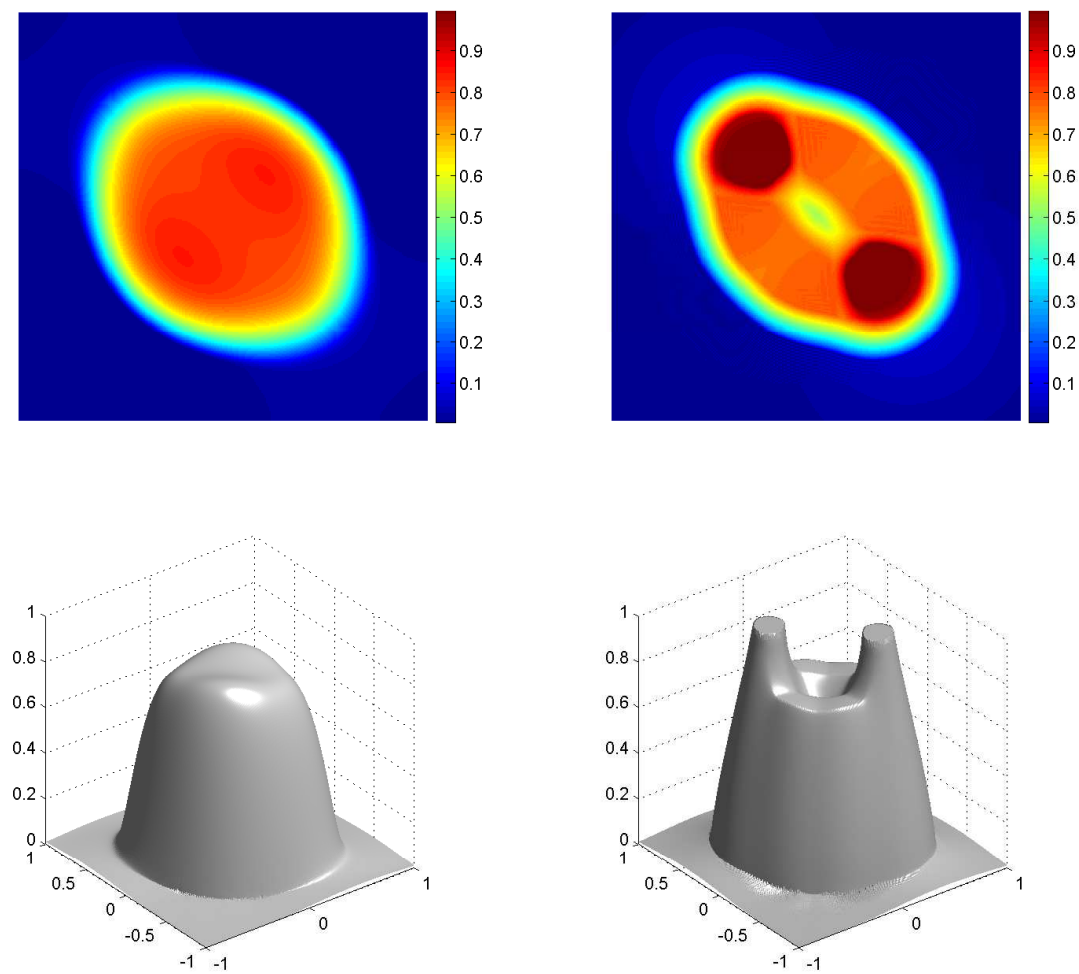

Figure 5.61: *Second chemotaxis example: Numerical solution for species u, at $t = 2.5$ for $p = 2$ (left), and $p = 6$ (right).*

$$|\nabla u|^{p-2}\frac{\partial u}{\partial \eta} = 0, \quad \frac{\partial v}{\partial \eta} = 0 \quad \text{on } \Sigma_T, \quad u(x,0) = u_0(x), \quad v(x,0) = v_0(x).$$

Here $\Omega = [0,10]^2$, $g(u) = \frac{u^2}{1+u^2}$ with $D_u = 0.33$, $D_v = 1$, and $\chi f(v) = \alpha\frac{1}{(1+v)^2}$ with $\alpha = 80$. The initial conditions consist in a random perturbation around $u = 1$ for the cell's density and $v_0 = 1$. In a first simulation we consider the simple case of $p = 2$ and we compare the result with an analogous experiment with $p = 5$. We evolve the system until $t = 2.0$, and show in Figure 5.62 a snapshot of the cell density at this instant for both cases.

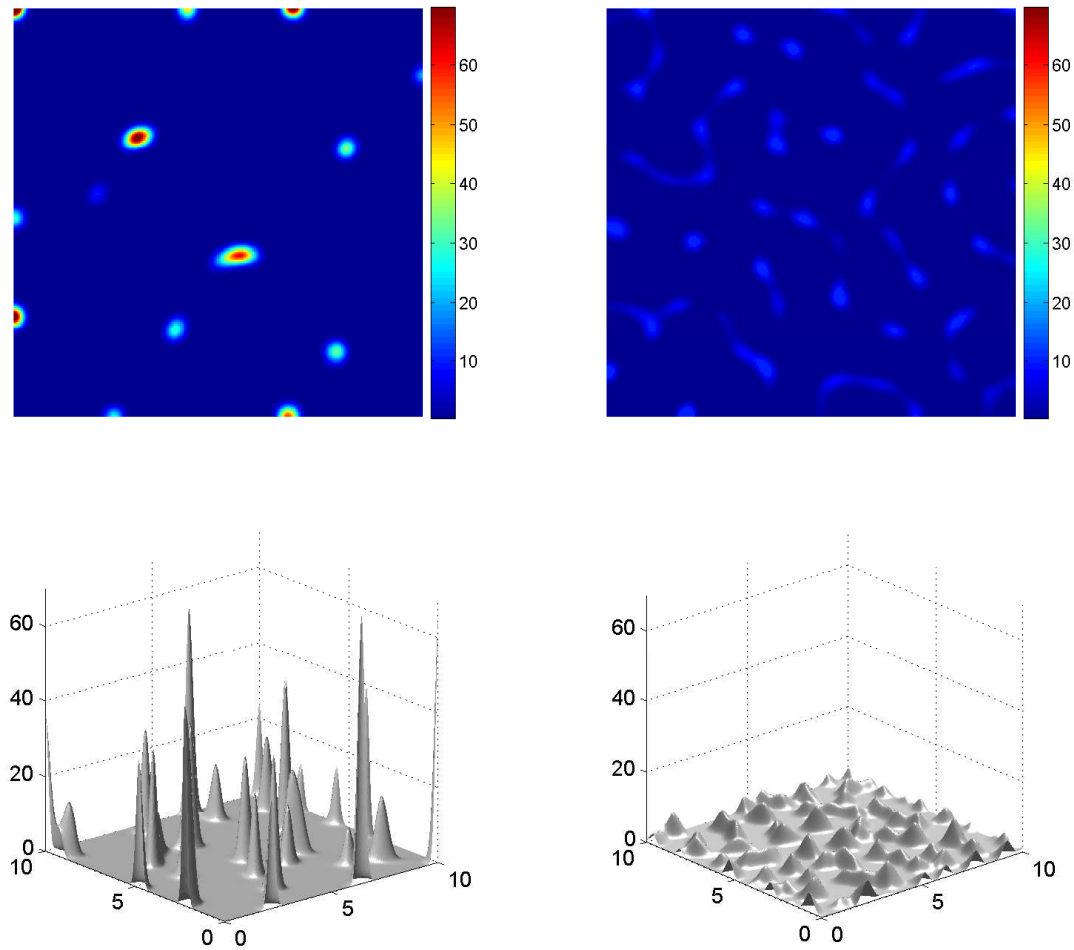

Figure 5.62: *Third chemotaxis example: Numerical solution for species u, at $t = 2.0$ for $p = 2$ (left), and $p = 5$ (right).*

As a fourth chemotaxis example, we consider a similar model used by J. Adler in the 60's for simulating the behavior of bacterial chemotaxis (see [52]).

$$\partial_t u = D_u \mathrm{div}\,(|\nabla u|^{p-2}\nabla u) + \mathrm{div}\,(\chi(1-u)f(v)\nabla v) + g(u,v) \quad \text{in } Q_T,$$
$$\partial_t v = D_v \Delta v + \frac{1}{V_2} g(u,v) \quad \text{in } Q_T,$$

where $\Omega = [-1,1]^2$, $g(u,v) = -\frac{V_1 uv}{K_1+v}$ with $V_1 = 0.35$, $K_1 = 4\times 10^{-6}$, and $\chi f(v) = \frac{K_2}{(K_3+v)^2}$, with $K_2 = 0.02$, $K_3 = 2\times 10^{-6}$. The remaining parameters are given by $D_u = 0.01$, $D_v = 0.05$, $V_2 = 0.001$ and the initial conditions are

$$u_0(x) = \begin{cases} 5\times 10^{-6} & \text{for } \|x\| \le 9.5\times 10^{-2} \\ 0 & \text{otherwise,} \end{cases}, \qquad v_0(x) = 2.64\times 10^{-5},$$

which means that the bacteria are initially located at the center of the domain, and the concentration for the chemoattractant (which in this case is galactose) is assumed to have uniform distribution (see [52]). The term $1-u$ in the cross diffusion takes into account the volume filling effect. The cell densities for both $p=2$ and $p=5$ are displayed in Figure 5.63. We remark that in this example, the pattern shown by the model with $p=5$ is qualitatively closer to the numerical results tested against experimental data (compare with [52]).

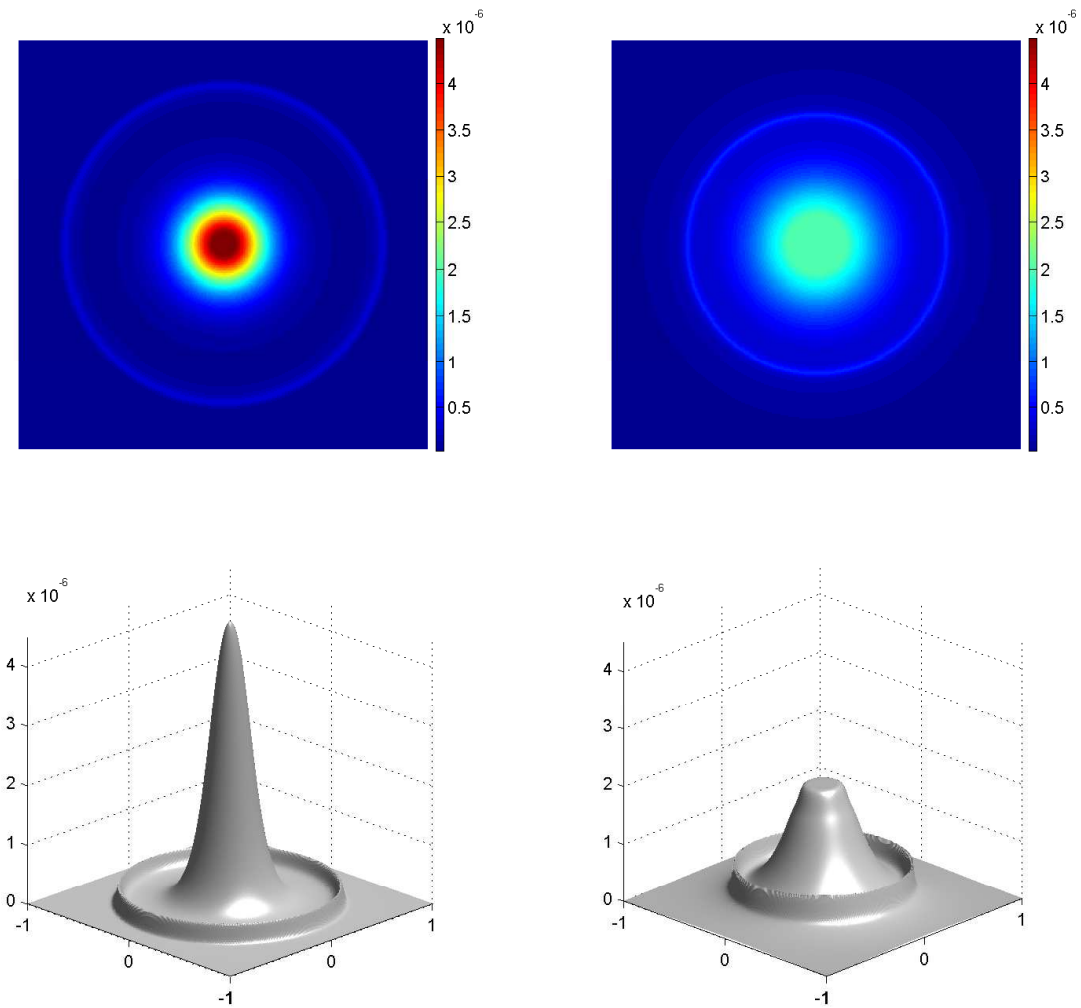

Figure 5.63: *Fourth chemotaxis example: Numerical solution for species u for $p=2$ (right), and $p=5$ (left) at the same instant $t=1$.*

More complex patterns can be driven by a slightly different model. Consider as a fifth chemotaxis example,

a quadratic domain $\Omega = [0, 16]^2$ and rewrite the first two equations of (1.45) in the form

$$\begin{aligned} u_t &= \nabla \cdot \big(\sigma |\nabla u|^{p-2} \nabla u - u\chi \nabla v\big) + g(u) \quad \text{on } Q_T, \\ v_t &= h(u, v) + d\Delta v \quad \text{on } Q_T. \end{aligned}$$

This model describes in particular the spatio-temporal aggregation patterns shown by the bacteria *Escherichia coli* (see e.g., [9]). Here $\chi = 7$, $g(u) = u^2(1-u)$, $h(u, v) = u - 32v$, $d = 1$ and $\sigma = 0.0625$. The initial concentration for the bacteria is randomly distributed: $(u_0, v_0) = (1 + \epsilon(x), 1/32)$, where $\epsilon(x)$ is a particular smooth perturbation which goes to zero near $(8, 8)$. We simulate the process until the solution reaches inhomogeneous stationary states, and again, from Figure 5.64 we see different patterns obtained by using both $p = 2$ and $p = 4$.

Let us mention, roughly speaking, that these numerical examples show at least qualitatively that the smaller the value of p, the steeper becomes the solution. This property is clearly related to the proportional relation between p and the Hölder exponent α, as we see the particular form of α (which depends on σ, and σ depending on s_1 and thus on n) and provided that we can bound uniformly $\|\nabla v\|^{p'}_{L^{p'p}(Q_T)}$. Also notice that in examples 4 and 5, growth functions $g(u, v)$ and $g(v)$ respectively, are considered for the equation modeling the dynamics of the cell's density. We point out that the inclusion of these terms is not considered in the previous performed analysis. Nevertheless, depending strongly on the growth structure of such terms (see e.g. [150]), natural changes may be applied to the proofs of existence and regularity of weak solutions, covering in this way the theory for these examples.

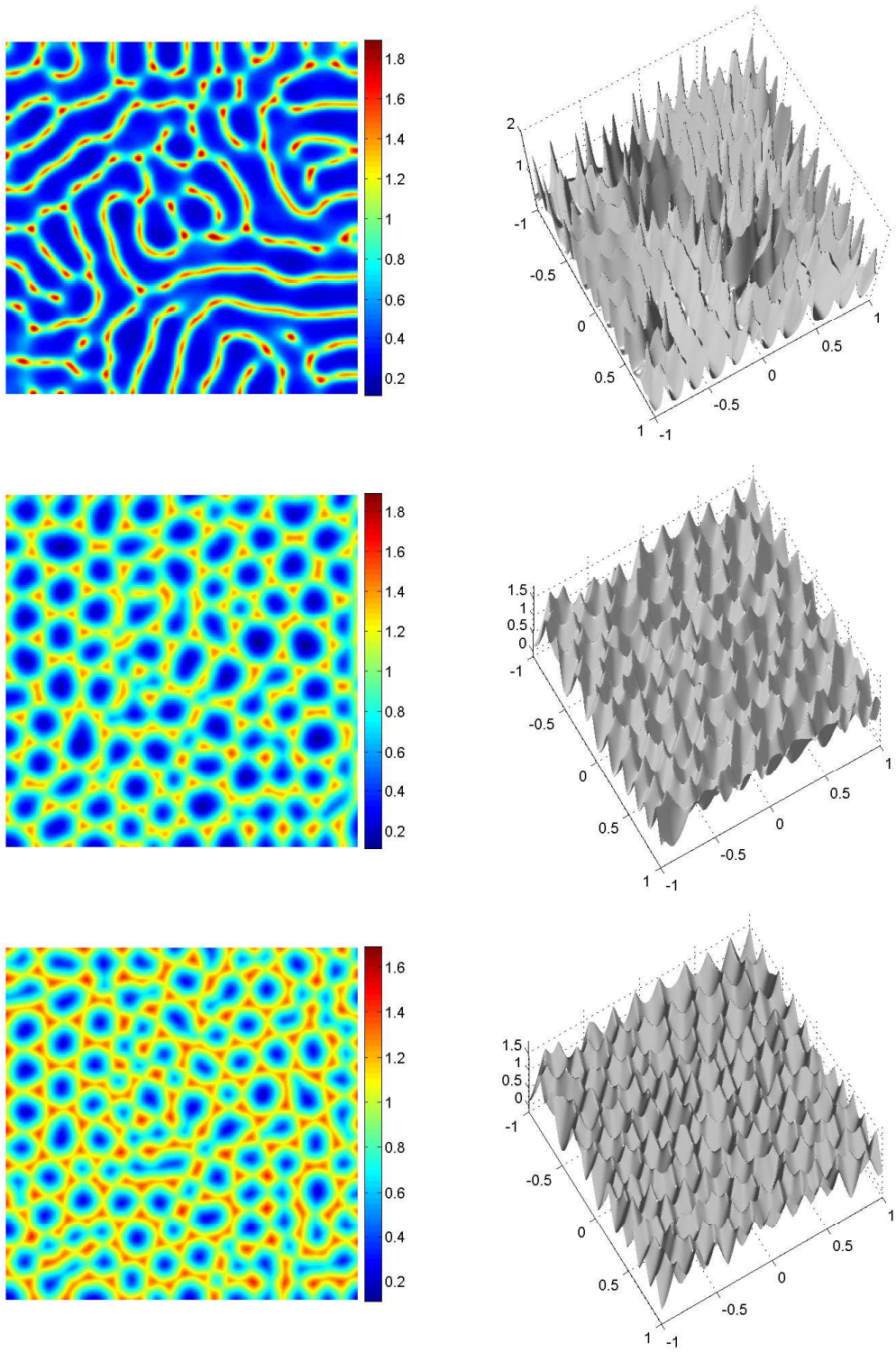

Figure 5.64: *Fifth chemotaxis example: Numerical solution for species u at $t = 25$ for $p = 2$ (top), $p = 4$ (middle) and $p = 6$ (bottom).*

Chapter 6

Summary and concluding remarks

In the previous Chapters of this thesis we have described the primary goals of our research, namely the numerical and mathematical analysis of degenerate parabolic equations, the construction of finite volume schemes for these problems, and the application of techniques arising from wavelet theory to improve the performance of the reference schemes. Two years ago we structured the proposal of this doctoral thesis in four main steps:

Implementation of a numerical method. Aim: A feasibility study, preliminary results and extension to the results in [135].

Application to sedimentation and traffic flow models. Aim: To use the multiresolution approach to improve existing FV results in these applications.

Study of reaction-diffusion systems. Aim: A feasibility study and preliminary results, extension of the previous steps to systems and 2-D.

Analysis of degenerate parabolic equations. Aim: Wellposedness theory for a class of solutions, regularity results for weak solutions, construction, implementation and convergence results for suitable FV schemes.

In addition to the successful development of these steps, we have also worked on the wellposedness and convergence analysis of a finite volume method for cardiac models. To finalize this thesis, a summary of the main findings, highly motivated by the numerical and computational challenges observed in the mathematical models considered, is discussed.

Implementation of a numerical method

We have shown that the multiresolution approach is a suitable tool for the study of degenerate parabolic equations. Concerning this subject we have presented numerical results using a fully space–time adaptive

finite volume-multiresolution scheme developed to be used for strongly degenerate parabolic equations. The strong degeneracy of the diffusive term leads to solutions that are discontinuous in general, and in particular exhibit sharp interfaces where the equation changes between parabolic and hyperbolic type. Multiresolution schemes are natural candidates of adaptive schemes to capture these interfaces along with the classical shocks appearing in hyperbolic regions. The numerical results shown herein confirm that the proposed schemes are indeed well adapted to this kind of equations. We have also examined the advantage of the multiresolution approach compared with standard FV schemes. In our experiments, we have obtained a considerable speed-up on the computations and also a substantial memory compression, while keeping the same accuracy order as in the reference schemes. The approximation order of the FV scheme is maintained due to a suitable choice of the threshold, which is a considerable improvement with respect to other multiresolution schemes where the tolerance is chosen in practice heuristically. Time step control is then introduced using an embedded RKF method which permits to adjust the time step automatically and to control the error. Different examples in one space dimension for sedimentation processes and traffic flow show the validity and efficiency of the new scheme. The interplay of the key ingredients mentioned above could represent an asset specially in the case of large number of mesh elements, systems, higher space dimensions and when the reference scheme is computationally expensive. Although we deal only with scalar and one space dimension applications, it is known that the main features of our method (i.e., Runge–Kutta Fehlberg time stepping, general multiresolution and FV schemes) are applicable for the mentioned extensions.

The success of the improvements to the reference scheme depends on the proper tuning of the parameters, especially for the adaptivity of the time stepping. Also it is known that the efficiency of the multiresolution strategy is problem dependent. These are very delicate issues, and they are subject of future work. Possible extensions include the use of penalization methods for complex domains and schemes with local time adaptivity.

Application to sedimentation and traffic flow models

We have used the developed multiresolution approach to improve existing FV results. Before discussing our results, we comment that the standings of both applicative models are slightly different. Numerous mathematical models have been proposed for one-directional flows of vehicular traffic; reviews of this topic are given in the monographs by Helbing [88], Kerner [104] and Garavello and Piccoli [79], as well as in the articles by Bellomo et al. [4, 5, 6]. These and other works vividly illustrate that the number of balance equations (for the car density, velocity, and possibly other flow variables) that form a time-dependent model based on partial differential equations, as well as the algebraic structure of these equations, is a topic of current research. Fortunately, all these models are spatially one-dimensional, and a circular road with periodic boundary conditions provides a setup that is both physically meaningful (since the flow is horizontal) and easy to implement for numerical simulation. This setup, on one hand, is widely used to compare different traffic models, and on the other hand allows to assess the local influence and long-term behavior of nonlinearities and inhomogeneities such as the ones introduced in Section 5.2.1.

While the traffic problem highlights the use of the scheme used herein to explore different models, the clarifier-thickener model calls for an efficient tool to perform simulations, on one hand, related to clarifier-thickener design and control [36, 39], and on the other hand, to parameter identification calculations [58, 17]. In fact, depending on the parameters, clarifier-thickener operations such as fill-up may extend over weeks and months [39], and require large simulation times, while the parameter identification procedures in [58, 17] proceed by solution of an adjoint problem, which needs storage of the complete solution of the previously solved direct problem. Clearly, methods that imply savings in both computational time and memory storage, such as the multiresolution scheme presented herein, are of significant practical interest for the clarifier-thickener model.

Both mathematical models considered herein exhibit three types of fronts that typically occur in solutions of (1.9), namely standard shocks (i.e., discontinuities between solution values for both of which (1.9) is hyperbolic), hyperbolic-parabolic type-change interfaces (such as the sediment level), and stationary discontinuities located at the discontinuities of $\boldsymbol{\gamma}(x)$. The basic motivation for applying a finite volume multiresolution scheme is that this device is is sufficiently flexible to produce the refinement necessary to properly capture all these discontinuities, and leads to considerable gains in storage as can be seen from the sparsity of the graded trees in our numerical examples. Moreover, Figure 5.20 confirms that we may effectively control the perturbation error, in the sense that the error of the resulting finite volume multiresolution scheme remains of the same order as that of the finite volume scheme on a uniform grid. We recall from Section 3.3 that the feasibility of this control depends on an estimate of the convergence rate of the basic discretization on a uniform grid, which is an open problem for strongly degenerate parabolic equations.

On the other hand, the basic finite volume scheme accurately resolves the discontinuities of the solution sitting at the jumps of $\boldsymbol{\gamma}(x)$ at any level of discretization; these discontinuities are not approximated by smeared transitions (as are discontinuities at positions where $\boldsymbol{\gamma}(x)$ is smooth), see [35]. This means that the refinement the multiresolution produces near these discontinuities, which is visible in Figures 5.22 and 5.23, and which is based on the adaptation of the refinement according to features of the solution (but not of $\boldsymbol{\gamma}(x)$), is possibly unnecessary, and that a more efficient version of the present method may be feasible.

Our results concerning these applications are given in [40, 41, 42].

Study of degenerate reaction-diffusion systems

We presented a feasibility study and preliminary results, as an extension of the previous steps to degenerate reaction-diffusion systems in two and three-space dimensions. We address the application of a MR method for FV schemes combined with LTS and RKF adaptive time stepping for solving several degenerate reaction-diffusion systems including the Keller-Segel equations, the Turing pattern-formation system, a model for flame balls instabilities, and the bidomain equations in electrocardiology. The numerical experiments illustrate that the used methods are efficient and accurate enough to efficiently simulate the phenomena mentioned above with affordable effort. This is a real advantage in comparison with more involved methods that require large scale computations on clusters. We here contribute to the recent work done by several groups in testing whether the combination of MR, LTS and RKF strategies is indeed effective for a relevant class of problems. From a numerical point of view, the plateau-like structures, associated with very steep gradients, of typical solutions motivate the use of a locally refined adaptive mesh, since we require high resolution near these steep gradients only. These areas of strong variation occupy a very reduced part of the entire domain only, especially in the case of sharp fronts. Consequently our gain will be less significant in the presence of chaotic solutions or when multiple waves interact in the considered domain. Based on our numerical examples, we conclude that using a LTS strategy, we obtain a substantial gain in CPU time speed-up for a factor of about 2 for larger scales while the errors between the MR-LTS solution and a reference solution are of the same order as those of the MR solution. On the other hand, using an MR-RKF strategy, we obtain an additional speed-up factor of about 4, but at the price of larger errors. However, in assessing our findings, it is important to recognize limitations. The high rates of compression obtained with our methods are problem-dependent and they may depend on the proper adjustment of parameters. We have only considered here very simple geometries, because all computations are concentrated on adaptivity and performance. Simulations on more complex and realistic geometries are part of possible future work. The motivation to employ explicit schemes only is the following. Even though implicit methods allow larger time steps, we need to iteratively solve a nonlinear system in each time step, using e.g. a Newton-Raphson method. The number of iterations is usually controlled by measuring the residual error, and cannot be controlled a priori. Thus, it appears difficult to assess the true benefits of a time-stepping strategy if the

basic time discretization is an implicit one. On the other hand, of course, for the Turing-type pattern formation problem, it is conceded that patterns appear when one eigenvalue goes from negative to positive. At steady state (when the pattern is visible) all the eigenvalues again have negative real part. Thus to converge to steady state once the domain of attraction of the pattern is reached, implicit methods offer significant advantages since they can use larger and larger time steps. We remark that for hyperbolic problems, the incorporation of an implicit time discretization to the MR-LTS strategy can possibly form a substantial improvement in the speed-up rate, as presented in [119]. Our results concerning these applications are given in [9, 10, 7].

Furthermore, we have focused our attention in the wellposedness and regularity analysis concerning one of the discussed models, the Keller-Segel equations. In [11] we have addressed the existence and regularity of weak solutions for a fully parabolic model of chemotaxis, with prevention of overcrowding, that degenerates in a two-sided fashion, including an extra nonlinearity represented by a p-Laplacian diffusion term. To prove the existence of weak solutions, a Schauder fixed-point argument is applied to a regularized problem and the compactness method is used to pass to the limit. The local Hölder regularity of weak solutions is established using the method of intrinsic scaling and the results represent a contribution to showing, qualitatively, to what extent the properties of the classical Keller-Segel chemotaxis models are preserved in a more general setting. We have formulated and implemented a suitable finite volume scheme and some numerical examples illustrate the behavior of the model.

Finally, in [8] we combine the modern theory of nonlinear PDEs with constructive numerical techniques to study rigorously the question of the convergence of a numerical scheme for solving the bidomain equations in electrocardiology. We successfully developed, implemented, and tested both robust and efficient numerical methods for this kind of problems. We here prove existence and uniqueness of the approximate solution obtained using finite volume methods, and it is also shown that the numerical scheme converges to the corresponding weak solution for the monodomain model, and also for the bidomain equations in the special case of fibers aligned with the axis. The proof of existence of discrete solutions is obtained using a fixed point argument, then we obtain a priori estimates; and then after stating space and time translation estimates, we pass to the limit using Kolmogorov's compactness criterion. Finally, from 2D and 3D examples we obtain experimental rates of convergence slightly above order h for both models.

Bibliography

[1] H. Amann, *Nonhomogeneous linear and quasilinear elliptic and parabolic boundary value problems*, Function spaces, differential operators and nonlinear analysis, pp. 9–126, Teubner-Texte Math. 133 Teubner Stuttgart 1993.

[2] R. Becker and R. Rannacher, *An optimal control approach to a posteriori error estimation in finite element methods*, Acta Numer. **10** (2001), pp. 1–102.

[3] J. Bell, M.J. Berger, J. Saltzman and M. Welcome, *Three-dimensional adaptive mesh refinement for hyperbolic conservation laws*, SIAM J. Sci. Comput., **15** (1994) pp. 127–138.

[4] N. Bellomo and V. Coscia, *First order models and closure of the mass conservation equation in the mathematical theory of vehicular traffic flow*, C. R. Mecanique, **333** (2005), pp. 843–851.

[5] N. Bellomo, M. Delitalia and V. Coscia, *On the mathematical theory of vehicular traffic flow I. Fluid dynamic and kinetic modelling*, Math. Models Meth. Appl. Sci. **12** (2002), pp. 1801–1843.

[6] N. Bellomo, A. Marasco and A. Romano, *From the modelling of driver's behavior to hydrodynamic models and problems of traffic flow*, Nonlin. Anal. Real World Appl., **3** (2002), pp. 339–363.

[7] M. Bendahmane, R. Bürger and R. Ruiz, *Numerical solution of the bidomain model in electrocardiology by a multiresolution space-time adaptive scheme*, preprint 2008-10, Depto. Ing. Mat., U. de Concepción, available from `http://www.ing-mat.udec.cl/`; submitted.

[8] M. Bendahmane, R. Bürger and R. Ruiz, *A finite volume method for cardiac propagation*, preprint 2008-26, Depto. Ing. Mat., U. de Concepción, available from `http://www.ing-mat.udec.cl/`; submitted.

[9] M. Bendahmane, R. Bürger, R. Ruiz and K. Schneider, *Adaptive multiresolution schemes with local time stepping for two- dimensional degenerate reaction-diffusion systems*, preprint 2007-35, Depto. Ing. Mat., U. de Concepción, available from `http://www.ing-mat.udec.cl/`; submitted.

[10] M. Bendahmane, R. Bürger, R. Ruiz and K. Schneider, *Adaptive multiresolution schemes for reaction–diffusion systems*, submitted.

[11] M. Bendahmane, R. Bürger, R. Ruiz and J.M. Urbano, *On a doubly nonlinear diffusion model of chemotaxis with prevention of overcrowding*, preprint 2008-16, Depto. Ing. Mat., U. de Concepción, available from `http://www.ing-mat.udec.cl/`; submitted.

[12] M. Bendahmane and K.H. Karlsen, *Analysis of a class of degenerate reaction-diffusion systems and the bidomain model of cardiac tissue*, Netw. Heterog. Media, **1** (2006), pp. 185–218.

[13] M. Bendahmane and K.H. Karlsen, *Convergence of a finite volume scheme for the bidomain model of cardiac tissue*, Preprint 2007-24, Depto. Ing. Mat., U. de Concepción, available from `http://www.ing-mat.udec.cl/`; submitted.

[14] M. Bendahmane, K. H. Karlsen and J. M. Urbano, *On a two–sidedly degenerate chemotaxis model with volume–filling effect*, Math. Models and Meth. Appl. Sci., **17**(5) (2007), pp. 783–804.

[15] M.J. Berger and R.J. LeVeque, *Adaptive mesh refinement using wave-propagation algorithms for hyperbolic systems*, SIAM J. Numer. Anal., **35** (1998), pp. 2298–2316.

[16] M.J. Berger and J. Oliger, *Adaptive mesh refinement for hyperbolic partial differential equations*, J. Comput. Phys., **53** (1984), pp. 482–512.

[17] S. Berres, R. Bürger, A. Coronel and M. Sepúlveda, *Numerical identification of parameters for a strongly degenerate convection-diffusion problem modelling centrifugation of flocculated suspensions*, Appl. Numer. Math. **52** (2005), pp. 311–337.

[18] S. Berres, R. Bürger, K.H. Karlsen and E.M. Tory, *Strongly degenerate parabolic-hyperbolic systems modeling polydisperse sedimentation with compression*, SIAM J. Appl. Math., **64** (2003), pp. 41–80.

[19] B.L. Bihari and A. Harten, *Multiresolution schemes for the numerical solution of 2-D conservation laws I*, SIAM J. Sci. Comput., **18** (1997), pp. 315–354.

[20] P. Biler, *Local and global solvability of some parabolic systems modelling chemotaxis*, Adv. Math. Sci. Appl., **8** (1998), pp. 715–743.

[21] P. Biler and G. Wu, *Two-dimensional chemotaxis model with fractional diffusion*, Math. Mod. Appl. Sci., in press.

[22] L. Boccardo, F. Murat and J. P. Puel, *Existence of bounded solutions for nonlinear elliptic unilateral problems*, Ann. Math. Pura Appl., **4**(152) (1988), pp. 183–196.

[23] Y. Bourgault, Y. Coudière, and C. Pierre, *Existence and uniqueness of the solution for the bidomain model used in cardiac electro-physiology*, Nonlin. Anal. Real World Appl., to appear.

[24] H. Brezis, *Analyse Fonctionnelle, Théorie et Applications*, Mason, Paris (1983).

[25] N.F. Britton, *Reaction-Diffusion Equations and Their Application to Biology*, Academic Press, New York (1986).

[26] M. Burger, M. Di Francesco and Y. Dolak-Struss, *The Keller-Segel model for chemotaxis with prevention of overcrowding: linear vs. nonlinear diffusion*, SIAM J. Math. Anal., **38** (2007), pp. 1288–1315.

[27] R. Bürger, A. Coronel and M. Sepúlveda, *A semi-implicit monotone difference scheme for an initial-boundary value problem of a strongly degenerate parabolic equation modelling sedimentation-consolidation processes*, Math. Comp., **75** (2006), pp. 91–112.

[28] R. Bürger, A. Coronel and M. Sepúlveda, *On an upwind difference scheme for strongly degenerate parabolic equations modelling the settling of suspensions in centrifuges and non-cylindrical vessels*, Appl. Numer. Math., **56** (2006), pp. 1397–1417.

[29] R. Bürger, S. Evje and K.H. Karlsen, *On strongly degenerate convection-diffusion problems modeling sedimentation-consolidation processes*, J. Math. Anal. Appl., **247** (2000), pp. 517–556.

[30] Bürger R, García A, Karlsen KH, Towers JD, *On an extended clarifier-thickener model with singular source and sink terms*, Eur. J. Appl. Math., **17** (2006), pp. 257–292.

[31] R. Bürger and K.H. Karlsen, *On some upwind schemes for the phenomenological sedimentation-consolidation model*, J. Engrg. Math., **41** (2001), pp. 145–166.

[32] R. Bürger and K.H. Karlsen, *On a diffusively corrected kinematic-wave traffic model with changing road surface conditions*, Math. Models Meth. Appl. Sci., **13** (2003), pp. 1767–1799.

[33] R. Bürger, K.H. Karlsen, C. Klingenberg and N.H. Risebro, *A front tracking approach to a model of continuous sedimentation in ideal clarifier-thickener units*, Nonlin. Anal. Real World Appl., **4** (2003), pp. 457–481.

[34] R. Bürger, K.H. Karlsen and N.H. Risebro, *A relaxation scheme for continuous sedimentation in ideal clarifier-thickener units*, Comput. Math. Appl., **50** (2005), pp. 993–1009.

[35] R. Bürger, K.H. Karlsen, N.H. Risebro and J.D. Towers, *Well-posedness in BV_t and convergence of a difference scheme for continuous sedimentation in ideal clarifier-thickener units*, Numer. Math., **97** (2004), pp. 25–65.

[36] R. Bürger, K.H. Karlsen and J.D. Towers, *A model of continuous sedimentation of flocculated suspensions in clarifier-thickener units*, SIAM J. Appl. Math. **65** (2005), pp. 882–940.

[37] R. Bürger and A. Kozakevicius, *Adaptive multiresolution WENO schemes for multi-species kinematic flow models*, J. Comput. Phys., **224** (2007), pp. 1190–1222.

[38] R. Bürger, A. Kozakevicius and M. Sepúlveda, *Multiresolution schemes for strongly degenerate parabolic equations in one space dimension*, Numer. Meth. Partial Diff. Eqns., **23** (2007), pp. 706–730.

[39] R. Bürger and A. Narváez *Steady-state, control, and capacity calculations for flocculated suspensions in clarifier-thickeners*, Int. J. Mineral Process., to appear.

[40] R. Bürger, R. Ruiz, K. Schneider and M. Sepúlveda, *Fully adaptive multiresolution schemes for strongly degenerate parabolic equations in one space dimension*, Math. Model. Numer. Anal., **42** (2008), pp. 535–563.

[41] R. Bürger, R. Ruiz, K. Schneider, and M. Sepúlveda, *Fully adaptive multiresolution schemes for strongly degenerate parabolic equations with discontinuous flux*, J. Engrg. Math., **60** (2008), pp. 365–385.

[42] R. Bürger, R. Ruiz, K. Schneider, and M. Sepúlveda, *Fully adaptive multiresolution schemes for an extended clarifier–thickener model*, submitted.

[43] J. Carrillo, *Entropy solutions for nonlinear degenerate problems*, Arch. Rat. Mech. Anal., **147** (1999), pp. 269–361.

[44] C. Chainais-Hillairet, J-G. Liu and Y-J Peng, *Finite volume scheme for multi-dimensional drift-diffusion equations and convergence analysis*, M2AN Math. Model. Numer. Anal., **37**(2) (2003), pp. 319–338.

[45] G.Q. Chen and E. DiBenedetto, *Stability of entropy solutions to the Cauchy problem for a class of nonlinear hyperbolic-parabolic equations*, SIAM J. Math. Anal., **33** (2001), pp. 751–762.

[46] G.Q. Chen and B. Perthame, *Well-posedness for non-isotropic degenerate parabolic-hyperbolic equations*, Ann. Inst. H. Poincaré Anal. Non Linéaire, **20** (2003), pp. 645–668.

[47] H. Chen and X.-H. Zhong, *Global existence and blow-up for the solutions to nonlinear parabolic elliptic system modelling chemotaxis*, IMA J. Appl. Math., **70** (2005), pp. 221–240.

[48] E. Cherry, H. Greenside, and C.S. Henriquez, *Efficient simulation of three–dimensional anisotropic cardiac tissue using an adaptive mesh refinement method*, Chaos, **13** (2003), pp. 853–865.

[49] A. Chertok and A. Kurganov, *A positivity preserving central-upwind scheme for chemotaxis and haptotaxis models*. Preprint (2007); available at `http://www.math.tulane.edu/~kurganov/pub.html`.

[50] G. Chiavassa and R. Donat, *Point value multiresolution for 2D compressible flows*, SIAM J. Sci. Comput., **23** (2001), pp. 805–823.

[51] G. Chiavassa, R. Donat and S. Müller, *Multiresolution-based adaptive schemes for hyperbolic conservation laws*, in: T. Plewa, T. Linde and V.G. Weiss (Eds.), Adaptive Mesh Refinement—Theory and Applications, Lecture Notes in Computational Science and Engineering, Springer-Verlag, Berlin **41** (2003), pp. 137–159.

[52] C. Chiu and J.L. Yu, *An optimal adaptive time-stepping scheme for solving reaction-diffusion-chemotaxis systems*, Math. Bio. and Eng., **4** (2007), pp. 187–203.

[53] A. Cohen, S. Kaber, S. Müller and M. Postel, *Fully adaptive multiresolution finite volume schemes for conservation laws*, Math. Comp., **72** (2002), pp. 183–225.

[54] P. Colli Franzone, P. Deuflhard, B. Erdmann, J. Lang, and L.F. Pavarino, *Adaptivity in space and time for reaction–diffusion systems in electro-cardiology*, SIAM J. Sci. Comput., **28** (2006), pp. 942–962.

[55] P. Colli Franzone and L.F. Pavarino, *A parallel solver for reaction-diffusion systems in computational electro-cardiology*, Math. Models Meth. Appl. Sci., **14** (2004), pp. 883–911.

[56] P. Colli Franzone, L.F. Pavarino, and B. Taccardi, *Simulating patterns of excitation, repolarization and action potential duration with cardiac Bidomain and Monodomain models*, Math. Biosci., **197** (2005), pp. 35–66.

[57] P. Colli Franzone and G. Savaré, *Degenerate evolution systems modeling the cardiac electric field at micro- and macroscopic level*, Evolution equations, semigroups and functional analysis (Milano, 2000), pp. 49–78, Progr. Nonlinear Differential Equations Appl., 50, Birkhäuser, Basel (2002).

[58] A. Coronel, F. James and M. Sepúlveda, *Numerical identification of parameters for a model of sedimentation processes*, Inverse Problems, **19** (2003), pp. 951–972.

[59] Y. Coudière and C. Pierre, *Stability and convergence of a finite volume method for two systems of reaction–diffusion in electro–cardiology*, Nonl. Anal.: Real World Appl., **7** (2006), pp. 916–935.

[60] Y. Coudière, C. Pierre, and R. Turpault, *Solving the fully coupled heart and torso problems of electro-cardiology with a 3D discrete duality finite volume method*, HAL preprint (2006), available from `http://hal.archives-ouvertes.fr/ccsd-00016825`.

[61] M.G. Crandall and A. Majda, *Monotone difference approximations for scalar conservation laws*, Math. Comp., **34** (1980), pp. 1–21.

[62] W. Dahmen, B. Gottschlich-Müller, and S. Müller, *Multiresolution schemes for conservation laws*, Numer. Math., **88** (2001), pp. 399–443.

[63] P. Deuflhard and F. Bornemann, *Scientific Computing with Ordinary Differential Equations*, Springer-Verlag, New York (2002).

[64] F. Dkhil, *Singular limit of a degenerate chemotaxis-Fisher equation*, Hiroshima Math. J., **34** (2004), pp. 101–115.

[65] E. DiBenedetto, *Degenerate Parabolic Equations*, Springer-Verlag New York (1993).

[66] E. DiBenedetto, *On the local behaviour of solutions of degenerate parabolic equations with measurable coefficient*, Ann. Scuola Norm. Sup. Pisa Cl. Sci., **4**(13) (1986), pp. 487–535.

[67] E. DiBenedetto, J.M. Urbano and V. Vespri, *Current issues on singular and degenerate evolution equations*, Handbook of Differential Equations, Evolutionary Equations, vol.1 pp. 169–286 Elsevier/North-Holland Amsterdam (2004).

[68] A.C. Dick, *Speed/flow relationships within an urban area*, Traffic Eng. Control, **8** (1966), pp. 393–396.

[69] M. Domingues, O. Roussel and K. Schneider, *An adaptive multiresolution method for parabolic PDEs with time step control*, ESAIM: Proc., **16** (2007), pp. 181–194.

[70] M. Domingues, S. Gomes, O. Roussel and K. Schneider, *An adaptive multiresolution scheme with local time-stepping for evolutionary PDEs*, J. Comput. Phys., (2008) doi:10.1016/j.jcp.2007.11.046.

[71] P. Drábek, *The p-Laplacian—mascot of nonlinear analysis*, Acta Math. Univ. Comen., **77** (2007), pp. 85–98.

[72] M. Efendiev, M. Kläre, and R. Lasser, *Dimension estimate of the exponential attractor for the chemotaxis-growth system*, Math. Meth. Appl. Sci., 30 (2007), pp. 579–594.

[73] B. Engquist and S. Osher, *One-sided difference approximations for nonlinear conservation laws*, Math. Comp., **36** (1981), pp. 321–351.

[74] E. Entcheva, J. Eason, F. Claydon, and R. Malkin, *Spatial effects from bipolar current injection in 3D myocardium: implications for conductivity measurements*, Computers in Cardiology, **7** (1997), pp. 717–720.

[75] S. Evje and K.H. Karlsen, *Monotone difference approximations of BV solutions to degenerate convection-diffusion equations*, SIAM J. Numer. Anal., **37** (2000), pp. 1838–1860.

[76] R. Eymard, T. Gallouët, and R. Herbin, *Finite volume methods*. In: Handbook of Numerical Analysis, vol. VII, North-Holland, Amsterdam (2000).

[77] E. Fehlberg, *Low order classical Runge-Kutta formulas with step size control and their application to some heat transfer problems*, Computing, **6** (1970), pp. 61–71.

[78] R. FitzHugh, *Impulses and physiological states in theoretical models of nerve membrane*, Biophys. J., **1** (1961), pp. 445–465.

[79] M. Garavello and B. Piccoli, *Traffic Flow on Networks*, American Institute of Mathematical Sciences, Springfield, MO, USA (2006).

[80] H. Garcke, B. Nestler, and B. Stoth, *A Multiphase Field Concept: Numerical Simulations of Moving Phase Boundaries and Multiple Junctions*, SIAM J. Appl. Math., **60** (2000), pp. 295–315.

[81] H. Greenberg, *An analysis of traffic flow*, Oper. Res., **7** (1959), pp. 79–85.

[82] E. Godlewski and P.A. Raviart, *Numerical Approximation of Hyperbolic Systems of Conservation Laws*, Springer-Verlag, New York (1996).

[83] B. Gottschlich-Müller, *Multiscale Schemes for Conservation Laws*, PhD. Thesis, RWTH Aachen (1998).

[84] W.S.C. Gurney and R.M. Nisbet, *The regulation of inhomogeneous populations* J. Theor. Bio., **52** (1975), pp. 441–457.

[85] M.E. Gurtin and R.C. McCamy, *On the diffusion of biological populations*, Math. Biosc. **33** (1977), pp. 35–49.

[86] E. Hairer, S.P. Nørsett and G. Wanner, *Solving Ordinary Differential Equations I. Nonstiff Problems*, Second Edition, Springer-Verlag, Berlin (1993).

[87] A. Harten, *Multiresolution algorithms for the numerical solution of hyperbolic conservation laws*, Comm. Pure Appl. Math., **48** (1995), pp. 1305–1342.

[88] D. Helbing, *Verkehrsdynamik*, Springer-Verlag, Berlin (1997).

[89] D. Harrild and C.S. Henriquez, *A Finite Volume Model of Cardiac Propagation*, Ann. Biomed. Eng. **25** (1997), pp. 315–334.

[90] M.A. Herrero and J.J.L. Velàzquez, *Chemotactic collapse for the Keller-Segel model*, J. Math. Biol., **35** (1996), pp. 177–194.

[91] A.L. Hodgkin and A.F. Huxley, *A quantitative description of membrane current and its application to conduction and excitation in nerve*, J. Physiol., **117** (1952), pp. 500–544.

[92] H. Holden, K.H. Karlsen, and N.H. Risebro, *On uniqueness and existence of entropy solutions of weakly coupled systems of nonlinear degenerate parabolic equations*, Electron. J. Differential Equations, **46** (2003), pp. 1–31.

[93] D. Horstmann, *From 1970 until present: the Keller-Segel model in chemotaxis and its consequences, I*, Jahresber. Deutsch. Math.-Verein., **105**(3) (2003), pp. 103–165.

[94] D. Horstmann, *From 1970 until present: the Keller-Segel model in chemotaxis and its consequences, II*, Jahresber. Deutsch. Math.-Verein., **106** (2004), pp. 51–69.

[95] P.R. Johnston, *The effect of simplifying assumptions in the bidomain model of cardiac tissue: Application to ST segment shifts during partial ischaemia*, Math. Biosci., **198** (2005), pp. 97–118.

[96] K.H. Karlsen, C. Klingenberg and N.H. Risebro, *A relaxation scheme for conservation laws with a discontinuous coefficient*, Math. Comp., **73** (2003), pp. 1235–1259.

[97] K.H. Karlsen and N.H. Risebro, *Convergence of finite difference schemes for viscous and inviscid conservation laws with rough coefficients*, M^2AN Math. Model. Numer. Anal., **35** (2001), pp. 239–269.

[98] K.H. Karlsen and N.H. Risebro, *On the uniqueness and stability of entropy solutions of nonlinear degenerate parabolic equations with rough coefficients*, Discrete Contin. Dyn. Syst., **9** (2003), pp. 1081–1104.

[99] K.H. Karlsen, N.H. Risebro and J.D. Towers, *L^1 stability for entropy solutions of nonlinear degenerate parabolic convection-diffusion equations with discontinuous coefficients*, Skr. K. Nor. Vid. Selsk., (2003), pp. 1–49.

[100] K.H. Karlsen, N.H. Risebro and J.D. Towers, *On a nonlinear degenerate parabolic transport-diffusion equation with a discontinuous coefficient*, Electron. J. Diff. Eqns., **93** (2002), pp. 1–23.

[101] K.H. Karlsen, N.H. Risebro and J.D. Towers, *On an upwind difference scheme for degenerate parabolic convection-diffusion equations with a discontinuous coefficient*, IMA J. Numer. Anal., **22** (2002), pp. 623–664.

[102] J. Keener and J. Sneyd, *Mathematical Physiology*, Corr. Second Printing, Springer-Verlag, New York (2001).

[103] E.F. Keller and L.A. Segel, *Model for chemotaxis*, J. Theor. Biol., **30** (1971), pp. 225–234.

[104] B.S. Kerner, *The Physics of Traffic*, Springer-Verlag, Berlin (2004).

[105] S.N. Kružkov, *First order quasi-linear equations in several independent variables*, Math. USSR Sbornik, **10** (1970), pp. 217–243.

[106] N.N. Kuznetsov, *Accuracy of some approximate methods for computing the weak solutions of a first order quasilinear equation*, USSR Comp. Math. and Math. Phys., **16** (1976), pp. 105–119.

[107] O.A. Ladyzhenskaya, V. Solonnikov and N. Ural'ceva, *Linear and quasi-linear equations of parabolic type*, Transl. AMS 23, Providence (1968).

[108] P. Lamby, S. Müller, and Y. Stiriba, *Solution of shallow water equations using fully adaptive multiscale schemes*, Int. J. Numer. Meth. Fluids, **49** (2005), pp. 417–437.

[109] P. Laurençot and D. Wrzosek, *A chemotaxis model with threshold density and degenerate diffusion*, Nonlinear Elliptic and Parabolic Problems: Progr. Nonlinear Differential Equations Appl., 64:273–290, Birkhäuser, Boston (2005).

[110] M.J. Lighthill and G.B. Whitham, *On kinematic waves. II. A theory of traffic flow on long crowded roads*, Proc. Roy. Soc. London Ser. A, **229** (1955), pp. 317–345.

[111] J.-L. Lions, *Quelques méthodes de résolution des problèmes aux limites non linéaires*, Dunod, Paris (1969).

[112] C. Mascia, A. Porretta, and A. Terracina, *Nonhomogeneous Dirichlet problems for degenerate parabolic-hyperbolic equations*, Arch. Ration. Mech. Anal., **163** (2002), pp. 87–124.

[113] A. Michel and J. Vovelle, *Entropy formulation for parabolic degenerate equations with general Dirichlet boundary conditions and application to the convergence of FV methods*, SIAM J. Numer. Anal. **41** (2003), pp. 2262–2293.

[114] M. Mimura and T. Tsujikawa, *Aggregating pattern dynamics in a chemotaxis model including growth*, Physica A, **230** (1996), pp. 499–543.

[115] G. Minty, *Monotone operators in Hilbert spaces*, Duke Math. J., **29** (1962), pp. 341–346.

[116] C. Mitchell and D. Schaeffer, *A two-current model for the dynamic of cardiac membrane*, Bull. Math. Bio., **65** (2001), pp. 767–793.

[117] S. Mochon, *An analysis of the traffic on highways with changing surface conditions*, Math. Modelling, **9** (1987), pp. 1–11.

[118] S. Müller, *Adaptive Multiscale Schemes for Conservation Laws*, Springer-Verlag, Berlin (2003).

[119] S. Müller and Y. Stiriba, *Fully adaptive multiscale schemes for conservation laws employing locally varying time stepping*, J. Sci. Comput., **30** (2007), pp. 493–531.

[120] J.D. Murray, *Parameter space for Turing instability in reaction diffusion mechanisms: a comparison of models*, J. Theor. Biol., **98** (1982), pp. 143–163.

[121] J.D. Murray, *Mathematical Biology II: Spatial Models and Biomedical Applications*, Third Edition, Springer-Verlag, New York (2003).

[122] J.S. Nagumo, S. Arimoto, and S. Yoshizawa, *An active pulse transmission line simulating nerve axon*, Proc. Inst. Radio Eng., **50** (1962), pp. 2061–2071.

[123] P. Nelson, *Traveling-wave solutions of the diffusively corrected kinematic-wave model*, Math. Comp. Modelling, **35** (2002), pp. 561–579.

[124] D. Noble, *A modification of the Hodgkin-Huxley equations applicable to Purkinje fibre action and pacemaker potentials*, J. Physiol., **160** (1962), pp. 317–352.

[125] S. Osher and R. Sanders, *Numerical approximations to nonlinear conservation laws with locally varying time and space grids*, Math. Comp., **41** (1983), pp. 321–336.

[126] M. Pennacchio and V. Simoncini, *Efficient algebraic solution of reaction-diffusion systems for the cardiac excitation process*, J. Comput. App. Math., **145** (2002), pp. 49–70.

[127] M. Pérez, R. Font and C. Pastor, *A mathematical model to simulate batch sedimentation with compression behavior*, Comp. Chem. Eng., **22** (1998), pp. 1531–1541.

[128] M. Porzio and V. Vespri, *Holder estimates for local solutions of some doubly nonlinear degenerate parabolic equations*, J. Diff. Eq., **103** (1993), pp. 146–178.

[129] W. Quan, S. Evans, and H. Hastings, *Efficient integration of a realistic two-dimensional cardiac tissue model by domain decomposition*, IEEE Trans. Biomed. Eng., **45** (1998), pp. 372–385.

[130] P.I. Richards, *Shock waves on the highway*, Oper. Res., **4** (1956), pp. 42–51.

[131] O. Roussel, *Development of a three–dimensional adaptive multiresolution algorithm for parabolic PDEs. Application to thermodiffusive flame instabilities*, PhD thesis, Université Aix-Marseille II (2003).

[132] O. Roussel and K. Schneider, *An adaptive multiresolution method for combustion problems: application to flame ball-vortex interaction*, Comp. & Fluids, **34** (2005), pp. 817–831.

[133] O. Roussel and K. Schneider, *Numerical study of thermodiffusive flame structures interacting with adiabatic walls using an adaptive multiresolution scheme*, Combust. Theory Modelling, **10** (2006), pp. 273–288.

[134] O. Roussel, K. Schneider, A. Tsigulin and H. Bockhorn, *A conservative fully adaptive multiresolution algorithm for parabolic conservation laws*, J. Comput. Phys. **188** (2003), pp. 493–523.

[135] R. Ruiz, *Métodos de Multiresolución y su Aplicación a un Problema de Ingeniería*, Tesis para optar al título de Ingeniero Matemático, Universidad de Concepción (2005).

[136] H. Saleheen and K. Ng, *A new three–dimensional finite-difference bidomain formulation for inhomogeneous anisotropic cardiac tissues*, IEEE Trans. Biomed. Eng., **45** (1998), pp. 15–25.

[137] J. Schnakenberg, *Simple chemical reaction systems with limit cycle behaviour*, J. Theor. Biol., **81** (1979), pp. 389–400.

[138] C.-W. Shu, *Essentially non-oscillatory and weighted essentially non-oscillatory schemes for hyperbolic conservation laws.* In: B. Cockburn, C. Johnson, C.-W. Shu and E. Tadmor, Advanced Numerical Approximation of Nonlinear Hyperbolic Equations (A. Quarteroni, Ed.), Springer-Verlag, Berlin (1998), pp. 325–432.

[139] J. Simon, *Compact sets in the space $L^p(0,T;B)$*, Ann. Mat. Pura Appl., (4) **146** (1987), pp. 65–96.

[140] K. Skouibine, N. Trayanova, and P. Moore, *A numerically efficient model for simulation of defibrillation in an active bidomain sheet of myocardium*, Math. Biosci., **166** (2000), pp. 85–100.

[141] J. Stoer and R. Bulirsch, *Numerische Mathematik 2*, Third Edition, Springer-Verlag, Berlin (1990).

[142] E. Süli and D.F. Mayers, *An introduction to numerical analysis*, Cambridge University Press, Cambridge (2003).

[143] J. Sundnes, G.T. Lines, X. Cai, B.F. Nielsen, K.-A. Mardal, and A. Tveito, *Computing the electrical activity in the heart*, Springer-Verlag, Berlin (2006).

[144] J. Trangenstein and C. Kim, *Operator splitting and adaptive mesh refinement for the Luo-Rudy I model*, J. Comput. Phys., **196** (2004), pp. 645–679.

[145] M. Trew, I. Grice, B. Smaill and A. Pullan, *A Finite Volume Method for Modeling Discontinuous Electrical Activation in Cardiac Tissue*, Ann. Biomed. Eng., **33** (2005), pp. 590–602.

[146] L. Tung, *A bi-domain model for describing ischemic myocordial D-C currents*, PhD thesis, MIT, Cambridge, MA (1978).

[147] A.M. Turing, *The chemical basis of morphogenesis*, Phil. Trans. Royal Soc. London Ser. B, **237** (1952), pp. 37–72.

[148] R. Tyson, S.R. Lubkin and J.D. Murray, *Model and analysis of chemotactic bacterial patterns in a liquid medium*, J. Math. Biol., **38** (1999), pp. 359–375.

[149] J.M. Urbano, *Hölder continuity of local weak solutions for parabolic equations exhibiting two degeneracies*, Adv. Diff. Eqs., **6** (2001), pp. 327–358.

[150] J.M. Urbano, *The Method of Intrinsic Scaling: A Systematic Approach to Regularity for Degenerate and Singular PDEs*, Lecture Notes in Mathematics, Vol. 1930, Springer-Verlag, New York (2008).

[151] M. Veneroni, *Reaction-Diffusion systems for the macroscopic Bidomain model of the cardiac electric field*, Nonl. Anal.: Real World Appl., to appear.

[152] A.I. Vol'pert, *The spaces BV and quasilinear equations*, Math. USSR Sb, **2** (1967), pp. 225–267.

[153] A.I. Vol'pert and S.I. Hudjaev, *Cauchy's problem for degenerate second order quasilinear parabolic equations*, Math USSR. Sb, **7** (1969), pp. 365–387.

[154] T.P. Witelski, *Segregation and mixing in degenerate diffusion in population dynamics*, J. Math. Biol., **35** (1997), pp. 695–712.

[155] Z. Wu, J. Zhao, J. Yin and H. Li, *Nonlinear Diffusion Equations*, World Scientific: Singapore (2001).

[156] A. Yagi, *Norm behavior of solutions to a parabolic system of chemotaxis*, Math. Japon., **45** (1997), pp. 241–265.

[157] W.-J. Ying, *A multilevel adaptive approach for computational cardiology*, PhD Thesis, Department of Mathematics, Duke University (2005).

[158] W.-J. Ying, D.J. Rose, and C.S. Henriquez, *Efficient fully implicit time integration methods for modeling cardiac dynamics*, Technical Report, Duke University (2007).